Nanostructuring $Gd_5(Si,Ge)_4$ multifunctional materials

João Horta Belo
MAP-FIS doctoral Program in Physics
Department of Physics and Astronomy
Faculty of Sciences
University of Porto
2017

Supervisor
Prof. João Pedro Esteves de Araújo, FCUP

Co-Supervisor
Prof. André Miguel Trindade Pereira, FCUP

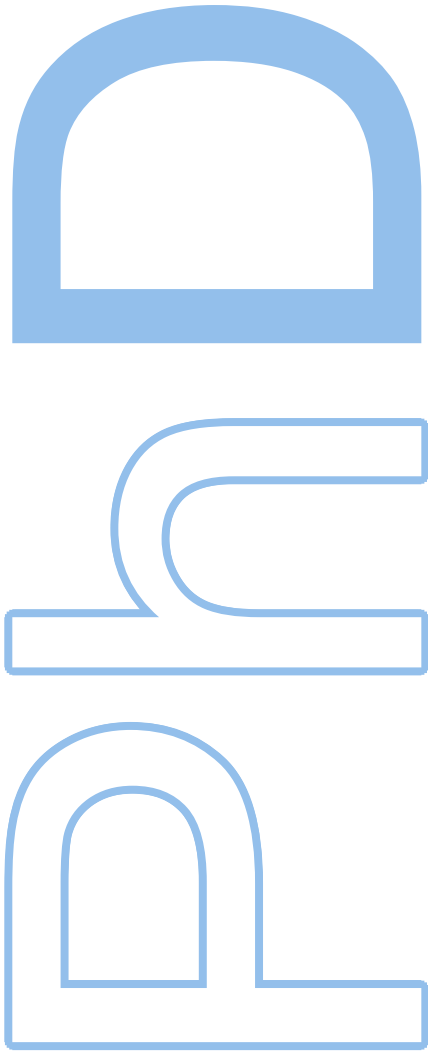

João Filipe Horta Belo da Silva

Nanostructuring $Gd_5(Si,Ge)_4$ multifunctional materials

Supervisor: *Prof. João Pedro Esteves de Araújo*
Co-Supervisor: *Prof. André Miguel Trindade Pereira*

Thesis submitted to the Faculty of Sciences of the University of Porto in partial fulfilment of the requirements for the degree of Doctor in Physics

Department of Physics and Astronomy
Faculty of Sciences of the University of Porto
2017

Institutions involved in this thesis:

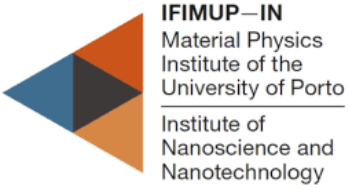

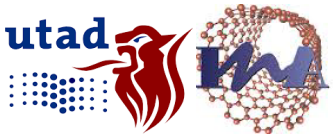

Funding:

Acknowledgements

This thesis describes the work developed during the last four years at the Multifunctional Magnetic Materials and Nanostructures group within IFIMUP-IN in Porto and also at INA in Saragoça. I would like to thank the organizations directly involved in this work: the Institute of Nanoscience and Nanotechnology (IFIMUP-IN) of the University of Porto and the Physics and Astronomy department of the Faculty of Sciences of University of Porto (FCUP) and the Instituto de Nanociencia de Aragon (INA) of the University of Saragoza. I would like to thank also the following institutions and all the staff that worked with me and made possible the challenging experiments performed, in particular the staff at Ames Laboratory, US Department of Energy, Iowa State University, Iowa, USA, at Blackett Laboratory, Imperial College, London, United Kingdom, and at Argonne Photon Source, Chicago, USA.

Furthermore, I would like to thanks to FCT for my PhD scholarship with reference SFRH/BD/88440/2012.

Fearing to forget someone, I must begin by saying that it was a privilege to work with all the Professors, colleagues and younger students from whom I got the chance to learn and grow as a man and as a scientist. Thank you!

I would not have had the privilege to work in IFIMUP-IN if it was not for Professor João Pedro, my supervisor, that was responsible for bringing me inside the group, giving me the opportunity that I will never forget. Thank you for your wise advices, for your endless in-depth knowledge and for your joy to share - your attitude towards science inspired and me and will continue to inspire the younger ones.

To Professor André Pereira, my co-supervisor, to whom all the words would not be enough to express my gratitude. Along the seven years I´ve been in IFIMUP, you were always my tutor, my teacher and my friend. Your energetic enthusiasm, your courage and your insightful knowledge make me feel blessed to have worked with you and to have you as a friend. Thank you for all the patience on my bad days, for all the international adventures, for all the beers and life advices, I just can not thank you enough.

To Professor Luis Morellón, my spanish ”supervisor”, for his great knowledge and important insights in thin film preparation. For his sympathy, and for making me feel at home from the very first day. Thank you for your trust and friendship.

To Professor João Bessa for his patience and the rich conversations. It really was the best finale for my thesis work to have had the privilege to learn from you Professor. Thank you for the enthusiasm and encouraging words.

To Gonçalo Oliveira, partner alongside during this journey. For all the pauses, for all the lab knowledge, for all the uncountable help and for your true and sincere friendship.

This would have been much harder without you alongside. You will continue to inspire me.

To Ana Pires, for all your patience, kindness and availability. Thank you for being there even when I was in a bad mood. Thank you for your will to learn and for the joy you bring to the workplace and for rapidly becoming one important pillar to me.

To João Ventura, for being the way you are. For the support in the most strangest ways and for the advices in the right time. For the constant bugging and endless support, for your trust and friendship.

To Irene Lucas, for being the friend, the teacher and the support in Saragoça. Thank you for your passion, your organization, your advices and your always positive attitude- I admire you deeply. Muchas gracias por todo!

To Pavel Strichovanec for all your patience and Sputtering insight. Thank you for teaching me and for your friendship.

To Vivian Andrade, for your patience too, for your energy and the will to change the world. Thank you for continuing this work and for your knowledge, effort and courage.

To Francisco Carpinteiro for the crucial help in harder times - when machines fail. Thank you for your patience and for your shared knowledge on all the lab work.

To Ravi Hadimani for the proficuous collaboration from which resulted several published articles and part of the results presented in this thesis.

To the fellow researchers at the Multifunctional Magnetic Materials and Nanostructures group: Ana Pires, André Pereira, Aurélio, Arlete Apolinário, Armandina Lopes, Bogdan Postolnyi, Catia, Catarina Dias, Célia Sousa, Daniel Silva, Francisco Carpinteiro, Inês Figueiredo, João Amaral, Gonçalo Oliveira, João Ventura, Joel Puga, José Miguel Teixeira, Monica Cerquido, Luís Guerra, Maria Paz, Mariana Proença, Marcelo Barbosa, Paula Quitério, Rui Costa, Rui S. Costa, Sara Pinto, Vivian Andrade. Thank you all for being my second family for so many years.

In particular thank you Arlete Apolinário and to Célia Sousa for their endless joy, kindness, friendship and example. To João Amaral for all the important insights and his will to teach. Thank you for always opened new windows in my future. Thank you for the conferences, dinners and beers. Thank you for your friendship.

To Professor Pedro Algarabel and Cesar Magen, for their important discussions and for the TEM analysis, respectively. To all colleagues and friends at INA, muchas muchas gracias!

To Doctor Yang Ren from the Advanced Photon Source in Argonne National Laboratory for the help during the Synchrotron High-Resolution X-ray Difraction measurements.

To Doctor Pedro Tavares and Lisete Fernandes for their sympathy and support on the XRD and SEM/EDS measurements at Universidade de Trás-os-Montes e Alto-Douro (UTAD).

To Professor João Pedro Conde and Dr. Virginia Chu for the very interesting collaboration work with the magnetostrictive cantilevers. I hope the future will bring us back to this work. Thank you Rui Pinto for being my guide and my teacher at INESC-MN in

Lisbon.

Thank you Rui for the most fruitful SEM sessions.

To Gonçalo, Ivo, Marcelo, Chico, Macau, Ricardo, Luís Guerra, Luís Custódio and Zé Pedro for the continuous the long Physics path and for the lifetime friendship.

To all my old time and closest friends for their support and patience, specially during my absences. Thank you for always being there, for the courage and the brotherhood.

Finally, I would like to thanks my mother and my sister for their infinite and continuous support and patience. For always being there and help me through the harder moments. To my grandmother for being an example, for being the source of love that never ends and for being the mother of us all. To my aunts, uncles and my cousins - thank you!

Thank you Mafalda, for being my safe harbor, my great companion and my love.

Resumo

Em 2015, o sector da refrigeração foi responsável por uma impressionante porção (∼ 17%) do consumo total de energia no Mundo e prevê-se que este valor aumente nos próximos anos[1]. De modo a reduzir a ”pegada” de carbono associada a esta tecnologia, dois problemas têm de ser resolvidos: 1) a redução da emissão de fluorocarbonetos; 2) a redução da energia consumida pelos sistemas de refrigeração através do aumento da sua eficiência. A par da refrigeração termoeléctrica e termo-acústica, a refrigeração magnética (RM), baseada no efeito magnetocalórico, é uma das tecnologias alternativas mais interessantes porque elimina o uso dos fluorocarbonetos e conseguirá atingir eficiências energéticas maiores[2]. Neste contexto, a família de compostos $Gd_5(Si_xGe_{1-x})_4$ é uma das famílias de materiais magnetocalóricos mais estudada, porque exibe um dos maiores efeitos magnetocalóricos num intervalo largo de temperaturas quando comparado com restantes materiais. Simultaneamente, exibe duas outras importantes propriedades magnéticas: a magnetoestrição colossal e a magnetoresistência gigante. Este conjunto de efeitos magnéticos surge do forte acoplamento spin-rede atómica, que é particularmente bem evidenciado pela transição magnetoestrutural que estes materiais atravessam[3]. Esta ágil interacção entre os graus de liberdade magnéticos e da rede atómica tornam-nos materiais muito sensíveis e capazes de sofrer transições magnetoestruturais pela variação de estímulos externos como, campos magnéticos[4], pressão[5] e/ou temperatura[4]. Contudo, praticamente não existem relatórios dedicados à micro e nanoestruturação destes materiais. Cientificamente, é crucial compreender como é que a interacção spin-rede se comportará com a redução de escala. Tecnologicamente, para além da miniaturização de frigoríficos (por exemplo, até à escala de um micro-chip), as nanoestructuras poderão ter um grande impacto na RM pois poderão permitir frequências de operação mais altas, uma vez que a sua elevada razão superfície/volume aumentará significativamente a rapidez das trocas de calor com um meio exterior[6]. Adicionalmente a nanoestruturação criará um conjunto de novas possibilidades nas tecnologias de sensores/actuadores como por exemplo: a gestão de micro-circuitos de calor, a colheita de energia[7], a ”strain-trónica”[8,9]. Visando os desafios acabados de referir, este trabalho relata os resultados mais importantes obtidos na nanoestruturação dos $Gd_5(Si_xGe_{1-x})_4$, estando dividido em duas grandes partes: (i) estudo de filme $Gd_5(Si_xGe_{1-x})_4$ nanogranular; (ii) optimização de filmes $Gd_5(Si_xGe_{1-x})_4$ contínuos. Na (i) parte, um filme $Gd_5Si_{1.3}Ge_{2.7}$ nanogranular, que consiste num aglomerado de nanopartículas com diâmetro médio de 80nm, foi depositado através da ablação por um laser de femtosegundos. A estequiometria do filme é idêntica à do alvo macroscópico usado. Contudo, as propriedades magnéticas

do filme são muito diferentes das do alvo, em particular: uma resposta magnética mais larga, um valor de pico menor para variação da entropia magnética (-ΔSm^{MAX}) e um aumento de 13 K na temperatura de transição magnetoestrutural (T_{MS}). Também o estudo da sua estructura átómica, através de diffracção de raios-X gerados em Sincrotrão, revelou um volume da célula unitária 2% inferior ao observado no alvo. No entanto, de um modo semelhante ao alvo, o filme também sofre uma expansão térmica gigante e anisotrópica ao longo da transição magnetoestrutural, exibindo uma expansão de volume de $\Delta V/V \sim 0.8\%$. É conjecturado que as mudanças nas propriedades magnéticas e estruturais observadas no filme são devidas ao stress intrínseco que existe na superfície das nanopartículas - equivalente à aplicação de uma pressão hidroestática[10]. Foi feita uma caracterização estrutural mais detalhada deste filme, estendida para as temperaturas abaixo e acima da T_{MS}, cobrindo o seguinte intervalo 90-340 K. Surpreendentemente, foi encontrado um comportamento particular da expansão térmica em dois intervalos, o que precede (90-140 K - regime LT) e o que sucede (255-430 K - regime HT) a transição magnetoestrutural: uma expansão térmica negativa (ETN). No regime LT, o coeficiente de expansão térmica medido foi: $\beta_{LT}=\Delta V^{LT}/\Delta T \sim$ -32.2 ppm K^{-1}, enquanto que no regime HT este coeficiente mais que duplica, $\beta_{HT} \sim$ -69 ppm K^{-1}, sendo muito maior do que o encontrado no Grafeno (-7 ppm K^{-1} [11]) e do que o observado no material ETN clássico, ZrW_2O_8 ,-28.2 ppm K^{-1} [12]. Este é um resultado inesperado uma vez que, em geral, não há qualquer sinal de um comportamento ETN em qualquer $RE_5(Si_xGe_{1-x})_4$ (RE - Terra Rara) composto macroscópico[13,14], sugerindo assim que se trata de uma consequência da redução de tamanho destes materiais. É também surpreendente porque é a primeira vez (do nosso conhecimento) que se verifica um comportamento ETN em nanopartículas magnéticas para temperaturas superiores à sua temperatura de ordenamento magnético. É sugerido que o mecanismo atómico responsável por este comportamento é a flexão das ligações químicas do importante tripleto atómico Ge3-Gd1-Ge3, uma vez que o ângulo entre estes três átomos, ϕ, revela um comportamento idêntico ao volume em função da temperatura - é sugerido que este comportamento se deve ao amolecimento da rede atómica causado pela redução de escala. Foram também avaliados os efeitos de quatro diferentes tratamentos térmicos nesta nanoestructura: 573, 673, 773 e 873 K durante duas horas a uma pressão de 10^{-5} mBar. Descobriu-se que os tratamentos térmicos abaixo de 773 K provocam uma supressão da transição magnetoestrutural, o que por sua vez leva a uma diminuição de 68% no valor da ΔSm^{MAX}. Duas notas positivas para estes tratamentos térmicos: a promoção de um aumento de 25% do seu T_C, para 253 K, aproximando-se assim da temperatura ambiente; e expansão da largura a meia altura da curva ΔSm(T), aumentando de 23 para 49 K. Estas alterações drásticas são atribuídas à supressão da fase O(II) através dos tratamentos térmicos.

Os estudos dinâmicos dos materiais multifuncionais têm uma importância crítica para as aplicações tecnológicas (uma vez que permitem simular as condições de um dispositivo em funcionamento no dia-a-dia) e também têm um interesse fundamen-

tal, pois permitem compreender melhor a evolução das transições. Neste contexto, a resistividade eléctrica do filme nanogranular de $Gd_5Si_{1.3}Ge_{2.7}$ foi estudada ao longo de 18 ciclos térmicos de aquecimento e arrefecimento no intervalo de temperaturas 100-300 K. De um modo geral foi encontrada uma dependência negativa na temperatura, revelando um comportamento tipo-semiconductor, em contraste com o comportamento tipo-metálico observado no alvo, que é causada pelo comportamento ETN observado à nanoescala. Esta tendência geral é interrompida por uma dependência positiva em dois passos que está associada às duas transições consecutivas: a magnetoestrutural e a puramente magnética. Uma análise mais detalhada da derivada da resistividade, $\partial\rho/\partial$T, demonstrou o comportamento tipo-avalanche cuja origem são as tensões criadas ao longo da transição magnetoestrutural (através da elevada expansão/compressão das nanopartículas). Finalmente, a deposição e caracterização de um conjunto de filmes $Gd_5(Si_xGe_{1-x})_4$ contínuos é descrita. Em comparação com filmes nanogranulares, os filmes contínuos são mais adequados para um amplo conjunto de aplicações, como a actuação magnética de um cantilever. Assim, de modo a realizar a deposição e optimização dos filmes $Gd_5(Si_xGe_{1-x})_4$ com a fase 5:4 desejada, duas abordagens foram seguidas: (i) a deposição de um filme multi-camadas (ii) a co-deposição de cada elemento químico em específico. Após as deposições, todos os filmes foram sujeitos ao mesmo tratamento térmico (450 °C durante duas horas, seguido de arrefecimento rápido). A caracterização estructural (XRD) e magnética (SQUID) permitiu concluir que existe uma espessura crítica ($\sim$ 20 nm) acima da qual a camada de Gd é cristalina e abaixo da qual é nano-cristalina/amorfa. De modo semelhante, a natureza amorfa foi também detectada nos filmes co-depositados. Ficou demonstrada a difusão do Ge através das camadas de Gd em todas as multicamadas. Em particular, nas multicamadas mais espessas, observou-se à destruição da estrutura hcp do Gd puro e à formação de uma diversidade de fases diferentes. Em particular, há duas fases favorecidas, a rica em Ge/Si, $Gd(Si,Ge)_{2-x}$ e a fase amorfa "a-interlayer", que competem entre si. Por sua vez, nas camadas mais finas e nos filmes co-depositados, a fase amorfa domina a competição, consumindo grande parte do Gd, não deixando que sobre nenhum para a formaçao de $Gd(Si,Ge)_{2-x}$. Desta forma, ficou demonstrado que, apesar dos 450 ° C serem suficientes para promover a difusão do Ge, não são suficientes para cristalizar e estabilizar a fase 5:4 desejada. Os tratamentos térmicos a elevadas temperaturas (800-900°C) demonstraram a possibilidade de formar mais de 50% da fase desejada, $Gd_5(Si,Ge)_4$. No entanto, estes tratamentos térmicos também promovem oxidação do Gd e a formação de diferentes fases com elevada percentagem de oxigénio. De um modo geral a elevada percentagem de fases ricas em oxigénio é explicada pela facilidade de penetração do oxigénio através do topo (devido à formação de cracks) e do fundo (através da difusão de oxigénio da camada de SiO_2 junto ao substrato). Desde modo ficou demonstrado que, tanto para nanograos no caso do filme nanogranular $Gd_5Si_{1.3}Ge_{2.7}$, como para os pequenos grãos cristalográficos ($\sim$ 100 nm) no caso dos filmes contínuos, a transição magnetoestrutural permanece. As-

sim sendo que o tamanho crítico, abaixo do qual os efeitos de superfíci dominam e a transição deve deixar de existir não foi ainda atingido.

Abstract

In 2015, the refrigeration sector consumed an impressive 17 % portion of the overall energy use worldwide and it is expected to increase[1]. In order to reduce the carbon footprint of gas-compression refrigeration technology, two main issues must be addressed: 1) reduce the emission of fluorocarbons; 2) reduce the energy consumption of refrigeration systems by increasing their efficiency. Together with thermoelectric or thermoacoustic technologies, magnetic refrigeration (MR), based on the magnetcaloric effect, is one promising alternative to gas-compression, because it eliminates the use of fluorocarbons and can deliver higher energetic efficiency[2].

The $Gd_5(Si_xGe_{1-x})_4$ family of alloys is one of the most studied magnetocaloric materials, since it exhibits large magnetocaloric effect for a wide temperature interval, together with other important magneto-responsive properties: the colossal magnetostriction and giant magnetoresistance. These extraordinarily responsive effects arise from their strong spin-lattice coupling particularly evidenced by the magnetostructural transition they undergo[3]. This agile interplay between magnetic and atomic lattice degrees of freedom makes them sensitive materials, capable to undergo magnetostructural transitions by the variation of external magnetic fields[4], pressure[5] and/or temperature[4]. There are, however, virtually no reports on micro and nanostructuring of these materials. From the scientific point of view, the importance of understanding the behavior of the magnetostructural coupling with the dimension reduction is crucial. From the technological point of view, besides the miniaturization of refrigerators (downwards to microchip size), nanostructures can have a great impact by allowing higher operational frequencies due to their higher surface-to-volume ratio and consequent faster heat exchange[6]. Moreover, nanostructuring will open new possibilities in the sensor/actuator technologies such as: micro-heat management circuitry, energy harvesting[7], and straintronics[8,9]. Aiming to address the above referred challenges, this work will highlight some of the most important results obtained on the nanostructuring of $Gd_5(Si_xGe_{1-x})_4$ materials by dividing the work in two main parts: (i) fundamental research on nanogranular $Gd_5(Si_xGe_{1-x})_4$ thin film and (ii) applied research on $Gd_5(Si_xGe_{1-x})_4$ continuous thin films.

Concerning part (i), a granular $Gd_5Si_{1.3}Ge_{2.7}$ thin film, consisting of a cohesive stack of nanoparticles with mean diameter of 80nm, was deposited by femtosecond laser ablation. The film stoichiometry was retained from the bulk $Gd_5Si_{1.3}Ge_{2.7}$ target. However, in contrast with its bulk counterpart, the thin film exhibited a broader magnetic response, a 13 K increase on its magnetostructural transition temperature (T_{MS}) and a lower $-\Delta Sm^{MAX}$. Its atomic structure was studied by Synchrotron XRD, revealing a

unit cell volume ~ 2% smaller than its bulk counterpart at room temperature. However, similarly to the bulk overall behaviour, a giant and anisotropic thermal expansion was also observed across the magnetostructural transition: unit cell volume variation, $\Delta V/V \sim 0.8\%$. The changes on the magnetic and structural properties are conjectured to be associated with the stress at the nanoparticles surface - such stress is equivalent to an hydrostatic applied pressure[10].

Furthermore, the detailed structural characterization of this thin film was extended to temperatures both below and above its T_{MS}~190 K, covering the 90-340 K temperature interval. Surprisingly, an unique thermal expansion behavior was found for the two intervals that precede (90-140 K - LT regime) and come after (255-340 K- HT regime) the magnetostructural transition: a negative thermal expansion. In the LT regime, it was found a coefficient of thermal expansion: $\beta_{LT}=\Delta V^{\mathbf{LT}}/\Delta T \sim$ -32.2 ppm K^{-1}, whereas in the HT regime it more than doubles, $\beta_{HT} \sim$ -69 ppm K^{-1}, being much larger than the one found in Graphene (-7 ppm K^{-1} [11]) and that observed in paramount NTE material, ZrW_2O_8 ,-28.2 ppm K^{-1} [12]. These are unexpected results since in general, there are no signs of NTE behavior in $R_5(Si_xGe_{1-x})_4$ bulk compounds[13,14] - suggesting NTE is a size-induced effect. Moreover, to our knowledge, it was the first time NTE behavior was detected in magnetic nanoparticles even above their magnetic ordering temperature. It is suggested that the atomic mechanism responsible for this effect is the bond flexing of the key Ge3-Gd1-Ge3 triplet chain, as this triplet ϕ angle mimics the volume temperature dependency - which is reported to be caused by size induced lattice softening.

Thermal treatments effects on this nanostructured material were also inspected by performing four different annealings: 573, 673, 773, and 873 K for two hours at a 10^{-5} mBar pressure. It was found that annealings below 773 K were responsible for the suppression of the magnetostructural transition, which lead to a $-\triangle Sm^{MAX}$ 68% decrease. On a positive note, there was a 25% increase in its T_C, which became closer to room temperature (T = 253 K) and an increasing of $\triangle T_{FWHM}$ from 23 to 49 K. These drastic changes in magnetic behavior for the annealed film were attributed to the suppression of the O(II) phase.

The dynamical studies of multifunctional materials are crucially important for technological applications and to deepen the fundamental knowledge about structural transitions. Hence, the $Gd_5Si_{1.3}Ge_{2.7}$ nanogranular thin film electrical resistivity was studied along 18 thermal cycles in the 100-300 K temperature interval. Overall, a negative electrical resistivity thermal dependency was observed (semiconducting-like), in contrast with the metallic-like observed in bulk Gd_5Si_x,Ge_{4-x} compounds, which is thought to be caused by the NTE behavior induced by the scale reduction. This general trend is interrupted by a two-step positive (metallic-like) thermal dependency, that are associated with the the two consecutive transitions: the magnetostructural and the purely magnetic one. A more detailed analysis of the resistivity derivative, $\partial\rho/\partial T$, displayed an avalanche-like behavior, whose origin is thought to be the severe strains induced in the nanoparticles by the magnetostructural transition (as it comprises large volume

expansion/compression).

Finally, the deposition and characterization of a set of continuous $Gd_5(Si, Ge)_4$ thin films was performed. Comparing to nanogranular, a continuous thin film is more suited for a wide range of applications, such as the magnetic actuation of a bi-layer system composed of a magnetostrictive and a cantilever. In order to pursue the deposition and optimization of the correct $Gd_5(Si, Ge)_4$ 5:4 phase, two main approaches were followed: the (i) multilayer and the (ii) co-sputtering of the specific pure chemical elements, which, after deposition, were subjected to the same thermal treatment (450^{o}C for two hours followed by air-quenching). Structural (XRD) and magnetic (SQUID) characterization allowed to conclude that Gd-Ge multilayers present a cross-over from crystalline to nanocrystalline/amorphous Gd in their as-deposited films at a critical thickness $\sim$ 20 nm. A similar amorphous-like nature was also found in the co-sputtered Gd-Ge and Gd-Si-Ge thin films, which must be associated with the increased disorder in thin multilayers and co-sputtered films. The annealing is enough to promote Ge-diffusion into the Gd layers in all the multilayers. In the thicker multilayers, it destroys the pure Gd hcp structure, but promotes the formation of a plethora of different phases. There are two favored phases, the Ge/Si-rich crystalline ($Gd(Si,Ge)_{2-x}$) and amorphous (a-interlayer) phases, as observed in previous reports in the literature. In the ”thicker” Gd-Ge multilayers here presented a competition between the crystalline $GdGe_{2-x}$ and the amorphous a-interlayer. Whereas, for the ”thinner” multilayers and the co-sputtered, the amorphous a-interlayer dominates the competition leaving virtually no Gd or Ge/Si to form the crystalline $Gd(Si,Ge)_{2-x}$ phase. It thus became clear from these studies, that despite 450^{o}C does promote Ge diffusion through Gd, it is not sufficient to achieve and stabilize the desired 5:4 phase. The high-temperature annealings demonstrated the possibility to form up to 50% of the desired $Gd_5(Si,Ge)_4$ phase. Nevertheless, a large amount of the Gd present in the film forms different Gd-oxide based phases. Such a generally high content of Oxides phases is explained by the easy Oxygen penetration into the film both through the top (due to the crack formation) and the bottom (due to Oxygen diffusion from the SiO_2 buffer layer) of the film. Both the small nanogranules ($\sim$ 80nm) in the $Gd_5Si_{1.3}Ge_{2.7}$ thin film and the small ($\sim$ 100nm) crystallite grain sizes in the continuous thin films, still undergo magnetostructural transition, revealing that the critical size below which the surface effects become dominating and the magnetostructural becomes suppressed was not yet reached.

Contents

List of Figures

List of Tables

List of Abbreviations

- **BB**, Bragg Brentano
- $\triangle\mu_0\boldsymbol{H}$, Magnetic induction variation
- $\mu_0\boldsymbol{H}$, Magnetic Induction
- μ_B, Bohr magneton
- **AFM**, Antiferromagnetic
- **APS**, Advanced Photon Source
- **BM**, Ball-Milling
- **BSE**, Backscattered Electrons
- **C**, Curie constant
- $\mathbf{C}_H$, Specific heat
- **CEMUP**, Centro de Materiais da Universidade do Porto
- **CFC**, Chlorofluorocarbon
- **CS**, Co-Sputtering
- **DC**, Direct Current
- **EDXS**, Energy Dispersive X-ray Spectroscopy
- ***F***,Helmholtz Free Energy
- **FC**, Field-Cooling
- **FCC**, Field-Cool Cooling
- **FCH**, Field-Cool Heating
- **FCUP**, Faculdade Ciências da Universidade do Porto
- **FM**, Ferromagnetic
- **FOMT**, First Order Magnetic Transition
- **FOPT**, First Order Phase Transition
- **FWHM**, Full Width at Half Maximum
- ***G***, Gibbs Free Energy
- **GMCE**, Giant Magnetocaloric Effect
- **GMR**, Giant Magnetoresitance
- **HCFC**, Hydrochlorofluorocarbon
- **HFC**, Hydrofluorocarbon
- ***HRSXRD***, High Resolution Synchrotron X-ray radiation diffraction
- ***HRTEM***, High-resolution transmission electron microscopy
- **IFIMUP-IN**, Instituto de Física dos Materiais da Universidade do Porto
- **INA**, Instituto de Nanociencia de Aragón
- **J**, Atom total angular momentum
- $\boldsymbol{J}_{eff}$, Effective magnetic exchange parameter
- **L**, Lattice
- ***M***, Magnetization
- **MCE**, Magnetocaloric Effect
- **ML**, Multi-layer
- **MR**, Magnetic Refrigeration
- **MSMA**, Magnetic Shape Memory Alloy
- **MMMN**, Multifunctional Magnetic Materials and Nanostructures
- **N**, Density of magnetic atoms
- **NP**, Nanoparticles
- **O(I)**, Orthorhombic I atomic structure
- **O(II)**, Orthorhombic II atomic structure
- **PB**, Parallel Beam
- **PLD**, Pulsed Laser Deposition
- **PVD**, Physical Vapour Deposition
- **RE**, Rare Earth
- **RF**, Radio Frequency
- **RT**, Room Temperature
- **S**, Entropy
- **SE**, Secondary Electrons

- **SEM**, Scanning Electron Microscopy
- **SOMT**, Second Order Magnetic Transition
- **SOPT**, Second Order Phase Transition
- **SQUID**, Superconducting Quantum Interference Device
- **STEM**, Scanning Transmission Electron Microscopy
- **TEM**, Transmission Electron Microscopy
- **UME**, Unidade de Microscopia Electrónica
- **XRD**, X-ray Diffraction
- N_A, Avogadro's number
- ΔT_{ad}, Adiabatic Temperature change
- μ_B, Bohr magneton
- θ_P, Curie-Weiss Temperature
- $\Delta\chi$, Variation of Magnetic Susceptibility
- μ_{eff}, Effective paramagnetic moment
- J_{AFM}, Antiferromagnetic interaction
- J_{FM}, Ferromagnetic interaction
- ΔS_M, Magnetic Entropy change
- χ, Magnetic susceptibility
- $M(H)$, M vs H
- $M(T)$, M vs T
- χ^{-1}, Reciprocal susceptibility
- σ, Stress
- ϵ, Strain
- T_C, Curie Temperature
- T_N, Néel Temperature
- T, Temperature
- T_{SR}, Spin Reorientation Temperature
- $\mathbf{k}_B$, Boltzmann constant

CHAPTER 1

PREFACE

This year, 2017, signals the 100th anniversary of the experimental discovery of the magnetocaloric effect (MCE) by Weiss and Piccard that have observed a sizable and reversible temperature change in Nickel near its Curie temperature in 1917[15]. Basically, the MCE consists of a temperature change upon the application of a magnetic field under adiabatic conditions. Such discovery occurred after preliminary works on heat generated in magnetic materials by magnetic field application by Thomson (1860s) in an initial version of the MCE and Warburg (1880s) on the heat generated by magnetic hysteresis losses[15]. Not long after Weiss and Piccard discovery, in the late 1920s, Giauque and Debye[16,17], independently, presented a thermodynamic explanation for the MCE and proposed an effective procedure for refrigerating systems at a temperature close to absolute zero, the adiabatic demagnetization. As will be detailed below, they found that the MCE depends linearly with the magnetization temperature derivative - the MCE of all magnetic materials will reach its maximum around the temperature where the magnetization derivative reaches its maximum - i.e. around the material magnetic ordering temperature. Throughout the 20th century, there was a very active search for optimum magnetocaloric materials for the different temperature ranges, i.e. with different magnetic ordering temperatures and high MCE. In the beginning of the century, the low temperature regime (specially close to absolute zero temperatures) was very successfully covered through the use of paramagnetic salts, allowing the achievement of sub-Kelvin temperatures[18]. Micro Kelvin temperatures were reached by using intermetallic paramagnetic compounds. However, due to the vast number of potential commercial applications, the near room temperature regime attracted much of the attention of the scientists from this community. Finally, in 1976 Brown has unveiled an impressive temperature change, ΔT_{ad}, $\sim$ 14 K for $\Delta\mu_0 H \sim 7$ T (variation of the magnetic field intensity) at its T = T_C (Gd) $\sim$ 294 K[19]. In the same year Brown filed his patent "Magnetic Heat Pumping", describing the method "to employ the heating and cooling effect of magnetization and demagnetization respectively in a cycle for pumping heat"[19] initiating a still ongoing race to the optimal room temperature magnetic heat pump. Many other intermetallic compounds whose T_C is higher than 290 K were found, but none with a MCE comparable to Gd. This situation changed in the 1990s with the discovery of a Giant MagnetoCaloric Effect (GMCE) on the FeRh alloy which reached ΔT_{ad} = 8 K, at T = 308 K, for $\Delta\mu_0 H$ = 2.5 T[20]. Unfortunately the same authors have

found that this effect was irreversible and consequently not applicable to real-life refrigerators. Shortly after, in 1997, Pecharsky and Gdschneider, discovered a similar GMCE on the $Gd_5Si_xGe_{1-x}$ x = 0.5 alloy ($Gd_5Si_2Ge_2$) and demonstrated that it was reversible[4]. Such result, immediately attracted the attention of several researchers, whom were responsible for the broad and detailed studies on the $R_5(Si,Ge)_4$ family. It was found that in addition to the GMCE, these materials also present a giant magnetoresistance[21], spontaneous generation voltage[22], and a colossal magnetostriction effect (up to ten times bigger than Terfenol-D)[23,24], $\Delta\mathbf{V}/\mathbf{V} \sim 1.1$ %. Such variety of effects outcome from the coupled magnetic and structural (magnetostructural) transitions that occur typically between high volume paramagnetic and low volume ferromagnetic phases. These first-order transitions can be driven by multi-stimuli such as temperature, magnetic field and pressure or combinations of these[5,13,25]. Consequently their transition temperature can be tuned by these stimuli but also by chemical composition in a wide temperature range of 5-350 K[26,27]. Together with the $R_5(Si,Ge)_4$ several other alloys families with strong magnetovolume coupling and GMCE were discovered, namely: $La(FeSi)_{13}$ and related compounds[28], the magnetic shape memory alloys[29] and the MnCoFeAsP and related compounds[30]. Nowadays, the MnCoFeAsP and the $La(FeSi)_{13}$ families are the ones deserving higher interest due to their demonstrated higher MCE[31] around room temperature and to the fact that they do not comprise expensive Rare-Earth elements. In parallel with the material science researchers efforts, there has been an intense effort from the engineering community to design and optimize the best magnetic heat pump/refrigerator. An increasing amount of patents have been filed and more importantly, more than 20 prototypes are currently being tested[32]. From an engineering point of view there are several critical parameters associated with the choice of the magnetocaloric material. Kitanovski and co-authors[32] have short-listed some and here some others are added: an appropriate magnetic ordering temperature, MCE intensity, a wide temperature range where the MCE occurs, a low operational magnetic field, a narrow magnetic and thermal hysteresis, good mechanical stability, high performance at high frequencies, high thermal conductivity and diffusivity, feasibility to shape, high electrical resistivity, good corrosion properties, price and availability for large scale use. Unfortunately there are strong correlations between these parameters. For instance it is well known that the MCE intensity is higher in first-order strongly magnetovolume coupled materials, however these materials normally present a narrow temperature range where the MCE occurs and a large hysteresis. On the other hand, second-order magnetocaloric materials present a wide temperature range where the MCE occurs, have negligible hysteresis, but present a lower MCE intensity. Several strategies have been embraced to optimize these parameters, specially starting with a first order material with high MCE intensity. For example, in order to reduce the magnetic hysteresis several approaches were performed such as chemical substitution[27], polymer-bonding[33], a multi stimuli approach[34] or microstructural designing by introducing porosity[35]. Thermal conductivity has also been enhanced through off-stoichiometric processes[36] or mi-

crostructural tuning[37]. Another strategy comprises the MCE materials size reduction. The pioneer work by Moore and co-workers has shown that it was possible to reduce the operational magnetic field up to 20% just by cracking a bulk sample into 100 μm size fragments[38]. The size reduction effects on magnetocaloric materials have just recently been attracting more attention, which as resulted in a large increase of papers published as shown, by Miller and co-workers[39], but still lagging behind other caloric materials in the nanoscalling race, as Moya and co-workers pointed out[40]. As will be detailed hereafter, the micro and nanostructuring have shown promising signs to tackle some of the problems addressed above with remarkable results. Recent reviews have also highlighted the role that scale reduction can have on the MCE development, in particular Smith and co-workers report "Several new materials concepts also seem worth exploring in greater detail. These include possible enhancements of the magnetocaloric effect in nanomaterials or nanocomposites, in thin films, and in superlattices/heterostructures. Whether such concepts will also be relevant on the scale of an actual device remains to be seen."[41]. Miller and co-workers report " The promise of applying nanoscience to magnetocalorics includes addressing these issues-designing, exploring, and discovering materials whose magnetocaloric properties are tunable and that can be combined in novel structures to maximize efficiency."[39]. Franco and co-authors have dedicated a whole section to the nanosctutured materials on their review "The Magnetocaloric Effect and Magnetic Refrigeration Near Room Temperature: Materials and Models", where they claim that "In nanostructured materials, the magnetocaloric response will not only depend on the characteristics of the bulk material (the composition of the phase), but will also be strongly dependent on other factors like particle size (and particle size distribution), particle concentration, interactions between particles, anisotropy, finite size effects, etc. Models have been proposed to take into account these effects."[31]. The following examples will illustrate Franco´s statement. Doblas and co-workers have engineered a smart nanostructuring of Gd - thin film multilayers of Gd/Ti - and have enhanced by $\sim$ 30% the magnetic field dependence of the MCE (in comparison with the bulk)[42]. Furthermore, while reducing the size of materials, the surface to volume ratio begins to increase significantly with positive consequences for the thermal diffusivity of the MCE material as was highlighted by Niemann and co-authors[6] and by our group[43]. By enhancing the diffusivity, the relaxation time for heat exchangers decreases which enables higher frequencies and hence higher cooling power engines. Although, typically micro and nanostructuring have detrimental effect on the MCE intensity, they do widen significantly the temperature window where the MCE occurs[6,43–45]. One obvious disadvantage of the size reduction is the loss of cooling power (which depends critically on the active mass/volume), however as also stated by Franco and co-authors there are a wide range of new possible cooling/heating applications such as: micro-refrigeration (micro-chip cooling), microfluidic reactors, magnetocaloric cooling fluids[46], etc. From the previous examples it becomes clear why the micro and nanostructuring can have an important role on helping solving some of the MCE materials issues nowadays. How-

ever, these are not the only reasons why to go to the micro and nanoscale. In particular, the tuning of the MCE by playing with the bi-system film-substrate properties has been demonstrated by the remarkable studies of Moya[40] and Mosca[47] and respective co-workers. The later work consisted in a smart strain engineering of 70 nm MnAs epitaxial thin films deposited onto two differently oriented GaAs substrates. The semiconductor GaAs (1 1 1) and (0 0 1) substrates induced different anisotropic strain on the MnAs thin film which in turn lead to large changes in the MCE intensity and in its temperature range. Following this work, Duquesne and co-workers were able to trigger the magnetocaloric effect of a MnAs(100 nm) thin film deposited in GaAs(001) substrate by employing surface accoustic waves[48]. More recently, Moya has exemplified how the MCE of a second order manganite epitaxial thin film can be greatly enhanced (ten-fold) via the substrate-thin film coupling - a $BaTiO_3$ substrate undergoes a first-order structural transition that extrinsically induces a giant MCE in a $\sim$ 35 nm $La_{0.7}Ca_{0.3}MnO_3$ thin film[40]. Moreover, new opportunities emerge for magnetocaloric nanoparticles, namely the hyperthermia therapy of tumour cells. Together with Karl Sandeman´s, Barati and co-authors have unveiled a practical use for the large thermal hysteresis observed in the 1^{st} order giant MCE materials, $La(FeSi)_{13}$. In fact, they have measured a specific absorption rate (which basically is a measure of the rate at which energy is absorbed by the human body when exposed to a radio frequency (RF) electromagnetic field) ten times larger than the one observed in the well studied 2^{nd} order iron-oxide materials and with an additional advantage, the self regulation due to their T_C around room temperature. They envisage a promising future for magnetocaloric large hysteresis nanoparticles in the hyperthermal therapy field[49]. More recently, Tishin, Egolf and co-authors have highlighted innovative work on the field of drug delivering. Tishin and co-authors have already two patents on this mechanism, which consists in a composite material composed by microsized MCE material and a thermosensitive biocompatible polymer: when desired a magnetic field can be applied to the composite which due to the MCE material will heat up the thermosensitive polymer and induce the release of drugs that initially were captive in the polymer[50]. Egolf and co-authors recurred to an older idea by Rosensweig[51] to distribute homogeneously a large amount of MCE nanowires in a biocompatible gel or fluid that will be injected into the cancer tumour[52]. In 2004, Love and co-authors have reported another interesting idea based on the Rosensweig principle - a magnetocaloric pump for microfluidic applications, such as the widely spread concept of a ”lab on a chip”[53]. By exposing a column section of magnetic fluid, composed of a magnetocaloric nanoparticles immersed in a liquid solution, to a uniform magnetic field it produces a pressure gradient. This occurs because the column section exposed to the magnetic field will heat up, due to the MCE, eventually up to its Curie temperature when it will loose its attraction to the magnetic field and will be dynamically displaced by a cooler (and still magnetically ordered) section of the magnetic fluid column. Preliminary results have demonstrated an order of magnitude increase in the fluid flow rate of a magnetocaloric system in comparison with a conventional magnetite based ferrofluid.

Moreover, Ortega and co-authors in their recent review ”Applications of exchange coupled bi-magnetic hard/soft and soft/hard magnetic core/shell nanoparticles” have underlined the importance of synthesize and study a core/shell soft/hard magnetocaloric nanoparticle system as it may ”lead to attractive effects”[54], eventually enhancing the magnetocaloric properties as it has been observed in bi-magnetic multilayers[55]. Besides applications based on the MCE, these strong magnetovolume coupled materials also show promising results for magnetostrictive or thermal strain based applications. In additions for these applications, the micro and nanostructuring can also lead to important innovations. The most remarkable example is the work reported by Chmielus and co-authors on the magnetic field induced strains in a micro-engineered NiMnGa foam[56]. The foam produced by a replication method developed by this group allowed to insert two groups of pores, the smaller with few micrometers size and the larger with few hundreds micrometers. Such microstructuring was crucial for the enhancement from 0.12% to 8.7% magnetic field induced strains (MFIS) and for its mechanical stabilization even after more than 200,000 cycles[56]. Nersessian and co-authors were the first to report a practical example of a $Gd_5(Si,Ge)_4$ based magnetostrictive composite[57]: ball-milled $Gd_5(Si, Ge)_4$ microparticles (< 600 μm) immersed in a resin matrix. Despite the random dispersion of the microparticles, a strain of $\sim$ 0.16 % was measured and a strain of $\sim$ 0.5 % was estimated for a specific oriented dispersion. One of the major problems with magnetic actuators is their Eddy current losses when actuated at high frequencies that reduce significantly the frequency bandwidth at which they can be actuated. Interestingly this problem can also be tackled by reducing further the magnetostrictive particles - estimated two orders of magnitude enhancement of the characteristic frequency when the particle size is reduced by one order of magnitude. More recently Liang group applied $Gd_5(Si,Ge)_4$ strain behaviour to create a magnetocaloric piezoelectric composite[58] and a $Gd_5(Si,Ge)_4$-Aluminium composite for tribological applications[59]. In the latter case, it was shown that the $Gd_5(Si,Ge)_4$-Aluminium composite improved the wear resistance of a commonly used Aluminium based alloy (Al 6061-T651) and have shown higher friction coefficient in the -25-150 °C temperature range. In the former work, an interesting multiphase magnetostrictive ($Gd_5(Si,Ge)_4$)-piezoelectric (PVDF) composite was developed to harvest energy converting magnetic into electrical (and vice-versa) energy. Less than 6 μm diameter $Gd_5(Si,Ge)_4$ microparticles were added to the PVDF matrix in three different portions. The maximum output voltage obtained was 0.11 V under a very small 10 Oe magnetic field, ensuring a power density, 14.3 mW cm^{-3} Oe^{-1}, higher than the sum of the two components when measured alone. In summary, from an engineering point of view, the above examples clearly demonstrate the wide range of possibilities that can be unveiled at the micro and nanoscale of multifunctional materials.

From a pure materials scientist point of view several interesting questions arise with the size reduction as well. Some of them were already mentioned above, such as the commonly observed temperature broadening of first-order transitions that results in a wider operational temperature range for MCE applications or the significant reduction of

the magnetic field necessary to induce these transitions. There are however more fundamental questions, such as: 1) the existence/absence of a critical size below which the magnetovolume coupling vanishes; 2) impact of the symmetry (magnetic, electrical..) break at the nanostructure surface; 3) the achievement and stabilization of the desired stoichiometric phases 4) interface film-substrate repercussion; 5) impact of scale reduction on the thermal expansion behavior, 6) the dynamical regime of phase transitions at the nanoscale. Wu and co-workers have recently performed the critical size question themselves and tried to find an answer to it for the MnFeNiGe system[60]. Through hand milling they were able to produce powders comprising microparticles ranging from hundreds to few μm diameter. For the $MnNi_{0.8}Fe_{0.2}Ge$ and $Mn_{0.82}Fe_{0.18}NiGe$ systems they found that for microparticles with diameter inferior to 15 μm the typical magnetostructural transition became incomplete - an approximately 40% fraction did not transform into the low temperature structure, coexisting with the 60% that continued to transform. They attributed this size-induced suppression to the rise of internal stress fields, as a result of two grain interfaces and microparticles surface stress. Such an intrinsic pressure enhancement stabilizes the lower volume phase and eventually lead to the incomplete suppression of the magnetostructural phase. The work by Mello and co-workers[61] illustrates well the second question as they have theoretically predicted the Dy magnetic behaviour for ultra-thin films. Dy is known to have a helical magnetic structure with a period of few unit cells (< 20) as ground state. However, they found that if a very thin film is produced (with a thickness lower than this period, t < 15 nm, the helical order will be truncated and pure ferromagnetic ordering will be favored by these spins, as will be detailed in chapter 2. The third question, a pre-requisite for all the previous and following questions, demands different strategies depending on the material that is to be nanostructured. For example, Lommel and co-workers[44], in order to surpass the significantly different vapor pressures of Fe and Rh, adopted a smart strategy which comprised the deposition of a multilayer system composed by Fe and Rh layers alternately grown by electron beam melting onto a glass substrate. As to promote interlayer diffusion and crystallization of the 1:1 phase, Lommel performed an annealing treatment at 565 °C for 5 hours. This author also tried two different strategies: 1) direct co-deposition of Fe and Rh by electron beam melting; and 2) by sputtering directly a $Fe_{0.50}Rh_{0.545}$ target. However, only the multilayer approach was able to successfully stabilize the FeRh phase. The fourth question was already embodied by the work of Mosca and co-workers on epitaxial growth of MnAs thin film on top of two differently oriented GaAs substrates. The stress induced in the film due to the lattice mismatch between the two different substrates and the thin film promotes different magnetic behaviors. Furthermore, Zheng and co-workers have found an unusual impact of the size reduction on CuO compound - a negative thermal expansion behavior (NTE), exemplifying the fifth question raised above. In contrast with its bulk low but positive thermal expansion, 5 nm CuO nanoparticles were reported to demonstrate a large NTE $\beta \sim$ -110 ppm K^{-1} (β is the coefficient of thermal expansion) up to their magnetic ordering temperature. Although still remains

unclear the origin of this effect, the authors hypothesized that the magnetovolume coupling is significantly enhanced by the scale reduction. Finally, the dynamical regime, referred in question number six, has been overlooked at the macroscale and almost completely ignored at the micro and nanoscale. Recently, however, a very interesting report by Uhlir and co-workers has remarked the importance of such studies as they unveiled a strong asymmetry in the magnetic transition of FeRh few micrometer stripes between the cooling and heating cycles[62]. At this point, it became more clear the importance of studying the scale reduction on multifunctional materials, both from a technological and a purely scientific point of view. This importance has been acknowledge by many, however a state of the art search reveals that there is still a long path to be run. Starting from the first-order magnetocaloric materials, the magnetic shape memory alloys (MSMA), the manganites and more recently the MM´X (M, M´ = transition metals, X = Si, Ge, Sn) compounds with hexagonal Ni_2In-type structure are the ones whose scale reduction studies have been increasing in the last years, specially for the MSMAs. Curiously, despite having similar magnetovolume couplings, the LaFeSi and the $R_5(Si,Ge)_4$ systems have received far less attention regarding their nanostructuring, in particular the latter family where, to our knowledge, there are virtually no reports on their nanostructuring. Our work plan can be summarized by the following points: - Synthesize nanoparticles and grow thin films by various methods based on the previously optimized bulk $R_5(Si, Ge)_4$ targets or in the individual elemental targets; - Optimize the desired 5:4 phase via ex situ thermal treatments (mimicking the bulk procedure); - Perform a thorough structural and magnetic characterization of the optimized $R_5(Si, Ge)_4$ nanostructures.

This work has been performed during the last four years and will be detailed in the following chapters.

CHAPTER 2

The Magnetocaloric Effect and an Overview of the $R_5(Si, Ge)_4$ compounds

2.1 The Magnetic Refrigeration and the Magnetocaloric Effect

At the end of 2015 the International Institute of Refrigeration (IIR) performed a global analysis and estimated that the air-conditioning and heat pump systems in operation worldwide are roughly 3 thousands millions ($3x10^9$) units which represent annual sales of roughly 300 thousands millions U.S. Dollars ($3x10^{11}$), more than the US automobile's industry annual sales, and accounts for more than 12 million jobs[1]. Furthermore, the increasing cooling needs in numerous fields such as food (preservation of food products), health (vaccines preservation and innovative cryotherapies), energy (industrial and building applications) and environmental domains (natural gas cryo-cooling) implies a significant increase of the numbers given above. Just in the United States of America (USA) the number of refrigeration-base employees is expected to grow by 21 % from 2012 to 2022. Such increase will be dramatically higher in developing countries such as India and China, where the middle class is predicted to boost by almost 3 thousand million people in 2030 - China alone was expected to increase by 20-fold its refrigerated storage capacity from 2007 to 2017[63]. In 2015, the refrigeration sector consumed an impressive 17% portion of the overall energy used worldwide[1]. Both due to the increasing demand and the global warming, this portion is expected to increase in the coming years. These large and increasing numbers are worrisome when one considers the two following features: the vast majority of the refrigeration power is still achieved nowadays through ozone depleting fluorocarbons gas-compression technology; despite the constant efficiency increase (a drop on the refrigeration consumption of around 65% was estimated for a typical household in the last 15 years) there is an alarming overall increase due to the higher demands. The actual gas-compression technology has a significant global warming impact that can be divided in: 20% due to the direct emission (leakage) of fluorocarbons (CFCs, HCFCs and HFCs) and 80% accountable for the indirect carbon emissions originated from the electricity generation required to power the refrigeration systems. Therefore, in order to reduce the carbon footprint of refrigeration

technology, two main issues must be addressed: 1) reduce the emission of fluorocarbons 2) reduce the energy consumption of refrigeration systems by increasing its efficiency. In fact the EU has implemented recently (starting on the 1st January 2015) an ambitious regulation to phase down the use of fluorocarbons that estimates a reduction down to 21% of nowadays amounts till 2031. In order to meet these requirements, alternative technologies are being considered. The ones showing most promising results are: thermoelectrics, thermoacoustics and magnetic refrigeration (MR)[2]. It is thought that these different technologies can and will coexist, each being applied to a specific sector. None of these technologies needs fluorocarbons - which would allow the immediate reduction on 20% off the refrigeration impact on global warming. Nowadays, the energetic efficiency of these alternatives is still below the gas compression systems, however, in particular the magnetic refrigeration has a great room for improvement being expectable to surpass the gas compression efficiency soon up to maximum values of 1.4 to 1.7 depending on different heating/cooling applications[2]. Besides the gas reduction, efficiency increase, MR appliances are expected to produce less noise than the nowadays appliances. The magnetic refrigeration is based on the magnetocaloric effect (MCE), which has a two-fold definition: 1) it is a temperature change undergone by a magnetic material when a field is applied in an adiabatic process (ΔT_{ad}); 2) it is an entropy change of a magnetic material when a magnetic field is applied in an isothermal process (ΔS_{iso}). According to thermodynamics, magnetic materials can be thought of as systems comprising three energy reservoirs: the phonons, as the vibrational excitations of the lattice, the magnetic states of the magnetic sublattice and the electronic contribution associated with the electron bands of the system. In the thermodynamics formalism, the total entropy of a magnetic system at constant pressure, can be written as:

$$S(T, H) = S_L(T, H) + S_M(T, H) + S_E(T, H) \tag{2.1}$$

where, S_L(T,H), S_M(T,H) and S_E(T,H) are the lattice, magnetic and electronic contributions to the total entropy S(T,H), for a specific temperature and magnetic field. Assuming the electronic contribution to the total entropy is negligible, one can consider only the lattice and magnetic terms. The MCE is intimately related to the interplay and energy flow between these two kinds of excitations.

In Figure 2.1 a), the effect that a magnetic field induces in a magnetic material during an adiabatic process is schematically drawn. In order to minimize the total energy the material magnetic moments tend to reorientate themselves along the direction of the applied magnetic field, thus decreasing the entropy associated to the magnetic sublattice (from a disordered to an ordered state). If this process occurs under adiabatic and reversible conditions (meaning no heat exchanges with the surroundings and maintaining a constant total entropy, Figure 2.1 a)) the system must compensate the decrease of magnetic entropy (S_M) by increasing the lattice entropy (S_L), in order to maintain the to-

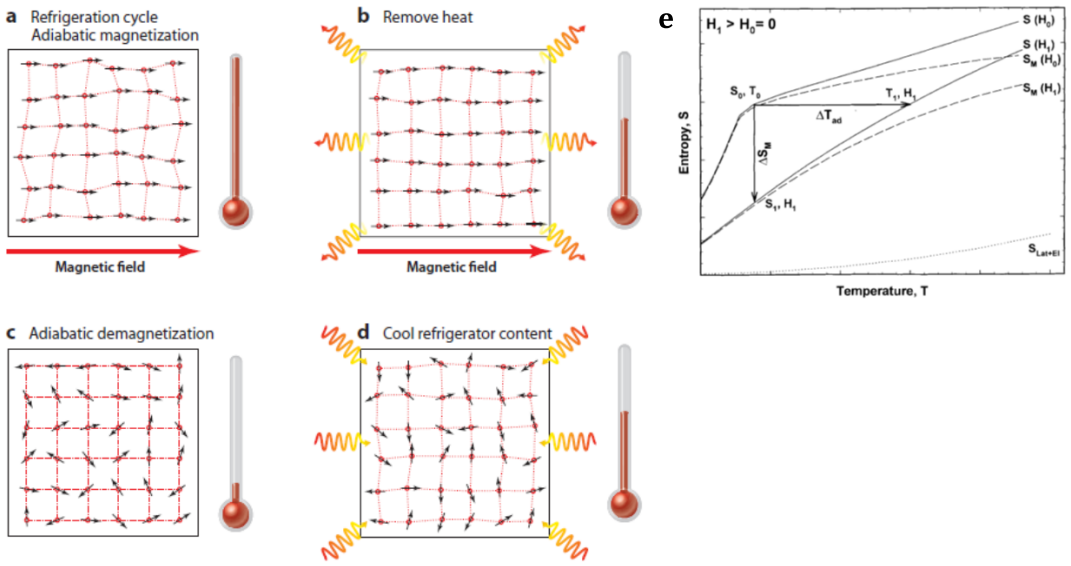

Figure 2.1 – The four stages of a magnetic refrigeration cycle as extracted from reference[31]. In a) a magnetic field is applied adiabatically to a magnetic material (represented by an atomic lattice with arrows as magnetic moments) heating up the material due to the MCE. b) While still maintaining the applied field the extra heat generated by the material is removed by an heat exchanger, cooling the material. c) The magnetic field is removed, cooling the material below its initial temperature. d) The material finally warms up again towards its initial temperature, by absorbing heat from the volume to be cooled down. e) A S-T diagram schematically representing the temperature dependence of the total entropy (solid lines) of a magnetic system for two different applied magnetic fields (μ_0H1 > μ_0H0 =0). The MCE can be defined by both the ΔS_m or by the ΔT_{ad}, represented by the vertical and horizontal arrows, respectively. The lattice and electronic entropy contributions are represented by the dashed line.

tal entropy constant. Thus, an entropy (energy) transfer occurs from the magnetic to the lattice reservoir, i.e. an increase in the material temperature. This temperature change is experimentally measurable and is identified as ΔT_{ad} (in Figure 2.1 e) as the horizontal arrow). During an isothermal process there is heat transfer to the surroundings and hence there are no constraints to the total entropy. In such a process, a magnetic field application decreases the magnetic entropy and consequently the total entropy of a material. This process is identified with the total entropy change, ΔS_{iso} (in Figure 2.1 e) as the vertical arrow). Both ΔT_{ad} and ΔS_{iso} characterize quantitatively the MCE and it is important to remark that both depend on the initial temperature of the process. ΔS_{iso} is related to the materials magnetization through the following Maxwell relation:

$$\frac{\partial S(T,H)}{\partial H_T} = \frac{\partial M(T,H)}{\partial T_H} \tag{2.2}$$

Along an isothermal process, integrating over the magnetic field variation range (between H_i and H_f) gives:

$$\Delta S_{iso}(T,\Delta H) = \int_{Hi}^{Hf} \frac{\partial M(T,H)}{\partial T_H} dH \tag{2.3}$$

which can be related to ΔT_{ad} by considering:

$$\frac{\partial T(S,H)}{\partial H_S} = -\frac{\partial S(T,H)}{\partial H_T}\frac{\partial T(S,H)}{\partial S_H} \tag{2.4}$$

together with the Maxwell relation 2.2, ΔT_{ad} can be written as a function of magnetization:

$$\partial T_{ad}(T,\Delta H) = \int_{Hi}^{Hf}\frac{\partial T}{\partial H_S}dH = -\int_{Hi}^{Hf}(T/C_H(T,H))(\frac{\partial M(T,H)}{\partial T_H})dH. \tag{2.5}$$

where $C_H = T(\partial S/\partial T)_H$ stands for the materials specific heat at constant field.

The magnetic refrigeration cycle based on MCE can be described in four steps as schematically represented in Figures 2.1 a-d). Firstly, by applying a magnetic field to the magnetocaloric material on an adiabatic process, the material temperature is increased by ΔT_{ad}. Hereafter, this extra heat is transferred to a heat exchanger (such as water), decreasing the temperature of the magnetocaloric material in a isofield process. Afterwards the field is removed and the magnetic moments become randomly oriented, increasing magnetic entropy and decreasing lattice entropy, i.e. decreasing the temperature of the magnetocaloric material by ΔT_{ad}. Finally the demagnetized material absorbs heat transferred by the heat exchanger from the volume that is to be refrigerated. The system arrives to the initial state where the cycle restarts again.

2.2 The Magnetocaloric materials

Considering equations 2.5 and 2.3 some simple features can be drawn in order to find the best magnetocaloric materials (MCM):

- Both ΔT_{ad} and ΔS_{iso} depend linearly on the magnetization temperature derivative, $(\partial M(T,H)/\partial T)$. This means that the MCE will be maximized for temperatures close to the magnetic ordering temperature (T_C, T_N, ..., for ferromagnetic and antiferromagnetic materials, respectively) where magnetization varies faster with temperature, i.e. where $(\partial M(T,H)/\partial T)$ is maximum.
- Since paramagnets and ferromagnets magnetization decrease with increasing temperature, $\partial M(T,H)/\partial T < 0$ and consequently $\Delta T_{ad} > 0$ and $\Delta S_{iso} < 0$;
- ΔT_{ad} is higher for a higher absolute temperature and for a lower heat capacity of the material at the specified temperature;

It is important to remark that what is considered to be an optimum magnetocaloric material depends on temperature range desired for a specific application. Hence, conventionally magnetic refrigeration can be divided in: low-temperature (0-80 K), intermediate-temperature (80-250 K) and room temperature refrigeration (250-350 K) regimes[64]. Another important remark consists on the physical limitation of the ΔS_{iso} value. For

each material there is an upper bound for the ΔS_{iso} that is associated with entropy difference between two extreme cases: the highest entropy state where all magnetic moments are completely disordered and the lowest entropy state where all magnetic moments are collinearly and parallel to each other. The entropy upper bound is: $S_m^{MAX} = Nk_B\ln(2J+1)$, where N is the density of magnetic atoms, k_B is the Boltzmann constant and J is the spin value of the magnetic atom. Paramagnetic salts magnetization follow very accurately the Curie-Weiss law, $\chi(T)=M(T)/H= C/(T-T_C)$, where $\chi(T)$ represents the magnetic susceptibility and C the Curie constant. Since their ferromagnetic coupling is very weak, their magnetic ordering temperature is close to 0 Kelvin. Consequently, as the temperature drops down to around absolute zero, their magnetization (and magnetic susceptibility) varies very fast, eventually diverging for a pure paramagnetic salt ($\partial M(T,H)/\partial T \rightarrow 0$) which leads to a large MCE at temperatures close to absolute zero. The Gd based paramagnetic salt, $Gd_2(SO_4)_3.8H_2O$, is a good example of this family of materials as it was the one used in the first adiabatic demagnetization refrigerator, constructed by Giauque in 1933[18]. In the following decades the research for good magnetocaloric materials focused on the paramagnetic salts for the low temperature regime. In the 1970s, the research was reoriented towards the intermetallic paramagnetic compounds, such as $PrNi_5$, due to their higher thermal conductivity which would result in the construction in 1984 of a two-step magnetic refrigerator, that was able to set a new temperature record of 27 μK, using a mixture of PrNi5 rods and Cu wires by Ishimoto and co-workers[65]. For the low temperature regime, the main focus of research was on the 4f metals (lanthanides) because of their higher available theoretical magnetic entropy, S_m^{MAX}. In particular the low T_N lanthanide metals, such as Nd, Er and Tm which have T_N's in the 20-60 K range. More recent research has shown that the magnetocaloric effect is higher for intermettalic compounds containing lanthanides, such as RAl_2 (with R =Er, Ho, Dy, ...)[66].

Despite the aero-spatial engineering potential applications, the intermediate temperature range (80-250 K) has received less attention in comparison with the other two. Nevertheless another lanthanide-rare earth, pure Dysprosium (Dy), was found to present a large found ΔT_{ad} = 2.2 K at 180 K under a ΔH = 2 T[67] due to its rich and complex magnetic structure. More recently (after the GMCE discovery) the $Gd_5(Si_x,Ge_{1-x})_4$ alloys with 0.08 < x < 0.43 have shown to be good candidates for this regime, presenting ΔT_{ad} values up to ten times higher than the ones discovered till then[26]. Later, other giant magnetocaloric families have also proved to have elements exhibiting a large MCE in the intermediate region, such as the $La(Fe_xSi_{1-x})_{13}$ and their hydrides[28] or the NiMnGa Heusler alloys[68].

The room temperature regime was always perceived as the most interesting temperature regime as it embraces more commercial possibilities. However, it was just in the late 1970s that a significant input was found: a $\Delta T_{ad} \sim 14$ K for a ΔH = 7T was measured in a pure Gadolinium, Gd, sample close to its Curie temperature, $T_C \sim 293$ K[19]. Attempting to improve the magnetocaloric effect of Gd-R alloys (where R is another

lanthanide) were tested but with no significant improvement[69]. Also many other intermetallic compounds whose T_C is higher than 290K were found, but none with a MCE comparable to Gd[70]. This situation changed at the end of the 1990s with the discovery of anomalously high MagnetoCaloric Effect on the FeRh alloy which reached ΔT_{ad} = 7 K, at T = 308 K, for a ΔH = 7 T[20]. However it was also proved that this effect was irreversible and consequently not applicable to real refrigerators. In 1997, Pecharsky and Gschneidner, discovered the Giant Magnetocaloric Effect (GMCE) on the $Gd_5Si_xGe_{1-x}$ x = 0.5 alloy and demonstrated that it is a reversible phenomena[4].

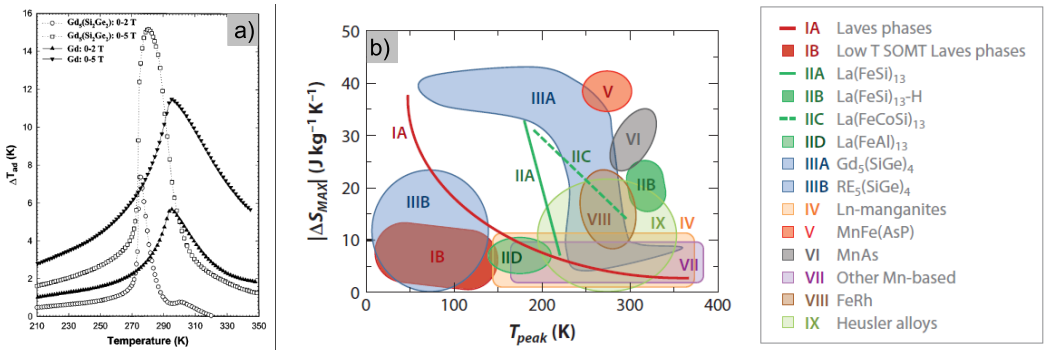

Figure 2.2 – a) ΔT_{ad} as a function of temperature measured in $Gd_5Si_2Ge_2$ (white symbols and dashed line) and Gd (black symbols and solid lines) under a $\Delta\mu_0$H = 2 and 5 T, extracted from reference[4]. b) Magnetic entropy change, ΔS_{iso}, as a function of each materials peak temperature (temperature at which ΔS_{iso}(T) reaches its maximum) of different compounds families presenting first and second order transitions, extracted from reference[31].

They measured a ΔT_{ad} = 15 K, at T = 275 K, for a $\Delta\mu_0$H = 5 T, significantly higher than the ΔT_{ad} = 12 K measured for pure Gd under the same field variation, as can be seen in Figure 2.2 a). The major reason behind the giant effects observed in FeRh and $Gd_5Si_2Ge_2$ is the fact that both undertake first order magnetic phase transition (FOMT), i.e., the order parameter that characterizes the transition (magnetization) changes very abruptly in a very narrow range of temperature, meaning that ∂M(T,H)/∂T) is higher than that of a second order phase transition (SOMT) at T_C. The Pecharsky and Gschneidner 1997 paper set a cornerstone for the room temperature magnetocaloric materials investigation as it boosted it in an unprecedent way, as is clear from the exponential increase on the number of papers published in this topic after 1997. In the following five years three other important compounds families presenting FOMT were discovered. In 2000, Hu and co-workers measured a large $\Delta S_{iso} \sim 4\ JK^{-1}Kg^{-1}$ under a magnetic field variation of just $\Delta\mu_0$H = 0.9 T in the Magnetic Shape Memory Alloy (MSMA), $Ni_{51.5}Mn_{22.7}Ga_{25.8}$[29] and since then there have been an intense research of the MCE of different MSMAs as is well reviewed by Planes and co-workers[68]. Wada and Tanabe found a comparable ΔT_{ad} = 13 K, at around T = 310 K under a ΔH = 5 T for the MnAs compound[71]. Just one year later Fujieda and co-workers discovered a large magnetocaloric effect in the $La(Fe_xSi_{1-x})_{13}$ and their hydrides families[72]. A giant ΔT_{ad} = 6.9 K, at T = 291 K, for a was measured for a $\Delta\mu_0$H = 2 T. Since then other families of compounds presenting FOMT and SOMT were discovered and among the most important

ones were summarized schematically in Figure 2.2 b), by Franco and co-authors[31].

2.3 The Magnetocaloric Effect dependencies in ferromagnetic materials

In this section a more detailed theoretical analysis of the magnetocaloric effect, in particular of the magnetic entropy change, will be given, considering ferromagnetic materials exhibiting first (FOMT) and second-order magnetic transitions (SOMT), as reported on our article[73]. The magnetic entropy change, ΔS_{iso}, dependency on the most important microscopic parameters of ferromagnetic materials, such as the Curie temperature (T_C), the spin value (J) and the magnetic field change (ΔH) will be detailed. In this work the FOMT and SOMT systems are considered, by using the Bean-Rodbell model[74], of magnetovolume interactions on the Weiss mean-field model[75]. As briefly reviewed in the previous section, one of the open questions is still to find the most suitable magnetocaloric material for the room temperature range. In particular, an intense debate still occurs on which kind of magnetic materials, FOMT or SOMT, are preferable for the RT magnetic refrigeration devices[76–79]. So far, the most promising compound families from the point of view of technological applications at RT include: $MnFe(P_{1-x}As_x)$, $La(Fe_xSi_{1-x})_{13}$, Si_x), $R_5(Si,Ge)_4$ (R is for Rare Earth), RM_2 (M is for Al, Co or Ni) and the manganites $R_{1-x}M_xMnO_3$ (M is for Ca, Sr and Ba). All these materials have been thoroughly characterized and their most important magnetic properties are known and are well reviewed in the following references[31,32,80–82]. The most conventional way to characterize the MCE of a given magnetic material is through the temperature dependence of its magnetic entropy change (ΔSm(T)) for a given applied field change ($\Delta\mu_0$H), namely through its peak value (ΔSm_{max}), Curie temperature (T_C), which establishes the optimal operating temperature, and the refrigerant capacity (product of full width at half maximum, $FWHM_{\Delta Sm(T)}$, and the ΔSm_{max}), which estimates the range of operating temperature. A considerable theoretical effort has been made on applying various models to the study of the MCE, from phenomenological theories[83–85] to microscopic models[86]. Nevertheless, there is still a notable lack of direct relations between the MCE and microscopic magnetic parameters, as evidenced in Lyubina et. al report[87]. During this work we have performed theoretical simulations to study the dependence of the ΔSm(T) curves on the following parameters: Curie temperature (T_C), spin value (J) and the applied magnetic field change ($\Delta\mu_0$H) for both first- and second-order magnetic transitions. The simulated ΔSm(T) curves were obtained within the basis of the molecular mean field theory[75], by solving numerically the following state equation for spin J,

$$M = NgJ\mu_B\mathcal{B}_{\mathcal{J}}\left(\frac{Jg\mu_B}{k_B}\frac{H+\lambda M}{T}\right), \tag{2.6}$$

where M is magnetization, N is the density of magnetic atoms, g the g-factor, μ_B the Bohr magneton, $\mathcal{B}_\mathcal{J}$ is the Brillouin function for spin J, k_B is the Boltzmann constant, H the applied magnetic field, T the temperature and λ the Weiss molecular mean-field exchange parameter. As was previously done[83], it is possible to include the Bean-Rodbell[74] volume dependency of the exchange energy and in this way simulate first and second order magnetic transitions.

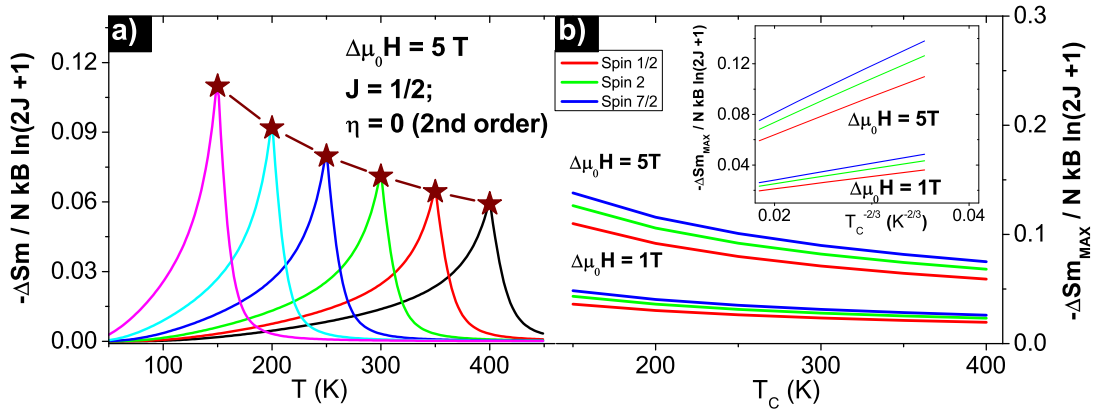

Figure 2.3 – a) Temperature dependence of the normalized magnetic entropy change for a set of simulated systems with T_C in the range 150-400 K undergoing second order magnetic transitions. In b) the dependence of the magnetic entropy change maxima on the Curie temperature for systems with different spin values and applied fields is plotted. In b) inset, the ΔSm_{max} is represented as a linear function of $T_C^{-2/3}$.

Fig. 2.3 a) shows the temperature dependencies of $\Delta Sm(T)$ normalized with the $Nk_B\ln(2J+1)$ factor (maximum entropy value) for a set of systems undergoing second order magnetic phase transitions in the 150-400 K temperature range. As can be seen in a) a strong attenuation of the ΔSm_{max} value with increasing T_C is observed. Contrarily, the FWHM increases significantly, i.e. a broadening of the $\Delta Sm(T)$ curves with increasing T_C is observed. Such evidence is a direct consequence of the fact that for a J value system the area under the $\Delta Sm(T)$ curve corresponds to the free energy change between a fully-ordered state at T<<Tc, and fully-disordered at T>>Tc, which is independent on the T_C value itself. In order to study the dependence of the ΔSm_{max} with the total spin number (J = 1/2, 2 and 7/2) and with the applied magnetic field amplitude (ΔH = 1 and 5 T), six different simulations were performed as shown in Fig. 2.3 b). As can be seen in this figure, the $\Delta Sm_{max}(T_C)$ curves show that there are no major changes in the overall behavior for different spins within the same applied field amplitude. Moreover, the ΔSm_{max} values are higher for higher total spin number within the whole T_C range, as was expected. Furthermore, it is found that the effect of increasing the applied field change (from 1 to 5 T) enhances this difference between the obtained $\Delta Sm_{max}(T_C)$ curves for systems with different J. At the lowest Curie temperature, 150 K, and for ΔH = 5 T, the J = 7/2 system achieves $\sim$ 14% of its maximum theoretical entropy change, in contrast with only 11 % for the J = 1/2 system. It is important to remark that these values

were normalized to the maximum theoretical value, $Nk_B\ln(2J+1)$, of each system. In the inset of Fig. 2.3 b), the ΔSm_{max} values for the three different spin value systems with ΔH = 1 and 5 T are represented as a function of $T_C^{-2/3}$. Although each spin value system presents a different slope, a linear dependence of ΔSm_{max} on $T_C^{-2/3}$ is clearly detected.

In order to interpret and justify the $T_C^{-2/3}$ dependency of the ΔSm_{max}, we performed simple analytical derivations starting from the Weiss mean field equation of state, eq. 2.6. This equation is rearranged in the following form:

$$\frac{Jg\mu_B}{k_B}\frac{H+\lambda M}{T} = \mathcal{B}_{\mathcal{J}}^{-1}\left(\frac{M}{Ng\mu_B J}\right), \tag{2.7}$$

where $\mathcal{B}_{\mathcal{J}}^{-1}$ represents the inverse Brillouin function for total angular momentum J.

Considering the Taylor expansion of the inverse Brillouin function[88], eq. 2.7 can be approximated to the following equation of state:

$$\frac{H}{M} = \frac{1}{C}(T-T_C) + \frac{K}{C^2}TM^2 + \frac{K'}{C^3}TM^4 + \dots, \tag{2.8}$$

where

$$K = \frac{2J^2+2J+1}{10J(J+1)k_BN}, \tag{2.9}$$

$$K' = \frac{44(2J+1)^2\left(J^2+J+1\right)-(2J+1)^2}{2800J^2(J+1)^2k_B^2N^2} \tag{2.10}$$

C the Curie constant,

$$C = \frac{NJ(J+1)g^2\mu_B^2}{3k_B} \tag{2.11}$$

and $T_C = C\times\lambda$. Our description is for an arbitrary spin value. Nevertheless, for the particular case of a J = 1/2, the inverse Brillouin function is simply $atanh(2M/Ng\mu_B)$, while for $J = \infty$ and 4, other approximate expressions are available[89,90].

By integrating on M, the free energy of the system is given:

$$G = G_0 - MH + \frac{1}{2C}(T-T_C)M^2 + \tag{2.12}$$

$$+ \frac{K}{4C^2}TM^4 + \frac{K'}{6C^3}TM^6 + \dots, \tag{2.13}$$

Equation 2.12 shares the same structure in even powers of M as the typical Landau theory expansion of the free energy[84,91], however with an explicit linear dependence of the higher-order Landau parameters on T.

The state equation allows an analytic description of the field dependence of the MCE (ΔSm) of a mean-field system, considering the temperature derivative of the free energy

expression in eq. 2.12:

$$-S_M = \frac{\partial G}{\partial T} = \frac{1}{2C}M^2 + \frac{K}{4C^2}M^4 + \frac{K'}{6C^3}M^6 + \dots \,, \tag{2.14}$$

From the state equation, the field dependence of magnetization at $T = T_C$ (critical isotherm) is:

$$M = \left(\frac{C^2}{K}\right)^{1/3}\left(\frac{H}{T_C}\right)^{1/3} + \dots \,. \tag{2.15}$$

The magnetic entropy change due to a field change from 0 to H at $T = T_C$ ($\Delta Sm(T=T_C) = \Delta Sm_{max}$) is then:

$$-\Delta Sm_{max} = \frac{1}{2C}\left(\frac{C^2}{K}\right)^{2/3}\left(\frac{H}{T_C}\right)^{2/3} + \dots \,, \tag{2.16}$$

Eq. 2.16 justifies the $T_C^{-2/3}$ dependency of ΔSm_{max} found in our second order systems simulations. It is important to stress that eq. 2.16 also allows to relate ΔSm_{max} with known parameters of these analytic ferromagnetic systems, such as: N, J and the applied magnetic field $\mu_0 H$ (in a field change from 0 to $\mu_0 H$). From eq. 2.16, it is obvious that these parameters values define the slope of the curve ΔSm_{max} ($T_C^{-2/3}$), hence explaining the different slopes obtained for J = 1/2, 2 and 7/2 and for the different applied field changes within the same spin number, as is seen in Fig. 2.3 b) inset. In fact, the ratios between the two slopes (one for $\Delta\mu_0 H = 1$ and the other for $\Delta\mu_0 H = 5$ T) obtained for the same J value system, are in fair agreement with the ratio of the two applied field change amplitudes, ($5^{-2/3}$). By substituting eqs. 2.9 and 2.11 into eq. 2.16 it is straightforward to observe that the dependency on N is simply linear, thus implying that, as expected, a material ΔSm is maximized for denser crystal structures.

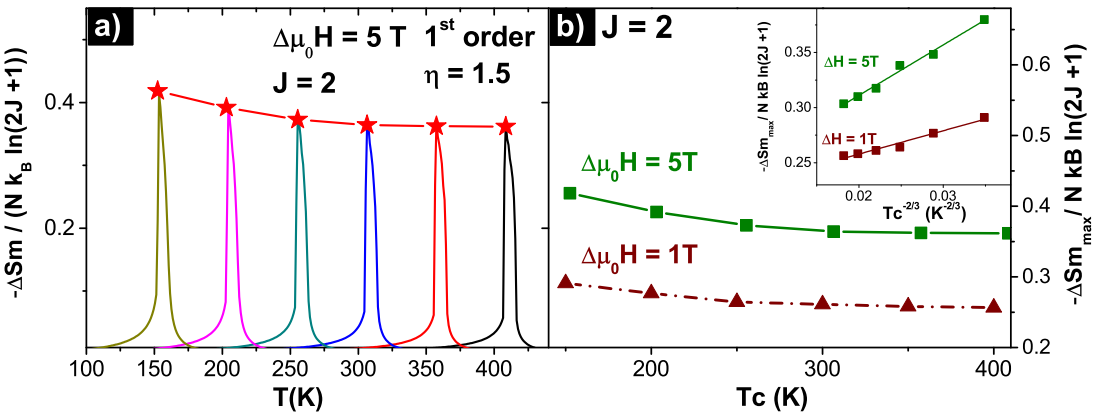

Figure 2.4 – a) Temperature dependence of the magnetic entropy change (normalized) for a set of simulated systems undergoing first-order magnetic transitions (η=1.5) with different T_C. In b) the dependency of the entropy change maxima (ΔSm_{max}) on the T_C for two different applied magnetic fields ($\Delta\mu_0 H$=1 and 5 T) is represented. In b) inset the ΔSm_{max} obtained for both applied fields is plotted as a function of $T_C^{-2/3}$.

Furthermore, by considering the volume dependence of the Curie temperature given by the Bean-Rodbell model[74], first order magnetic transition systems (FOMT) were also simulated and studied. Surprisingly, the same overall decreasing behavior of ΔSm_{max} with increasing T_C is found, as is seen in Fig. 2.4 a). As was already pointed out in the literature[84], the shape of the simulated first-order $\Delta Sm(T)$ curves resembles the experimentally observed half bell shape. For these curves no significant changes in the FWHM values were observed between systems with different T_C. Nevertheless, the area under the curve $\Delta Sm(T)$ does not change due to the same reasoning mentioned for the second-order systems case. Moreover, in Fig. 2.4 b), the Curie temperature dependence of the ΔSm_{max} for first-order systems with $\Delta\mu_0 H$ = 1 and 5 T are plotted. For both cases the monotonically decreasing behavior of $\Delta Sm_{max}(T_C)$ is verified. As expected, the ΔSm_{max} values are higher when the applied field is higher within the simulated T_C range. When comparing the ΔSm_{max} normalized values for J=2 first- and second-order systems (which is valid as both systems were normalized with the same factor - $Nk_B\ln(2J+1)$) it is clear that the first-order system has much higher values than the second order ones. This difference is constant (~ 0.22) for the T_C range considered, showing that a magnetovolume coupling strong enough to promote first-order transition with small applied field changes, is responsible for a significant increase in the maximum magnetic entropy change.

Finally, in Fig. 2.4 b) inset, these ΔS_{max} values are plotted as a function of $T_C^{-2/3}$. The linear relation of ΔS_{max} with $T_C^{-2/3}$ is again observed. The different slopes are associated with the different applied fields, in accordance with eq. 2.16.

In order to compare the simulations, specifically the $T_C^{-2/3}$ dependency presented above, with experimental results, a set of data from second and first order magnetic transition systems was collected from the literature and plotted as a function of $T_C^{-2/3}$ in Fig. 2.5 a) and b). As is clearly seen, for these second and first order magnetocaloric alloy families, ΔS_{max} follows the $T_C^{-2/3}$ dependency predicted by our calculations and modelling. The second order magnetic systems here presented were extracted from: $Gd_{1-x}Tb_xCo_2$ (for $\Delta\mu_0 H = 2T$)[92], $La_{2/3}(Ca_{1-x}Sr_x)_{1/3}MnO_3$ (for $\Delta H = 1$ T)[93] and $Dy(Co_{1-x}Fe_x)_2$ (for $\Delta\mu_0 H = 1$ T)[94]. Also for these experimental results, different slopes are observed which probably result from their specific J and $\Delta\mu_0 H$ parameters, as was shown by eq. 2.16.

The first order magnetic systems data were all measured with a $\Delta\mu_0 H = 5$ T and were extracted from: $MnFe(P_{1-x}As_x)$[95], $Gd_5(Si_xGe_{1-x})_4$ for $x < 0.4$[80] and RCo_2[96]. These represent a wide set of different magnetocaloric materials, thus validating the far-ranging nature of the $T_C^{-2/3}$ dependency found by our calculations. It is interesting to note that the lattice entropy contribution, which is not taken into consideration in the model, does not invalidate observing the $T_C^{-2/3}$ dependency in the studied systems. One would assume that throughout the composition ranges shown for each system in Fig. 2.5, this contribution is either negligible or approximately constant. This is particularly relevant in first-order systems (such as $Gd_5(Si_{1-x}Ge_x)_4$), where the lattice entropy change contri-

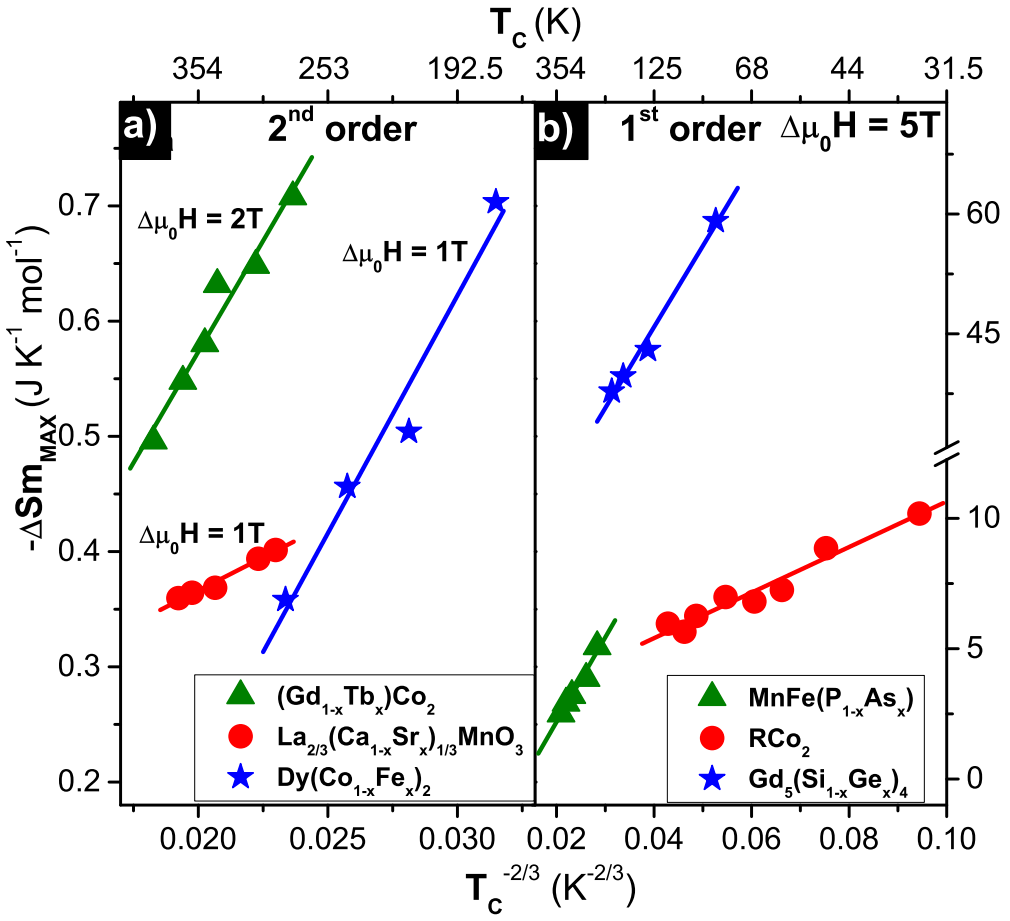

Figure 2.5 – a) ΔSm_{max} experimental data (in J K^{-1} mol^{-1} units) as a function of $T_C^{-2/3}$ for the second order magnetic transition compounds families: $Gd_{1-x}Tb_xCo_2$ (green Deltas), $La_{2/3}(Ca_{1-x}Sr_x)_{1/3}MnO_3$ (red circles) and $Dy(Co_{1-x}Fe_x)_2$ (blue stars). b) Also ΔSm_{max} ($T_C^{-2/3}$) experimental and normalized data for the first-order magnetic transition compounds families: $MnFe(P_{1-x}As_x)$ (green Deltas), RCo_2 (red circles) and $Gd_5(Si_xGe_{1-x})_4$ (blue stars). The plotted lines are linear fits to the presented data.

bution should in principle be largely independent on composition, as long as a particular structural transition occurs. The fact that other first and second order magnetocaloric families do not show this behavior allows us to induce that such systems must have more complex magnetocrystalline interactions than the constant magnetovolume coupling considered in these calculations. Particularly for the $La(Fe_{13-x}Si_x)H_y$ family, the main reason for not exhibiting this behavior is most probably its complex set of minima in its total energy as a function of spin moment, which turns the transition from the paramagnetic to the ferromagnetic state into a series of consecutive transitions, as was found experimentally in reference[96]. Whereas, for the $MnAs_{1-x}Sb_x$ family, both the change from a first to a second order magnetic transition for low Sb concentration and the phenomenological fact that the T_C is lowered with Sb concentration, induce the lowering of ΔSm_{max} when T_C decreases, as was reported in Reference[71] by our team. With this simple contribution we believe that we helped to show that the magnetovolume coupling plays a decisive role on the enhancement of the magnetic entropy change compared

to an increase of J, under magnetic field changes typically used in magnetic refrigeration prototypes. Therefore in the magnetocaloric materials search, efforts should be focused on optimizing magnetic coupling mechanisms as opposed to substituting magnetic ions. Finally, starting from the molecular mean field magnetization equation, an approximation of the ΔSm_{max} as a function of T_C, H, J and N was achieved, allowing a direct estimation of the ΔSm_{max} for a given mean field system. Unfortunately, FOMT materials with strong magnetovolume coupling, tend to become unstable after several thermal and magnetic cycles. They undergo large lattice expansion/compression across the transition, which undermine the stability of the material itself and eventually can lead to its degradation. Considering this experimental information, an ideal material for practical applications should possess a giant entropy change, however with a minimal lattice relative expansion/compression: a material in the crossover region between the SOMT to the FOMT materials.

2.4 The $R_5(Si_xGe_{1-x})_4$ family

As became clear from the section 2.2, the $R_5(Si_xGe_{1-x})_4$ alloys family is of great interest for the magnetic refrigeration research subject. Despite nowadays is not considered to be in the top-three materials for near future magnetic refrigeration applications - mostly due to their high cost (Gd and Ge are expensive elements) and their scarcity in the planet[97,98]. The $R_5(Si_xGe_{1-x})_4$ family was discovered back in 1966 by Smith and co-workers, namely the R= Nd, Sm, Gd, Tb, Er and Y Germanides and Tb, Er and Y Silicides[99]. In the next year, Holtzberg and co-workers[100] published the magnetic data on the family $Gd_5(Si_xGe_{1-x})_4$, when they have found Gd_5Si_4 T_C was 336 K, an anomalous result considering it is 40 K higher than that of pure Gd and also the fact that the Gd_5Ge_4 having a similar atomic structure presented an antiferromagnetic (AFM) fundamental state with $T_N \sim 115$ K. They were able to determine with great accuracy the crystallographic phase diagram of $Gd_5(Si_xGe_{1-x})_4$ distinguishing the two different orthorhombic structures of Gd_5Ge_4 and Gd_5Si_4 (O(II) and O(I), respectively) and an unidentified phase for $0.5 < x < 0.7$. Despite these intriguing aspects, the $Gd_5(Si_xGe_{1-x})_4$ spent thirty years in the shadow, without deserving any significant interest from the materials science community. So, just in 1997, with the discovery of Pecharsky and Gdschneider[4], this family was brought again to light and since then an intensive study has been made and more interesting properties have been found other than the GMCE, such as Colossal Magnetostriction[101] and Giant Magnetoresistance[21]. These properties are a consequence of the extreme sensitivity exhibited by these compounds under variations of both external (temperature, magnetic field, pressure) and internal parameters (stoichiometry[26] and doping[102] on the magnetocaloric properties of the $Gd_5Ge_2Si_2$ alloy). Such an extreme sensitivity is thought to be intimately related to the atomic structure, magnetic sublattice and their interplay and this is why it is important to understand them both and to try to

unveil their strong correlation.

2.4.1 The Structural and Magnetic Phases

In the $R_5(Si_xGe_{1-x})_4$ family there are essentially three different crystallographic structures: Orthorhombic I or Sm_5Si_4-like (Pnma space group), Monoclinic (P 1121/a space group) and Orthorhombic II or Sm_5Ge_4-like (also Pnma space group). These structures do not differ so much from each other, and they can be visualized in Figure 4.5, as a stack of stable slabs with sub nanometer height (along *b* axis) and infinite width (along *a* and *c* axis). These slabs are constituted by blocks of two different polyhedral: a pseudo-cube with the rare-earth atoms organized in a body cubic centered structure (Figure 4.5 a)) and another pseudo-cube where the rare-earth atoms also lie at the vertices but in the center a pair of Si/Ge atoms is placed.

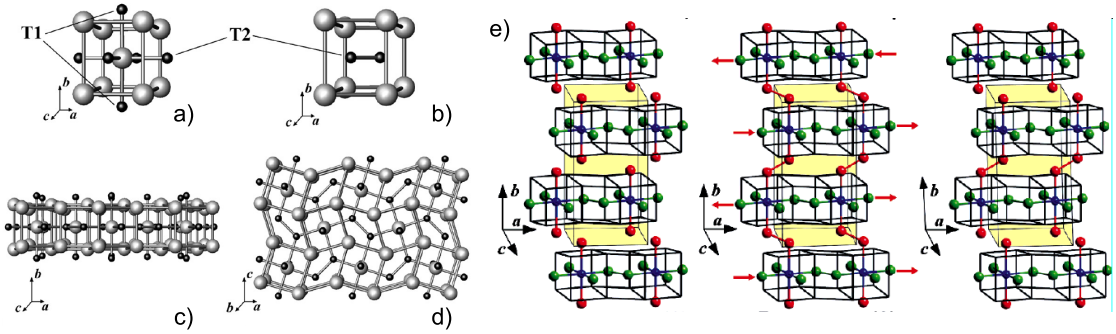

Figure 2.6 – Schematic representation of the atomic structure of $R_5(Si_xGe_{1-x})_4$ compounds, where the grey and bigger spheres represent the Rare Earth atoms and the smaller and black spheres represent Si or/and Ge. Two pseudocubes with ,a,) and without ,b), the rare earth at its center. In c) a perspective of the *a*-*b* plane (so-called slab) is given with the pseudocubes connected along the *a*-axis. In d), a perspective of the *a*-*c* plane where the two pseudocubes are connected to each other, as extracted from[103]. In e) a schematic representation of the *a*-*b* plane is given with the unit cell highlighted in dark yellow parallelepiped. The major difference between the three structures is the interslab bonding, where the left structure (O(II)) shows no covalent bonds between the Si,Ge atoms (here represented in red spheres), the middle (O(I)) shows all interslab covalent bonds formed and the right one shows only half of these bonds formed, as extracted from[13].

These two pseudo-cubes are connected to each other via T2-T2 Si/Ge atoms bonding along the *a*-*c* plane, forming a slab with infinite length and width. On the other hand, the Si/Ge atoms in the T1 sites (interslab) are responsible for the connection between slabs, stacking them along the *b* direction (Figure 4.5 e)). The major difference between the three crystallographic structures is the number of covalent bonds at the T1 sites. Nowadays, it is well known that: O(II) structure does not have any T1-T1 bonds between slabs, Monoclinic has only half of these bonds formed, while the O(I) has all the bonds formed (as schematically pictured in Figure 4.5 (e) at the left, right and middle, respectively). Therefore, T1-T1 bonds assume a capital importance on the definition of the crystallographic structure and any structural transition occurs through their formation or breaking[104]. The majority of the $R_5(Si_xGe_{1-x})_4$ compounds can assume any of these three structures. The structure they assume at some specific moment depends on

external parameters (temperature, magnetic field and pressure) and internal ones (stoichiometry, x). Pecharsky and co-workers[105], using experimental data, formulated an empirical expression relating the ratio between the metallic rare-earth (r_R) and the Si/Ge (r_T) atoms radii to the room temperature adopted for a specific $R_5(Si_xGe_{1-x})_4$ composition, where (r_T) is simply $r_T = r_{Si} \cdot f_{Si} + (1\text{-}f_{Si}) \cdot r_{Ge}$. By comparing a large amount of data they found radii ratios ranges for the three different structures. Hence for Gadolinium case if r_R/r_T lies in the [1.362-1.338] range the adopted structure should be O(I), if it lies in the [1.334-1.327] its M and if its [1.322-1.307] its O(II).

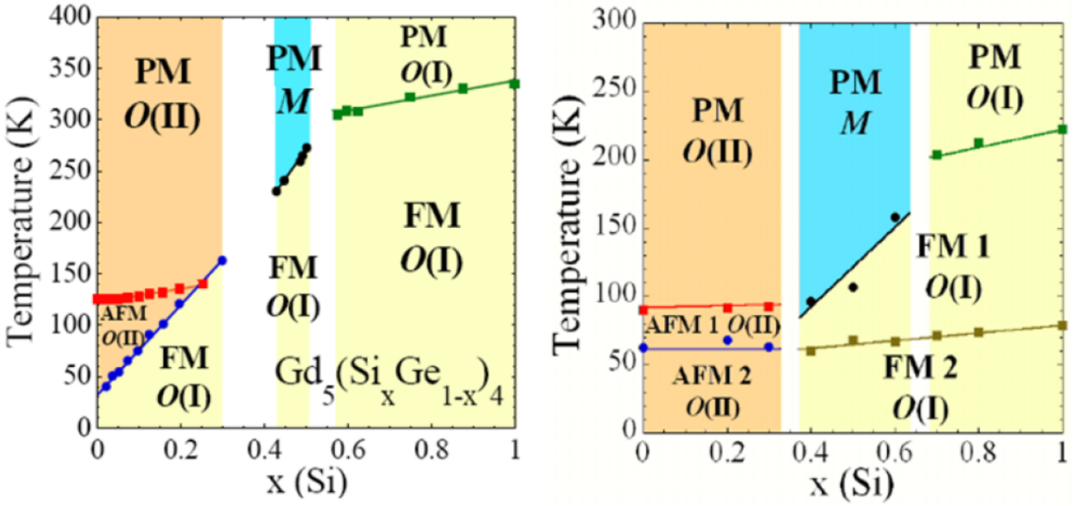

Figure 2.7 – Phase diagram of $Gd_5(Si_xGe_{1-x})_4$,a), and $Tb_5(Si_xGe_{1-x})_4$,b), identifying the atomic and magnetic structures and delimiting their temperature and stoichiometry (x) regions. AFM, FM and PM stands for antiferromagnetic, ferromagnetic and paramagnetic states.

In figure 2.7 the structural and magnetic phase diagrams of Gd (a)) and Tb (b)) systems are represented. As can be seen, specially in the Si-rich region of the diagrams, the ferromagnetic state is typically hosted by the O(I) structure, while the paramagnetic (PM) and antiferromagnetic (AFM) configurations are hosted by M and O(II) structures. Several studies have been performed in order to understand the relation between structural and magnetic phases[105–107]. In particular, Choe and co-workers[104] studied the mediation of the 4f localized magnetic moments coupling by conduction band electrons (using the RKKY interaction model[108] to investigate the behavior of the effective exchange parameter, J_{eff}, as a function of r, the Gd-Gd distance between neighboring slabs along the b-axis). They came to the conclusion that, within a range of realistic Gd-Gd distances (that are smaller for the O(I) structure due to the full formation of interslab T1-T1 bonds), J takes a positive value for the O(I) structure, meaning that it represents a ferromagnetic coupling, in accordance with the experiment. Also concluded that AFM (negative J_{eff}) configuration is more favorable for the r values observed in the M and

O(II) structures. Another interesting work used X-ray Magnetic Circular Dichroism to probe $Gd_5Si_2Ge_2$, demonstrating that Ge-Ge interslab covalent bonds enhance the exchange coupling parameter J_{eff} in two ways: by making shorter the Gd-Gd distances but also because the Ge-Ge bonds themselves become magnetically polarized favoring the bridging of ferromagnetism across adjacent slabs[109].

2.4.2 The Magnetostructural transition

As mentioned earlier, the $R_5(Si_xGe_{1-x})_4$ present other giant effects induced by different external parameters. For instance, under temperature sweep, they can exhibit a colossal thermal expansion up to $\sim 1.4\%$[110] and a giant electrical resistance change $\sim 22\%$[21]. Similar changes can also be obtained when only a magnetic field is applied at a fixed temperature[21,24]. The same applies to the solely action of external pressure[25,111]. In fact when there is an isotropic temperature change or an isothermal entropy change under the application of an external pressure, the effect is known as Barocaloric effect or more generally mechanocaloric effect. This variant of the MCE is being subjected of an increasing number of reports since 2010 when Manosa and co-workers have measured it in the NiMnIn MSMA[112]. This extremely high sensitivity to external parameters is mostly due to the easiness with which magnetic and structural transitions are induced by their variation. For instance, the GMCE of $Gd_5Si_2Ge_2$ is a consequence of a simultaneous magnetic and structural (magnetostructural) transition (from a [M, PM] to a [O(I), FM] state) induced by a sufficiently strong magnetic field. Several theoretical studies helped disclose the thermodynamic origin of this transition. Namely, Paudyal and co-workers[113] developed a pioneering work based on the fundamental thermodynamic equations and on results from first principles calculations, which allowed the theoretical estimation of the temperature dependencies of several magnetic properties (including the MCE) of the $Gd_5Si_2Ge_2$ compound. They plotted the free energies of both structures in competition (M and O(I)) as a function of temperature and from the behavior of these curves they were able to estimate the magnetostructural transition temperature (the signaled crossing point) as being $T_S^{theor} \sim 265$ K (corroborating the experimentally obtained $T_S^{exp} \sim 275$ K). T_S is defined as the temperature at which the crossing ΔFmin[M] = ΔFmin[O(I)] occurs, i.e. the temperature above which one structure becomes energetically more favourable than the other. The influence of a magnetic field is to promote a more moderate ΔF(T) curve with temperature. This effect is enhanced for the lower T_C structure (M, in this case), leading to the increase of T_S (as was also confirmed experimentally[4]. So, at room temperature, the magnetostructural transition can be induced by the application of a magnetic field that feeds the system with enough energy to overcome the small energy gap between its two competing structures. By doing so, the system will not only change its crystallographic structure, but also its magnetic structure, from a paramagnetic (Monoclinic ordering temperature is only at 209 K) to a ferromagnetic phase (Orthorhombic ordering temperature is 301 K),

due to their different Curie temperatures - i.e. at 275 K the O(I) structure is already in its FM state because its T_C is 301 K. Based on this model, it becomes clear that the (∂M(T,H)/∂T), and consequently the MCE, will be enhanced for systems where T_S is very close (but higher) to the lower T_C[114]. Our group extended this work to $Tb_5Si_2Ge_2$ and Tb_5Ge_4 compounds[76,115,116]. It was shown that for $Tb_5Si_2Ge_2$ the structural and magnetic transitions are slightly decoupled in temperature as suspected by experimental work[76]. Whereas for the Tb_5Ge_4 compound the large energy gap ΔF(O(II)-O(I)) was demonstrated to be unsurpassable by experimental available magnetic fields at any temperature[116].

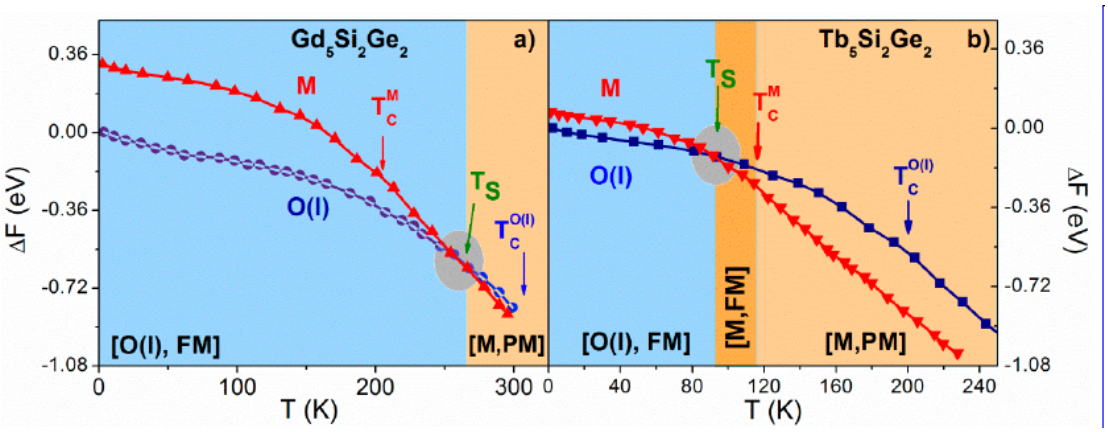

Figure 2.8 – Free energy as a function of temperature considering the magnetic entropy and the first principles calculations (F(T=0 K)) for both M and O(I) structures for the a) $Gd_5Si_2Ge_2$ and b) $Tb_5Si_2Ge_2$ compositions, as extracted from our article[115]. T_S is defined as the temperature at which the crossing ΔFmin[M] = ΔFmin[O(I)] occurs.

From a microscopic point of view, these structural transitions can be imagined as a sliding of the slabs along the a axis, with adjacent slabs sliding in opposite directions generating a shear displacement as pictured by the arrows in Figure 4.5 e). Such movement decreases T1-T1 atomic distances, promoting the formation of the covalent bonding at interslab connections that were broken in the M/O(II) structure. No major changes occur inside the slabs which maintain approximately the same interatomic distances. Nevertheless, the overall unit cell suffers visible changes: as mentioned its *a* parameter undergoes a drastic contraction (up to $\Delta a/a \sim$ - 1.6%), whereas its b and c parameters show smaller expansion ($\Delta b/b \sim$ +0.3% and $\Delta c/c \sim$ +0.7%[101], resulting in an overall volume contraction. In particular, the T1-T1 interslab interatomic distance has a colossal contraction of about 30% across the transition. In fact, the $R_5(Si_xGe_{1-x})_4$ MCE giant intensity can be explained in the light of these magnetostructural transitions. As Pecharsky and co-workers explained[23,117] the measured ΔS_{iso} can be decomposed in two parts: $\Delta S_{iso}^{T} = \Delta S_{iso}^{M} + \Delta S_{iso}^{St}$, where ΔS_{iso}^{St} corresponds to the entropies difference from the two atomic structures involved in the magnetic field-induced structural transition and the ΔS_{iso}^{M} represents conventional purely magnetic entropy changes. Their estima-

tions found that for $\Delta\mu_0 H < 2$ T, the ΔS_{iso}^{St} is responsible for more than half of the ΔS_{iso}^{St} for Gd_5Ge_4, $Gd_5Si_{2.09}Ge_{1.91}$ and $Gd_5Si_2Ge_2$ compounds, being almost two times the ΔS_{iso}^{M} value. The ratio $\Delta S_{iso}^{St}/\Delta S_{iso}^{M}$ decreases with increasing $\Delta\mu_0 H$, being close to 1 for $Gd_5Si_{2.09}Ge_{1.91}$ and 1.5 for $Gd_5Si_2Ge_2$ compound at $\Delta\mu_0 H = 5$ T. Additionally, they found a linear proportionality between the ΔS_{iso}^{St} and the volume difference between the two structural phases (note: some structural transitions occur without changing their space group) $\Delta V/V$ - i.e. the larger the $\Delta V/V$ the larger the ΔS_{iso}^{St} and in most cases (except the cases where the signal of ΔS_{iso}^{St} is inverse to that of ΔS_{iso}^{M}) the larger the ΔS_{iso}^{T} [117].

2.5 Nanostructured Magnetocaloric materials

As mentioned above, the production, characterization and optimization of magnetocaloric nanostructures is still in its early steps. A paradigmatic example of this delay is the Gd film: to our knowledge, they were first deposited and studied in 1966[118], however their magnetocaloric properties were only accessed for the first time in 2010 in a multilayered Gd/W film[119]. Fortunately, since then Gd and Gd based thin films were the object of interesting and thorough works, such as those of Miller and co-workers[39,120,121]. In particular they have deposited an MgO/W(5nm)/Gd (40nm)/W(5nm) heterostructure via magnetron sputtering of high purity W and Gd targets and they have found an entropy change peak at T = 284 K associated with the second-order magnetic phase transition, with a value of approximately 3.4 J K^{-1} Kg^{-1} under a $\Delta\mu_0 H = 3$T, one third the value observed for bulk Gd[122]. On the other hand the measured ΔS_{iso} full width at half maximum (FWHM) was 70 K, significantly wider than that of bulk Gd under similar conditions. Finally, its relative cooling power was estimated at 240 J Kg^{-1}, close to that of bulk Gd 410 J Kg^{-1}. Miller's group also studied the importance of pre-gettering the sputtering chamber prior to Gd deposition. In particular for 30 nm Gd thin films grown by RF-Sputtering onto 450°C pre-heated Si oxidized substrates, they have found that pre-heating the substrate holder at 600 °C and then sputter Gd for 30 min, in order to the Gd react with any residual amounts of Oxygen that were not removed during the vacuum pumping process, was an important step towards the improvement of the magnetocaloric properties. Namely, the maximum magnetic entropy, ΔS_{iso}^{max}, the relative cooling power and the overall saturation magnetization which were increased by $\sim$ 50%, $\sim$30% and $\sim$35%, respectively[120]. In Figures 2.9 a) and b), the ungettered (red circles), the gettered (blue squares) and the bulk Gd magnetic entropy change as a function of temperature is plotted. The authors attributed such significant improvement (ungettered vs gettered) to a lowering of the Gd oxide content and to an improved film roughness and morphology.

Furthermore, another hot topic study on Gd thin films was devoted to the dependence of their Curie temperatures (T_C) on the thin film growth details. Gadjdzik and

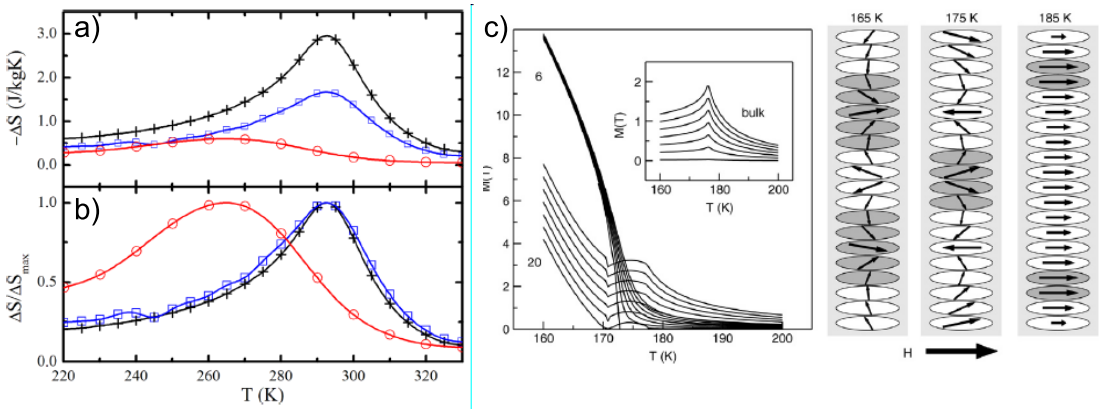

Figure 2.9 – a) The magnetic entropy change $\Delta S_{iso}(H, T)$ of a 30 nm Gd film grown at room temperature (red circles), grown at 450 °C after pre-gettering (blue squares) and bulk Gd (black crosses). The ΔS_{iso}^{max} were 0.6, 1.7 and 2.9 J K^{-1} Kg^{-1} under a $\Delta\mu_0 H$ = 1 T. b) Same data normalized to ΔS_{iso}^{max}. These figures were extracted from Reference[120]. c) Theoretical magnetization estimation for Dy films with 6 and 20 monolayers under a 0.06 T applied magnetic field. The bulk Dy magnetization curves are shown in the inset for the same external field values. And in the right-side a schematic representation of the spin structure in the 20 layers film, at different temperatures. The gray symbols indicate a slightly larger thermal value of the total angular momentum. These figures were extracted from Reference[61]

co-workers[123] found that the depression of the Curie temperature of ultra thin (d) epitaxial Gd films varies in the 150- 300K range and as $\Delta T_C \propto d_{Gd}^{-\lambda}$ where λ equals 1 for d_{Gd} < 11 nm , evolving to λ = 1.6 for thicker films. They have attributed such evolution to a dimensional cross-over between a 2D and a 3D-Ising or Heisenberg ferromagnetism. In addition they have also found what is the minimal Gd island area capable of hosting long-range ferromagnetic order: 12000 [2]. A more fine T_C tuning in the 290-310 K range was achieved by inducing a ”negative” pressure via Hydrogen atoms injection into Gd film or nanocrystals, enhancing its unit cell volume and its T_C[124,125]. In comparison with bulk, nanostructured Gd hexagonal close packed (hcp) atomic structure is compromised by three main factors: amorphization[126], the high portion of Gd_2O_3 oxide phase[120] and the Gd fcc phase formation[127–129]. These factors depend strongly on the preparation conditions such as: pressure, substrate temperature, growth rate, grain size, etc.. Other pure Rare-earths nanostructures have deserved an increasing interest triggered by the innovative theoretical works by V. Mello and F. C. M. Filho and respective co-workers[61,130,131]. In contrast to Gd, Terbium (Tb), Dysprosium (Dy) and Holmium (Ho) present strong anisotropic magnetic properties, because of their incomplete 4f orbitals. As previously referred, Dy is known to have a helical magnetic structure with a period of few unit cells (< 20) as a ground state. However, if a very thin film is produced (with a thickness lower than this period, t < 15 nm), the helical order will be truncated. Furthermore, the spins at the film surface will experience a symmetry break and will reduce their correlations with second neighbors[61]. This theoretical work has shown that in such circumstances the pure ferromagnetic ordering will be favored by these spins and ultimately, by applying a magnetic field strong enough (> 0.06 T) it is

possible to completely suppress the helical magnetic state in favor of a collinear ferromagnetic one, as evidenced by the estimated magnetization versus temperature curves plotted in Figure 2.9 c). Obviously such transformation will lead to an enhanced overall magnetic moment and consequently an enhancement of the MCE in comparison with the bulk form. Experimentally, R = Tb and Dy thicker (100 nm) films deposited by DC Sputtering onto an oxidized and pre-heated (350 °C or room temperature) Si substrate have shown magnetic transitions temperatures slightly lower to their bulk counterparts, as Scheunert and co-workers have shown[132]. Surprisingly, they have also found the suppression of the antiferromagnetic helical magnetic state for such thicker films, resulting in a direct transition from paramagnetic to ferromagnetic state for both the Dy and the Tb thin films, which is hypothesized not to be a consequence of the surface spins, but rather a result of the lattice expansion caused by strain in these films.

Let us know consider nanostructures of binary alloys, such as the Iron-Rhodium (FeRh) thin film. As mentioned in the previous chapter, Lommel and co-workers were able to successfully grow a FeRh thin film[44] using a multilayering approach. Both the electrical transport and magnetic measurements evidenced the presence of the bulk characteristic first-order transition, despite being much more broadened (about 200 K) in comparison with the (~15 K) observed in bulk, as can be confirmed in Figure 2.10 (a). Also the thin film overall magnetic moment was about one third of the bulk one.

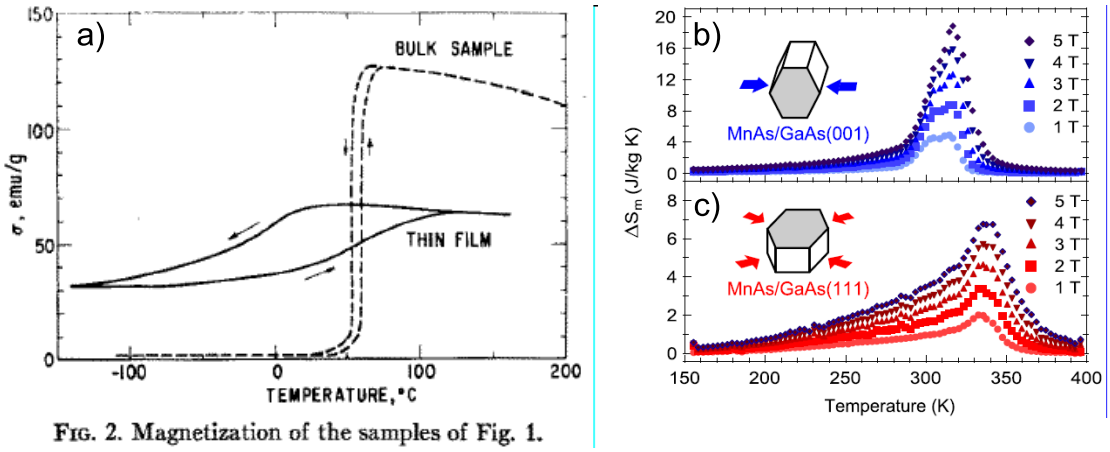

Figure 2.10 – a) The thin film (continuous line) and bulk (dashed line) FeRh magnetization versus temperature plot, extracted from Reference[44]. In b) and c) are represented the magnetic entropy changes, $\Delta S_{iso}(T)$, as a function of temperature of two MnAs films deposited on top of a GaAs (001) and (111) oriented substrates for five different $\Delta\mu_0 H$, extracted from Reference[47].

More recently, several studies on FeRh films have been published. In particular, Zhou and co-workers have shown that a 100 nm epitaxially grown FeRh thin film on top of MgO substrate undergoes a giant a lattice parameter change ~ 0.66% (almost twice the value obtained for the bulk counterpart) across the magnetostructural transition[133]. The authors attributed this result to a distortion of the tetragonal structure due to the relationship between the film and the substrate. Magnetic measurements have

also shown thermal and magnetic hysteresis (M(T) and M(H) curves, respectively, confirming the first-order nature of this transition, resulting in a GMCE, in fact the highest intrinsic effect measured in thin films so far: $\Delta S_{iso}^{max} \sim 20$ J K^{-1} Kg^{-1}. In polycrystalline FeRh a narrowing of the thermal hysteresis, from 200 K to 50 K, was achieved through a post-deposition annealing at 600 °C for 1 hour[134]. The most surprising result arose from annealed FeRh nanoparticles. Hillion and co-workers have demonstrated that a 970 K post-deposition annealing of a FeRh nanoparticles ensemble embedded in a carbon matrix enables the so-called B2 atomic structure and the ferromagnetic phase, which remains stable at T = 3 K and therefore do not present the typical AFM-FM transition observed in bulk and thicker FeRh thin films[135]. The authors ascribed this unique FM order to the finite-size induced atomic structural relaxation, specially closer to the nanoparticles surface. Mosca and co-workers, as referred in previous chapter, acknowledged the fact that MnAs ferromagnetic interactions are strongly anisotropic and susceptible to subtle structural changes, grew MnAs epitaxial films on top of two Gallium Arsenide (GaAs) substrates with different orientations ((0 0 1) and (1 1 1))[47]. In the bulk counterpart the α-MnAs phase crystallizes in a ferromagnetic hexagonal NiAs-type structure at room temperature, which is stable up to 318 K, when it transforms into an Orthorhombic β-MnAs and PM phase by a first-order phase transition that implies a 2% volume contraction. They grew MnAs 70 nm epilayers by Molecular Beam Epitaxy on heat treated (260 °C) substrates. The complete process was monitored by reflection high-energy electron diffraction (RHEED) diagrams, which together with XRD allowed to ensure the desired epitaxial relations. Due to the large mismatch between substrate and film unit cells, the (1 1 1) substrate induces a strong (0.82%) compressive strain in the basal plane leading to a premature appearance of the low volume β phase and consequently to a smoothing of the magnetostructural transition. This does not happen in the (1 0 0) case due to the different configuration of the unit cells, and hence its transition occurs in a narrower temperature interval. As expected, such constraining reflects on the MCE of both cases leading to a sharper and higher MCE for the less constrained (1 0 0) case:~ 20 J K^{-1} Kg^{-1} in comparison with ~ 7 J K^{-1} Kg^{-1} (1 1 1) case, as can be seen in Figures 2.10 (b) and (c). A remarkable and innovative example of how to take advantage of these materials multifunctionality was given by Duquesne and co-workers[48]. They have designed and deposited a multilayer system composed by a 1 μm Zinc Oxide (ZnO) piezoelectric layer deposited on the top of a gold buffer layer (300 nm), which was on top of epitaxially grown 100 nm MnAs epilayer wich in turn was on the top of a GaAs substrate. By emitting an acoustic surface wave triggered by an electrical emitter patterned on the ZnO piezoelectric layer in an interval range around room temperature (0-600 °C), the authors observed that ultrasonic waves (170 MHz) are strongly attenuated by the MnAs phase coexistence (up to 150 dB/cm). They showed that such attenuation was caused by the MnAs GMCE and hence they demonstrated the two-way relationship between mechanical control and magnetic properties and their (almost) endless opportunities. Although more scarce, there are also few interesting works

on MnAs nanoparticles[136–138]. In particular, Tian and co-workers have synthesized MnAs nanoparticles from two arrested precipitation reactions: a slow heating method (A-type) and a high temperature rapid injection method (B-type). Curiously, they have found major differences between the two sets of nanoparticles. Namely, for the A-type they unveiled a similar magnetostructural transition α–>β as the one observed for the bulk counterpart although with a smoother lattice parameters/volume change. On the other hand, the slightly smaller B-type MnAs nanoparticles do not undergo the magnetostructural transition as they stabilize the low-volume β structure, being kinetically arrested. They hypothesize that such difference between A and B-type nanoparticles can be due to the impurity ion inclusions inside MnAs nanoparticles inherent to the method used that might be trapping the β phase[138]. The MSMAs are probably the most studied magnetocaloric/multifunctional materials at the nanoscale as evidenced by Dunand and Mullner review[139]. Basically, phase stability, grain size and surface effect are referred as the main intrinsic differences between the bulk and thin films. The strong magnetoresponsive properties found in their bulk counterpart have already been found in thin films, such as: MCE, giant magnetoresistance, and magnetic field induced strain[140]. Their martensitic transformation can be affected by the substrate choice[141], size effect (grain size and thickness)[142], phase compatibility (between martensite at low temperature and austenite at high temperature) and heat treatment procedures[143]. Since epitaxial growth occurs for a preferential orientation it will have a direct impact on the the reorientation mechanisms under a magnetic field. For example, for GaAS (001) and Al_2O_3 (110) Teichert and co-workers found the austenite phase at room temperature, whereas for MgO (100) the two phases (austenite or martensite) were observed[144]. Other studies have been focusing on the influence of the thickness in the martensitic transformation, namely Ranzieri and co-workers[140] have investigated epitaxial NiMn-Ga films on MgO (1 0 0), with thicknesses in the 10-100 nm range and have showed that martensitic transformations occurs only above 40 nm. The scenario is different for polycrystalline thin films as Vishnoi and co-workers have found[145]. They have studied polycrystalline NiMnSn films deposited on Si substrates in the 120-2500 nm thickness range and observed a suppression of the martensitic transformation below 410 nm as evidenced by the magnetization versus temperature curves plotted in Figure 6.1 (a)-(f).

One advantage of growing these materials in thin film form is the potential of reducing the first-order nature of their transition, due to the strong coupling to the substrate. Niemann and co-workers found that in epitaxial Ni-Co-Mn-In on MgO (0 0 1) the fraction of the film closer and hence coupled to the substrate remained in the ferromagnetic austenite phase, indicating that the coupling completely suppressed the martensitic transformation[6]. The ABO_3 compounds with perovskite structure, where A and B can be 3d or 4f elements, are fertile in different forms of magnetism and MCE. One of the great discoveries in this type of compounds was carried out by Jin and co-authors when they deposited a $La_{1-x}Ca_xMnO_3$ (with x$\sim$0.67) thin film by PLD that exhibited negative isotropic magnetoresistance effect more than three orders of magnitude higher than the

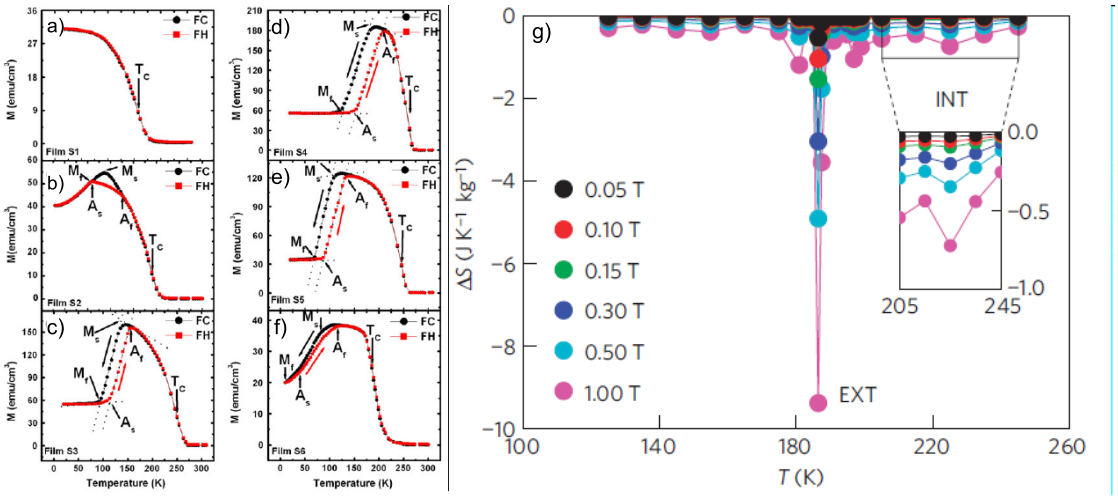

Figure 2.11 – a)-f) Cooling and heating Magnetization curves of NiMnSn thin films deposited on top of heated (550 °C) Si (100) substrate by DC magnetron sputtering with 120, 410, 1014, 1412, 2022 and 2518 nm thick film as extracted from[145]. g) Magnetic entropy changes $\Delta S_{iso}(T)$ of the $La_{0.7}Ca_{0.3}MnO_3$ film on top of a $BaTiO_3$ substrate for different applied magnetic field changes. In the inset, the $\Delta S_{iso}(T)$ associated with the second order magnetic transition of $La_{0.7}Ca_{0.3}MnO_3$ thin film is highlighted.

typical value observed in superlattice films[146]. These epitaxial films exhibit magnetoresistance values as high as 127 000 percent near 77 K and approximately 1300 percent near room temperature. Wang and co-workers have found a not so colossal magnetoresistance of 24.5% accompanied by a magnetic entropy change of -2.22 J K^{-1} Kg^{-1} for a 1 T field variation at 260 K in a pulsed laser deposited $La_{0.78}Ag_{0.22}MnO_3$ thin film[147]. Furthermore, a remarkable breakthrough was achieved by Moya and co-workers in 2013 when they observed a giant and reversible MCE in a epitaxial $La_{0.7}Ca_{0.3}MnO_3/BaTiO_3$ thin film system[148]. The $BaTiO_3$ substrate undergoes a rhombohedral-orthorhombic structural transition near 190 K, which is further away from the Curie temperature of the $La_{0.7}Ca_{0.3}MnO_3$ film. However, since there is a strong strain mediated feedback between the film and the substrate, the substrate first-order structural transition induces an abrupt thin film magnetic transition and consequently a colossal magnetic entropy change of ΔS_{iso}^{max}~9 J K^{-1} Kg^{-1}, which is ten times higher than the purely magnetic second-order transition undergone by the $La_{0.7}Ca_{0.3}MnO_3$ alone. In addition this system shows reversibility of a typical second-order transition. As the authors highlight there is room for exploring different bi-nanostructures with two comparable volume fractions and enhanced interfacial areas, such as the core-shell nanoparticles configuration or matrix immersed nanoparticles. This is a brilliant example of how smart nanostructuring designs can enhance the bulk MCE and give origin to new properties. Despite its remarkable MCE and strong magnetovolume coupling, to our knowledge the La-Fe-Si alloys family still has not been subjected to thin film fabrication.

In a similar position is the $R_5(Si,Ge)_4$ family, that, to our knowledge had only one report published concerning its thin film production before 2015. That paper reported

an attempt to crystallize the correct 5:4 stoichiometric phase of a $Gd_5Si_2Ge_2$ thin film deposited by sputtering with a DC/RF-magnetron equipment into a Si_3N_4 (silicon nitride) buffer layer which is on top of a Si (100) substrate[149]. In this work Sambandam and co-workers found that the as-deposited 100 nm $Gd_5Si_2Ge_2$ thin film is amorphous and that ex-situ annealings are needed to crystallize the 5:4 phase. They have performed three annealings up to 700 °C, 900 °C and 1150 °C and discovered that despite the higher temperature annealing promotes crystallinity (and possibly the 5:4 phase) the silicon nitride buffer layer decomposes at this temperature and loses its ability to prevent Si diffusion into the thin film and consequently the thin film becomes enriched by extra Si. The $R_5(Si,Ge)_4$ microscale has deserved more attention, namely by Trevizoli and co-workers, who showed that by using pulverization powder metallurgy technique it is possible to tailor the particles size distribution and influence the magnetic properties of the $Gd_{5.09}Ge_{2.03}Si_{1.88}$ alloy[150]. They noticed that residual tension is formed during the sintering and it has a direct influence on the suppression of the first-order phase transition, as evidenced by its absence for particle sizes below 53 μm. On the other hand, bigger particles (106 and 149 μm) retain the coupled magnetostructural transition and consequently exhibit an almost bulk-like magnetic entropy value of $\Delta S_{iso}^{max} \sim$ 14 J K^{-1} Kg^{-1}. Alternatively, Ball milling (BM) is one of the most attractive routes to scale-down to the micrometer length scale. Rajkumar and co-workers presented 1-5 μm ball milled $Gd_5Si_2Ge_2$ and $Gd_5Si_2Ge_{1.9}Fe_{0.1}$ microparticles[151]. They observed a phase segregation (from the bulk one M-phase towards a M+O(I) mixture of phases) in the 32h ball milled $Gd_5Si_2Ge_{1.9}Fe_{0.1}$ sample, manifested by two different magnetic transitions and also observed a drastic decrease (in comparison with the bulk counterpart) in the magnetic entropy change value (to 0.45 J K^{-1} Kg^{-1}, under a $\Delta\mu_0$H=2T) for the $Gd_5Si_2Ge_2$ sample. Recently, Giovanna do Couto and co-workers reported a higher MCE for shorter milling times (4 h) and lower mean particles size, 0.5 μm, also for $Gd_5Si_2Ge_2$[152]. They measured a $\Delta S_{iso}^{max} \sim 4$ J K^{-1} Kg^{-1} for a $\Delta\mu_0$H=5 T, corresponding to an 80% reduction when compared with bulk counterpart value of 20 J K^{-1} Kg^{-1}. Similarly to Rajkumar report, Giovanna also associated the MCE reduction to the suppression of the amount of sample undergoing a first-order transition, namely by its transformation into an amorphous phase due to the increased milling time.

CHAPTER 3

Experimental Techniques

3.1 Summary

This chapter is divided in two parts. First, the synthesis procedures to produce bulk, nanoparticles and thin film samples will be briefly described, while the second part will be dedicated to the characterization techniques used to study these materials. The first part will start with the arc-melting discharge procedure to produce the bulk samples that were characterized (not detailed here) and then used as target materials on the production of nanostructured samples. The nanostructures were produced by two major deposition techniques: Femtosecond Pulsed Laser Deposition and DC/Rf-Sputtering - which will be introduced and briefly compared. In order to optimize the nanostructured samples several post-treatments (annealings) were performed that will be portrayed here. The second part is dedicated to the characterization techniques used to study the morphology, chemical composition, thin film thicknesses and nanoparticle diameters (Transmission and Scanning Electron microscopes - TEM and SEM - and Energy X-ray Dispersive Spectroscopy, EXDS), crystalline structure (X-ray diffraction ,XRD), magnetic behavior (Superconducting Quantum Interference Device, SQUID) and electrical transport.

3.2 Sample Preparation

3.2.1 Bulk materials

3.2.1.1 Arc-melting discharge furnace

The method that was used for the bulk target samples synthesis was the arc-melting discharge furnace at Centro de Materiais da Universidade do Porto (CEMUP). This is a simple process but very effective and hence used widespread on the production of $R_5(Si_xGe_{1-x})_4$ materials[153,154]. The process begins with cutting, cleaning and weighting the corresponding amounts of the constituent elements, in order to ensure the desired stoichiometry: mass of R element (here R = Gd), mass of Si and Ge, so that the number of moles ratio $N_{Gd}/(N_{Ge}+N_{Si})$ is $\sim$ 5/4 and the N_{Si}/N_{Ge} to be determined by the x value. The elements were purchased from Alfa Aesar company with 99.9 %

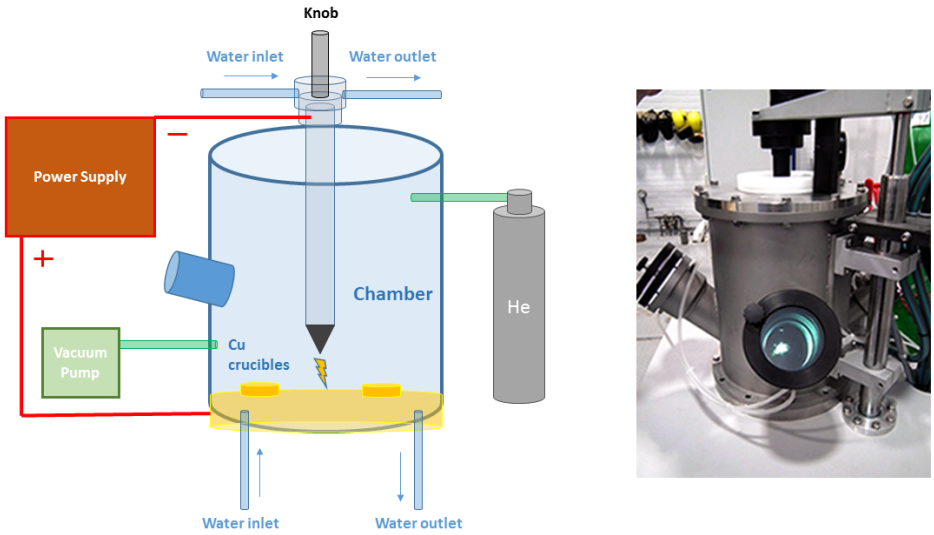

Figure 3.1 – Schematic representation of an arc-melting furnace set up together with a photograph of a real arc-melting furnace. It is constituted by five main parts: a vacuum isolated chamber, vacuum pump system, water cooling system, high purity Argon pressurized bottle and a high power supply

weight percentage purity (for Gd) and 99.9999 % higher (for Si and Ge). The weighted amounts (with a ∼0.2 mg uncertainty) of the three elements were placed in the Copper cavities (crucibles) present in the Copper plate of the arc-melter as can be seen in Figure 3.1. Since Gd is a highly reactive element to oxygen, a large Ti sample (∼ 20 g piece) is placed in another crucible to serve as an oxygen capture reservoir (getter) and hence reduce the amount of oxygen present in the chamber. The furnace elements are schematically reproduced in Figure 3.1. It is constituted by five main parts: a vacuum isolated chamber, vacuum pump system, water cooling system, high purity Argon pressurized bottle and a high power supply. The chamber is composed by a water-cooled hollow Copper base with cavities that are connected to the positive terminal of the power supply (see below). The other (negative) terminal is connected to a hollow water cooled steel rod whose end is a Tungsten tip that is suspended from the top of chamber. This rod is controlled by the user from the outside using the knob that is connected to it and which allows its horizontal and vertical motion to change from one crucible to the next. The vacuum pump and the Argon bottle are connected to the chamber via inlets and outlets. The melting process starts by vacuum isolating the chamber down to P < 10^{-3} mBar, followed by several purges (four or more) of Ar gas (6N) in order to considerably reduce the oxygen partial pressure in the chamber. The discharge can only occur if a sufficiently high Argon pressure is present in the chamber, and hence after the purging, the chamber is filled with Ar up to 1 - 1.5 Bar. Once verified the water flow and the Ar pressure stability, the tungsten tip is placed just above the crucible where the elements are at a distance of typically ∼ 2 cm, the electrical discharge can start. The arc is initiated with a strong electrical discharge that creates a stable arc between

the Tungsten tip and the Copper plate. Depending on the voltage/current applied it is estimated that at the end of the arc a temperature of 2000 - 3000 °C is reached. To produce the $Gd_5(Si_xGe_{1-x})_4$ here studied a typical 80 A current intensity was used. Hence, during the first approximation of the arc to the crucible where the individual elements are placed, these transform into an unique alloy button after being for a few seconds exposed to the arc. The arc is then alternatively moved from the button crucible to the Ti getter crucible. It is important to remark that the button cools down (when the arc is removed from the crucible) in a non-homogeneous way due to the different cooling temperatures: the bottom is in contact with a 10-15 °C cooled Copper plate, whereas the upper part of the button is in contact with a warmer surrounding atmosphere (difficult to estimate) due to the arc ionization. This fact leads to the crystallization of the upper surface of the button on small hexagon-like shapes and to the crack formation in the most interior part. Finally, the recently formed button is turned upside down and the process (purges, 1 Bar Ar filling, arc-discharge) is repeated. This process is repeated three times to increase the elements homogenization inside the button. The last step is to extract the resulting button and to measure its weight to check for weight losses (possibly due to the non-melting of some elements pieces). The $Gd_5(Si_xGe_{1-x})_4$ buttons produced were typically within the 3-5 grams range and the weight losses during the melting were insignificant (always less than 3%).

3.2.2 Thin film Deposition

3.2.2.1 Pulsed Laser Deposition

The Pulsed Laser Deposition (PLD) was developed shortly after the technical realization of the first laser in 1960[157], when Smith and Turner used the ruby laser to deposit a film for the first time[158]. However, it was only in the mid-1980's, that pulsed laser deposition gained a widespread popularity amongst the thin film deposition techniques, mostly because of the successful high-T_C superconductors thin film research[159,160]. Since then, it has been applied in thin film deposition of a broad set of materials, such as: multiferroics[161], colossal magnetoresistive manganites[162], metals and metallic alloys[163].

PLD is a physical vapour deposition technique (PVD) which means that it is characterized by a process in which the material goes from a condensed phase to a vapor one and then back to a condensed (thin film) phase. The technique basic principle is extremely simple: it uses pulses of laser energy to remove material from the surface of a target which will end up on top of a substrate that lies parallel to the target, as shown schematically in Figure 3.2. The laser beam is focused into the target material by a mirror system and can have a pulse duration in the femto to nanosecond interval, a wide range of energies and also of repetition frequencies (from 0.1 to 1000 Hz). The most common PLD systems have pulse durations of 25 ns, energies in the range 0.01-0.5 J and repetition rates around 10 Hz). The target absorbs the laser electromagnetic

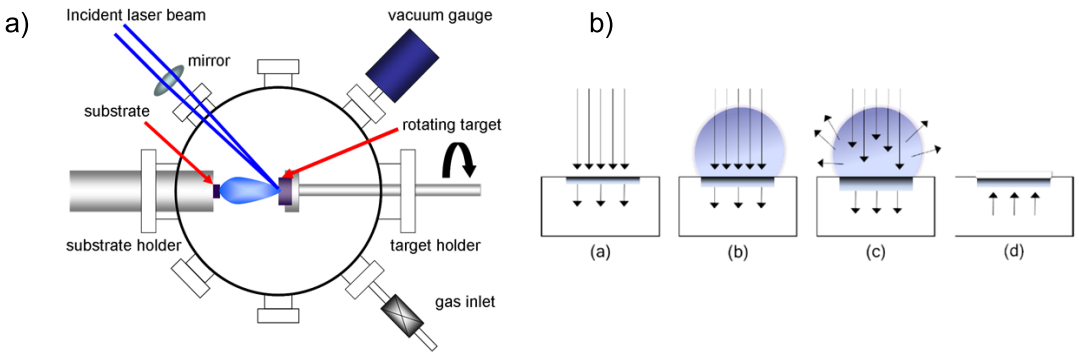

Figure 3.2 – a) Schematic representation of a Pulsed Laser Deposition system, extracted from Reference[155]. The basic mechanism relies on the incidence of a pulsed laser beam that is focused on a spot at the target surface. Due to its energy, the beam sputters material at the target surface, which creates a plume (blue cloud-like shape) that travels from the target towards the substrate. b) A schematic representation of the four-stage process that begins when the laser beam hits the target, as extracted from Reference[156].

energy which is then converted in electronic excitation, and afterwards, if the energy fluence (defined as the laser pulse energy per unit area on the target surface) is above a certain material-specific threshold, it is converted into thermal energy, causing vaporization of the target material. A plume is formed composed of energetic species such as atoms, molecules, ions, clusters and particles of different sizes which fly perpendicularly to the target surface. This navigation can occur either in vacuum or in the presence of a background gas, such as Argon, Helium,.... The ejected material finishes its travel at the substrate surface where it is deposited, which can be heated or not. The substrate is located some centimeters away from the ablation target. The ablation can hence be divided in three main processes: 1. the vaporization of the material, 2. transport of the vaporized material towards the substrate and 3. the deposition and growth of the thin film in the substrate. The first process comprises the interaction of the laser pulse with the target material. This interaction is governed by several laser and target parameters, but essentially the ablation process consists in a subsurface heating of the target material, either by the laser pulse or by the recoil pressure exerted by the material ablated in the initial part of the pulse[164]. The laser ablation resultant from one laser pulse is pictured in Figure 3.2. In a first stage, a), the target surface is heated by the laser pulse (long arrows), causing it to melt and initiate the vaporization. The molten material is represented by the shaded area and the short arrows represents the in-depth heat-wave motion of the solid-liquid interface. The solid-liquid interface 3.2 b) propagates with a velocity that depends on the target properties - in particular on its thermal conductivity

- hence dissipating the laser energy throughout the target in-depth profile during the time that the pulse lasts. Simultaneously, the plume of evaporated material is formed in front of the target and because of the highly energetic and explosive nature of this process the plume is roughly stoichiometric, i.e. roughly all atoms present in the target are ablated independently of their chemical nature which creates a plume that retains the stoichiometry of the target material. In a third stage, c), the plume begins to absorb energy directly from the laser beam giving rise to complex secondary laser interactions that include: excitation and ionization of species in the plume and a reduction of intensity of the radiation reaching the target. In the last stage, d), the heat dissipation in the target ceases and the solid-liquid interface starts to reverse its motion. On the second process the initial propagation of the plume is thus one dimensional[156,164] The velocity of the evaporated species is supersonic, with common values being typically order of 10^6 cm/s[156,164]. This regime occurs up to a distance from the target comparable to the laser spot dimensions[156]. Beyond this regime, the plume motion is three-dimensional and is governed by the collisions of the ejected particles with each other and with the background gas.

Finally, the deposition and growth of the thin film in the substrate occurs. The substrate temperature and the deposition rate are determinant factors for the thin film growth, enabling higher epitaxy (high temperature and low deposition rate) or amorphization (low temperature and high deposition rate). Another interesting possibility is the occurrence of 1-100 nm diameter nanoparticles at the substrate originated by the interaction of the plume with a background gas. For this purpose a noble gas (in order to prevent chemical reactions) must be used and its pressure increased. In this way the atoms in the plume will suffer higher number of collisions during their time of flight (between the target and the substrate), losing its energy and eventually condensing in an agglomerate - nanoparticle.

However if the purpose of the study is to produce nanoparticles, the nanosecond pulse duration laser systems presents a major disadvantage which are the requirements of specific optimization of the background gas pressure and addressing complex issues such as the expansion of the plume in the ambient gas and the in flight chemical kinetics. These difficulties can be overcome if a femtosecond (fs) pulse duration laser is used. In fact a fs laser ablation needs no background gas and in contrast with what happens for longer pulse durations (ns and even picoseconds), the fs pulses do not interact with the ejected material, thus avoiding the complex secondary laser interactions and enabling a more efficient energy transfer from the laser to the target material during the above mentioned third stage of the materials vaporization. In addition, the fs pulses heat the target material to temperatures higher than the longer pulses of similar energy fluence, since the whole beam energy is transferred to the target much more rapidly, inhibiting its dissipation throughout in-depth material[165]. This highly efficient energy transfer enables the evaporation of nanoparticles of virtually all elements and compounds[166–168]. Finally, the tuning of the nanoparticle size distribution can be realized via the optimiza-

tion of fewer parameters in comparison with the longer pulses, namely the laser pulse energy, repetition rate, laser wavelength and focusing conditions. The nanogranular thin film which will be thoroughly described in the following chapters was deposited by femtosecond pulse laser beam at Department of Electrical and Computer Engineering, Iowa State University, Ames, Iowa, USA.

3.2.2.2 Sputtering

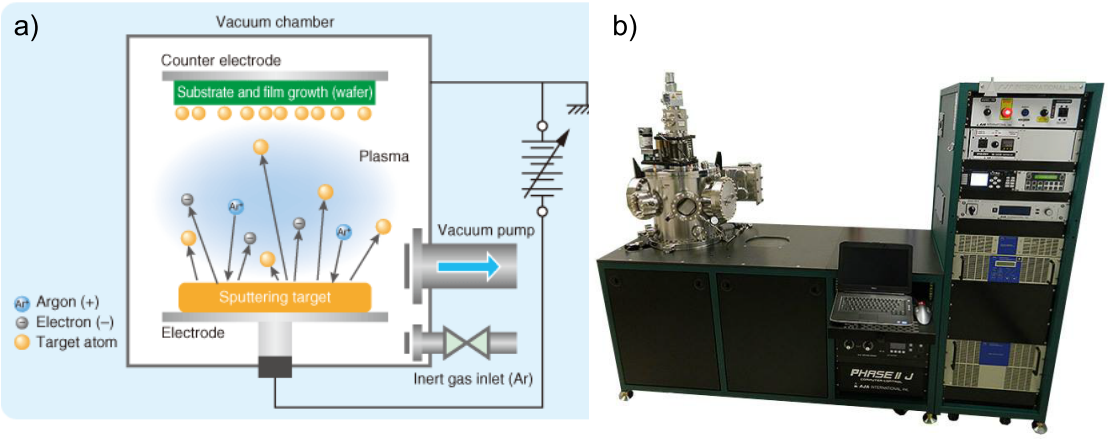

Figure 3.3 – a) Schematic representation of the sputtering phenomena, with a chamber filled with ionized Ar gas that is accelerated by voltage towards the sputtering target[169]. The target sputtered atoms then fly towards the substrate initiating the film growth. b) Picture of the AT e ATC orion series thin film deposition systems Sputtering system used at INA[170].

Sputtering is physical vapour deposition technique, where the deposition occurs via the ion bombardment (in contrast with the laser beam) of a specific target (single or multi element). The greatly accelerated ions transfer their momentum to the target inducing its atoms ejection towards the substrate, where the thin film will grow, as represented in Figure 3.3 a). In contrast with PLD, here the presence of an inert noble background gas in the deposition chamber is mandatory. This low reactant noble gas is ionized by applying either a continuous (DC) or an alternate radio frequency (RF) electrical voltage, originating a plasma. In this electrical circuit, the cathode is the target which means that the noble cations will be strongly accelerated towards it. The highly accelerated cations beam will hit the target and transfer their linear momentum to the target atoms. If the cations momentum is high enough the target atoms will be ejected (sputtered) with a wide energy distribution (10^{-2} eV up to about 10^{4} eV)[171]. The sputtered atoms will ballistically fly from the target towards the substrate, condensing there, as schematically pictured in Figure 3.3 a). As occurred in the PLD system, here the background gas will also have a quenching effect - higher pressure will mean higher number of collisions and higher in-flight energy dissipation and hence lower impact energy at the substrate. The RF alternated voltage is used to sputter non-metal materials (such as silicon), as it prevents the charge accumulation at the insulating target surface (which ultimately

can lead to the sputtering suppression). By alternating the electrical potential with RF Sputtering, the surface of the target material can be cleaned of a charge accumulation at each cycle. On the positive cycle electrons are attracted to the target material giving it a negative bias. On the negative portion of the cycle, ion bombardment of the target occurs. A typical radio frequency of 13.56 MHz is used for the RF power supply equipment. If a set of magnets is placed below the target holder, a magnetic field parallel to the target can be created to trap electrons, enhancing both the probability of the initial gas ionization process and allowing a plasma to be generated at lower pressures which reduces both background gas incorporation in the growing film and energy losses in the sputtered atom through gas collisions - consists of magnetron sputtering. Magnetron Sputtering hence allows higher deposition rates. In contrast with the PLD system, a multi-element thin film can not be sputtered from a multi-element compound target, mostly because of the relatively large targets needed for these systems (typically 50 mm diameter). For the sake of example, a $Gd_5Si_2Ge_2$ 50 mm diameter and 10 mm thick target sample, besides being very expensive (would imply a $\sim$ 150 g of Gd which alone would cost more than 300 euros) would require a very large arc-melting furnace and the ability to shape it into the desired circular form. Instead, companies sell an unique element target and the thin film is produced by the deposition of the different targets into the same substrate. This process makes it crucial to have a reliable and updated calibration procedure of each target deposition rate for different (at least three) power sources. Two major approaches were followed in this work: 1. co-sputtering and 2. multi-layering. In the first one, the three elements (Gd, Si and Ge) were sputtered simultaneously (with the Si target being sputtered via a RF-source, while Gd and Ge via a DC source) with different power sources in order to match the deposition rates so that during the same deposition time the stoichiometric desired amounts of Gd, Si and Ge are in fact deposited. The second approach consisted in depositing alternatively Gd, Si and Ge, in the correct thicknesses to match the desired stoichiometry, hence constructing an initially multilayered thin film. In order to enable the mixture of these thin single-element layers, post-heat treatments were performed. The thin films used in this thesis were sputtered in a DC and RF magnetron sputtering Phase II J by AJA International Inc. company at Instituto de Nanociencia de Aragón (INA) as pictured in Figure 3.3 b). In comparison with PLD technique, DC-RF Sputtering is an industrial technique in the sense that it allows higher deposition rates (and hence faster thin film depositions) on larger substrate areas while warranting more reproducible thin films. However its major drawback is the difficulty to assure a multi-element thin film correct stoichiometry. As a first approach towards the thin film deposition of these materials, thick (thickness higher than 300 nm) films were deposited and hence no special care was taken when choosing the substrate. The substrate used in both PLD and Sputtering depositions was a 1 μm SiO_2 layer on the top of a (001) Silicon substrate.

3.2.2.3 Post Heat Treatments

Similarly to what occurs in the $Gd_5(Si_xGe_{1-x})_4$ bulk compounds[106,153,154], post heat treatments also assume an important role on the crystallization of the 5:4 phase in $Gd_5(Si_xGe_{1-x})_4$ thin films. After the thin film deposition, several post-treatments (annealings) were performed for two different purposes: to generate the 5:4 $Gd_5(Si_xGe_{1-x})_4$ stoichiometric phase in the as-deposited films; within the 5:4 crystallographic phase in the as deposited film, thermal treatment is performed in order to promote/relegate a higher content of a Si-rich (or Ge-rich) 5:4 phase, depending on the nominal stoichiometry.

The thermal treatments were always performed inside a quartz tube. Most of the thermal treatments were done under vacuum pressure ($< 10^{-6}$ mBar) by pumping through a primary (rotary: 1000-10^{-3} mBar) and a secondary (diffusion: down to 10^{-6} mBar) system. The exception was made when an Argon gas was flowing inside the tube and sucked by the outlet to the vacuum pump ensuring a continuous Argon flow. The samples were wrapped in Tantalum foil which had a getter function to absorb Oxygen (most effectively for temperatures higher than 500 °C). The wrapped samples were placed at the end of a closed quartz tube and its other end was connected to the pump system (and to the Ar inlet). Several different thermal treatments procedures were tested, such as: 1. Placing the quartz tube inside the furnace only when the furnace was already at the annealing temperature, T_{ann}, and at the end of a fixed time, t_{ann} extract the tube out of the furnace and let it cool at the room temperature although still under vacuum (air quenching) ; 2. Similar procedure, except that besides air quenching the sample is cooled at the maximum cooling rate inside the furnace ($\sim$ 4-5 °C/min); 3 The sample is both heated and cooled under a specific heating and cooling rate; The annealing temperatures tested were within the 300-1000 °C range and the annealing times ranged from 15 min up to 24 hours.

3.3 Sample Characterization Techniques

3.3.1 Scanning Electron Microscopy and Energy Dispersive Spectroscopy

Scanning Electron Microscopy (SEM) and Energy X-ray Dispersive Spectroscopy (EXDS) are important and attractive techniques to get complementary information about microstructure and chemical composition of a various range of materials, including nanoscale materials as nanoparticles and thin films.

SEM is basically composed of an electron gun, a somewhat complex electromagnetic optical system and a set of different detectors for particles and electromagnetic waves that can be added and replaced depending on the specific needs. The gun produces a high energy electron beam (20-30 kV) that is focused by an electromagnetic

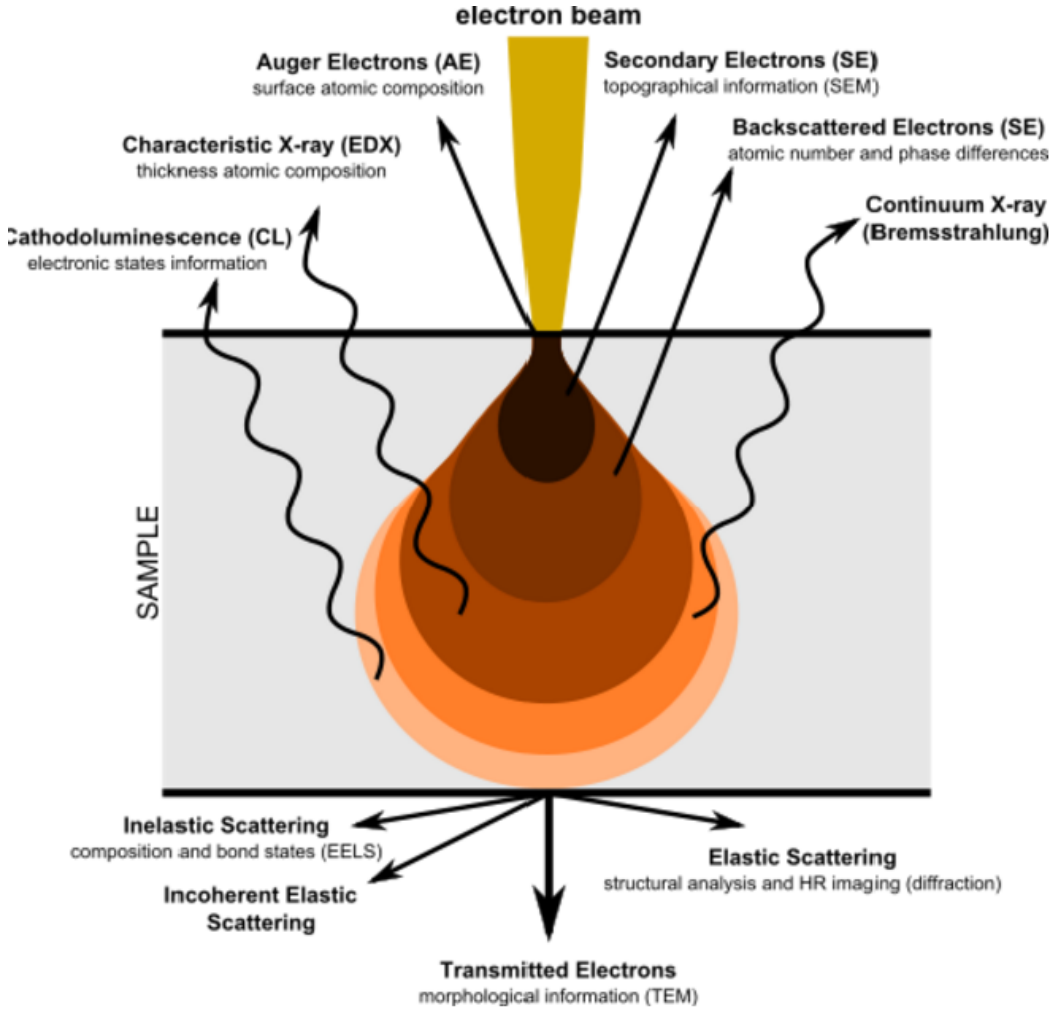

Figure 3.4 – Schematic diagram picturing the phenomena resulting of the interaction of highly energetic electrons with matter. Several different electrons and electromagnetic radiation are scattered (or transmitted) after this interaction, from which different morphological, chemical and crystallographic information about the sample studied can be acquired. Extracted from reference [172].

optical system into a small spot, irradiating locally the sample surface. By controlling a set of coils it is possible to move the spot front and backwards, scanning a specific surface area and creating an image through the detected electrons that were backscattered or that were ejected during the interaction of the electron beam with the materials surface. In more detail, when a beam of high-energy electrons hits a surface sample there are many interactions happening in the near surface region (the interaction ”pear” depends strongly on the beam energy, but is typically in the few micrometers range), resulting on a variety of particles and radiation emergent from the sample, as schematically pictured in Figure 3.4. SEM constructs an image based on the detection of two types of these emergent particles: backscattered and secondary electrons. The later are resultant of inelastic scattering interactions between the incident beam and the weakly

bounded conduction band electrons in metals or valence electrons in insulators and semiconductors. Their intensity is dependent on the depth where the interaction took place, which makes their detection a useful tool to image the topography of the surface, creating a 3D-like image. As for the backscattered electrons they are the original electrons from the incident beam that suffer elastic scattering with the electrons or nuclei of the first atoms at the sample surface. This scattering is strongly dependent to the atomic number of these atoms and so their detected intensity adds contrast to the image (the brighter the spot the larger the atomic number) and helps unveiling impurities and distinguishing between grains with different crystallographic phases and corresponding different electronic densities. The image resolution depends on many factors such as the incident beam energy, the electromagnetic optical system (beam spot size), the detectors resolution, and also the experimental conditions (sample preparation) among others. Currently, the majority of SEMs can easily reach the 50 nm lateral resolution, although there are already High-resolution SEMs on the subnanometer scale[173]. To have more accurate information about the chemical elements present in the sample, the EXDS technique which is commonly incorporated in SEM setup, was used. The EXDS are detected by X-ray detectors, that measure the X-ray radiation resulting from the interaction between the electron beam and sample. These X-rays are normally generated from the atomic de-excitation: when an electron, originally from an outer shell, comes to occupy a hole state on an inner shell that was left empty by an electron extracted by the energy transferred from the incident electrons. So, as the energy between core shells is different for different atomic species, this method can estimate the chemical composition of the sample just by detecting the energy and intensity of the emitted x-rays and by comparing it with database X-ray emission energy values. EXDS is able to detect atomic species in very low fractions present in the sample. However in order to be analyzed by SEM or EXDS, the samples must be stable under high vacuum (very low pressure is required for the beam stabilization and accurate detection), must be electrically conductive, so that their surface maintains electrical neutrality avoiding electrical charge accumulation and must be thermal and structurally stable to handle the incident beam without suffering major transformations. In this work, the samples studied fulfill the previous requirements (electrically conductive, stable under high vacuum). For the thin film samples the cross-sectional studies (thin films were cut and their cross-section area was inspected) were of utmost importance in order to: 1. confirm the thin films thickness (that was previously estimated through profilometer studies) and 2. to evaluate qualitatively the atomic diffusion of the different atomic species along the depth of the thin film. SEM and EXDS studies presented in this work were performed at Centro de Materiais da Universidade do Porto (CEMUP) in a FEI Quanta 400FEG ESEM / EDAX Genesis X4M equipment.

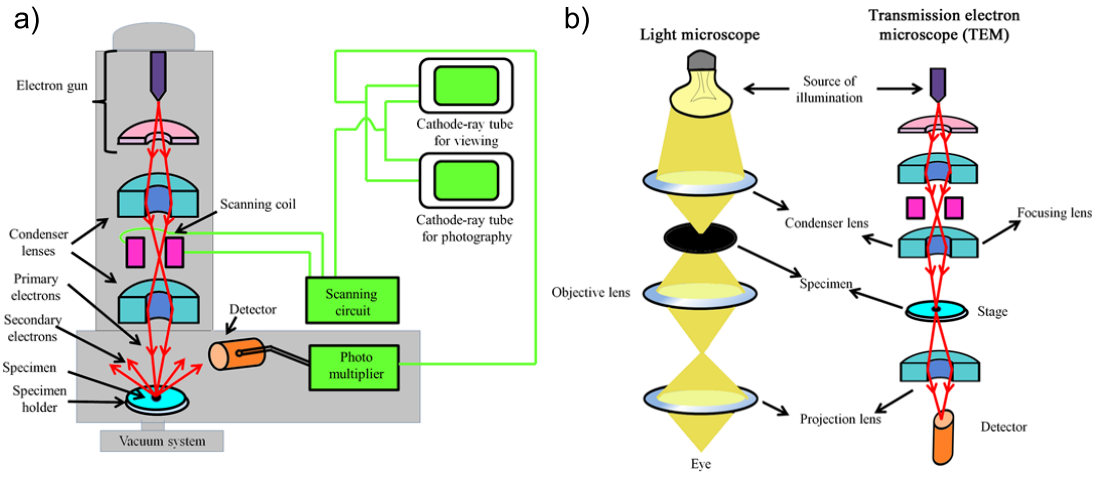

Figure 3.5 – a) Schematic diagram of a Scanning Electron Microscope main components. b) Basic schematic representation of Transmission Electron Microscope in analogy with a simple Light Microscope, as extracted from [174].

3.3.2 Transmission Electron Microscopy

The Transmission Electron Microscope (TEM) is basically composed by the same main components as SEM, namely: an electron optical column, a vacuum system, the necessary electronics (lens supplies for focusing and deflecting the beam and the high voltage generator for the electron source), and control software. Its main difference to SEM is, as the name unveils, that the resulting image is formed by the electrons transmitted through the sample in contrast with the scattered electrons in SEM. Another important differences are: (i) sample preparation is more detailed for TEM, in particular the sample thickness should typically be below 100 nm; (ii) SEM focuses on the sample's surface (or a few hundreds of nanometers below the surface) morphology and its chemical composition, whereas TEM can provide details about internal composition, crystallographic structure (grains orientation and composition); (iii) To ensure that the electrons cross the sample, a much higher acceleration voltage is typically used in comparison with SEM; (iv) TEM has higher resolution (typically below 1 nm) than SEM; (v) SEM can provide a 3-dimensional image, while TEM only can provide a 2-dimensional picture.

In fact, both in SEM and TEM, the electron column includes elements analogous to those of a light microscope, as can be seen in Figure 3.5 b). The light source of the light microscope is replaced by an electron gun, which is built into the column. The glass lenses are replaced by electromagnetic lenses. Unlike glass lenses, the power (focal length) of magnetic lenses can be changed by changing the current through the lens coil. The eyepiece or ocular is replaced by a fluorescent screen and/or a digital camera. The electron beam emerges from the electron gun, and passes through a thin specimen, transmitting electrons which are collected, focused, and projected onto the viewing device at the bottom of the column. The entire electron path from gun to camera must be under vacuum.

Typically each TEM can be modified into a scanning transmission electron microscope (STEM mode) by the addition of a system that rasters the beam across the sample to form the image, combined with suitable detectors, as represented in the SEM diagram in Figure 3.5 a). Scanning coils are used to electrostatically deflect the beam, after which the beam is collected using a current detector such as a Faraday cup, which acts as a direct electron counter. Also similarly to SEM, EXDS analysis is also possible in TEM. Hence, EXDS analysis in STEM mode is particularly suitable to scan a sample depth and inspect the chemical composition of different crystallographic grains.

Furthermore, to inspect the crystallography of specific nanosized-grains, a High-resolution transmission electron microscopy (HRTEM) is highly desirable, as it has an enhanced resolution that is around 0.05 nm[175].

A small set of optimized thin films were selected and analysed with a HRTEM, FEI Tecnai F30 operated at 300 kV and the EXDS analysis was performed in STEM mode at Instituto de Nanociencia de Aragón (INA)[176].

3.3.3 X-ray Diffraction

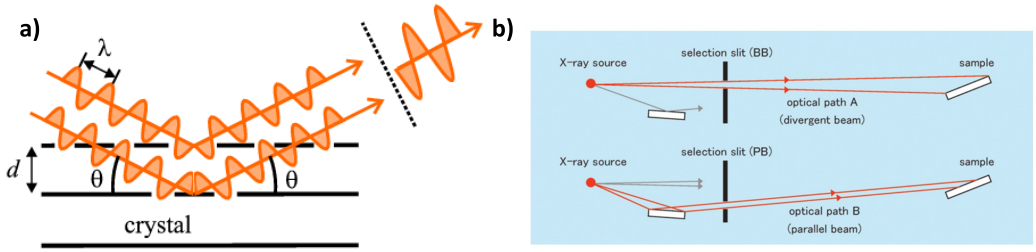

Figure 3.6 – a) Schematic representation of Bragg Law, where the parallel lines represent the atomic planes which are separated by a distance, d, and the orange waves illustrate the incident and diffracted X-ray beam with wavelength, λ . b) Representation of Bragg Brentano (up) and the Parallel (down) X-ray beams, as extracted from reference[177].

The structural characterization of the deposited films was performed by X-ray diffraction. Since the X-rays wavelength is comparable to the interplanar distances in crystalline materials, X-ray diffraction is a very useful technique to: detect the crystallinity/amorphization nature of the sample and help to identify the crystalline phases present in the sample (bulk and thin film). The diffraction principle is pictured in Figure 3.6 a). As can be seen, each atom in a periodic lattice scatters X-rays waves and when these waves add coherently it gives rise to a diffraction pattern with minima and maxima intensities. As Bragg stated, if we imagine a crystal as a set of planes of atoms then in order to have constructive interference, the difference of paths that the X-rays (accounting for incident and scattered paths) travel has to be equal to an integral multiple of the wavelength. This was summarized in the formal expression of the Bragg law,

$$2d_{hkl}sin(\theta) = \lambda \tag{3.1}$$

where $2d_{hkl}$ represents the distance of the family of atomic planes normal to the hkl direction[178]. Consequently, a family of atomic planes *hkl* will be responsible for an intensity peak at some specific angles θ_i and vice-versa i.e. the spacing between atomic planes determines the peak positions in the θ axis. A basic Diffractometer is constituted by four major parts: the X-ray source (typically its Copper) at the incident side, X-ray detector at the detector side, sample-holder/goniometer at the middle and the connection to a PC with the proper data acquisition software. The X-ray source is composed by a tube with one or more windows (that are transparent to X-rays), vacuum isolated, which has a W filament in one end and a target (typically Copper) at the other. When heating the filament, electrons are extracted from the W material and are accelerated by an electric field (in the 30-50 kV range, typically) towards the target (typically Copper). Some of these electrons cause abrupt transitions in the Cu atoms, which emit electromagnetic radiation with well defined wavelength in the 0.1-50 Å range - X-rays. The X-rays that hit the sample surface are required to be monochromatic and focused on the sample region which is attained through an optical system composed by several elements as monochromators and slits. Two geometries are mostly used: the Bragg-Brentano (for bulk/powder sample diffraction) and Parallel Beam (for thin films). As can be seen in Figure 3.6, in the Bragg Brentano (BB) the X-ray beam is divergent with a determined solid angle that can be tuned by slits along its optical path, whereas the in the Parallel Beam (PB), as the name says, both the incident and diffracted beams are parallel. The PB geometry although typically less intense, does not depend critically on the sample position, morphology or shape due to their parallel waves nature, hence being particularly suitable for the thin film diffraction[177]. The XRD measurements here presented were performed in two equipments: Panalytical, X-Pert Pro X-ray equipment at Unidade de Microscopia Electrónica (UME) da Universidade de Trás-os-Montes e Alto Douro and the Rigaku XRD Smartlab System at our own institute, Instituto de Física de Materiais da Universidade do Porto (IFIMUP). The major difference between the two equipments is the maximum current source that is 30 and 200 mA in the Panalytical and in the Rigaku system, respectively. Tests on the same samples were performed in both equipments and found to reveal no major changes. Generally, each measurement consisted of a scanning of the detector from 20 to 65 °2θ degrees with a 0.017 ° step and at a rate of 1 °/min.

3.3.4 High - Resolution Synchrotron X-Ray Radiation Difraction

The High Resolution Synchrotron X-ray radiation diffraction (HRSXRD) technique basically uses the same diffraction principle as the normal XRD, so that the major differences are the X-ray production and detection. In short, here the X-rays are generated by accelerated charged particles that travel along curvilinear particle accelerator. The

resulting radiation can range from the infrared to the X-ray wavelengths, but currently, due to recent developments on optical systems, a high collimation and very small wavelengths can be achieved. Simultaneously, a very high brilliance can be achieved (typically, 10^8 times higher than conventional x-ray tubes) which allows shorter exposition times, smaller sample sizes and higher resolution, in comparison to normal XRD[179]. HRSXRD typically uses the transmission geometry, where the intensity of the transmitted and scattered beam are measured (see Figure 3.7)

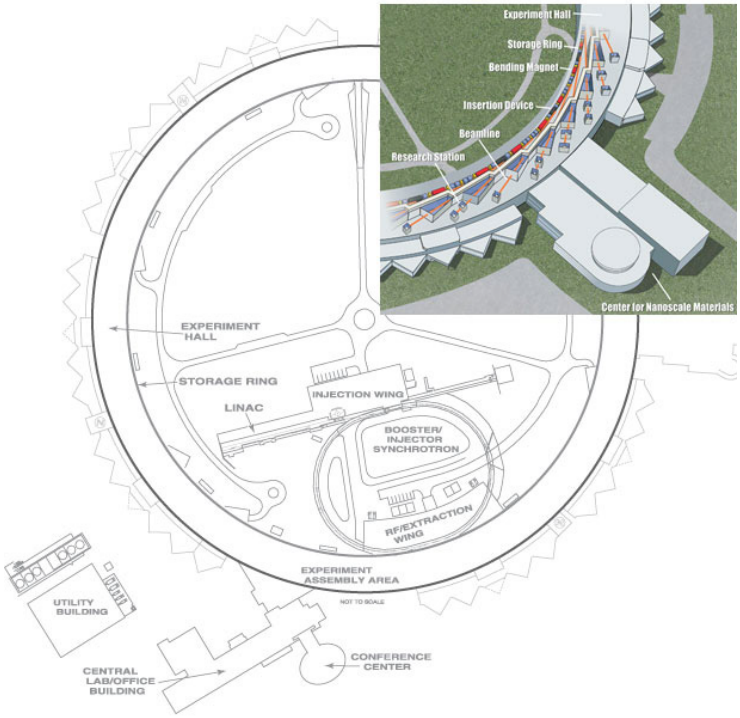

Figure 3.7 – Schematic overview of the Advanced Photon Source in Argonne, Illinois, USA.

The measurements presented here were done at the Advanced Photon Source (APS), at Argonne, Illinois, USA. The APS is one of the most brightest storage ring-generated x-ray beams of the world. As one can see from figure 3.7, the APS is constituted by 5 major parts: the linear accelerator (LINAC), the booster synchrotron, the electron storage ring, insertion devices and experiment hall. The process starts at the LINAC (inside the ring in figure 3.7) where electrons are emitted from a cathode that is heated up to 1100 °C and are accelerated to 450 MeV reaching velocities higher than 99.999 % of the speed of light (c). From the LINAC they are inserted into the Booster, a circular accelerator that, as the name induces, boosts the electrons velocities to values higher than 99.999999 % of c. This extra force is supplied by electrical fields in four radio frequency cavities. At the time they enter the main storage ring (1104 m perimeter), electrons have 7 GeV of energy, and become confined into a narrow beam that is bent on a circular path by hundreds of powerful electromagnets. The APS is called a

third-generation synchrotron ring because it was optimized for insertion devices, which are periodic sets of magnets that by inducing electron oscillations into small curvature paths allow higher radiation quality, that is quantified by the brilliance and flux. These two quantities are dependent on the number of photons per second with a narrow energy band and per unit solid angle both in horizontal and vertical directions. Finally, the Experimental Hall is where researchers are together with their corresponding experimental apparatus, it is divided in 35 lines each corresponding to an individual laboratory that has a direct access to the storage ring beamline. The specific measurements reported in this work were performed at 11-ID-D surface XRD beamline, with a λ = 0.774901 Å wavelength radiation 450 x 50 μm spot-size beam, which is commonly used on thin film diffractions mainly in structural and phase transition studies. Two dimensional diffraction patterns were collected using a Pilatus area detector, and converted to the conventional one-dimensional diffraction curves using the Fit2D program. In the 90-350 K temperature range, 52 spectra were obtained at a 5 K step on heating. An Oxford cryostream system was used for the temperature control. The analysis was done by refinement of these HSXRD spectra. This was realized through FullProf Studio package software, downloaded from FullProf team website and that nowadays constitutes one of the most prestigious softwares to perform XRD spectra refinements[180]. This software adopts the Rietveld Method[181], whose basic idea is the minimization of the least square deviation of a theoretical function, yi_{calc} relatively to the experimental function, yi_{obs} (XRD output spectra) and can be expressed as:

$$M = \Sigma_i W_i (yi_{obs} - (1/c) yi_{calc})^2 \tag{3.2}$$

where W_i is related to the statistical variance of the observation and c is an overall scale factor. The theoretical function depends on many factors among which the most important ones are: the peaks shape, width, position and relative intensity. Each spectrum can be refined considering one or more crystallographic phases are present. So, initially the user is supposed to introduce the peak shape, background, and the space group, lattice parameters and atomic positions of each phase believed to be present. With this input the program starts the iterative process (refining the above mentioned parameters) that will eventually converge to a theoretical function close to the observed one (this can be checked visually and with several quantitative agreement factors such as χ^2). Normally the refinement can be divided into two parts, a first one, named Le Bail after his author[182], that does not take into account the peaks relative intensities and can just provide quantitative information about lattice parameters and phases proportions. The second part just starts when a good enough matching was achieved with Le Bail method. Here the peaks relative intensities are considered, as well as, each phase atomic positions. This ensure an accurate refinement, from which one can extract atomic positions, interatomic distances and angles.

3.3.5 SQUID Magnetometry

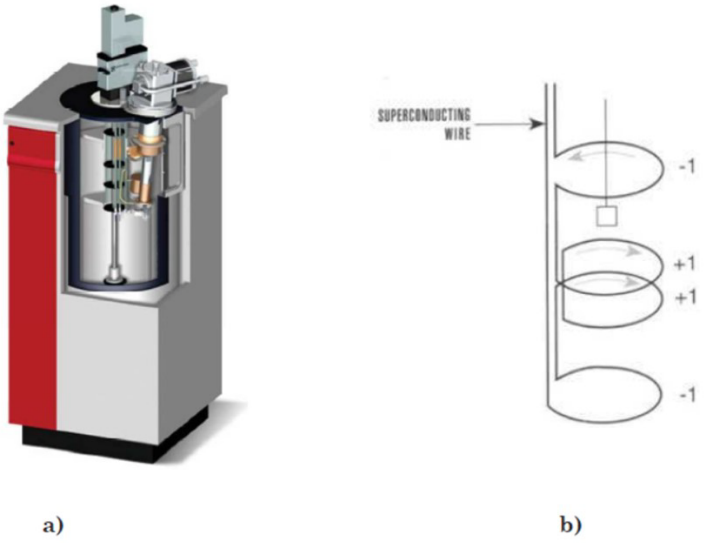

Figure 3.8 – a) View of the SQUID equipment. The samples are inserted from above into a chamber, and are centered with respect to the superconducting coils (b). Figures extracted from [183]

SQUID stands for Superconducting Quantum Interference Device and is a very high sensitivity (10^{-10} A m^2) magnetometer. This is an integrated device, basically containing a Superconducting magnet immersed in a Helium bath and a Superconducting detection coil system. The former is responsible for the application of a magnetic field that can be as high as 5.5 T, or higher in recent modules. The coil system as seen in Figure 3.8, is responsible for the sample magnetization measurement and is constituted by four Superconducting coils. Each coil has a Josephson junction which is the main responsible for SQUIDs high sensitivity as it makes the Superconducting coil in a high sensitive voltmeter, via the magnetic induction effect. Each coil carries a DC current in the direction pictured in the Figure 3.8. The magnetization measurement is done by moving the sample vertically from the initially centered position. This vertical movement changes the magnetic flux across the coils which in turn induces a voltage/current change on the Josephson junctions. Such change is measured by the voltage oscillations, which are discretized in units of magnetic flux quanta (10^{-14} T m^{-2}). Generally, its main applications are the measurement of a material magnetic moment as a function of temperature and magnetic field amplitude. Its huge advantage is indeed the high sensitivity which allows both the measurement of bulk samples magnetic moment and low moment samples such as thin films and nanostructures. The measurements presented here were performed in our institute, IFIMUP, with a SQUID that has a 5.5 T superconducting magnet and allows magnetic moment measurements in the temperature range 4-380 K. For this work, the temperature dependence of the magnetization for a fixed applied field

(M(T)) and the magnetic field dependence of the magnetization for a fixed temperature (M(H)) curves were measured. Because of the strong coupling between crystallographic and magnetic structure these measurements played a crucial role not only on determining important magnetic quantities. The magnetic entropy change, -ΔSm (the entity quantifying magnetocaloric effect), was estimated following Caron and coworkers procedure[184]. In short, magnetic isotherms (M(H)) were extracted for several temperatures in the desired temperature range. However, in between each isotherm, the sample would be heated up to a temperature higher than the magnetic ordering temperature and then cooled down to the following isotherm.

3.3.6 Transport Measurements

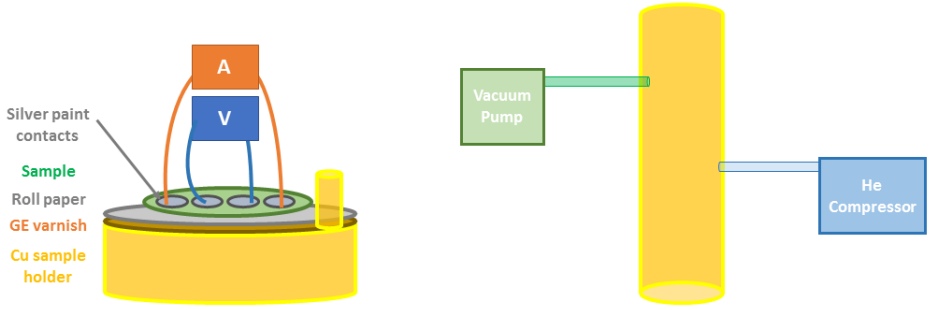

Figure 3.9 – At the left, a schematic view of the sample and its four electrical contacts, connected to a voltmeter (inner) and current source (outer contacts), placed on top of the Copper sample holder glued with GE varnish and roll paper. At the right the outside view of the cylinder cryostat connected to a vacuum system and to a He compressor.

The electrical resistivity was measured in a closed cycle cryostat in the 10-320 K temperature range. The sample holder is a cylindrical Cu block with a thread which incases in the cold tip of the cryostat. On its surface is placed a thin leaf of smoking roll paper embedded with GE-varnish, which is a good electric insulator and a good thermal conductor. This varnish also allows to fix the samples to the sample holder. On the sample holder plate there are 4 connection wires used to establish the electric contacts with the sample: 2 wires to measure voltage - placed in the two inner contacts of the sample surface - and 2 wires to provide the electrical current that crosses the sample - placed in the two outsiders contacts, as represented in Figure 3.9. The electrical contact between the sample and the wires is achieved with Silver paint. Once the electrical contacts are established, the sample holder is attached to a Copper structure and closed in what comprises to be the cryostat. The cryostat is connected with a inlet and a outlet to a Helium compressor that allows cooling from room temperature down to $\sim$ 10 K. Heating the sample surrounding space is achieved through a resistor heater down from 10 K up to 300 K. The cooling and heating rate is controllable by a program-

able temperature controller using a thermocouple sensor. The temperature sweeping time-rate has to be small (about 0.5 K/min to 1 K/min) so that thermal equilibrium can be closely approached, according to the required accuracy of the measurements. The Labview developed software used allows monitoring graphically the experimental results, in real-time, enabling the continuous verification of the measured data. All the transport property measurements of this thesis were carried out at our Institute, Instituto de Física de Materiais da Universidade do Porto (IFIMUP).

CHAPTER 4

$Gd_5(Si,Ge)_4$ nanogranular thin films displaying large magnetocaloric effect and complex thermal expansion behavior

4.1 Introduction

In this chapter a thorough investigation of a nanogranular $Gd_5(Si_xGe_{1-x})_4$ thin film will be described with special focus on its magnetic and structural properties, specially its magnetocaloric effect and its peculiar thermal expansion behavior. In particular, emphasis will be given to the effect of nanostructuring on these properties.

4.1.1 Giant Magnetocaloric/Magnetostrictive Effects in nanostructures

As mentioned in chapter 2 it was found that the GMCE results from the strong spin-lattice coupling evidenced by the $Gd_5(Si_xGe_{1-x})_4$ materials and in particular to the magnetostructural transition they undergo[3]. This agile interplay between magnetic and atomic lattice degrees of freedom makes them sensitive materials, capable of undergoing magnetostructural transitions induced by the variation of different external stimuli[21,24,25,111]. Since the discovery of the GMCE[4], an intense and devoted effort was focused on the bulk magnetocaloric materials and on macroscale magnetic refrigeration systems. In clear contrast, the nanoscalling processing of magnetocaloric materials received far less attention, despite the new opportunities it can unveil, scientifically and technologically, as listed in chapter 2. In particular, the nanostructuring of $Gd_5Si_2Ge_2$ materials has been ignored, with the exception of a test report on $Gd_5(Si_xGe_{1-x})_4$ thin film[149].

4.1.2 Negative Thermal Expansion

The great majority of materials expand when heated up and contract when cooled down - it is called a positive thermal expansion (PTE). The $R_5(Si_xGe_{1-x})_4$ bulk materials are no exception to this list. Typically, on heating they have a normal coefficient of thermal expansion (CTE - β) in the temperature interval below their structural transition temperature, $\beta_{bt} \sim 25$ ppm K^{-1} [185]. However, along the transition, they exhibit a giant positive

thermal expansion, $\beta_{MS} \sim 200$ ppm K^{-1} [185], as they typically transform from the ferromagnetic, low-volume to the paramagnetic, high-volume phase. After the transition, they tend to resume they normal thermal expansion, $\beta_{at} \sim 25$ ppm K^{-1} [185]. There are, however, an increasing number of materials discovered in the past 20 years, which exhibit a negative thermal expansion (NTE), among which the ZrW_2O_8 is a paramount example[12,186,187]. Another relevant example is the other class of strongly coupled (atomic structure and magnetism) materials, whose behavior is the opposite of the $R_5(Si_xGe_{1-x})_4$ bulk materials. Materials such as the $La(FeSi)_{13}$ (also presenting giant MCE), undergo a giant structural transition, from a low-temperature high-volume phase to a high-temperature low-volume phase. Such transitions can compensate (Invar effect[188]) or even overcome the conventional PTE[189]. However, to our knowledge, this effect was only observed below their magnetic ordering temperature, whereas above it, the materials recover their normal PTE. In light of the remarkable technical advances in nanofabrication over the past 20 years (nanoparticles, nanowires, multilayers) there has been an increasing effort to study nanomaterials thermal expansion. Two remarkable examples have been given by Li[190] and then Zheng[189] and co-workers which demonstrated the emergence of NTE in Au and CuO nanoparticles (-25 and -110 ppm K^{-1}, respectively), in contrast with their bulk counterparts PTE.

4.2 Experimental details

A thin film deposited by a femtsecond pulsed laser ablation (with a 9.1 mJ cm^{-2} laser fluence before focusing and a repetition rate of 1000 Hz) from a multi-grain $Gd_5Si_{1.3}Ge_{2.7}$ target prepared from high purity materials by the arc-melting method. Both femtosecond laser deposition and arc-meting techniques are described in chapter 2. A thin film (t$\sim$ 780 nm) of the same composition was deposited onto a 1 μm SiO_2 layer on the top of a (001) silicon substrate heated up to 200°C and at a pressure of $\sim 1.2x10^{-6}$ mBar. The rate of deposition was about $\sim$ 0.65 nm/sec. The thin film morphological and chemical analysis was performed through SEM images and EXDS spectra. The magnetic properties, in particular the magnetic field and the temperature dependence of the thin film magnetization were assessed by a SQUID magnetometer, in the 0-5.5 Tesla and 5-330 K field and temperature intervals, respectively. The thin film atomic structure and its temperature dependence was evaluated by High Resolution Synchrotron X-ray radiation diffraction (HRSXRD) experiments performed in Advanced Photon Source, APS Argonne, Illinois, USA, specifically at the 11-ID-D surface XRD beamline. A λ = 0.774901 Å wavelength radiation and a 450 x 50 μm beam-spot size were used. Each diffractogram was obtained isothermally. A total of 52 diffractograms were extracted in the 90-340 K temperature range, with a 5 K step, on heating. Rietveld refinements of each spectra allowed to study the atomic structure evolution while heating, as detailed in chapter 3.

4.3 Experimental results

4.3.1 Morphological Characterization

In order to evaluate the morphology of the thin film, a Scanning Electron Microscope (SEM) was used, enabling cross-section and top views, as is depicted in Figure 4.1 a) and b), respectively. As expected from the ultrashort laser pulses used for deposition[165,191], the thin film has a granular-like morphology (Figure 4.1 (b)), consisting on a stack of nanoparticles with a Lorentzian distribution of diameters: average diameter ~80 nm and a full width at half maximum of ~80 nm (inset of Figure 4.1 (b)). Furthermore, as is clear from the cross section view, the thin film thickness is very irregular throughout the whole sample. The thin film chemical composition was inspected by EXDS analysis and was found to be similar to the target material with a ~ 5% variation, i.e. $Gd_{5\pm0.25}Si_{1.3\pm0.07}Ge_{2.7\pm0.14}$. The maximum accelerating voltage of the electron beam was determined to be 15 kV. A Monte-Carlo simulation was performed to evaluate the interaction depth between a 15 kV electron beam and a film of this composition. It was concluded that at depth of ~ 500 nm the interaction is strongly attenuated being almost negligible at ~ 800 nm and hence the results obtained refer exclusively to the interaction with the thin film and the contribution from the SiO_2 buffer layer or the Si substrate should be negligible. Furthermore, since the Gd M spectroscopy line overlaps completely with Ge L_α at E ~ 1.18 keV (as can be seen in inset of Figure 4.1 a)), the K line of Germanium and Silicon (9.8 kV and 1.74 kV, respectively) and L line of Gadolinium (6.05 kV) were considered for composition calculations.

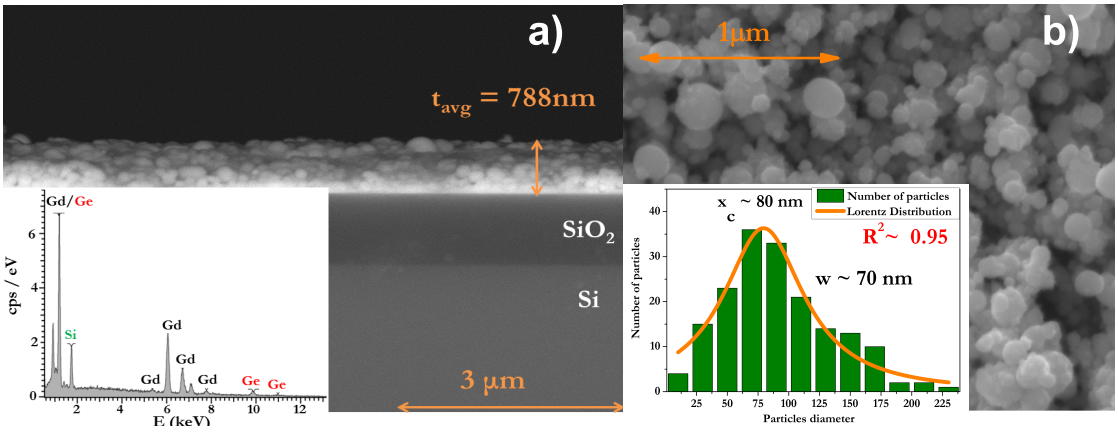

Figure 4.1 – SEM cross section, a), and top view, b), of the ~ 788 ± 59 nm thin film. An EXDS spectrum of a representative area is represented in a). The particles diameter histogram is presented in b) inset.

4.3.2 Structural Characterization

High Resolution Synchrotron X-ray radiation diffraction measurements of the thin film sample were carried out at the beamline 11-ID-D, Advanced Photon Source, Argonne National Laboratory. In a preliminary analysis only the patterns extracted in the 120-250 K temperature interval were refined and analyzed, whereas the remaining patterns, in the 90-150 K and 250-340 K temperature ranges, were thoroughly analyzed for a more complete study of the thin film thermal expansion behaviour, as will be detailed below.

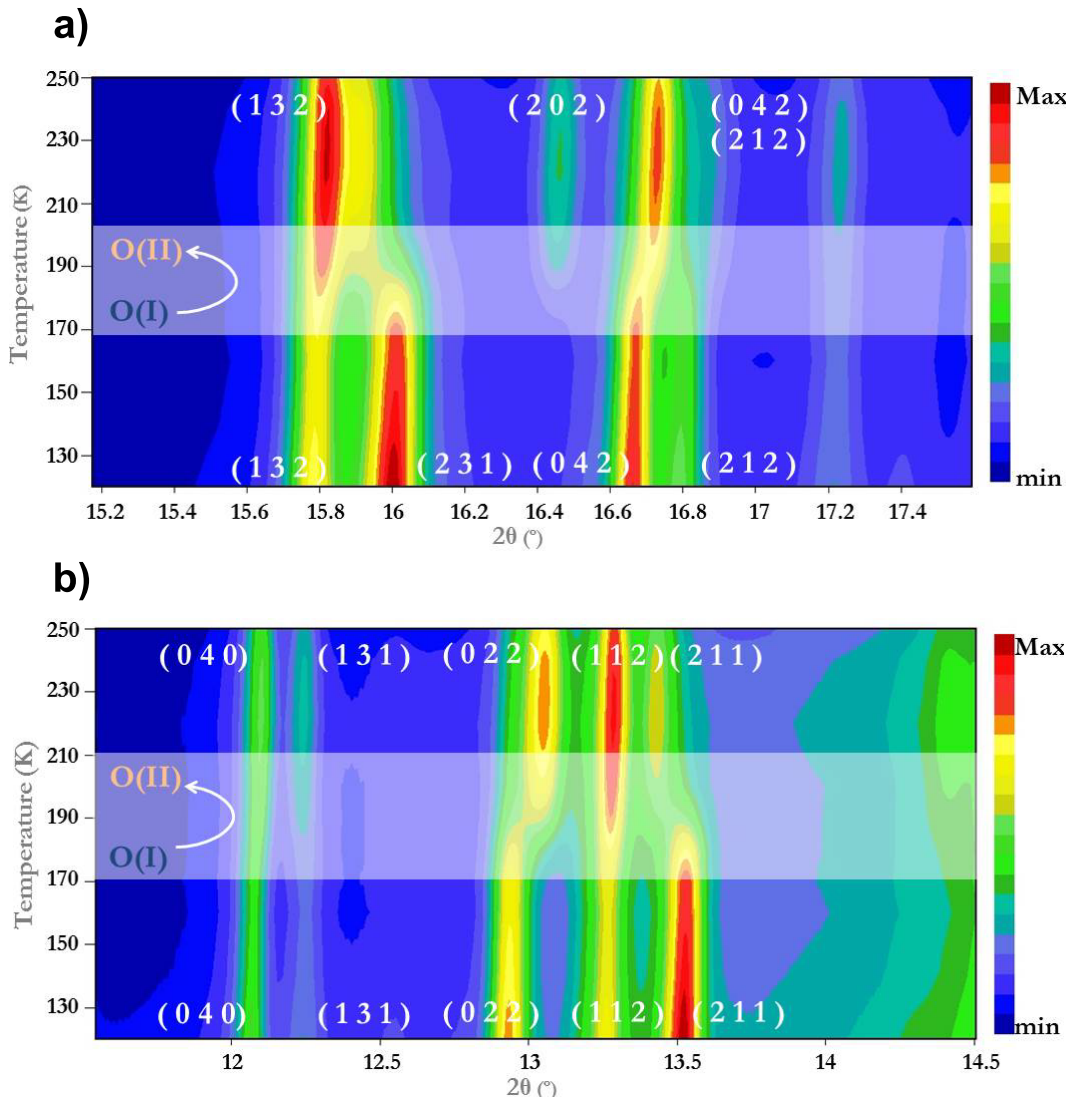

Figure 4.2 – 2D Contour plot of the collected and analyzed Synchrotron x-ray diffracted spectra as a function of temperature (120-250 K range) in the [15; 17.6] a) and [11.5; 14.5] b) 2θ interval.

The figures 4.2 a) and b) present the spectra represented as contour plots. In Fig. 4.2 a), at T ~ 170 K, it is clear that the four most intense peaks, associated with (2 3

1), (0 4 2), (1 3 2) and (2 1 2) Miller indices of the O(I) structure, begin to change their relative intensities and 2θ positions, whereas at $2\theta \sim 16.5°$ an additional peak emerges. In the same temperature interval, other changes on the peaks intensities occur: the peaks (2 1 1), (0 2 2), (1 1 2) of the O(I) phase are transformed into (1 1 2), (0 2 2), (2 1 1) of the O(II) phase, as can be seen in Figure 4.2 b). Such drastic changes of the peak intensities and positions clearly point to a O(I) $\rightarrow$ O(II) structural change, in accordance with similar behavior observed in bulk materials[110]. In the 150-170 K temperature range, the Rietveld refinement reveals the presence of a single phase: Gd_5Si_4-type [O(I)] structure. Above T=175 K, an additional structural phase is required for the refinement, specifically the Sm_5Ge_4-type [O(II)]. From 4.3 b) it can be observed that the O(II) phase fraction increases continuously from $\sim$ 11% at 175 K up to $\sim$ 54% at 190 K, where it becomes the majority phase. The O(II) phase fraction stabilizes and reaches $\sim$ 65% of the total volume at 220 K, showing that major changes in the phase fractions occur in the [175, 220] K temperature interval. At room temperature, the major structural phase possesses the following lattice and volume parameters: a = 0.759(4) nm, b = 1.472(3) nm, c = 0.771(6) nm and V = 0.862(7) nm^3 which are smaller than the bulk counterparts, such as $Gd_5Si_{1.5}Ge_{2.5}$ single crystal : 0.7658 nm, 1.4793 nm, 0.77554 nm and 0.87863 nm^3 ($\sim$ 2% higher than the thin film)[110]. In fact, the shrinkage in nanoparticles unit cell has been observed in previous metallic nanoparticles deposited with a femtosecond pulse laser, where it was attributed to the nanoparticles intrinsic surface stress (see discussion below in section 4.5.1)[192–195]. The temperature dependence of majority phase lattice parameters (a, b/2 and c) and volume are represented in Figure 4.3 a), where a giant and anisotropic change of the lattice parameters is displayed at T$\sim T_S \sim$ 190 K: Δa/a $\sim$ 1.2%, Δb/b $\sim$ -0.03% and Δc/c$\sim$ -0.4%, adding to a ΔV/V $\sim$ 0.81%, similar to bulk counterparts[101,110]. Comparing the obtained values with other reported strain effects, one finds that the Δa/a (12000 ppm) is 10 times larger than the recently reported 1300 ppm upper limit on $Co_{1-x}Fe_x$ thin films[196], than the 2000 ppm presented by commercial Terfenol-D[197], being in the same order of magnitude as the recently reported strain values of the shape memory alloys $MnNi_{1-x}Fe_xGe$[198], the improved NiMnGa foams[56] and the $BiFeO_3$ piezoelectric thin films[199].

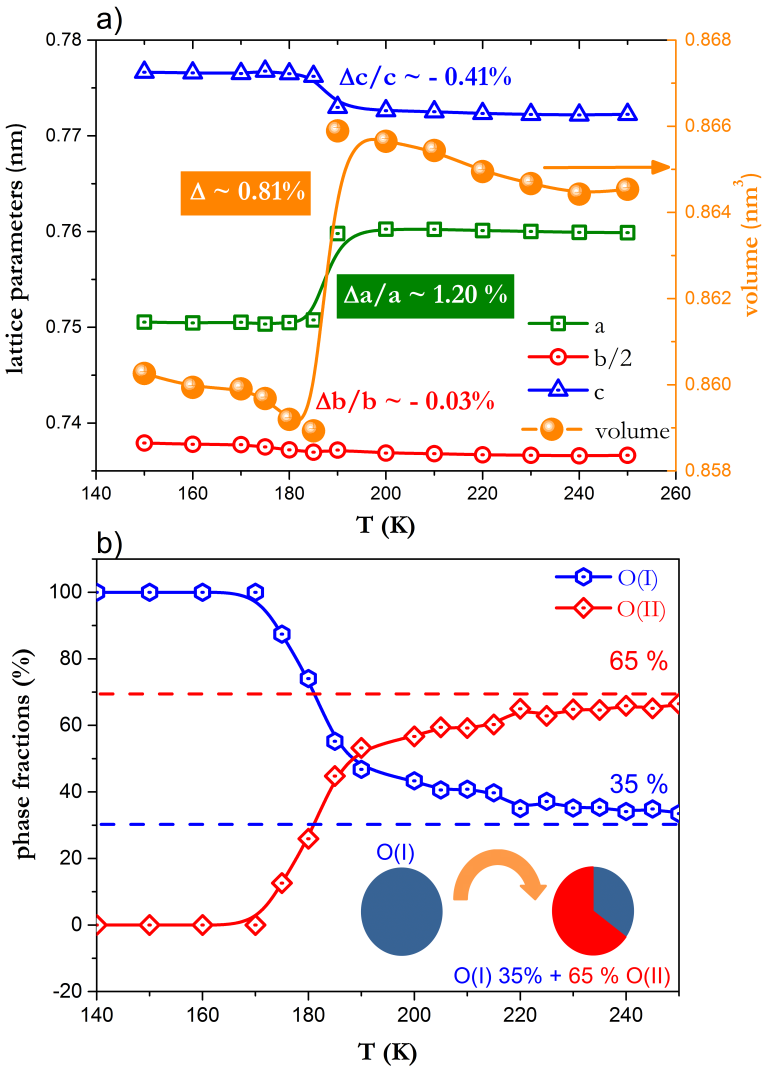

Figure 4.3 – Temperature dependence of the two phase fractions present, b), and the majority phase lattice parameters and volume, assigned to the left and right y-axis, respectively in a). The standard deviations for the parameters are not shown on the plots because they are smaller than symbol sizes.

4.4 Negative Thermal Expansion at the nanoscale

As mentioned above, the temperature regions below (90-150 K - LT) and above (255-340 K - HT) deserve a closer and detailed look at their thermal expansion behavior. In Figure 4.4 the most intense reflections, associated with the (1 3 2), (2 3 1), (2 0 2) and (0 4 2)/(2 1 2) Miller indices, are represented for LT a) and HT b).

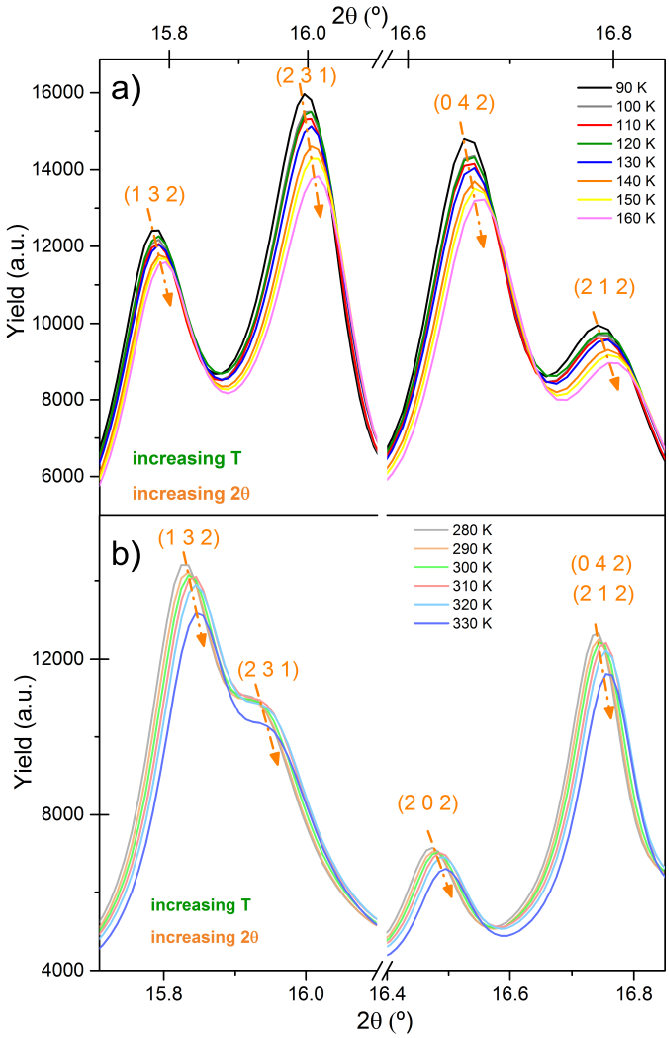

Figure 4.4 – Synchrotron X-ray diffraction data for $Gd_5Si_{1.3}Ge_{2.7}$ nanogranules extracted for fixed temperatures with a 10 K step in the 90-160 K (LT),a), and 280-330 K (HT), b), temperature intervals, respectively. The 2θ interval evidences the four most intense peaks associated with the atomic planes identified with the respective Miller indices in parenthesis. While increasing temperature an increase of each peak 2θ position is observed, signalling the negative thermal expansion of the $Gd_5Si_{1.3}Ge_{2.7}$ nanogranules.

As can be seen, all peaks shift towards higher 2θ values as the temperature increases. Such 2θ behaviour is a clear-cut signature of NTE. The Rietveld refinement of each diffractogram allows to monitor the atomic structure temperature dependence. The relative unit cell volume, V, and lattice parameters, a, b and c of the nanogranules are plotted in Figure 4.5 a) and b) as a function of temperature. The nanogranules volume V contracts in the whole temperature range, except in the temperature interval where the magnetostuctural transition occurs, described in the previous subsection. The nanogranules NTE splits in two different behaviors. In the LT regime, all three lattice parameters contract linearly as T increases, with the slopes $\alpha_a{}^{LT} = \Delta a^{\mathbf{LT}}/\Delta T \sim$ -13.0 ppm $K^{-1} > \alpha_b{}^{LT} = \Delta b^{\mathbf{LT}}/\Delta T > \alpha_c{}^{LT} = \Delta c^{\mathbf{LT}}/\Delta T$, summing up to a large and negative volume thermal expansion, $\beta_{LT}=\Delta V^{\mathbf{LT}}/\Delta T \sim$ -32.2 ppm K^{-1}. The inherent contraction is inter-

rupted by the previously reported magnetostructural transition, across which the unit cell greatly expands with $\beta_{MST}=\Delta V^{MST}/\Delta T \sim +64.5$ ppm K^{-1}, up to T= 210 K. Then the contraction resumes exhibiting a transient-regime (TR) up to 240 K with a smaller and somehow irregular rate than in the LT region ($\beta_{TR} \sim$ -23.8 ppm K^{-1}). The HT-regime begins at 255 K, enhancing the volume contraction up to a giant $\beta_{HT} \sim$ -69 ppm K^{-1} NTE value all along a ~ 90 K wide temperature interval around room temperature, 255-340 K.It must be remarked that 340 K was the highest measured temperature and thus it is not possible to state whether the NTE behavior continues or not beyond this temperature. The *a*-contraction increases again, surpassing its LT value, as occurs for the *b*

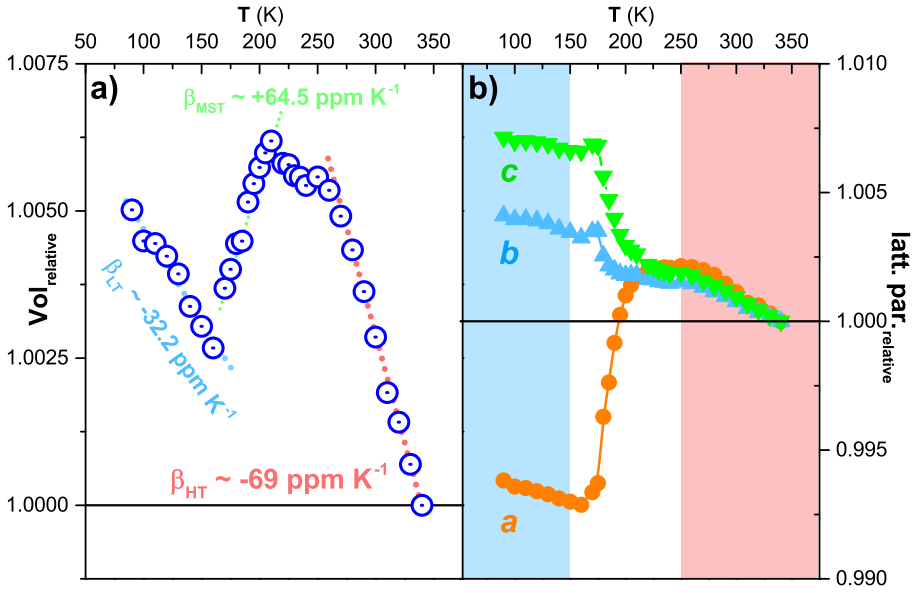

Figure 4.5 – a) Temperature dependence of the $Gd_5Si_{1.3}Ge_{2.7}$ nanogranules relative unit cell volume (blue open circles). The volume values were normalized to *V*(T = 340 K) and the linear fits in the 90-150 K, 175-210 K and 255-340 K temperature ranges are presented. b) $Gd_5Si_{1.3}Ge_{2.7}$ nanogranules relative *a*, *b* and *c* lattice parameters values as a function of temperature. Lattice parameters values were also normalized with their respective value at T = 340 K.

and *c* values - overall in this region: $\alpha_a{}^{HT} \sim 23.2$ ppm $K^{-1} > \alpha_c{}^{HT} > \alpha_b{}^{HT}$. The contraction force is clearly enhanced in the HT regime. One notes that the observed β_{HT} is much larger than the ones found in Graphene (-7 ppm K^{-1} [11]), and more than doubles that observed in ZrW_2O_8 ,-28.2 ppm K^{-1} [12]. Although the observed β_{HT} in this nanogranular film is smaller than the ones exhibited by CuO nanoparticles (-110 ppm K^{-1}) and bulk $Ca_2RuO_{3.74}$ (-115 ppm K^{-1})[200] samples, it is retained even above the magnetic ordering temperature, in contrast with the two latter examples. Additionally, in the HT region, a β of an O(II) single-phase nanogranules, $\beta_{O(II)} \sim 88$ ppm K^{-1} can be estimated, considering the observed β (-33.2 and -69 ppm K^{-1}) and the phase fractions, 35% O(I) and 65% O(II), present in this temperature region. These are unexpected results since in general, there are no signs of NTE behavior in $R_5(Si_xGe_{1-x})_4$ bulk compounds[13,14,82]. Therefore, the NTE emerges as a consequence of the relevant size reduction in this nanogranular film.

4.4.1 Magnetic Characterization

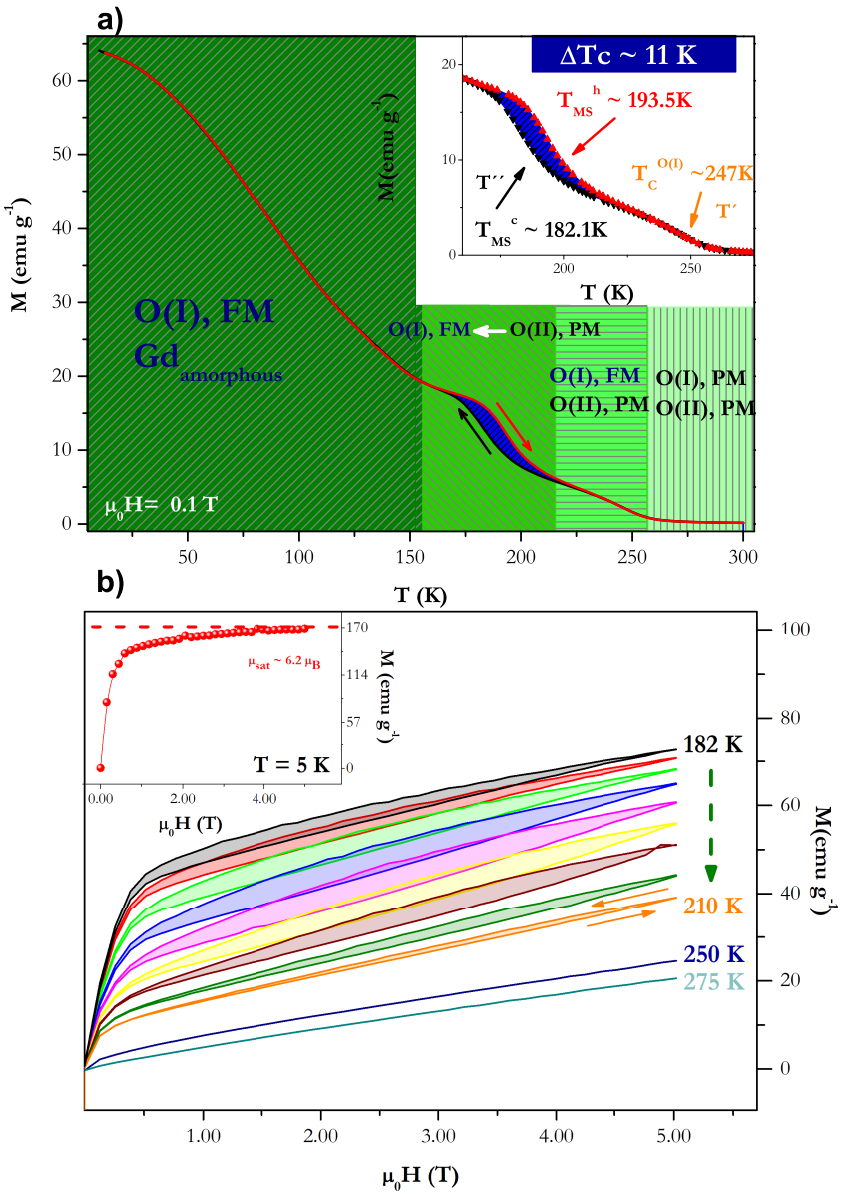

Figure 4.6 – Magnetization as a function of temperature with a constant applied magnetic field of 0.1 T (a) and a focused region in the inset. (b) Magnetization isotherms ,M(H), measured in the 182-210 K temperature range at 250 K and at 275 K with increasing (lower curves) and decreasing (upper curves) applied magnetic fields. In b) inset, the M(H) at 5 K is presented and the magnetization saturation, at $\mu_0 H$ = 5 T, is indicated.

The magnetization temperature dependence was measured first on cooling and then on heating in the [10, 300] K temperature range with a constant 0.1 T applied magnetic field. The rate of cooling and heating was the same and equal to 2.333 K/min. Afterwards, the film was cooled again to 5 K, in order to measure the M vs H curve at this temperature. The M vs H isothermal curves were measured according with the loop method in the

[135, 275] K temperature range, with increasing and decreasing field and a step of ~ 0.125 T[184]. Figure 7.1 a) presents the magnetization temperature dependence, on cooling and heating, in the 10-300 K temperature range under a constant applied field of μ_0H = 0.1 T. On cooling, two paramagnetic to ferromagnetic transitions are observed: one at T = T″ ~ 194 K and a second one around T = T′ ~ 247 K. From Figure 7.1 a), it can be observed that there is an overlap between the cooling and heating curves, except for the region between 170 and 225 K, where thermal hysteresis is observed (blue area in Figure 7.1 a)). Such a temperature interval is coincident with the one observed in the XRD data (shown in Figure 4.2 a) and 2 b), where the O(I) → O(II) structural transition is observed, unveiling the occurrence of a simultaneous magnetic and structural transition, i.e. a magnetostructural transition, [O(II),PM] → [O(I), FM].

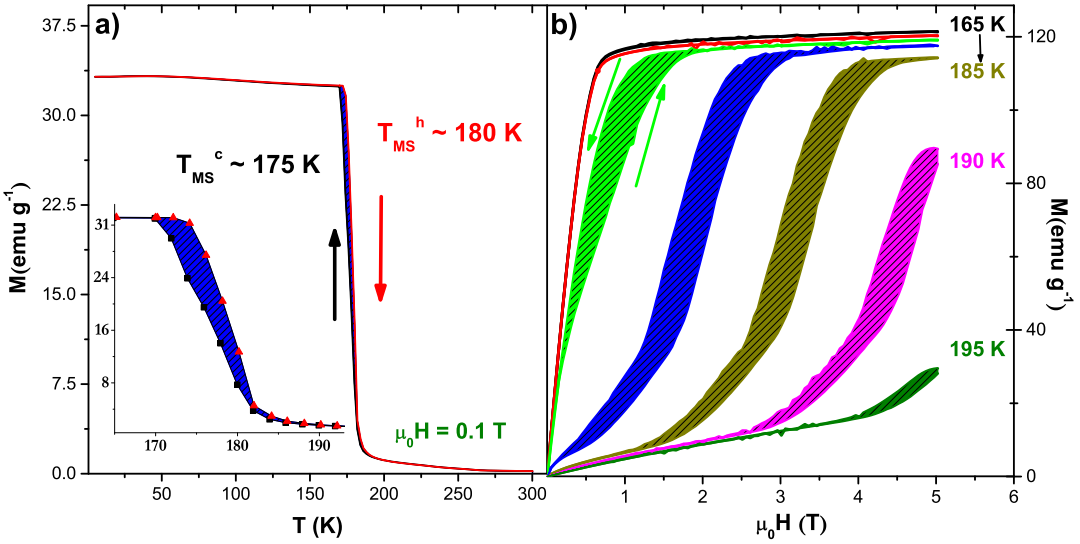

Figure 4.7 – $Gd_5Si_{1.3}Ge_{2.7}$ bulk target magnetization as a function of temperature on cooling (black curve) and on heating (red curve). The thermal hysteresis is highlighted in blue. A magnified M(T) curve is presented in the inset, where the transitions are signaled with T_{MS}^{c} ~ 176 K and T_{MS}^{h} ~ 180 K, which were determined by the averaged maximum of the derivative of the curves. The observed thermal hysteresis is $\Delta T_{MS} = T_{MS}^{h} - T_{MS}^{c}$ ~ 4.2 K.

In comparison with the bulk target $Gd_5Si_{1.3}Ge_{2.7}$, the thin film T″ transition occurs about 13 K above the one found for the bulk sample, as can be compared with Figure 4.7 a) and in reference[80]. Furthermore, the T′ transition constitutes a fingerprint of a purely ferromagnetic ordering of the high-temperature O(I) phase, i.e, $T' = T_C^{O(I)}$, corroborating with the structural characterization analysis - an arrestment of a minority O(I) phase up to high temperatures. Moreover, the continuous magnetization increase down to 10 K probably arises from a Gd-based paramagnetic amorphous phase, as previously observed in long ball milling studies[152]. In Figure 4.7 b) M vs H isothermal curves are depicted for the 182-210 K temperature range and T = 250, 275 K. These curves were measured according with the loop method, i.e. after each isotherm the film was warmed up until the paramagnetic (PM) region (at 300 K) and then cooled down to 100 K and again heated up till the desired temperature. Magnetic hysteresis (highlighted

in color in Figure 7.1 b)) is present in the 182-210 K temperature region. Typically in the bulk systems, the metamagnetic transition exhibits a pronounced S-type shape between the two magnetization states, as can be seen in 4.7 b) and in reference[26]. In this thin film, the M(H)s curves are smoother, leading to a large hysteresis reduction when compared with the bulk counterpart. In the literature this peculiar M(H) shape has been generally associated with disorder that might be caused by microstrain, structural defects, chemical disorder, etc...[6,201].

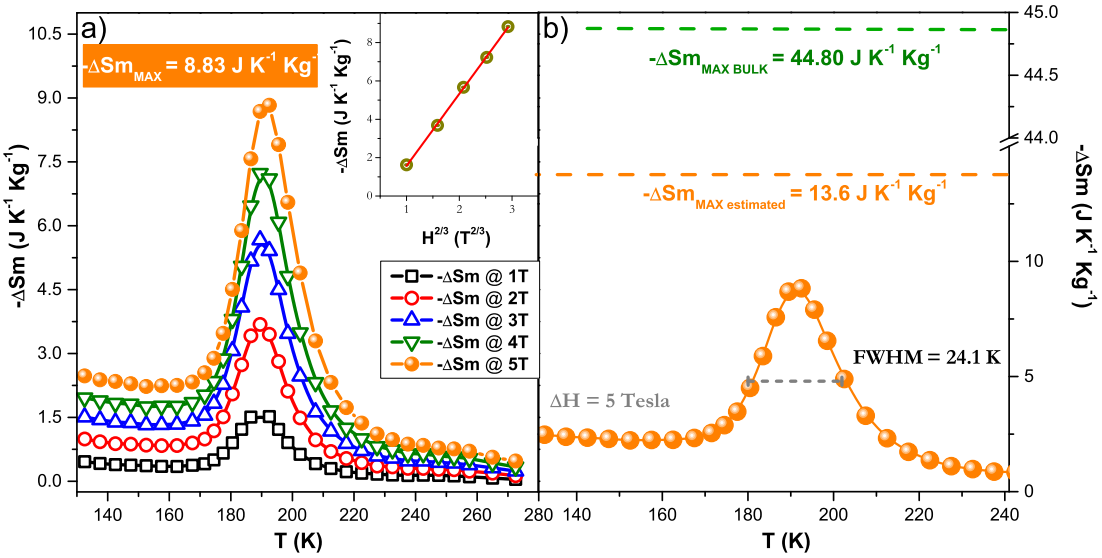

Figure 4.8 – (a) Magnetic entropy change (ΔSm) as a function of temperature in the 135-275 K temperature range. In the inset the $-\Delta Sm^{MAX}$ is plotted against the applied magnetic field changes to the 2/3 power. (b) The 0-5 T $-\Delta Sm$ (T) curve is plotted alone with the maximum values normalized to the ~ 65% mass from the O(II) phase that effectively contributes to the magnetic entropy change in the 135-235 K temperature (orange dashed line), and for a similar composition bulk value (green dashed line), as extracted from Reference[80].

The temperature dependence of the magnetic entropy change ($-\Delta Sm$ (T)), plotted in Figure 4.8 a), was estimated in accordance with Luana et al report[184]. Its peak value, $-\Delta Sm^{MAX} \sim 8.8 \pm 1.7$ J kg^{-1} K^{-1}, occurs at T = Tpeak = $T_{MS} \sim 192$ K, and the full width at half maximum (FWHM) is ~24 K for a field variation of $\Delta\mu_0 H = 5$ T. Hence, the refrigerant capacity is $RCP_{FWHM} \sim 212$ J K^{-1}. Such a large change in the thin film entropy is a consequence of the strong coupling between the magnetic spin and the lattice (as observed in its bulk counterpart), evidenced by the occurrence of a simultaneous magnetic and structural transition - magnetostructural transition. Furthermore it is important to stress that the $-\Delta Sm^{MAX}$ mass and volume normalization performed are clearly an underestimation of the real $-\Delta Sm^{MAX}$ of the film, since this normalization assumes that the whole film volume contributes to the entropy change and this is not true. In particular because there is a ~ 35% amount of O(I) arrested phase, which does not transform into O(II) and hence does not contribute to the $-\Delta Sm$ in the 150-240 K temperature interval. Recalculating, by subtracting the ~ 35% volume fraction, gives an estimated

corrected value of $-\Delta Sm^{MAX}_{corrected} \sim 13.6$ J kg^{-1} K^{-1} for $\Delta\mu_0$H = 5 T (see Figure 4.8 b). Such value is lower than that of the $-\Delta Sm^{MAX}_{bulk}$ ($\sim$ 43 J kg^{-1} K^{-1} for $\Delta\mu_0$H = 5 T[80]), however its complemented with a larger FWHM (which constitutes further evidence of strain disorder[201]) and reduced hysteretic losses). Such reduction can be evaluated by averaging the area in between the M(H) curves over the $T_C^{cooling}$-$T_C^{cooling}$ +20 K temperature range, resulting in $\sim$ 12 J kg^{-1} , almost three times lower than the value presented by the target sample, $\sim$ 43 J kg^{-1}. Hence, if the hysteretic losses are subtracted to the thin film refrigerant capacity, the efficient RCP is estimated to be RCP_{eff} 200 J kg^{-1}. The obtained $-\Delta Sm^{MAX}_{corrected}$ and RCP values are higher than the observed in manganites thin films, such as $La_{0.67}Sr_{0.33}MnO_3$[202], $La_{0.56}Sr_{0.44}MnO_3$[39] or $La_{0.7}Sr_{0.3}MnO_3$ on $SrRuO_3$ superlattices[203]; Gd multilayered films[120]; or NiMnGa thin films[204], being only lower than the epitaxial MnAs[47] and FeRh[133] thin films as can be confirmed in table 4.1. In comparison with the bulk GMC materials[31], the thin film presents a lower $\Delta Sm^{MAX}_{corrected}$. However, its reduced hysteretic losses and broadened ΔSm^{MAX}(T) curve ensure a promising RCP (higher than the promising Pt doped NiMnGa system[205] and virtually equal to the $Gd_5Si_2Ge_{1.9}Fe_{0.1}$ magnetic refrigerant[27]).

Table 4.1 – Magnetocaloric effect of a set of thin film materials presenting the highest $-\Delta Sm^{MAX}$ reported so far in the literature.

Chemical composition	Thickness (nm)	$-\Delta Sm^{MAX}$ (J K^{-1} Kg^{-1})	T$'$ (K)	$\Delta\mu_0$H T	RCP (J kg^{-1})	Reference
$Gd_5Si_{1.3}Ge_{2.7}$	788	8.83 (13.6)	190	5	212 (323)	This work
$Gd_5Si_{1.3}Ge_{2.7}$	788	7.2 (11.1)	190	4	156 (241)	This work
$Gd_5Si_{1.3}Ge_{2.7}$	788	5.7 (8.8)	190	3	121 (187)	This work
$Gd_5Si_{1.3}Ge_{2.7}$	788	3.7 (5.7)	190	2	75 (116)	This work
$Gd_5Si_{1.3}Ge_{2.7}$	788	1.6 (2.5)	190	1	32 (50)	This work
W/Gd/W	5/40/5	1.4	275	1	52	[119]
W/Gd/W	5/40/5	3.2	275	3	240	[119]
Ta/Gd/Ta	5/30/5	1.6	285	1	70	[120]
$La_{0.7}Sr_{0.3}MnO_3/SrRuO_3$	8	2.35	325	2	125	[203]
NiMnGa	400	1.7	346	1		[204]
NiMnGa	400	8.5	346	6	170	[204]
NiCoMnIn	300	< 5	353	6	<200	[6]
$La_{0.67}Sr_{0.33}MnO_3/SrTiO_3$	20	1.1	321	1	15	[202]
$La_{0.67}Sr_{0.33}MnO_3/SrTiO_3$	20	1.54	321	1.5	50	[202]
MnAs	70	4	300	1	>120	[47]
MnAs	70	17	300	5	774	[47]
$La_{0.56}Sr_{0.44}MnO_3$	31	2	270	6	185	[206]
FeRh	100	20	320	5	431	[133]

As in the bulk counterpart case, the magnetic-field induced structural transition undergone by this nanogranular thin film contributes with a so-called $-\Delta Sm_{latt}$ to the overall entropy change induced by magnetic field change. As detailed by Pecharsky and coworkers, such a large structural change is expected to contribute to $\sim$ 50 % of the total $-\Delta Sm^{MAX}$[77]. The film higher surface to volume ratio is an advantage towards the enhancement of the heat exchanges rate occurring in a magnetic refrigerator[207], thus allowing an increase of the cycling frequency and consequently its cooling power[208].

In contrast with the observations in bulk specimens[26] it is clear that up to 5 T, the magnetization curves do not achieve a fully saturated state: the saturation magnetization at 5 K is $\mu_{Sat} \sim 6.2 \pm 0.8\ \mu_B$, slighlty lower than the theoretical 7 μ_B. The difference can arise from the presence of small paramagnetic Gd amorphous phase(s) amount.

4.5 Discussion

4.5.1 Magnetic response smoothing

The simultaneous observation of a Tc increase together with the shrinkage of the unit cell are hallmarks of stress and strain presence for the $Gd_5(Si, Ge)_4$ materials[5,78,209]. Typically, $Gd_5(Si_x,Ge_{1-x})_4$ with x ~ 0.3-0.4 compounds present a T_C pressure dependence of $\partial T_C/\partial P \sim 1.2$ - 1.5 K/kBar[210,211]. Considering the ~ 13 K T_C increase in thin film comparing with bulk, this means that an equivalent intrinsic pressure in the 8-11 kBar range is present. This in total accordance with the pressure estimation performed to account for the observed unit cell shrinkage $\Delta V = V_{bulk} - V_{film}$, i.e, by using the compressibility (κ = [0.00158, 0.00190] $kBar^{-1}$)[212] and P = $(\Delta V/V)(1/\kappa)$ a pressure value in the 9-11 kBar range is obtained. Hence, independent structural and magnetic characterization analysis indicate pressure/stress as the most probable cause for the observed changes in the thin film behavior in comparison with the bulk. Such stress in thin films can arise from the preparation method and from strain induced by the substrate-film interface stress (which is typically the main stress mechanism in (hetereo)epitaxial thin films). Because of the granular morphology, the substrate-film interface should be rather irregular and hence its induced stress can be discarded as the main mechanism. Nevertheless, due to the small nanoparticles diameters, the surface stress that naturally occurs in nanoparticles and which is inversely proportional to its diameter can not be neglected. Despite the difficulty associated with the complex calculation of the surface pressure of these nanoparticles, it is known that it should lie in the 1-50 kBar values for nanoparticles with less than 100nm diameter[213]. Considering that the mean particle size of the nanoparticles in this thin film is ~80 nm, it outcomes that their intrinsic surface stresses can explain the observed results (increase of T_C and unit cell volume reduction). Furthermore, the observed smoothening of the magnetic responses and the magnetic hysteresis reduction are a plausible consequence of the distribution of surface pressures associated with the different nanoparticles diameters along the film. This suggestion can lead to advanced production methodologies, namely tuning the nanoparticle size distribution ensemble (e.g. by changing laser parameters[193]) as a strategy towards magnetic hysteresis reduction, which is of pivotal importance for the efficiency improvement of the magnetic refrigeration process[27,207].

4.5.2 Nanogranular $Gd_5Si_{1.3}Ge_{2.7}$ flexible-lattice framework

In the literature there are four different mechanisms identified as main causes for NTE behavior: **(i)** abnormal electronic band temperature dependence, **(ii)** magnetovolume coupling, **(iii)** atomic radius contraction and **(iv)** the tension effect, as reviewed by Takenaka et. al in reference[214]. **(i)** The abnormal electronic bands temperature dependence is enhanced at the nanoscale, namely through the quantum-like induced separation of its discrete energy levels, as was observed in 4nm Au nanoparticles[190]. This effect should only develop for ultra small nanoparticles, where the electron mean free path is higher than the nanoparticles size, hence leading to perturbations of the energy level states. Since the nanogranules here presented have a mean diameter of 80 nm, the electronic confinement is not expected, neither significant perturbation of its electronic discrete levels. However, the 80 nm size does not rule out phonon confinement, as observed in Si-Ge $\sim$ 100 nm nanowires[215]. **(ii)** In magnetovolume based NTE bulk materials, such as $La(FeSi)_{13}$[216], the volume coupling is strong enough to induce a magnetostructural transition (from a low to a high unit cell volume on cooling), however conventional PTE is recovered at temperatures below and above the magnetostructural transition. Another interesting magnetovolume based NTE was found while reducing the dimensions of CuO[189]. In this case, the NTE emerged in 5 nm CuO nanoparticles as a consequence of size reduction. Although here the NTE also emerges with size reduction, the fact that it is retained even at temperatures above the magnetic ordering temperature, discards the magnetovolume coupling as NTE primary cause. **(iii)** The atomic radius contraction phenomenon occurs in systems where there is a charge transfer between two neighboring atoms, resulting in a contraction of the donor and an expansion of the acceptor, as reported for $Sm_{2.75}C_{60}$[217] or $LaCu_3Fe_4O_{12}$[218] bulk materials. Nevertheless, similarly to the magnetovolume coupled NTE materials, this phenomenon occurs only below a critical temperature. Despite the NTE behaviour here reported is not completely understood, some important underlying mechanisms deserve highlight. The nanogranules showed a mixture of two concurrent Orthorhombic phases, O(I) and O(II), with 35% and 65% fractions at room temperature, respectively; below $\sim$ 150 K, only the O(I) phase exists, but upon gradual heating it converts incompletely (65%) into O(II), while 35% remain in the O(I) arrested phase. These two Orthorhombic structures share the same spatial group, Pnma, but the O(I) has a smaller unit cell volume (1.2% smaller) than O(II). Such cell can be decomposed in two rigid slabs that lie in the *ac* plane and are stacked by weaker bonding (or its absence in O(II)) along the *b* axis, originating a flexible interslab region as seen in Figure 4.9 a)[13]. Each rigid slab consists of two pseudo body-centered cubes with Gd atoms at their vertices and centre having two Si/Ge as next neighbors. In the interslab region there is one non-equivalent Si/Ge position (Ge3) that can be covalently bonded (unbonded in O(II)) with the equivalent Si/Ge position of the adjacent rigid slab. The presence/absence of this bonding is the main mechanism responsible for the differences between the two structures vol-

umes. Alternatively, these structures can also be viewed as a stacking of octahedrons with Gd1 at the centre, Si/Ge1 and Si/Ge2 in the four vertices in the horizontal ac plane and the Ge3 in the two vertices along the *b* direction, as illustrated in Figure 4.9 a). The Ge3 form an important triplet chain with the Gd1, Ge3-Gd1-Ge3, whose angle is ϕ, as highlighted in Figure 4.9 b).

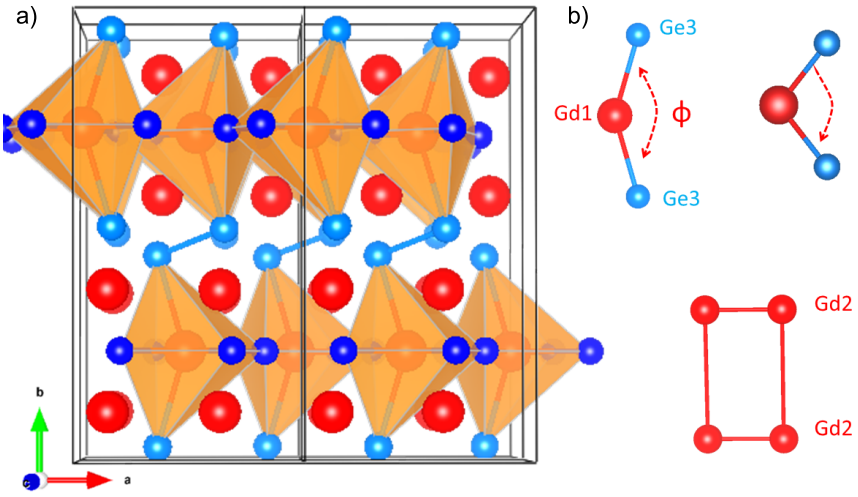

Figure 4.9 – a) Schematic representation of the Orthorhombic Pnma space group structure of $Gd_5Si_{1.3}Ge_{2.7}$. b) Octahedra constituent Ge3-Gd1-Ge3 triplet system (Ge3 represented as blue small spheres and Gd1 as red larger sphere) and the slabs constituent Gd2 atoms (also as red spheres). For schematic clarity Gd3 atoms are not exhibited.

In the light of this alternative view, it becomes even clearer the structural importance of the triplet chain Ge3-Gd1-Ge3 on both the octahedra stability and its connection with the next-near octahedra along the ***b*** axis. A closer look into the Ge3-Gd1-Ge3 angle temperature dependence, ϕ(T), is given in Figure 4.10. As can be seen, ϕ(T) mimics the volume behavior and a linear correlation between the two is observed for LT and HT, as represented in Figure 4.10 inset. This striking resemblance helps unveiling the potential atomic mechanism behind the NTE behavior. As temperature increases, the Ge3-Gd1-Ge3 chain flexes, decreasing its angle ϕ and thus decreasing the two adjacent slabs distance, which results in a contraction of all lattice parameters and consequently of its volume. This complex angle behavior contrasts with the almost invariant intraslab distances, Gd2-Gd2, both in the LT and HT temperature regions, supporting the triplet chain importance, as plotted in Figure 4.10. Following this reasoning, the potential for Ge3-Gd1-Ge3 transverse vibrations, which correspond to a bond bending static image, is energetically more favorable than for longitudinal vibrations[187]. This means that a low-amplitude and low-frequency vibration of the Gd1 atom along the ***ac*** plane leads to the bending of the triplet bonds and so to a volume contraction. Such mechanism, known as tension effect (**(iv)** NTE cause), is similar to the one observed in the open framework materials (OFM) AP_2O_7 such as ZrW_2O_8[12,219], ZrP_2O_7[220] and $Ag_3[Co(CN)_6]$[221]. In fact, the triplet chain Ge3-Gd1-Ge3 is analogous to the M-O-M triplet found in such OFM

(where M = Ti, Zr, P, V,...) in the sense that both involve the simultaneous presence of lighter and mobile (Ge/O) bonded to heavier and more inert atoms (Gd/M) (in particular, the atomic number ratio Z_{Gd}/Z_{Ge} is equal to the ~ Z_P/Z_O responsible for the ZrP_2O_7 NTE). Moreover, the triplet chain Ge3-Gd1-Ge3 is known to have a critical importance on the magnetovolume coupling in these materials[222]. Although it remains unclear why, this angle behaviour sets markedly the difference between the nano and bulk lattice temperature dependencies. For bulk counterparts a typical small angle variation of ~ 0.8 º-1 º is observed over a 100K temperature range[14] (in contrast with the large 5.5º variation observed here for the 60 K-wide LT region). The bulk and the nano underlying atomic mechanisms are similar in the sense that for both, the slabs (where the octahedra lie) remain basically invariant with the temperature increase, while the interslab region is noticeably flexible. However, in the nano case this interslab flexibility is demonstrated via the flexing of the elastic Ge3-Gd1-Ge3 chain, whereas in the bulk case the two adjacent slabs slide apart each other, moving in opposite directions and maintaining the ϕ angle almost constant.

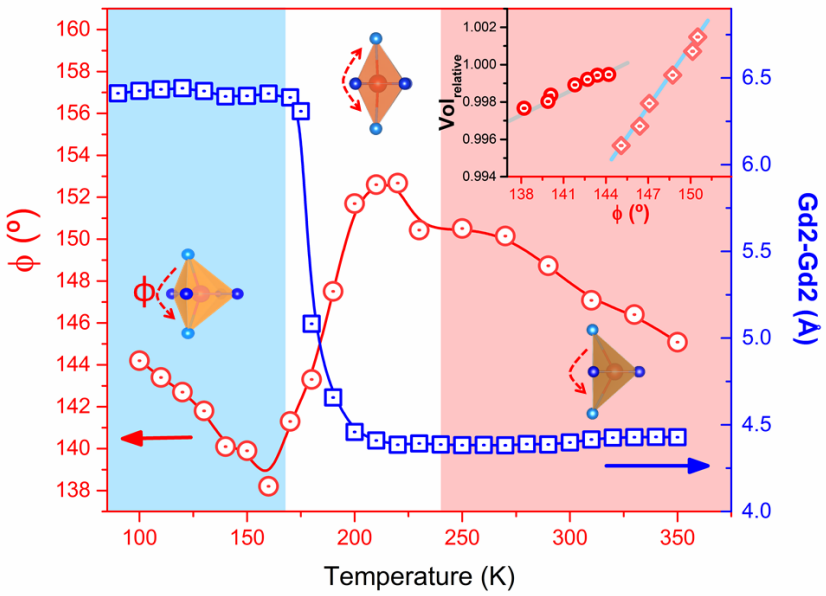

Figure 4.10 – Temperature dependence of the ϕ angle between the key Ge3-Gd1-Ge3 triplet atomic chain in the left y-axis and of the Gd2-Gd2 intraslab interatomic distance in the right y-axis. In the inset the relative unit cell volume is plotted against the ϕ angle revealing its linear correlation.

The reason for the volume contraction to occur more steeply in the HT than in the LT region is still unsettled. One hypothesis is that in the LT region the magnetovolume effect can be acting in opposition to the overall NTE (towards PTE, as occurs in their bulk counterparts), therefore counterbalancing the nanogranules overall tendency to contract. This hypothesis is reinforced by the strong covalent interslab Ge-Ge bonds that are found in the O(I) structure in LT region. Such bonds are restraining the atoms movements, hence inhibiting a stronger contraction. A more general mechanism differentiating the nano and bulk behaviors can be conjectured. As, referred above, there is

an intrinsic stress at the nanogranules surface whose value is inversely proportional to the nanoparticle diameter, d[10] and that for this system it provides an equivalent hydrostatic pressure in the 8-11 kBar range. This large size-induced stress can be identified as the major difference between the bulk and the nanoscale, and hence can be considered the driving force of the reported NTE in this $Gd_5Si_{1.3}Ge_{2.7}$ nanogranular ensemble. The pressure induced lattice softening was already observed in few bulk NTE materials[223]. In these materials, pressure was able to dramatically change the Young's modulus, softening the atomic lattice and changing its phonon spectra. Considering this scenario, it is plausible to assume that the $Gd_5Si_{1.3}Ge_{2.7}$ nanogranules surface stress is inducing a lattice softening, changing the phonon spectra and promoting the Ge3-Gd1-Ge3 transverse vibrations and the consequent NTE behavior. Hence, as suggested by Barrera and co-authors review[187], the higher surface/volume ratio for nanogranules and the fact that the coordination numbers are lower at the surface, generally promotes more open structures enhancing the role of the tension effect and therefore leading to changes in the thermal expansion behavior, as was observed here. Unfortunately, the reports covering the $R_5(Si_xGe_{1-x})_4$ bulk compounds lattice thermal dependence under external pressure fall just below the estimated 8-11 kBar threshold. However, there are signs of pressure induced lattice softening in $Gd_5(Si_2Ge_2)$ single crystals, such as the decrease in amplitude of $\Delta \boldsymbol{a}/\boldsymbol{a}$ across the magnetostructural transition or the reduction of the thermal expansion coefficient of the α_b coefficient[224]. This is a strong motivation to extend the studies to higher external hydrostatic pressures in $R_5(Si_xGe_{1-x})_4$ bulk compounds. Furthermore, thorough Raman spectroscopy and inelastic Neutron Scattering studies (in $R_5(Si_xGe_{1-x})_4$ bulk and nanoscale) would certainly deepen the understanding of the PTE-NTE crossover with scale reduction.

4.6 Conclusions

In conclusion, in this chapter it was presented for the first time a $Gd_5(Si_xGe_{1-x})_4$ thin film which retains the magnetostructural transition as observed in its bulk counterpart. It shows a broad magnetic response than the bulk target, exhibiting a lower $-\Delta Sm^{MAX}$, but a higher FWHM and a large magnetic hysteretic losses reduction. These changes on the magnetic responsive features are conjectured to be associated with the stress distribution on the nanoparticles surface arising from the broader size distribution of nanoparticles. The nanoparticles intrinsic surface stress is thought to cause a unit cell volume decrease and a T_C increase. Therefore a distribution of nanoparticles sizes implies a distribution of unit cell volumes and $T_{C's}$. Additionally the ability to tune the nanoparticles distribution sizes by modifying the deposition conditions will allow a tuning of the magnetic responses. The observed magnetocaloric properties result in a promising refrigerant capacity at the nanoscale. Simultaneously, a giant and anisotropic thermal expansion was also observed across the magnetostructural transition. As ob-

served in bulk compounds the thermal expansion is highly anisotropic: the a-parameter changes $\Delta a/a \sim 1.2\%$ in comparison with the much smaller variation of the other parameters: $\Delta b/b \sim$ -0.03% and $\Delta c/c \sim$ -0.4%. Such anisotropy is in accordance with the interslab adjacent movement expected for the magnetostructural transition and previously observed in the parent bulk compound. Furthermore, an unique giant negative thermal expansion has been observed in $Gd_5Si_{1.3}Ge_{2.7}$ nanogranules in two temperature regions including room temperature 255-340 K, expanding the set of giant effects observed in these materials (magnetocaloric, magnetoresistive and magnetostrictive). The observed NTE emerges as a consequence of the scale reduction and its main atomic mechanism is thought to be the bond flexing of the key Ge3-Gd1-Ge3 triplet chain. Size-induced NTE behaviour had already been observed in several magnetic nanoparticles, however here, unprecedentedly, the NTE behavior is retained even at temperatures higher than the magnetic ordering temperature. Despite the fact that further studies on the bulk and nanoscale are needed to unveil the broader origin of this size induced effect, it is suggested that the nanogranules large surface stress leads to lattice softening and low frequency vibrations that result in an overall contraction behavior which competes with the magnetovolume expansion force below the magnetic ordering temperature. The $Gd_5Si_{1.3}Ge_{2.7}$ 80 nm range nanogranules can be particularly suited to compensate PTE materials when mixed in a composite[225], which has a wide range of technological applications such as Bragg gratings optical fiber coatings[226] or in printed circuit boards[227]. Moreover, these results open a wide range of new possibilities such as, to explore the influence of particle size distributions and film thicknesses on the magnetic and structural coupling, the $\Delta Sm(T)$ curve and the NTE behaviour, exploring the nanostructuring process as a strategy to tune the MCE towards the development of nano/micro refrigerators. Their multifunctionality and giant striction features can help the development of high sensitivity strictive sensors/actuators (due to strain), and bring opportunities for artificial multifunctional materials, such as multilayer deposition with piezoelectric materials.

CHAPTER 5

Thermal treatments and thermal cycling effects on $Gd_5(Si,Ge)_4$ nanogranular thin film

In this chapter, focus will be given to the effects of thermal cycling and ex-situ thermal treatments specially on the magnetic and structural transitions undergone by the nanogranular $Gd_5Si_{1.3}Ge_{2.7}$ thin film. Electronic transport measurements were performed as a function of temperature and thermal cycle, whereas the thermal treatments effects were inspected through structural and magnetic measurements. The information acquired was used as input in the following Chapter.

5.1 Introduction

Thin film properties are typically very sensitive to thickness, substrate type, oxygen content, as well as deposition and annealing parameters etc.[47,120,228]. Simultaneously, for $Gd_5(Si,Ge)_4$ bulk materials, thermal treatments have been reported in the literature as a very important tool for both the minimization of secondary phases and optimization of the crystallographic phases responsible for the GMCE[153,154,229,230]. In particular, it was reported that annealings at temperatures below 700 K lead to an increase of the Orthorhombic I, O(I) phase, hence minimizing the MCE in $Gd_5Si_2Ge_2$ bulk material[229,231]. In opposition, it was found that high annealing temperatures, e.g. at T=1473 K, induce a phase transformation from lower volume, O(I), to higher volume phase, Monoclinic, M, promoting an increase in the MCE as reported by us in reference[154]. However, for thin films, i.e. when the dimensions of a material are reduced, their phase diagram suffers drastic changes due to the different diffusion processes. In particular, the phase stabilization temperatures tend to be significantly smaller, meaning that less energy is necessary to activate atomic diffusion at the micro/nanoscale. Therefore, in order to unveil the effects of annealing in the still unexplored $Gd_5Si_{1.3}Ge_{2.7}$ thin film, we studied the influence of annealing temperatures on the formation/suppresion of the different crystallographic phases and their influence on morphology, structure and magnetic properties.

Many other physical questions concerning the $Gd_5Si_{1.3}Ge_{2.7}$ thin film remain to be answered, namely on its intriguing martensitic magnetostructural transition, its dynamic

behavior and its thermal stability. As referred in chapter 2, since the discovery of the GMCE[4], other families of compounds exhibiting GMCE were discovered such as, MnFeP(As,Ge)[232], $La(FeSi)_{13}$[72] and their hydrides[233] and the Heusler alloys, as NiMnSn[234], all sharing a common feature with the $Gd_5(Si_xGe_{1-x})_4$, the strong coupling between lattice and spin degrees of freedom. In fact the Heusler alloys, also undergo a martensitic-like magnetostructural transition[234], whose study is critical for a wide range of technologies. Therefore, the importance of having a deeper knowledge of all martensitic-like transitions features is transversal to the general materials scientists and more particularly to the magnetic sensors/actuators community. In the last 10 – 20 years a huge and successful effort has been applied in the thorough characterization and understanding of these materials properties in a lab environment in static or quasi static conditions. However, far less attention was given to dynamical studies including large number of cycles behavior (mimicking a real-life device), which are crucially important for technological applications, magnetic refrigeration and others, and also unveil very interesting and complex physical mechanisms. Such studies are even more important since these materials strong spin-lattice coupling imply huge structural changes. In particular, Skokov and co-workers found a decrease of hysteresis under magnetic field-cycling, along with an undesired decrease of the adiabatic temperature change ΔT_{ad} on a polycrystalline $La(Fe,Si)_{13}$ sample[235]. Interestingly, Waske and co-workers have observed another phenomena: the phase arrest after the first cycle on a virgin $La(Fe,Si)_{13}$ sample[236]. They have also remarked the different and asymmetric behavior under cooling and heating, recalling the importance of such features on the performance of a magnetocaloric material (MC) in a real-life device. On the $R_5(Si,Ge)_4$ materials, Sousa and co-workers, have performed detailed electrical resistance measurements under thermal cycling on a bulk $Gd_5Si_{0.4}Ge_{3.6}$ compound, concluding that the martensitic-like transition evolves here through a sequence of discontinuous steps or avalanches, which tend to diminish as the system undergoes more thermal cycles. Hence, in each cycle there is a decrease of the detrimental thermal and magnetic hysteresis associated with the transition[237], adding a contribution to a cumulative ”learning” process. Perez-Reche and co-workers detected the acoustic emission across the magnetostructural transition of a $Gd_5Si_2Ge_2$ sample, confirming its burst-like character and evidencing the differences between heating (athermal) and cooling cycles[238]. These examples unveil the importance of the dynamical regime and the need for a more thorough study of its physical phenomena, namely: phase arrest, asymmetry between the transitions directions, nature of transition kinetics,... Although a variety of useful techniques have been applied in these studies, here we highlight the electrical transport measurements because its short range nature associated with the electron mean free path (nanometer scale), which is the most suitable key to access detailed information on the mechanisms ruling these transitions at the micro and nanoscale[239–241]. So far, only reports devoted to bulk compounds were mentioned, however an increasing research task force is being dedicated to study these materials at the micro and nano

dimensions. A relevant example is the recent work by Uhlir and co-workers devoted to mesostructures (micron-sized stripes) of FeRh that unveiled a strong thermal asymmetry and an avalanche-like nature in the FeRh magnetostructural transition[62]. Recently we reported a systematic study focused on thermal cycling effects on the long-range order magnetic and structural properties of this same $Gd_5Si_{1.3}Ge_{2.7}$ granular thin film, using extreme cycling tests. There, we have observed a complete loss of the majority O(II) phase after 1000 cycles, which is the phase that undergoes the magnetostructural transition. Consequently, a linear decrease of the ΔS_{max} as a function of the number of thermal cycles, was observed. Such O(II) phase suppression was attributed to chemical disorder induced by the internal strain and stress during the thermal cycles, promoting the loss of crystallinity, concomitant with a decrease of the magnetization and the magnetic entropy change. In the present chapter we were particularly interested in gather information to answer to the following questions: what are the differences between a magnetostructural and a purely magnetic transition evolution? Are there precursor effects or any major asymmetries ? is there microcrack formation ? Besides this, there are implicit consequences of materials miniaturization, such as the smaller grain size and the enhanced role played by chemical/structural disorder/inhomogeneity, which can change relevant length scales by tens/hundreds of nanometers. Several characterization techniques that are traditionally adapted to study bulk (magnetocaloric) materials, such as Differential Scanning Calorimeters or conventional X-ray diffraction, cannot probe such small scales[39]. Therefore to tackle the above questions, electrical transport measurements in a wide temperature range 100-300 K and for several thermal cycles (1-18 cycles) were performed. Since resistance critically depends on the electron mean path, which in turn depends on the grain size and disorder level, it is a very sensitive technique to detect any small change in the dynamics occurring from one cycle to the next, and even from one temperature value to the next (30 mK steps). This high resolution sensitivity can be further enhanced, to around two orders of magnitude, through local numerical extraction of the electrical resistivity data derivative, $(\partial\rho/\partial T)$. This quantity is particularly sensitive to small structural changes[237] and also to transition precursor effects.

5.2 Experimental details

The preparation details of $Gd_5Si_{1.3}Ge_{2.7}$ thin films were given before in chapter 3. In order to study the effects of different annealing temperatures, the samples were wrapped in a tantalum sheet, placed into a crucible, and introduced in a quartz tube with a Zirconium getter to help to prevent oxidation. Four different annealing temperatures were chosen for the present study: 573, 673, 773, and 873 K, with a fixed annealing time of 2 hours under vacuum (below $\sim 10^{-5}$ mbar). The samples were fast cooled by immersing the sealed quartz tube in water, in order to quench the crystal structure. The morpholog-

ical and structural characterization of the thin films was ensured by Scanning Electron Microscopy (SEM) and grazing incidence X-ray Diffraction (XRD). The magnetic measurements were performed in a commercial (MPMS Quantum Design) Superconducting Quantum Interference Device (SQUID) magnetometer. The magnetic entropy change [$-\Delta S_{max}m(T)$] was estimated from the measured magnetic isotherms, M(H), at different temperatures, following the loop method[184]. The electrical resistivity was measured with the standard four-point potentiometric method using a DC current of 2 mA, stable to $1{:}10^6$. The four electrical contacts were established by Gold sputtering four points evenly spaced along a straight line and Silver paint to bond them together with Copper wires on top of a ~ 3 x 6 mm piece cut from the larger deposited thin film, as illustrated in Chapter 2. The voltage was measured with a Keithley 182 nanovoltmeter with a resolution of 10 nV during the measurements. The thin film was glued with GE varnish to a Copper support and its electrical resistance (R) was measured uninterruptedly along 18 thermal cycles (cooling and heating) in the 100-300 K temperature range with a 0.5 K min^{-1} rate. Afterwards, the same sample was removed from this setup and its magnetization was measured again in SQUID magnetometer.

5.2.1 Training cycling across the magnetostructural transition through electrical resistivity measurements ρ(T)

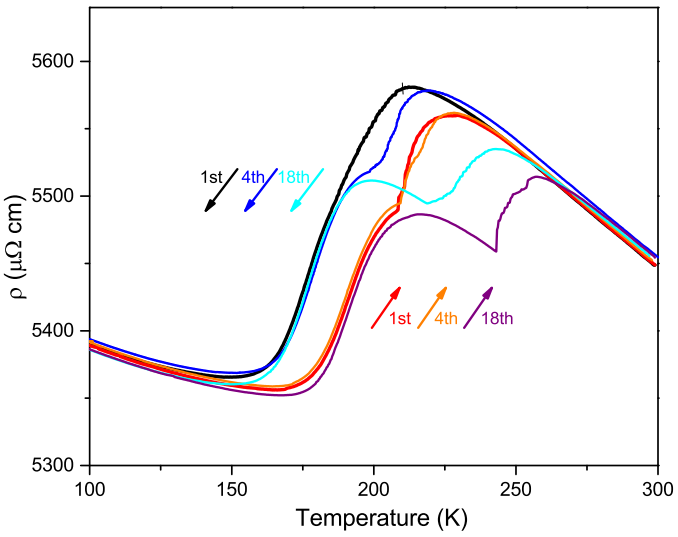

Figure 5.1 – $Gd_5Si_{1.3}Ge_{2.7}$ thin film electrical resistivity as a function of temperature in the 100-300 K temperature range for the 1st, 4th and 18th cooling and heating runs.

Since the electrical resistivity is sensitive to long-range (electron bands, major structural changes) and to short-range effects (electron scattering within nanometer mean free paths) it will unveil important information regarding the thermal dependence at both

scales. Simultaneously, it is a key property to reveal and disentangle such processes, in particular during heating and cooling runs and along successive thermal cycles. Hence, the electrical resistivity (ρ) of the as-deposited $Gd_5Si_{1.3}Ge_{2.7}$ thin film was measured along 18 uninterrupted thermal cycles (cooling/heating) in the 100-300 K temperature range with a 0.5 K min^{-1} rate. Such temperature range was chosen as it comprises the magnetostructural (FOPT) and the purely magnetic (SOPT) transitions, as well as their bounding ρ(T)-regimes just outside. Figure 5.1 displays the results obtained in the 1st, 4th and 18th thermal cycles. One sees that the six ρ(T) curves (3 cooling/heating pairs) overlap almost completely from 100 to 150 K, and above 275 K, both within and between thermal cycles. The formation of permanent chemical or short-range disorder, as well as micro-cracks (under thermal cycling), is thus negligible in our nanogranular film. Within the transition(s) 150-275 K interval, there is a considerable thermal hysteresis in ρ(T) heating and cooling curves and also sudden ρ(T)-discontinuities (burst-like processes that will be detailed below). (i) Under heating, the intrinsically hysteretic (FOPT) magnetostructural transition develops smoothly, starting at $\sim$ 160 K and reaching a maximum rate of change at $T_h^{'} = T_h^{ms} \sim$ 191 K for the 1st heating run; The $T^{'}$ remains unaltered in the 18th cycle. The magnetostructural transition has no ρ-discontinuities and retains the same ρ(T) shape under thermal cycling. In contrast, the (SOPT) purely magnetic transition always starts with a sharp ρ-step, observed at $T^{''} \sim$ 210 K in the first heating run. This value shifts considerably to higher temperatures in successive thermal cycles (e.g. $T^{''} \sim$ 244 K in the 18th heating cycle), and some fine details of the transition evolve as well. (ii) Under cooling, the magnetic transition starts smoothly over $\sim$ 13 K below the heating curve and then develops in a dense succession of small ρ-irregularities (see in Figure 5.1) which ends at the onset of the magnetostructural transition. There, it evolves to a smoother decreasing behavior whose maximum rate of change is achieved at $T_h^{'} = T_h^{ms} \sim$ 177 K. A thorough characterization of such details is presented below. The magnitude of absolute ρ values in our film ($\sim$ 5400 $\mu\Omega$.cm) is very large compared with the commonly reported values for the $R_5(Si_xGe_{1-x})_4$ compounds , $\rho\sim$ 500-1000 $\mu\Omega$.cm in the 100-300 K range[242–244]. The high residual resistivity (ρ_r) is insensitive to thermal cycling contrasting with the bulk counterpart cases, where chemical disorder and the formation of microcracks/pontual defects significantly increases ρ_r from one cycle to the next[237,245]. Hence its invariability implies a large inter-grain cohesion, as well as high chemical and local structure (short-range) stability. Moreover its low-T and high-T negative ρ(T) thermal dependence also contrast with the typically positive thermal dependence observed in the bulk counterparts and entails a semiconducting like behavior for this thin film. The origin of this negative slope is intrinsically related with the negative thermal expansion behavior reported in the chapter 4, as will be detailed below. One can approximate the residual resistance by $\rho_r(T) = \rho_0 + \alpha.T$ in the upper temperature range, above $T^{'''}$, where ρ_0=5978 $\mu\Omega$.cm, α= - 1.768254 $\mu\Omega$.cm K^{-1}. By subtracting ρ_r(T) linear term from the total resistivity ρ(T) measured in the 18th thermal cycle one obtains $\rho^{'}(T) = \rho(T) - \rho_r(T)$ for heating and cooling, as displayed in Figure 5.2. The $\rho^{'}$(T)

curves resemble the typical ρ(T) behaviour presented by the $R_5(Si_xGe_{1-x})_4$ compounds and nicely disentangle both transitions and their thermal hysteresis. Furthermore it also allows to weight the role of each transition on the overall resistivity change as represented in Figure 5.2. One notes that the magnetostructural transition is responsible for $\Delta\rho'_{MS}$ ~ 63% resistivity variation whereas the magnetic one is responsible for $\Delta\rho'_{M}$ ~ 37% of the total resistivity variation across the two transitions, $\Delta\rho'_{T}$. Such resistivity changes fractions are in complete accordance with the phase contents, O(II) (65%) and O(I) (35%), obtained by Synchrotron XRD and detailed in Chapter 4.

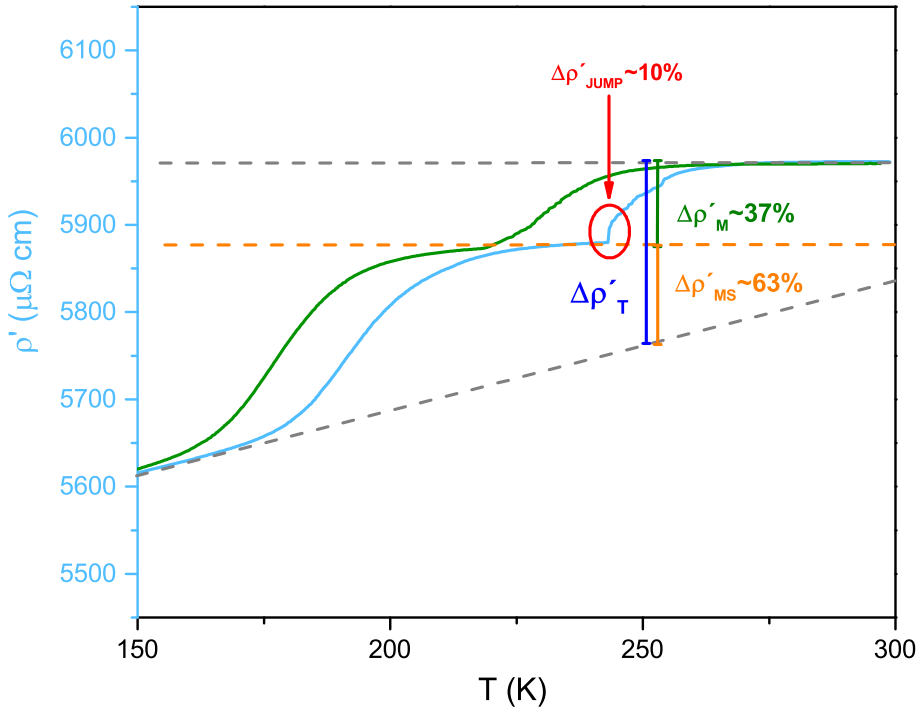

Figure 5.2 – The 18th cycle heating and cooling ρ'(T) curves, obtained by subtracting the high-temperature negative slope of ρ(T). The estimated overall $\Delta\rho'_{T}$ at T =250 K is decomposed in two parts $\Delta\rho'_{MS}$ and $\Delta\rho'_{M}$. A ρ_r(T) discontinuity is also highlighted in red and held responsible for a 10% portion of the overall variation.

5.2.2 Temperature dependence of $\partial\rho/\partial$T

A better insight into the above features, enabling the disentanglement of finer details of the magnetostructural and magnetic transitions when they partially overlap, is given by local $\partial\rho/\partial$T(T) curves.

5.2.2.1 Heating runs

Figure 5.3 displays $\partial\rho/\partial T$ curves for two heating runs, the 3rd (partially overlapped transitions) and 18th (separated transitions). The magnetostructural transition produces a smooth and positive Lorentzian-type $\partial\rho/\partial T$ curve, with its peak at $T_h' = T_h^{ms} \sim 191$ K and the same curve shape and magnitude for both runs. Thus, the lattice and the magnetic

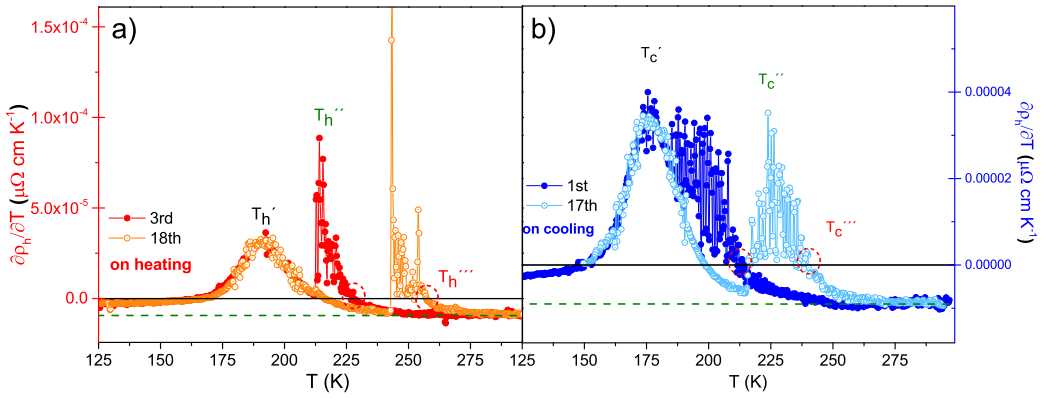

Figure 5.3 – Resistivity temperature derivative, $\partial\rho/\partial T$, in the 125-300 K interval for the 3rd and 18th heating runs, a), and 1st and 17th cooling runs, b). T' signals the temperatures at which $\partial\rho/\partial T$ is maximum across the magnetostructural transition, i.e. in the 150-210 K interval. T'' and T''' signal the first spike and the crossover of $\partial\rho/\partial T$ back to negative values, respectively. They represent the onset and the end of the magnetic transition.

structures must have the same physical characteristics around T_h^{ms} for all heating runs. In contrast, the magnetic transition starts with a very sharp positive spike in $\partial\rho/\partial T$ at T_h'', equivalent to a ρ-discontinuity. Since it is observable at the macroscopic level, this is a demonstration of an avalanche-type process that affects the electronic conduction in the film (or particular regions of it; see below). The $\partial\rho/\partial T$ curve then follows a relaxation-like regime (see Figure 5.9) with a few smaller spikes, which evolve and smoothly fade away. Considering T'' as the abrupt onset of the magnetic transition, under the adopted thermal cycling conditions (see Discussion), one sees that it is considerably shifted to higher temperatures under cycling: T''=213 K in the 3rd and 246 K in the 18th heating run, as seen in Figure 5.4 b). A more complete set of $\partial\rho/\partial T$ heating curves (3,5,7,15 and 18th) is in Figure 5.4 a), confirming the described characteristics.

5.2.2.2 Cooling runs

Figure 5.3 b) display two $\partial\rho/\partial T$ curves obtained under cooling (1st and 17th runs) with the same time rate as for the heating runs (0.5 K min^{-1}). In general terms, the curves resemble those obtained under heating. In particular, at temperatures sufficiently above T_c' they have the same negative resistivity coefficient, $\partial\rho/\partial T$ = -8.6x10^{-4} $\mu\Omega$.cm K^{-1}. With subsequent cooling, $\partial\rho/\partial T$ smoothly rises, through a relaxation-type regime as observed in heating curves, but now described in the opposite sense. As the sample

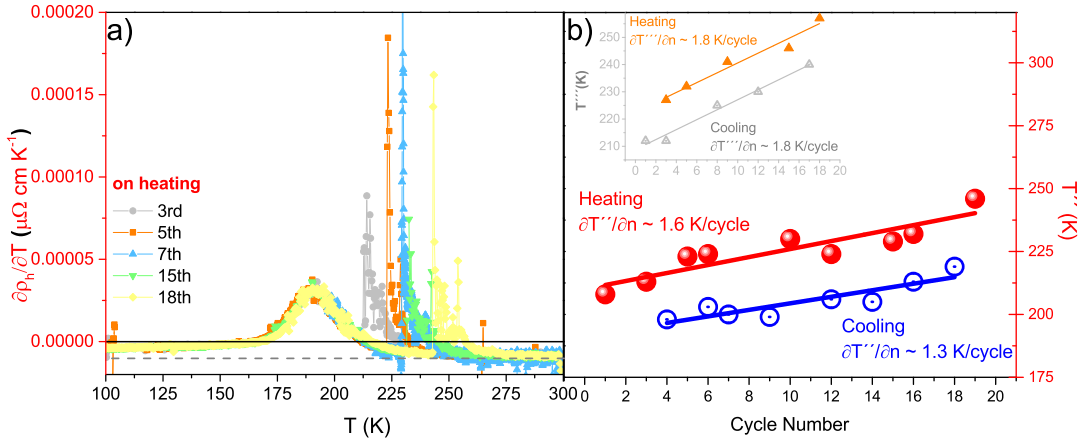

Figure 5.4 – Resistivity temperature derivative, $\partial\rho/\partial T$, in the 125-300 K interval for the 3rd, 5th, 7th, 15th and 18th heating runs, a). b) Evolution of T_c'' and T_h'' on the number of cooling and heating runs, respectively. Linear extrapolation estimation gives a 1.3 K/cycle and 1.6 K/cycle, respectively. In figure b) inset the same linear behavior, with a 1.8 K/cycle slope, is observed for cooling and heating of T''' against the number of runs.

enters the central part of its magnetic transition, a succession of wiggly spikes of similar magnitude develops on top of an average Lorentzian-like $\partial\rho/\partial T$ bump (Figure 5.3 b)). In the 1st run, despite the spiking blur effect overlapping with the forthcoming magnetostructural transition, a rough estimation of the its onset is made possible: $T_c'' \sim 190$ K. For the 17th run (well separated transitions) one has $T_c'' \sim 219$ K and a well developed Lorentzian-type $\partial\rho/\partial T$ anomaly associated to the magnetostructural transition, with $T_c' \sim 175$ K in all cooling runs. Figure 5.4 b) shows the linear rise of T'' on heating and cooling versus the corresponding cycle number (n). Regarding T', it keeps the same value for each type of run : $T_c' \sim 175$ K under cooling and ~ 191 K for heating.

5.2.3 Magnetization temperature dependence before and after cycling

The thin film magnetization temperature dependence was measured before and after the resistivity cycles, while heating and cooling under a magnetic field $\mu_0 H = 0.1$ T. As can be seen in Figure 5.5, there is a general magnetization decrease after the resistivity cycles. Before and after resistivity cycling curves follow the same path down to around 275K, where they split, with the magnetization after cycles (m_{af}) lying below the curve before cycles (m_{be}). Their splitting difference increases slightly across the magnetic transition. The major changes are observed along the (FOPT) magnetostructural transition, where the splitting increases significantly setting the (m_{af}) at about half of the (m_{be}) value at T = 100 K. During the magnetostructural transition there is a clear decrease of the thermal hysteresis presented by the both pairs of heating and cooling curves. As is clear from the temperature derivatives curves, $\partial m/\partial T(T)$ no significant change is observed in the transitions (magnetostructural and magnetic) temperatures (defined as the temperatures for which $\partial m/\partial T(T)$ reaches a local minima). The (SOPT)

magnetic transition is only slightly affected by resistivity cycles as can be confirmed by comparison with the two pairs of $\partial m/\partial T(T)$ curves presented in Figure 5.5 b), becoming slightly narrower and less intense. A more drastic change is observed in the shape and intensity of the $\partial m/\partial T(T)$ across the magnetostructural with a large maxima decrease. In fact, after cycling the higher magnetization temperature derivative occurs along the magnetic transition, in clear-cut contrast with the measurements before cycling.

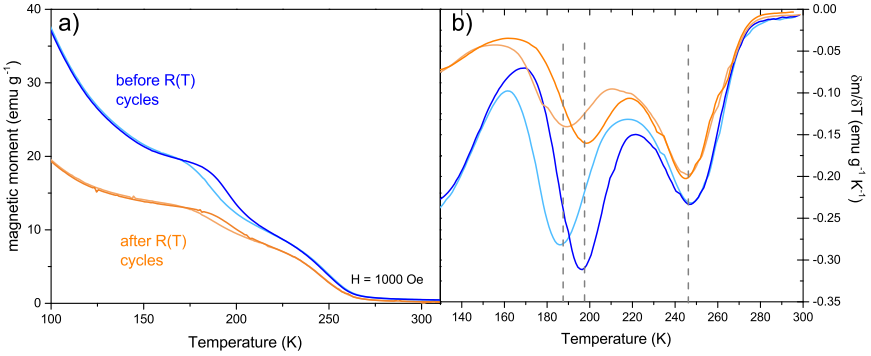

Figure 5.5 – a) Magnetization as a function of temperature while heating and cooling, before (upper blueish curves) and after (below and orange curves) the resistivity cycles under an applied magnetic field of μ_0H=0.1 T. Magnetization temperature derivative as a function of temperature, $\partial m/\partial T$ of curves represented in b).

5.3 Effect of thermal annealings on structural and magnetic properties on nanogranular films

A different piece of the as-deposited $Gd_5Si_{1.3}Ge_{2.7}$ thin film was cut and subjected to different thermal annealings as explained in the Experimental Details section. Morphological, structural and magnetic characterization of the annealed films was performed. Figure 5.6 a) shows the temperature dependence of magnetization for the $Gd_5Si_{1.3}Ge_{2.7}$ as-deposited film with no annealing performed - same curve that was displayed in Chapter 4. As mentioned previously, on heating, it is observed that a first-order phase transition (FOPT) occurs from an Orthorhombic O(I) ferromagnetic to an Orthorhombic O(II) paramagnetic phase at T ~ 194 K. However, this transition is incomplete and approximately 33% of the O(I) phase does not transform into O(II), meaning that at T ~ 230 K the film consists of: two thirds [O(II), PM] and one third [O(I), FM] phase, as described earlier. At T~247 K, a purely magnetic second-order phase transition (SOPT) of the remaining [O(I), FM] phase occurs, changing its magnetic state from the FM to PM state. The effect of the annealing procedure, in magnetization, is shown in Figure 5.6 b). In fact, upon annealing at 573 and 673 K, the thin films only present the SOPT at 249 K, whereas the FOPT is no longer seen at 194 K.

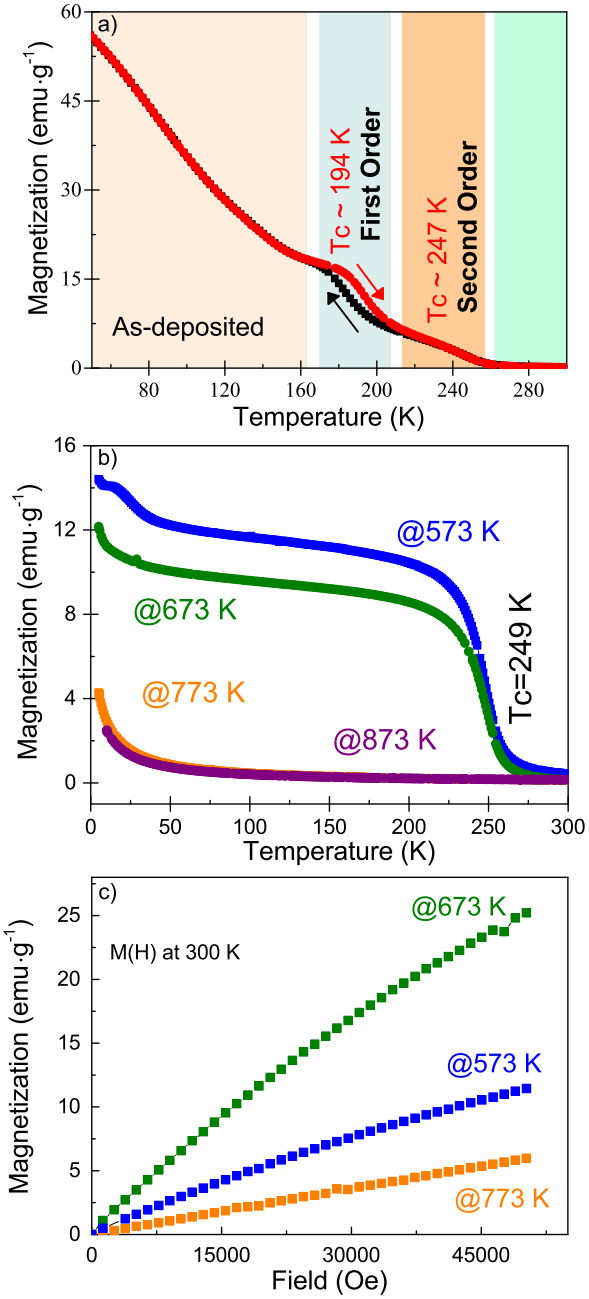

Figure 5.6 – The temperature dependence of the magnetization for the as-deposited ,a), film and for the samples annealed at: 573, 673, 773 and 873 K b) measured at μ_0H=0.1 T; and c) Magnetization as a function of the magnetic field for the same annealing temperatures, measured at 300 K.

If the annealing temperature is further increased, i.e., above 773 K (Figure 5.6 b), the two magnetic transitions become suppressed, and the film exhibits a pure paramagnetic behavior. Figure 5.6 c) presents the M(H) curves measured at 300 K for films annealed at different temperatures, showing that the magnetic moment is higher in the sample annealed at lower temperature, 673 K.

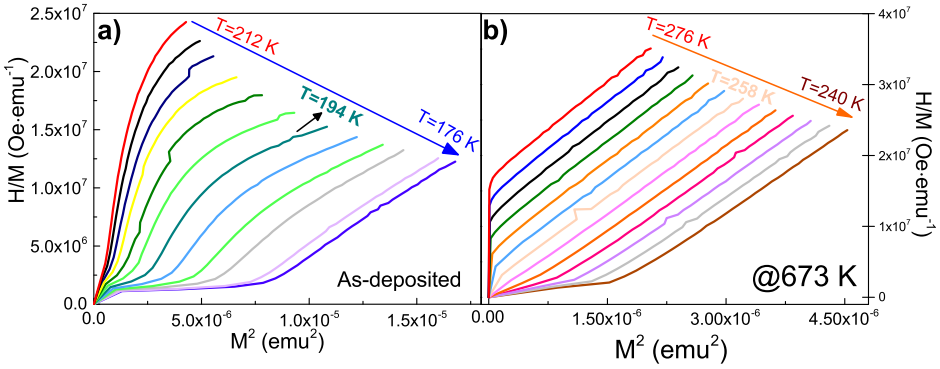

Figure 5.7 – Arrott plots, H/M as a function of M^2 for a) $Gd_5Si_{1.3}Ge_{2.7}$ as-deposited film measured in the 176-212 K temperature range and b) film annealed at 673 K measured in the 240-276 K temperature range.

For the assessment of the nature of the thin films phase transitions and in order to confirm the suppression of the Magnetostructural Transition, MST-FOPT, Arrott plots of the as-deposited and the annealed at 673K films were constructed and represented in Figure 5.7 a) and b), respectively. For the as-deposited the H/M vs M^2 exhibits a different behavior, resembling an "*S*" shape, as M^2 increases. Such behavior is the signature of a first-order phase transition [76,246] at $T_C \sim 194$ K. On the contrary, the H/M vs M^2 curves of the film annealed at 673 K show a monotonous positive slope, confirming the second-order nature of the magnetic transition at ~ 247 K in the annealed film. Such analysis clearly distinguish the two transitions and allows to confirm their association with the two crystallographic phases present in the film at room temperature.

Therefore, these results suggest that the annealing induces a suppression of the O(II) phase, since its lower temperature FOPT was no longer detected in the magnetic characterization. In order to corroborate this hypothesis, X-ray diffraction measurements were performed for all films. These are shown in Figure 5.8 a). The as-deposited sample presents peaks corresponding to both the O(I) and the O(II) phase . After the thermal treatments, there is evidence for the decrease and vanishing of the peaks corresponding to the O(II) phase, such as: (0 4 0) - 24.1 °, (2 1 1) - 26.5 ° and (1 6 4) - 61.8 ° [247]. Concomitantly, there is an increase in the number of peaks corresponding to the O(I) phase, such as reflections: (2 2 1) - 29.1 °, (1 3 2) - 31.7 ° and (1 4 3) - 44.5 ° [248]. These results confirm the suppression of the FOPT observed in Figure 5.6 b), as a direct consequence of the decrease of O(II) phase. The 33.2 ° and 47.4 ° peaks appear only after the thermal treatments and there is no correspondence to the O(I)/O(II) phases. Indeed, these peaks must correspond to the Gd_2O_3 phase [249], which may have formed because of the higher reactivity between Gd and O. This phase is observed just in low amounts due to the presence of Tantalum and Zirconium getters during the annealing process. Many examples of phase transformations induced by annealing process on bulk $Gd_5Si_2Ge_2$ alloys can be found in the literature [153,154]. In these, several phenomena are responsible for the phase transformation such as, diffusion of Si which may

favor the O(I) phase[250] and stress release by the heating process[229].

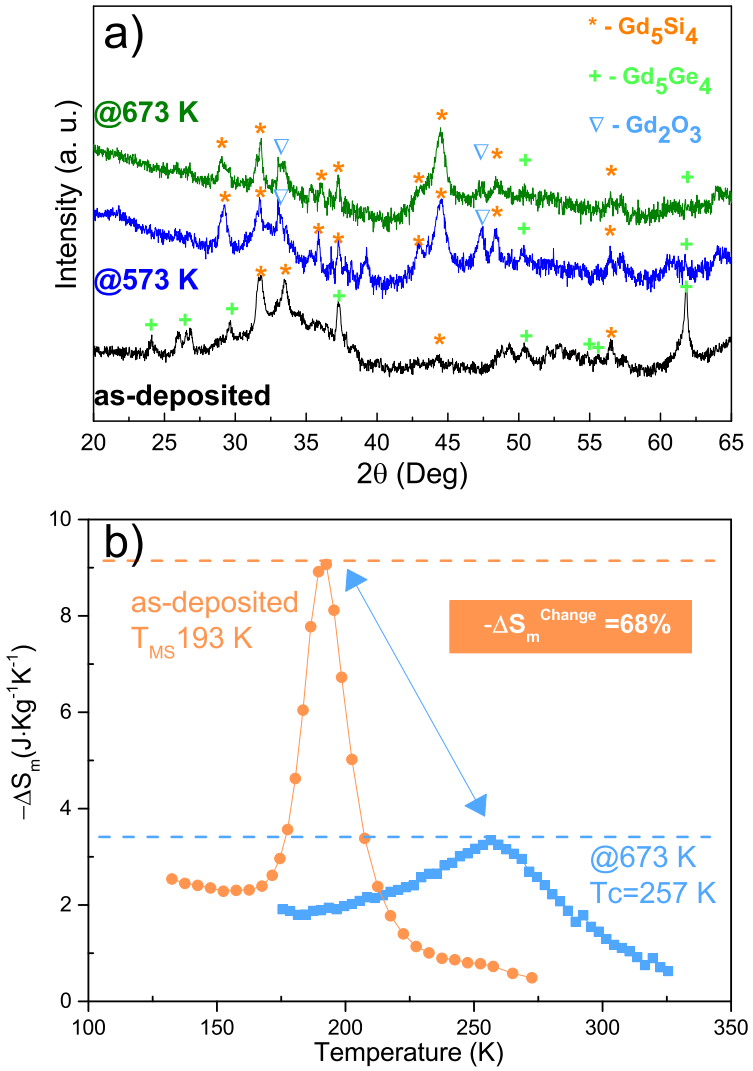

Figure 5.8 – a) XRD pattern of the as-deposited film and films annealed at 573 and 673 K. The peaks are marked with symbols corresponding to different crystallographic phases; b) Temperature dependence of the -ΔSm of the as-deposited film and the film annealed at 673 K under an applied magnetic field change of 5 T.

Figure 5.8 b) shows the -ΔSm of the as-deposited and annealed (at 673 K) films. The maximum magnetic entropy change, $-\Delta Sm^{MAX}$, is 9 J K^{-1} Kg^{-1} at around 193 K for the as-deposited film. After annealing there is a ~ 68% decrease of the $-\Delta Sm^{MAX}$ value, to 3.5 J K^{-1} Kg^{-1} which now occurs at T ~ 257 K. This decrease results from the suppression of the [O(II), PM] → [O(I), FM] MST that occurs in the as-deposited film at T ~ 193 K. Moreover, the temperature at which -ΔSm is maximum was found to increase by ~ 25%, i. e., from 193 to 257 K, towards room temperature. As detailed before,

materials presenting coupled magnetic and structural transitions exhibit a much higher MCE because of their extremely large $\partial M/\partial T$ value at the transition (which is a critical parameter for the enhancement of the magnetic entropy change) and the extra entropy change associated with the lattice transformation, $-\Delta S_{lattice}$ [77,115]. Therefore, the reduction of the $-\Delta Sm^{MAX}$ value with annealing temperature was expected since the MST was suppressed. Previously, in $Gd_5Si_2Ge_2$ bulk material, Pecharsky and co-workers found a $-\Delta Sm$ decrease and a T_C increase in samples annealed at 670 and 870 K and attributed such reduction to the enhancement of the O(I) phase with the annealing treatments[153]. Furthermore, the Full Width at Half Maximum (FWHM) was estimated from the $-\Delta Sm$ curves and an increase with the annealing process was observed, from ΔT_{FWHM} = 23 to 49 K. This larger FWHM is a signature of a SOPT. In this thin film it might also be associated with strain disorder[201], as each different nanoparticle size implies a different intrinsic stress and strain. Hence the Lorentzian distribution of these nanoparticle sizes entail a similar distribution of stress/strain along the film which manifests both in the magnetic and structural properties of the film. From the magnetic point of view it leads to a broadening of the transition (and the mentioned enhancement of the FWHM), as explained in Chapter 4, and also to the broadening of the x-ray diffraction peaks. The refrigerant capacity value (RCP = ΔSm^{MAX} x FWHM) was estimated to be $\sim$ 203 J kg^{-1} and $\sim$ 160 J kg^{-1} for the as deposited and 673 K annealed film, respectively, with a $\Delta\mu_0 H$=5 T field variation. Hence, despite the large 68% decrease on the $-\Delta Sm^{MAX}$, the thermal treated film shows only a small decrease on its RCP (21%) because of its larger FWHM. This means that there is an expansion on the interval of operational temperatures for potential magnetic refrigerator/sensor. Additionally, the T_C tuning achieved with annealing proves that this procedure is a good strategy to enhance these thin films operational temperature towards room temperature. The effect of heat treatments on the phase conversion and consequently on the magnetocaloric properties of some thin films have been recently reported in the literature. For example, in the case of a pure Gd thin film, it was shown that higher temperatures treatments (under pre-gettering conditions) enhance the cubic phases of Gd, which is one of the causes for the higher transition temperature, larger MCE and larger FWHM[120]. Similarly, in the case of NiMnGa and $La_{0.8}Ca_{0.2}MnO_3$ thin films, the in-situ or post deposition thermal treatments play a crucial role on their phase stabilization (martensitic and monoclinic phases, respectively) and hence consequently favoring their magnetocaloric properties[251,252].

5.4 Analysis and Discussion

As a preliminary analysis, an overall comparison between these results and the ones obtained for bulk compounds can be made. To our knowledge, there are no reports on transport measurements of the bulk $Gd_5Si_{1.3}Ge_{2.7}$ compound, however a rough comparison can be made with Ge-rich $Gd_5Si_xGe_{1-x}$ compounds. For instance, in the

$Gd_5Si_{0.4}Ge_{3.6}$ bulk compound[253], a similar overall high resistivity behavior was found for T > 50 K - with a high resistivity (HR) state at higher temperatures and a low resistivity (LR) state at low temperatures. In fact, as reviewed by Mudryk and co-workers[82], such resistivity evolution across a first-order transition is similar in all studied $R_5Si_xGe_{1-x}$ compounds. Also the thermal hysteresis across their first order transitions is commonly observed in bulk electrical resistivity studies, which is due to the large magnetovolume coupling present in these materials. Despite these common features there is a striking difference to the bulk ρ(T) curves: the negative ρ(T) slope here shown both at the LR and HR state, typical of a semiconductor temperature activated electrical transport regime. In the parent compounds the overall behavior is metallic-like, with the electrical resistance increasing with increasing temperature. This size-induced change in the resistivity thermal dependence (positive at bulk to negative values at nanoscale) is a direct consequence of the change in the behavior of the volume thermal expansion. As detailed in chapter 4, at the nanoscale the volume thermal behavior assumes an unique negative thermal expansion behavior that contrasts with the conventional positive thermal expansion observed in the bulk counterparts. The influence of the thermal expansion behavior on these electrical resistivity curves becomes even more explicit when the ρ(T) slopes ratio between the HR and the LR states, $(\partial\rho/\partial T_{HR}) / (\partial\rho/\partial T_{LR}) \sim 2.1$ is compared with the volume V(T) slopes ratio, $(\partial V/\partial T_{HR}) / (\partial V/\partial T_{LR}) \sim 2.2$. Such correspondence can easily be explained through the simple relationship between spatial dimension and the electrical resistance: $R = \rho\, L/A$, where A is the cross section area that the electrons cross and L the distance between electrical contacts in the sample. When plotting ρ curves, both L and A are assumed as constants throughout the whole temperature range. However, since the nanoparticles present a polycrystalline nature and the volume thermal expansion is rather isotropic, it is correct to assume that L will vary linearly with volume and therefore the R(T) slopes ratio can indeed be roughly explained via the volumes slopes, V(T), ratio. However, a closer look at the LR low-temperature state shows that ρ(T) does not have a linear temperature dependency, but instead a quadratic one as can be confirmed by the small but positive linear temperature dependency of $\partial\rho/\partial T$ in these temperature range (Figures 5.3 and 5.4). Hence $\partial\rho/\partial T = \partial\rho/\partial T(100\ K) + BT$. Since $\partial\rho/\partial T$ (100 K) is very small and a similar behavior has been observed in these materials bulk counterparts[254] it is correct to approximate $\partial\rho/\partial T = BT$ and consequently $\rho(T) = BT^2+C$. Such a quadratic temperature dependency can be associated with the electron scattering on spin waves (electron-magnon scattering) as was also found on their bulk counterpart[254]. In fact this hypothesis is reinforced by the constant and temperature-independent $\partial\rho/\partial T$ value observed in the HR state, $\sim -8.6\times10^{-4}\ \mu\Omega.cm\ K^{-1}\ \Omega\ K^{-1}$. Here the paramagnetic state is stable and consequently no electron-magnon scattering can occur and the typical electron-phonon interaction dominates, explaining the linear electrical resistance behavior, $\rho(T) = CT$, observed.

The general evolution from a high resistivity (HR) state at higher temperatures towards a low resistivity (LR) state at low temperatures can be attributed to several mech-

anisms and here just two of them will be highlighted: **(i)** the decrease of conduction electrons with the increase of unit cell volume and **(ii)** the increase in the electron-phonon scattering above the transition temperature. The former one was firstly explained by Choe and coworkers when they showed, using the Zintl-Klemn formalism, that the isolated Si,Ge atoms and their dimers (Si)Ge-Ge(Si) have different formal charges associated, namely -4 and -6 (3 electrons per atom), respectively, i.e. dimmers need less electrons then two unbounded Si,Ge atoms (two electrons less)[255]. Hence, in a unit cell, the number of free electrons increases linearly with the number of (Si)Ge-Ge(Si) dimers formed. A basic calculation shows that this means that there are 3 or 1 electron per unit cell assigned to the conduction band for the O(I) or O(II) structure, respectively. Its effect on the resistance behavior had already been pointed out by Sousa and co-workers and Hall measurements consistent with this scenario were performed by J. Stankiewicz and co-workers[256]. The later effect **(ii)**, proposed by Levin and coworkers, simply argues that, since the higher temperature structures are more loosely bonded and hence more disordered, it means that their electron-phonon scattering will be higher[242]. In comparison with the bulk behavior, the overall resistivity change from the LR to the HR state, $\Delta\rho_T \sim 4\%$ is lower than the ~ 20 and 66% observed in the $Gd_5Si_{1.7}Ge_{2.3}$[257] and $Gd_5Si_{0.4}Ge_{3.6}$ bulk compounds[253]. This smoothing is also noticeable in the temperature window width where the transition occurs (hysteresis area), as it is much larger ($\sim$ 100 K) than the bulk counterparts (typically $\sim$ 40K). Such broadening, also displayed in the magnetic response properties (M(T) and M(H) curves), as already explained, can be attributed to strain disorder - a distribution of volumes implies a distribution of nanoparticles intrinsic strain.

The two-step nature of the resistivity evolution can be explained by attributing each step to a specific magnetic transition: low temperature step to the magnetostructural transition and high temperature one to the purely magnetic one. Such correspondence can be made because: 1) the steps and magnetic transitions are coincidental, i.e. occur at the same temperature and 2) as detailed in Figure 5.2, $\Delta\rho'_{MS}$ and $\Delta\rho'_{M}$ are accountable for 63% and 37% of the overall resistivity change, $\Delta\rho_T$, corroborate very well with the 65% and 35% phase fractions estimated through the Synchrotron X-ray diffraction data analysis detailed in chapter 4. Considering the $\partial\rho/\partial$T bursts, they had already been observed in electrical resistance, calorimetric and magnetization measurements of Ge-rich $Gd_5(Si_xGe_{1-x})_4$ and $Gd_5(Si_2Ge_2)$ bulk compounds[237,258,259] and as remarked by the corresponding authors, reveal that the mentioned transition occurs in an avalanche mode. In particular as illustrated by Bessa and coworkers[237] this means that the system evolves through a series of discontinuous steps or avalanches of the order parameter with an associated energy loss and consequent thermal hysteresis, as observed here. Moreover it is important to highlight the asymmetry between the more smoothen and the more abrupt avalanche natures during cooling and heating runs, respectively. Such asymmetry is well known in martensitic transformations, where the avalanches are more intense in the reverse martensitic transitions (heating) than in the

forward (cooling) direction[260,261]. In the $Gd_5Si_2Ge_2$ bulk material[262] the observed asymmetry was inverse, i.e. higher avalanches for cooling than for heating. This is explained by the inverted symmetry relations between the high and low temperature phases for this specific composition. Similarly, the $La(FeSi)_{13}$ bulk material exhibits a similar evolution[263]. Although in the case, the $Gd_5Si_{1.3}Ge_{2.7}$ avalanche-like behavior appears to be associated with the purely magnetic order transition, it is important to remark the strong influence the magnetostructural transition has on it. Severe strains are created due to the large volume changes across the magnetostructural transition both inside each nanoparticle and in between neighboring nanoparticles. We suggest that these magnetostructural induced local-strains are responsible for inhibiting the purely magnetic transition of the O(I) arrested phase. Finally, when sufficient thermal energy is provided, the magnetic transition is carried away abruptly in avalanche-like steps, possibly associated with different sets of similar-size nanoparticles. In order to deepen the understanding of this earthquake-like behavior, the $\partial\rho/\partial T$ data was subtracted to an exponential baseline and was plotted against a relative temperature, $t = T - T''$ as depicted in Figure 5.9. This subtracted $\partial\rho/\partial T$ curve was fitted with an exponential law, $\partial\rho/\partial T \sim A_0 \exp(-t/\lambda)$, where A_0 is the initial amplitude at T'' and λ represents the relative temperature at which the $\partial\rho/\partial T$ drops down to around one third of its initial value A_0, i.e. $\partial\rho/\partial T(T'' + \lambda) \sim 0.367 * A_0$. It was found that both A_0 and λ vary slowly with the thermal cycles, with $\lambda \sim 6.8$ K for the 1st cycle and ~ 8.84K for the 18th cycle. The λ value gives an estimation of the energy involved in these discontinuous local transitions. To trace the evolution of these avalanches with thermal cycles, the characteristic temperatures that signal the beginning (T'') and end (T''') of this burst-like regime were plotted in Figure 5.4 b). A linear dependence was found for both temperatures, with T''' evolving slightly faster than T'' with the thermal cycles. Moreover, T''' evolves similarly on heating and on cooling, whereas T'' evolves faster on heating in comparison with cooling experiments. Taking into account the drastic volume changes ($\Delta\mathbf{V}/\mathbf{V} \sim 1\%$) these nanoparticles undergo across this transition it is possible to conjecture that such transition temperatures evolution is due to the internal stress build up associated with each compression-expansion cycle (that eventually completely suppresses the magnetostructural transition, as previously shown in one our report[264]). According to Morellon and coworkers, an increase in the transition temperature of $\partial T_C/\partial P \sim 3$ K $kBar^{-1}$ is expected for the bulk $Gd_5Si_{0.4}Ge_{3.6}$ (which also undergoes a O(II)-O(I) structural transition)[265].

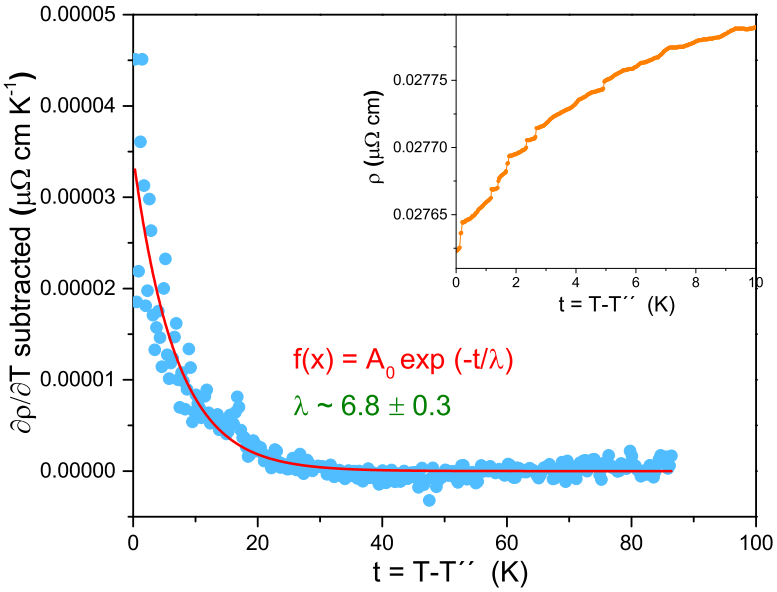

Figure 5.9 – $\partial\rho/\partial T$ for first cycle on heating subtracted by the exponential baseline depicted at the inset as a function of relative temperature t= T - T″. The red line represents an exponential law fitting to the subtracted $\partial\rho/\partial T$ data. In the inset, the associated first cycle ρ(T) data is plotted against absolute temperature.

Considering the linear and monotonic increase of T''_h of 1.6 K/cycle it is possible to hypothesize that an estimated pressure of 0.56 kBar is occurring at each cycle. Levin and coworkers[245] discarded this explanation as they argue that such a high pressure combined with the brittle nature of these bulk materials would destroy the sample. However, in this case the nanoparticles stacking form a lower density material, ensuring more liberty for each nanoparticle to expand and contract without the formation of any major crack. In fact the absence of cracks is supported by the constant value of the residual resistance (there are no significant changes on each ρ(T) curve, except in the transition temperature region), in contrast to what happens for all $Gd_5Si_xGe_{4-x}$ bulk materials[82,237,245].

Another interesting feature is the ~ 25% reduction of the thermal hysteresis area across these transitions. Our group thoroughly studied these nanoparticles magnetic behavior as a function of thermal cycles in a previous work where the thermal hysteresis reduction was attributed to the intense build up stress mentioned above[264]. As explained, the large volume reduction/increase across the structural transition on cooling/heating leads to a gradual arrest of the low-volume phase that hinders the structural transition and eventually suppresses it (after a thousand cycles as observed in our previous work). Such effect was also verified in other $Gd_5Si_xGe_{4-x}$ compounds[237,266] and also in other compounds families presenting a first-order transition, namely the NiMnGa[267] and Manganites[268]. In all the cited examples it was always the low-volume phase that become arrested. Sousa and co-workers[237] explained that the complex free energy landscape exhibited by these compounds at temperatures near transition are at

the origin of mesoscale phase separation. Then the path followed by the system along the transition will be greatly influenced by disorder, which in this case might be represented by inter and intraparticle boundaries, arrested O(I) phase and/or amorphization. Hence, each time the system crosses the transition it will change this disorder, which in turn will change the system percolation path across the transition and the avalanche formation and propagation. In general, this evolution can be understood as a learning process in which the system is permanently searching for an optimized path, avoiding high energy barriers and finally reducing thermal hysteresis, as was also observed in this case. Such picture corroborates with the obtained λ increase with the thermal cycles, as the system in order to avoid large energy barriers prefers to evolve in smaller steps that summed up take longer (or demand higher energies) to go trough, but become much more reproducible, as reported by Perez Roche[262].

5.5 Conclusions

In this work, a high resolution transport measurement study was performed on the as-deposited $Gd_5Si_{1.3}Ge_{2.7}$ thin film, comprising an ensemble of nanoparticles. This study was extended for 18 thermal cycles allowing to deepen the understanding of the system evolution. A general negative thermal dependence was observed revealing a semiconducting-like behavior. Such behavior contrasts with the metallic-like observed in bulk $Gd_5Si_xGe_{4-x}$ compounds and is thought to originate on the size reduction effect on the thermal expansion behavior (that is positive at the bulk scale but negative at the nanoscale) that was thoroughly described in chapter 4. This general trend is interrupted by a two-step positive, metallic-like thermal dependency that is caused by two consecutive transitions: a magnetostructural at lower temperatures and a purely magnetic order at higher temperatures. A strong correspondence between the phase fractions content undergoing each transition and the resistivity change across each step can be made. A general picture for the avalanche-like behavior observed in the high temperature step was proposed based on the severe strains induced by the magnetostructural transition. This picture is compatible with the cycle evolution of the temperatures at which the avalanche-like regime begins and ends assuming an internal stress formation that builds up at every thermal cycle due to the large volume induced change across the magnetostructural transition. The magnetic and electrical resistivity thermal hysteresis reduction with thermal cycles was explained in light of a learning process through which the system is permanently searching for an optimized percolation path which corroborates with the positive dependency of the thermal activation energy with the number of cycles. Furthermore, the invariance of the residual resistivity values under cycling, contrasting with the bulk counterparts behavior, is a clear-cut signal of the absence of major cracks in the overall thin film, which in turn might be the result of the higher degree of freedom in this low-density material. Hence, this work demonstrates the impor-

tance of using a short-range order probe, such as the electron mean free path, to sense mesoscopic physical mechanisms. These short-range order techniques will have an enhanced relevance on the inspection of micro and nanostructures as pointed by Miller and co-authors[39] and soundly exemplified by Uhlir and co-workers recent report[62].

Concerning thermal treatments, it was found that annealings below 773 K were responsible for the suppression of the Magnetostructural Transition. This was confirmed by the absence of the O(II) phase crystallographic peaks observed in the XRD measurements of the annealed films. The suppression of the structural phase, responsible for the GMCE, prompted a 68% decrease in the magnetic entropy change peak value and a 21% decrease in its Refrigerant Capacity. Nonetheless, there was a 25% increase in its T_C, which became closer to room temperature (T = 253 K) and an increasing of ΔT_{FWHM} from 23 to 49 K in its operational temperature interval were found upon annealing. Most importantly, it was unveiled the critical thermal treatments parameters to modify the magnetic and structural transitions of a $Gd_5(Si,Ge)_4$ at the nanoscale, demonstrating the possibility to tune them. These findings are crucial for future applications in magnetic refrigerators/sensors operating at room temperature. Hence this work demonstrates that, as in the bulk case, thermal treatments are an important tool to tune and optimize different crystallographic phases, such as the one responsible for the FOPT.

CHAPTER 6

Continuous $Gd_5(Si,Ge)_4$ thin films

In this chapter the focus will be given to the deposition, characterization and optimization of a variety of $Gd_5(Si_x,Ge_{1-x})_4$ continuous films including the end members (x=0 and 1) and the intermediate compositions with 0.25 < x < 0.75. The knowledge acquired in chapter 5 regarding thermal treatment parameters in granular $Gd_5(Si,Ge)_4$ thin film was fundamental for the study presented in this chapter, specially for the initial thermal treatments, as will be detailed. Distinctively from the high-energetic femto-second Pulsed Laser Deposition (PLD) used in the deposition of the granular $Gd_5(Si_x,Ge_{1-x})_4$ thin film, the continuous films presented in this chapter were deposited by DC and RF Sputtering and following two main approaches: co-sputtering and multilayer depositions. Their basic characterization was performed through X-ray diffraction and SQUID magnetometry, which by comparison with the bulk counterparts and the thin films themselves allowed to optimize the deposition conditions and post-deposition heat treatments. As will be demonstrated, the major challenge was to crystallize the desired 5:4 ($Gd_5(Si_x,Ge_{1-x})_4$) crystallographic phase. Finally, the films with higher 5:4 phase content will be presented and characterized in more detail.

6.1 Introduction

6.1.1 Gd-Si-Ge: The 5:4 phase and others

The 5:4 crystallographic phase formation is an issue of crucial importance as this is the phase that warrants the multi-stimuli giant responses of the Gd-Si-Ge based materials. The difficulties associated with its formation have been identified by its early discoverers, Smith, Holtzberg and their respective co-workers in the 1960s[99,100]. In fact, there are two main constraints: first is the 5:4 (5 moles of Gd to 4 moles of Si, Ge or a mixture of Si and Ge) stabilization and the second is that within the 5:4 stoichiometry it is common to have two 5:4 phases with different Si/Ge ratios, x. The 5:4 stabilization problem must be tackled first and just afterwards its monophasic nature issue will be addressed. The 5:4 stabilization is not straightforward due to the emergence of other phases during the synthesis procedure, the so-called spurious phases which have atomic ratios Gd : Si/Ge different than the 5:4. The most common spurious phases in the bulk scenario are the 5:3 and 1:1 ones, which, as can be seen in the Gd-Ge and Gd-Si phase diagrams in

Figure 6.1, are the the 5:4 immediate next-neighbors. Hence, there is a small window of opportunity for the formation of the 5:4 phase, which we will be our target.

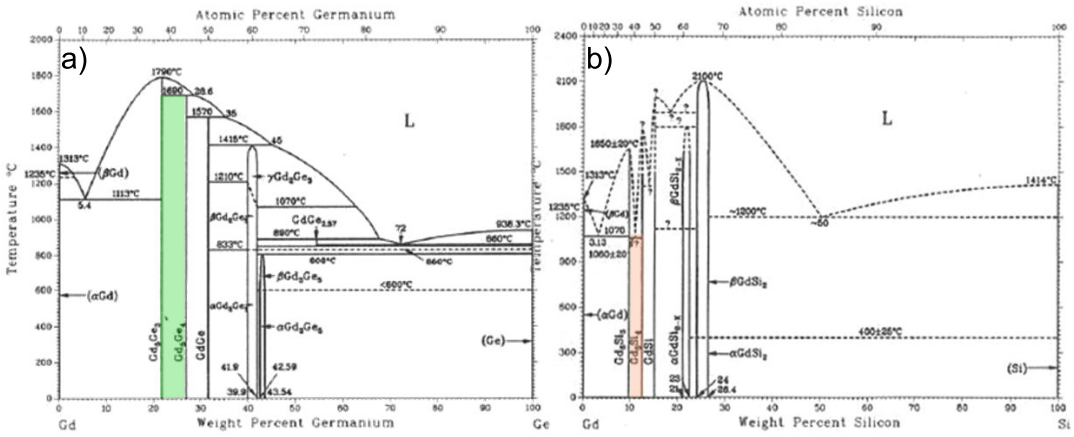

Figure 6.1 – Gd-Ge, a), and Gd-Si ,b), phase diagram where the phases are schematically represented as a function of Ge and Si weight percent, x. The horizontal lines delimiting the phases areas in the upper part represent each phase formation temperature. The 5:4 phase is highlighted in greenish, a), and reddish, b), rectangles. Gd-Ge and Gd-Si phase diagrams are represented as in references[269,270], respectively

These two phases occur as a result of a partial eutectic-like decomposition that occurs on cooling to room temperature after the high-temperature synthesis procedure. An eutectic reaction is defined as a decomposition of a liquid phase into two solid ones that typically adopt a lamellar microscopic configuration as seen in several $R_5(Si_x,Ge_{1-x})_4$ examples[271,272]. Such configurations allow quicker atomic diffusion between different crystallographic phases. The two Gd-Si and Gd-Ge phase diagrams, portrayed in Figures 6.1 a) and b), represent the bulk scenario, i.e. their information was collected from a wide range of compounds synthesized at the macroscale. At the nanoscale the same phases are expected to form. However, due to various size-related effects such as surface effects, morphology and microstructure, their phase formation temperature can change dramatically, as observed in the granular $Gd_5(Si_x,Ge_{1-x})_4$ thin film, in chapter 5.

The impact of nanoscale is patent in various examples. An interesting one is that of ice nanocrystals can have melting temperature 130 K lower than bulk ice[273], or tin and other metals, whose nanoparticles melting temperature decrease as the nanoparticles radius decrease[274]. In particular, the suppression of melting point with nanoparticles size has been predicted theoretically by Gibbs and Thomson[275].

In the thin film form, there are several reports on the diffusion and phase formation of Gd Silicides and Germanides (due to their very low Schottky barrier) however, unfortunately, very few claim or show any signs of the 5:4 phase formation. Molnar and co-workers have shown that a Gd thin film deposited on a Si substrate can form different Si-rich silicides due to the Si diffusion from the substrate (that acts as an endless Si source) towards the film. Depending on the annealing temperature and on the film thickness, a profile of different Silicides phases along the Gd film thickness is observed[276].

The Si diffusion was prompted by short (5 minutes) annealings at temperatures in the range 200-600°C. They found for a 50-150 nm thick Gd film, initially the $GdSi_{1.7}$ is formed until all Gd is "consumed" and afterwards the Si-richer $GdSi_2$ phase emerges, eventually becoming the majority one. The scenario is slightly different if the Gd film thickness is 250 nm, since in this case the $GdSi_{1.7}$ continues to be the majority phase at the end of the annealing. Baglin and co-workers have demonstrated the different mobilities of Si, Ge and rare-earth metal through Rutherford Backscattering Spectra (RBS) analysis of rare-earth thin films deposited on top of Si and Ge substrates which afterwards were subjected to one hour anneallings at different temperatures in the 400-1000^{o}C range. They found that the Rare-Earth atoms are almost immobile until 900-1000 ^{o} C as expected from their higher radius, whereas the first Silicide formation occurs 500°C below. They estimate that, on an absolute scale, the activation temperatures for Ge/Si and the Rare Earth metals are: 300/800°C and 450/950°C, in Germanides and Silicides, respectively, meaning that the activation temperature for Rare Earths is almost the double of that of Si and Ge[277]. Jin and co-workers found identical results for channeled Gd ions implantation into Si (111) and (001)[278]. Vaskovskii and co-workers have deposited a Gd/Si multilayer system at room temperature with Gd and Si layers within the ranges 7.5-40 nm and 0.2-2 nm, respectively. They subjected the thin films to a one hour 450^o C annealing and described the emergence of three phases: amorphous, amorphous-crystalline and crystalline based on the magnetization results. They found that the amorphous phase content tends to decrease for thicker Gd layers, being less than 20 % for 40 nm or thicker Gd layers. In contrast, the amorphous content tends to be enhanced for Si layers thicker than 1 nm[126]. Moreover, in their structural characterization they claim that some of the crystalline content is of the 5:4 stoichiometry, although this is not confirmed by the magnetic behavior.

In summary, there is a wide variety of studies on Gd thin films deposition on Si substrates demonstrating the occurrence of several different Gd silicides, such as: $GdSi_2$, $GdSi_{2-x}$, $GdSi_{1.65}$, $GdSi_{1.7}$, Gd_5Si_3[279] and also amorphous Gd-Si phases[280]. Although scarcer information is available for the germanides counterpart, given its similarities with Si, namely their Gd-Si and Gd-Ge parallel phase diagrams and their similar diffusion mobility on Gd[277], it is plausible to assume that the same stoichiometric compositions occur on a Gd-Ge thin film system. The complexity increases when the ternary Gd-Si-Ge system is considered, since all the previous phases can occur with different Si/Ge ratios. In order to distinguish them its important to deepen our knowledge mainly on their crystal and magnetic structures. In their bulk counterpart, the $GdSi_{2-x}$ phases crystallize in an Orthorhombic Imma space group for $0 < x < 0.35$, and in a Hexagonal structure, P6/mmm space group, for $x = 0.35$. In this concentration range, all Gd silicides are paramagnetic at room temperature and down to low temperatures, where they undergo a magnetic transition towards an antiferromagnetic (AFM) state with Néel temperature (T_N) in the 24-33 K range[281]. The monosilicide GdSi adopts the FeB-type Orthorhombic structure with Pnma symmetry and is paramagnetic at room temperature,

ordering antiferromagnetically at $T_N \sim 55$ K. It exhibits a large magnetic anisotropy and distinct magnetic field induced transitions at T = 4 K[282]. Unfortunately, to our knowledge there is no sufficient information on both the atomic and the magnetic structure of the Ge counterpart, GdGe.

Gd_5Ge_3 adopts a Mn_5Si_3-type hexagonal structure with a P63/mcm symmetry and it also presents a major PM-AFM transition at $T_N \sim 82$ K. In addition it presents two minor magnetic transitions at 50 K and 36 K, exhibiting a thermal irreversibility in this temperature range[283]. Furthermore, by applying a magnetic field isothermally, in the 5-20 K range, two magnetic-field induced transitions are observable up to 8 Tesla. The lower field of these field-induced transitions is magnetically irreversible leading to a small magnetic hysteresis, whereas the higher field transition is reversible and shows no hysteresis. Despite these transitions it was also confirmed that even a 30 T field is not enough to induce a FM state on this compound. The Gd_5Si_3 also stabilizes in the Mn_5Si_3-type hexagonal structure with a P63/mcm symmetry[284] and also has an AF ordering at low temperature, however it presents a lower T_N (55 K)[285], very close to the T_N exhibited by the monosilicide GdSi. Hence, as shown in preliminary measurements by Narasimhan and co-workers[286], the $Gd_5(Si_xGe_{1-x})_3$ shows an enhancement of its AFM exchange interactions, increasing its T_N, with the increase of Ge content. Furthermore, the Gd richer Gd_3Ge_4 phase can also be formed. It stabilizes in the Orthorhombic with the Cmcm symmetry and like the above mentioned phases is PM at room temperature down to $T_N \sim 29$ K, where it orders antiferromagnetically[287].

6.1.2 Gd metal and its oxides

In its bulk scale, Gadolinium is a silvery-white malleable and ductile Rare Earth metal. It typically crystallizes in hexagonal close-packed (hcp) α-form at room temperature, but, when heated to temperatures above 1235°C, it transforms into a body centered cubic (bcc) structure known as its β-form[288]. Although, there are several studies reporting slightly different Gd Curie temperatures (+/- 5 K), the value $T_C \sim 293.5$ K reported by Nigh and co-workers is widely cited[289].

At the nanoscale, there are wider possibilities both for the atomic and magnetic structures, as demonstrated by the work of Kirby and co-workers on Gd thin film deposition[120]. They have found that by pre-gettering the deposition chamber with Gd, favors the formation of Gd bcc β-form phase in a 30 nm Gd thin film deposited on top of a Ta (5 nm) buffer layer and covered by a (5 nm) Ta capping layer. In addition they observed a Curie temperature evolution from 275 K (room temperature) towards 295 K (600°C) with increasing substrate temperature. Yamada and co-workers found different results for thicker (750 nm) Gd thin films deposited on top of heated glass substrates: all Gd films crystallized in their hcp structure and its c-axis preferential orientation was favored with increasing substrate temperature[124]. Accordingly, Rubio-Zuazo and co-workers have unfold that also the deposition chamber pressure plays a fundamental

role on the preferential orientation of ~ 400 nm Gd thin films deposited on top of naturally oxidized Si substrate. They concluded that all films crystallize in the hcp structure, however those deposited at Argon pressures lower/higher than $3x10^{-3}$ mBar grow with a (1010)/(0002) preferential orientation[290]. Furthermore, different nanostructures were also grown, such as Gd nanoparticles assembled by Spark Plasma Sintering (SPS) of a bulk Gd piece, as studied by Zeng and co-workers. They were able to grow 15 and 100 nm diameter nanoparticles and reported Curie temperatures of 289 K and 294 K, which represented a decrease in comparison with their own Gd bulk T_C ~ 296 K[291]. Such T_C reduction can be a consequence of different scale induced effects (atomic structure, surface effects,...), however, the fundamental cause should be the significant reduction of crystallographic and hence magnetic domains, as highlighted by these authors.

Fewer studies have been devoted to the amorphous-like Gd thin film deposition. Gambino and McGuire prepared Gd_xGe_{1-x} amorphous thin films by e-beam evaporator technique and reported a Curie temperature around 163 K for a Gd-rich composition (x=0.8) and a continuous decrease down to 139 K for x=0.55. Interestingly, for Ge-richer compositions (x < 0.55) the films showed no magnetic ordering until 4 K, revealing a pure paramagnetic behavior[292]. The same authors found a simpler dilution effect on Gd_xGe_{1-x} amorphous thin films with a linear relation between T_C and the composition (x) from 0 K for x=0.15 to 118 K for x=0.72[293]. By extrapolating this T_C linear behavior to the Gd-richer region they estimate a T_C ~ 183K for a pure Gd amorphous thin film, which corroborates the value previously measured by Heiman and Kazama[294].

A major issue with the Rare-Earth elements and in particular Gd is its extreme reactivity to Oxygen. As found by Burnham and Jameson, a ~ 100 nm thick Gd thin film can grow a 15 nm thick oxide layer just by being left at room temperature for two months[295]. Furthermore they also found that Gd oxidation was fast at the beginning but shortly afterwards starts to slow down, following an inverse logarithmic rate. Molnar and co-workers found that Gd oxide formation occurs via two processes: oxygen penetration through Gd grain boundaries and by lattice diffusion. They have shown that the grain-boundary Oxygen penetration can be drastically decreased by the introduction of some Si into the Gd film which thereby will accumulate preferentially at the Gd grain boundaries, hence blocking Oxygen diffusion. In this way they estimated a reduction of six times less Gd_2O_3 amount in comparison with a Si-free Gd thin film[296]. There are two major Gd oxide phases, Gd_2O_3 and GdO, where the sesquioxide is the most common form and can adopt several different crystallographic structures, such as cubic, hexagonal and monoclinic, whereas the cubic (face centered) and monoclinic are the most common at room temperature[297]. The Gd_2O_3 exhibits an almost perfect paramagnetic behaviour from low temperatures up to room temperature, with its reciprocal susceptibility following accurately the Curie-Weiss formula[298,299]. Probably due to the high temperature formation, GdO has been scarcely investigated and to our knowledge no significant information regarding its magnetic properties is available[300]. Since the early

days on rare-earth thin films deposition, the oxidation has been an issue that has been tackled with different and combined preventive measures. Its importance is enlarged when the rare-earth thin films must undergo any kind of in-situ or post heat treatment, as the increasing temperature favors the rare-earths oxidation process. As mentioned above, Kirby and co-workers have found that gettering the deposition chamber prior to deposition by heating up the sample holder up to 600°C and pre-sputtering Gd during 30 minutes allows to double the ratio between the Gd and Gd oxide phases content, as sputtered Gd, deposited at the chamber walls, will react with the residual Oxygen left in the chamber after vacuum pumping. They observed the formation of GdO and Gd_2O_3 and their increased content with higher substrate temperature and in particular to the large enhancement of the GdO cubic phase, which became the dominant phase in 600°C heated substrate[120]. Another widely used preventive technique is to deposit a thin layer, known as cap layer, of a different material whose purpose is to protect the underlayer film from oxidation. A significant effort has been devoted to the search of the best capping layer specifically for rare-earth thin film protection, although sometimes with contradictory results. An illustrative example of contradictory results is the Pt/Er system for which there are comprehensive results suggesting that Pt capping layer remains essentially unaffected until temperatures below 700°C[301], whereas there are other suggesting it starts reacting with Er at around 300°C , eventually forming $ErPt_2$, below 700°C[302]. Despite the potential contradictions, that can result of slightly different deposition and heat treatment conditions, it is always instructive to learn about different capping-film systems. From all the periodic table elements, the refractory metals are possibly the ones presenting more suitable properties for being capping agents, because of their great stability up to high temperatures, low-diffusion coefficients and low miscibility with rare-earths. Molybdenum, Mo, was found to prevent any major oxidation and remain immiscible with Er and Tb thin films under temperatures below 300°C[303]. Tungsten, W, although being rather efficient in preventing oxidation in an Er/Si system, it was also shown that it actively reacts with Si to form WSi_2 at 800°C[304]. WSi_2 formation is undesirable because it induces a highly compressive stress on the rare-earth film which can lead to the formation of lumps (very irregular morphology) and eventually to cracks leaving opening holes for the Oxygen to diffuse. Titanium, Ti, has proved to be a good capping agent until 600°C when its oxygen permeability starts to increase. Hence, above this temperature it is common to observe the formation of Erbium oxide or even Er-Si-O amorphous or crystalline phases[305]. Moreover, above 500°C, Ti was observed to form $TiSi_2$[302]. In fact, as explained by Thompson and co-authors, in general, a refractory metal and a rare-earth metal are mutually insoluble, and they do not react to form intermetallic compounds at low temperatures. Additionally, since the lowest reaction temperature is the one between rare-earth metal and Si, the formation of rare-earth metal silicide is expected to occur first[302].

6.2 Gd-Si-Ge continuous thin films deposition

The films presented below were deposited by DC and RF Sputtering following two main approaches: co-sputtering and multilayer depositions, as illustrated by the scheme in Figure 6.2. In attempting to crystallize the 5:4 phase, several ex-situ annealings were performed, which can be separated in two major groups: low temperature (T < 500 °C) and high temperature (T > 500° C), as schematically pictured in Figure 6.3. Their structural and magnetic characterization was performed through X-ray diffraction and SQUID magnetometry, which by comparison with the bulk counterparts and the thin films among themselves allowed to optimize the deposition conditions and post-deposition heat treatments. In order to mimic the nanogranular deposition, all films were deposited on top of a thermally oxidized, SiO_2 ($\sim$ 800 nm), Si substrate. Gd, Si and Ge targets with 99.95% purity were used during the depositions. All substrates were cleaned under the typical cleaning protocol: 5 minutes ultrasounds in an acetone bath, 5 minutes ultrasounds in an ethanol bath, deionized water shower and finally drying with a N_2 gun. Prior to every thin film deposition, the chamber was evacuated by a vacuum system comprising a primary rotating pump (pressure down to 10^{-3} mBar) and a turbomolecular pump that guaranteed a 10^{-7} mBar pressure inside the chamber. Then a 10 minutes pre-getttering of the chamber was performed by sputtering the Gd target while the shutter was closed, typically leading to a decrease in the chamber pressure down to 10^{-8} mBar. The working Argon pressure was set to 4 mBar. Four different substrate temperatures were used: room temperature (most depositions), 200°C, 400°C and 600°C. Concerning buffer and capping layers, different procedures were followed: no buffer (direct deposition into SiO_2/Si substrate) and no capping layer, only capping layer (in particular, Pt), or both buffer and capping layers (Ta).

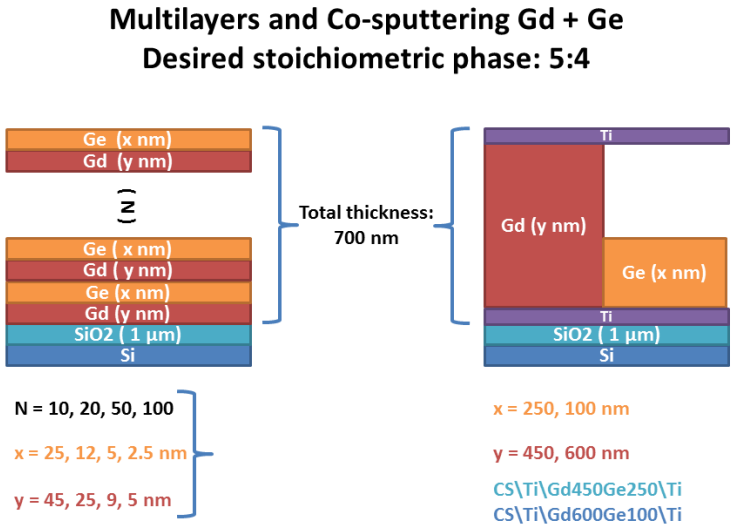

Figure 6.2 – Schematic representation of the binary Gd-Ge multilayer and co-sputtering approaches. Four different multilayered and two co-sputtered binary Gd-Ge thin films were initially deposited.

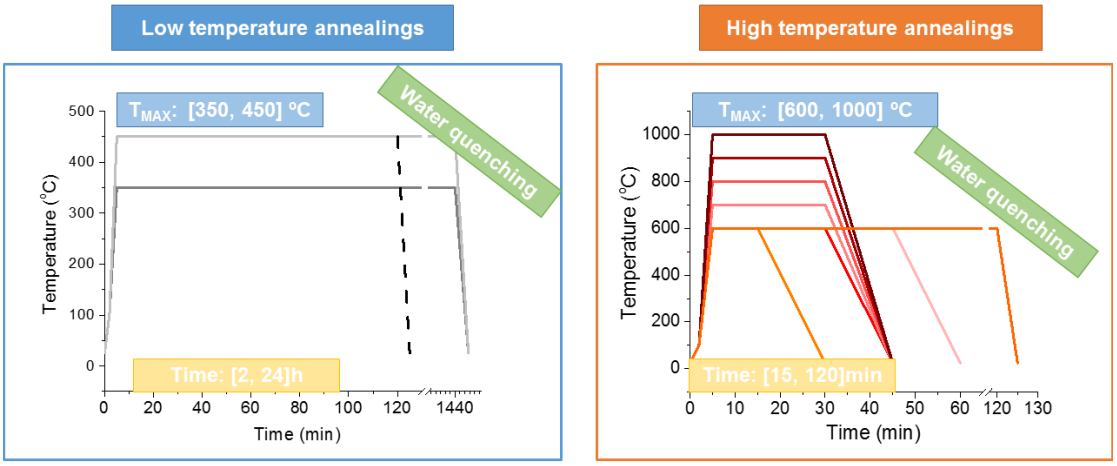

Figure 6.3 – Schematic representation of the low and high temperature annealings procedures performed on both co-sputtered and multilayered thin films.

6.2.1 Low-temperature annealings

For the sake of comparison, prior to the Gd binary and ternary Germanides and Silicides depositions, a pure Gd thin film was deposited under the same conditions and was subjected to identical ex-situ thermal treatments. Their morphological, structural and magnetic characterization is displayed in Appendix A.

6.2.1.1 Binary GdGe films: Multilayered

In this first thin films set, all depositions were carried at the same working pressure (4 mBar), same target-substrate distance (20 cm) and same substrate temperature (room temperature). For multilayered Gd-Ge binary film, Gd and Ge were always deposited with DC power source set at 80 W, which previous calibrations allowed to estimate the deposition rates for Gd and Ge at ~ 10.8 nm/min and ~ 9.7 nm/min, respectively. For Co-sputtered Gd-Ge films, CSGd450Ge250 and CSGd600Ge100, the Gd power was maintained constant, 80 W, whereas the Ge power was reduced to 48 W (5.9 nm/min) and to 20 W (2.2 nm/min) respectively, in order to synchronize the Gd and Ge deposition, hence promoting its intermixing during the deposition. As illustrated in Figure 6.2, four different Gd-Ge multilayered films were deposited, where the last layer was Ge in order to help prevent Oxygen penetration: 25 nm Ge layer on top of a 45 nm Gd layer repeated 10 times, 12 nm Ge layer on top of a 25 nm Gd layer repeated 20 times, 5nm Ge layer on top of a 9 nm Gd layer repeated 50 times, 2.5 nm Ge layer on top of a 4.5 nm Gd layer repeated 100 times. Hence, the four multilayered films have the same overall thickness, 700 nm, and only the individual Gd and Ge layers thicknesses were varied, but retaining the 5/4 ratio between Gd and Ge number of atoms.

Scanning electron microscopy (SEM) images were taken with backscattered electrons (BE) of the as-deposited and annealed at 450°C for two hours. The as-deposited and annealed MLGd45Ge25 multilayered films are shown in Figure 6.4 a) and b), respectively, as an illustrative example. The as-deposited overall thickness estimated from the cross-section images is ~ 670 nm, whereas the annealed film is more irregular with an average ~ 645 nm. The Gd and Ge individual layers (brighter and darker, respectively) are clearly seen in the as-deposited film, a), although their individual thicknesses estimation is difficult due to the comparatively thick interface region. Contrarily, in the annealed film no contrast is observed and is not possible to distinguish the two layers. The indistinguishability between layers and the smaller overall thickness of the annealed film are clear-cut signs that the annealing promoted the Gd-Ge inter-diffusion. Since Gd atomic mass number (64) is the double of that of Ge (32), Gd is expected to be almost immobile, whereas Ge is the main diffusing species. In fact, as mentioned in previous section "Gd-Si-Ge: 5:4 and other phases", there are reports showing that the Gd and Ge mobility are similar for significantly different activation temperatures: 800° C for Gd and 300°C for Ge[277]. Top view film images were also extracted (although not presented here), revealing an homogeneous surface. EXDS measurements were performed in order to check Gd and Ge fractions and the stoichiometry in the annealed film. Unfortunately, their correct amounts estimation is difficult because: low-energy electrons, used to minimize the interaction pear region between the electons and the SiO_2 buffer layer, results in an overlap between Gd and Ge K-electronic band, hence inhibiting their correct amount estimation.

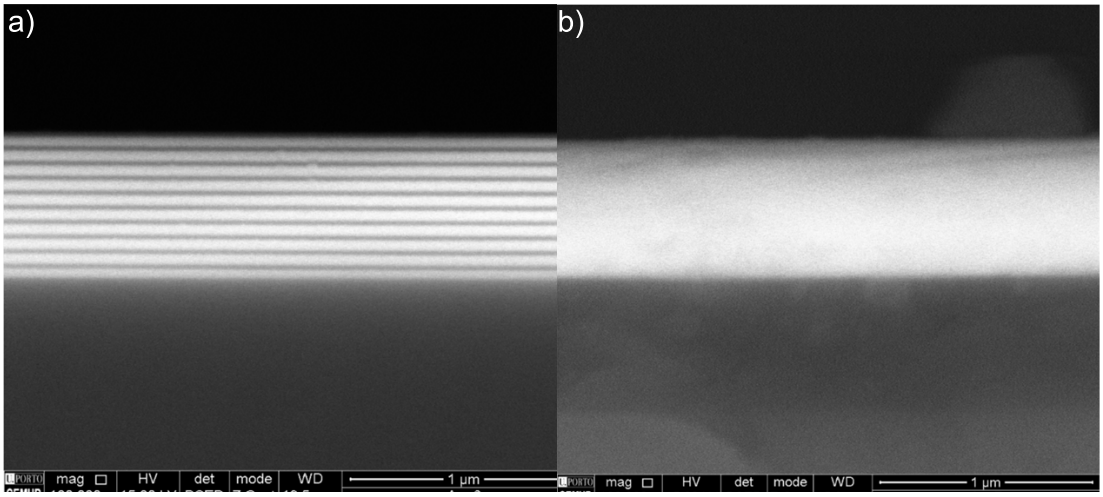

Figure 6.4 – Scanning Electron Microscope (SEM) cross-section view of the as-deposited, a), and annealed at 450°C for two hours, b), of MLGd45Ge25 multilayered thin film.

X-ray diffraction patterns of the as-deposited and the annealed set of films are presented in Figure 6.5 a) and b), respectively. As can be seen in Figure 6.5 a), $ML10Gd_{45}Ge_{25}$ presents a similar pattern as the one exhibited by the pure Gd thin film: hcp structure, P63/mmc space group, with a strong preferential orientation towards the (0 0 2) Miller

index atomic plane. The major difference is the 32.3° and 28.1°, (1 0 1) and (1 0 0) Miller index atomic planes, whose intensity ratio is larger for the multilayered film. The thinner, MLGd23Ge13, presents a very similar pattern, with the above mentioned intensity ratio enhanced even further. Interestingly, the individually thinner multilayers, MLGd9Ge5 and MLGd4.5Ge2.5, do not exhibit any of the three characteristic peaks in the 28-33 ° 2θ interval, but instead present a broader bump covering completely this 2θ region, as more clearly seen in Figure 6.5 a) inset. This bump is more intense for the MLGd9Ge5 and more smeared for the MLGd4.5Ge2.5 thinner multilayered film. Moreover, two less-intense peaks appear in these two films at 2θ = 21.2° and 23.8° and the two higher 2θ peaks, also associated with Gd hcp phase, at 2θ = 60.6° and 64° disappear. Such a peak broadening and eventually smeared out Gd peaks is a consequence of smaller crystallite sizes and eventual loss of crystallinity or amorphization of Gd as have already been observed in Gd-Si and and Gd-Fe multilayers, for thin Gd layers[306–308]. Furthermore, the broad peak must also have a contribution from a Gd-Ge amorphous phase, which as shown in previous Rare-Earth-Silicon/Ge multilayered films, is commonly found at the interlayer region in these similar multilayered systems[303]. The 2θ = 21.3° and 23.6°, despite their difficult phase indexation are thought of being associated with the Ge-rich phases, $GdGe_2$ and $GdGe_{2-x}$ phases.In fact, these two reflections emerge in the individual thicker films after annealing, as can be seen in Figure 6.5 b). A drastic transformation, different than the one undergone by the pure Gd thin films, occurs in the thicker multilayered films: the clearly defined hcp structure becomes smeared with broadened peaks in the 28-33 ° 2θ interval. New peaks emmerge at 25.8°, 36.6°, 52.7°, 54.7° and 56.5°, which are associated with the Ge-rich phases, $GdGe_2$ and $GdGe_{2-x}$ phases (such as Gd_3Ge_5)[276,280,309,310]. The two MLGd45Ge25 and MLGd23Ge13 annealed films present similar spectra with slight differences for the higher 2θ peaks. Distinctly, the two individually thinner multilayers MLGd9Ge5 and MLGd4.5Ge2.5 show a different transformation after the annealing: their large bump-like peak around $2\theta \sim$ 32-33° became less intense and broader, whereas their low 2θ peaks decreased their intensity. One major peak is found for all multilayers, except the individually thinner one, at 2θ ~28.6 ° that is attributed to the Gd sesquioxide, Gd_2O_3. A Ge-Oxide phase, GeO_2, signalled by the intense 61.8° peak is present also for all samples. It is important to remark that the 43.3° and 63.4° peaks are not to be considered as they come from the metal sample holder and become visible in some sample measurements.

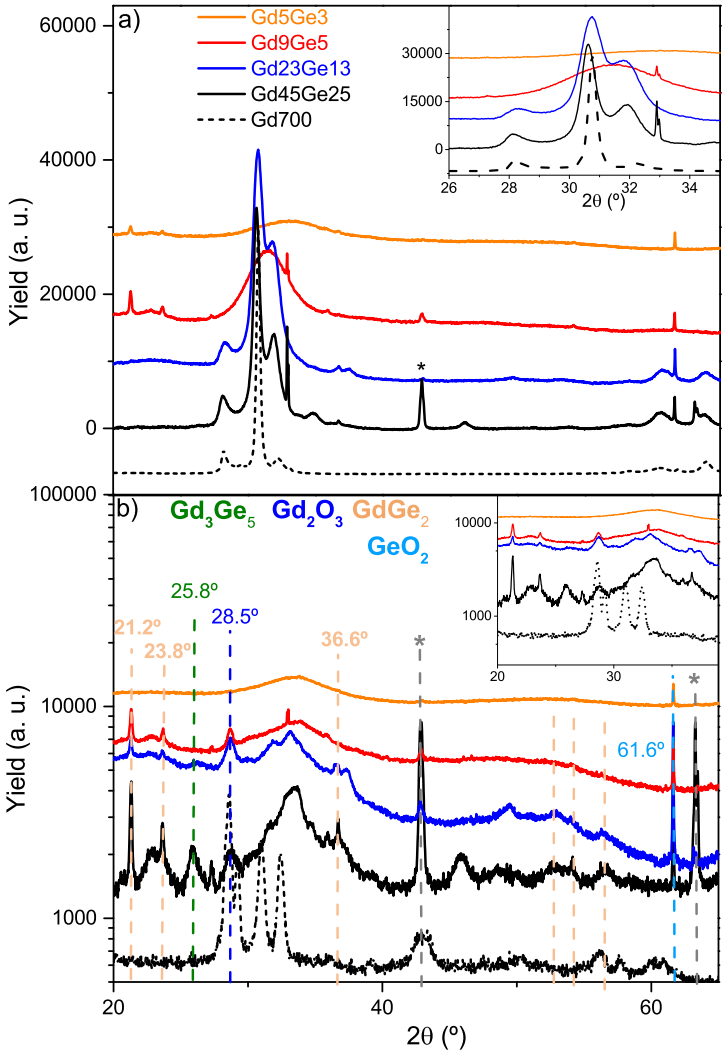

Figure 6.5 – X-ray diffractograms for as-deposited, a), and annealed at 450°C for two hours, b), set of Gd-Ge multilayered thin films, plotted together with the Pt covered Gd pure thin films in the 20-65° 2θ interval. The 26-35° 2θ region is highlighted in the inset. Peaks signalled with asterisk are due to the XRD sample support.

SQUID magnetometry was used to inspect the magnetization of the as-deposited and annealed multilayered films as a function of temperature, M(T), in the 5-330 K range, under a constant applied magnetic Field, μ_0H=0.1 T, and as a function of magnetic field in the 0 - 5 T range at T = 5 K, as can be seen in Figure 6.6 a) and b) and insets, respectively. The as-deposited M(T) curves reveal the different behaviors between the two thicker and the two thinner multilayered films. The former exhibit two major changes in their M(T) curve: a broader transition centered at T = T_C ~ 267 K (determined by the derivative $\partial M/\partial T$ minimum) and an even broader transition that begins at 178 K and as its center at T = T' ~ 100 K. The high-temperature transition is a clear-cut signature of the pure Gd phase as it is occurs at approximately the same temperature as the pure and as-deposited Gd thin film (shown in Figure 6.6 a) in dashed curved) and corresponds to

a typical paramagnetic-ferri(o)magnetic transition.

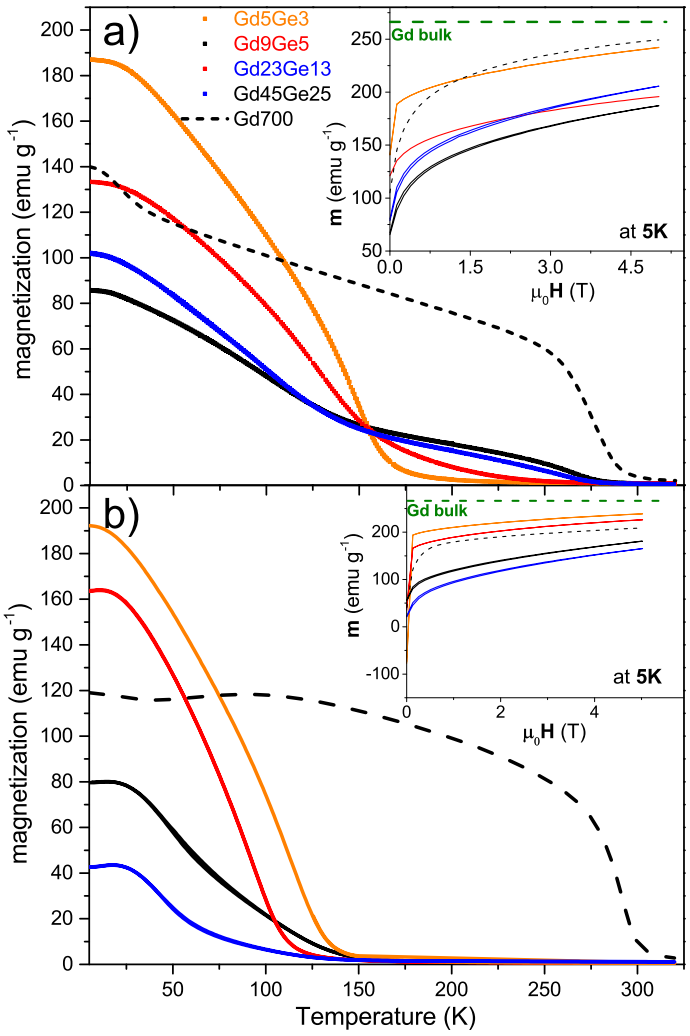

Figure 6.6 – Magnetization of the as-deposited, a), and annealed at 450°C for two hours, b), set of Gd-Ge multilayered thin films, plotted together with the Pt covered Gd pure thin films in the 5-300K temperature interval and under an applied magnetic field μ_0H=0.1 T. In the inset, the magnetization versus the applied magnetic field isothermal curve extracted at 5 K is plotted for all films.

The origin of the lower temperature transition is more difficult to identify as there are multiple possible causes. Interestingly, a remarkably similar low-temperature transition is displayed by the thinner multilayered films, which in turn do not exhibit the high-temperature pure Gd phase. In fact, the MLGd9Ge5 sample reveals an intermediate behavior between the MLGd4.5Ge2.5 and the thicker multilayers, as a small magnetic order begins to form below T = $T''_{MLGd9Ge5}$ ~ 250 K, but the major ordering just occurs below, at T = $T'''_{MLGd9Ge5}$ ~ 150 K. The MLGd4.5Ge2.5 begins to order below T = $T''_{MLGd4.5Ge2.5}$ ~ 200 K, reaching the center of this broader transition at T =

$T'_{MLGd4.5Ge2.5} \sim 150$ K. Despite their different behaviors all multilayered films demonstrate two similar features: magnetization plateau below 25 K and absence of thermal hysteresis. Their M(H) isotherms evidence the absence of a magnetization saturation regime, as had been previously noticed in the pure Gd films, which is explained by the presence of phases at the paramagnetic state, namely the Gd_2O_3. The Pt covered pure Gd thin film presents the higher magnetization at 5 T, ~ 250 emu/g, representing 93 % of the expected theoretical value for Gd, and is followed by the thinner multilayer MLGd4.5Ge2.5 value (~240 emu/g, 90 %), MLGd23Ge13 (~205 emu/g, 76 %), MLGd9Ge5 (~195 emu/g, 73 %)) and finally the thicker MLGd45Ge25 (~187 emu/g, 69 %). It is important to stress that an uncertainty up to ~ 15 % must be expected due to the errors associated with the Gd atoms estimation (errors in thickness, area, and mass density). Besides the presence of the Gd_2O_3 phase and their inhibitor character for the multilayers magnetization at 5 T at 5 K it is possible to conjecture other sources contributing to these multilayer magnetic behavior, in particular the modification of FM correlations in Gd multilayers with other FM or PM layers, as observed previously[311,312]. On the other hand, the M(T) curves are more conclusive as they corroborate the XRD results, confirming the presence of Gd hcp phase with large (>100 nm) crystallite sizes signalling the difference between the two thinner multilayers. In this case, there are three possible explanations: 1) the Gd crystallite size becomes too small (supported by the broadening of XRD peaks) and Gd Curie temperature decreases down to the 100-200 K range[313,314], 2) there is a large spin reorientation below 100-200 K range as observed in previous pure Gd thin film depositions[315], 3) the formation of a Gd-Ge amorphous phase whose magnetic ordering temperature occurs in 100-170 K interval[292]. As displayed in Figure 6.6 b), the 450°C for two hours annealing promoted significant changes on the magnetization temperature profile of the multilayers. In particular, the high-temperature ordering (T > 250 K) became suppressed in the thicker multilayers as well as the small magnetic ordering process observed in the thinner multilayers above 150 K. The thicker annealed films, MLGd45Ge25 and MLGd23Ge13, exhibit similar M(T)'s curve: a broadened transition that starts at ~ 184 K/160 K and reaches its center at 50 K/40 K, respectively. There are two other more subtle changes from their as-deposited behavior: the small thermal hysteresis within the magnetic transition region (in particular in the 50-100 K interval); along the transition M(T)'s curve assume a more concave nature in comparison with the typical ferromagnetic convex behavior (such change is more clearly observed in the magnetization second temperature derivative, that becomes pronouncedly negative in the annealed films in contrast with the almost invariant for the as-deposited sample). In comparison, the annealed thinner multilayered films continue to present a concave-like M(T) curve shape (similar to the as-deposited films behavior). In these thinner films the annealing seems have sharpen the magnetic transition, shifting its beginning temperature to lower temperatures $T = T'' \sim 150/165$ K and its center to $T = T''' \sim 95/114$ K, for MLGd9Ge5 and MLGd4.5Ge2.5 respectively. No thermal hysteresis is promoted with the annealing. Concerning their M(H) curves at

5 K there was a general 4-11 % decrease on the multilayers magnetic moment at 5 T, except for the ML50Gd_9Ge_5, where a 15 % increase was observed. This magnetic moment decreasing tendency can be ascribed to the expected increase in Gd_2O_3 phase with annealing. However, their general field dependency remains similar.

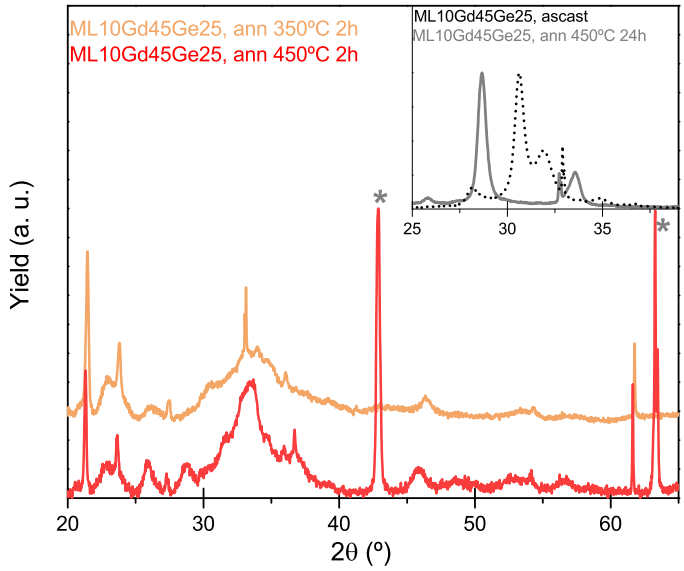

Figure 6.7 – X-ray diffractograms for annealed samples: 450°C for two hours (red line) and 350°C for two hours (orange line). In the inset the 25-40° 2θ region is highlighted for both the as-deposited and the longer annealed sample (450°C for 24 hours (grey)). Peaks signalled with asterisk are due to the XRD sample support.

Additionally, two more annealing treatments were performed in order to give an idea of the temperature and time dependencies: 350°C for two hours and 450°C for twenty four hours, with similar vacuum pressure and cooling rates as before. As seen in Figure 6.7, no significant changes were observed in the low-temperature (350°C) annealing in comparison with the 450°C, meaning that a similar set of different crystallographic phases are observed at this temperature: mostly the Ge-rich $GdGe_2$ and $GdGe_{2-x}$ phases. Contrarily, the longer annealing, 450°C for twenty four hours, highlighted in the inset of Figure 6.7, exhibits significantly different XRD pattern, with the disappearance of the main Gd reflections in the 25-35° interval and the appearance of three new peaks assigned to the Gd sesquioxide. This result suggests that almost all Gd is consumed into the Gd_2O_3 sesquioxide during the 24 hours, despite the vacuum pressure. Consequently, no Gd is left to form any of the Gd-Ge phases. These results are corroborated by the magnetic characterization portrayed in Figures 6.8 a) and b). The longer annealed film shows nearly zero magnetization down to $\sim$ 20 K, where it begins to increase - presenting an almost perfect paramagnetic behavior. Such paramagnetic character is underlined by the magnetization temperature derivative behavior: constant throughout the whole temperature interval down to $\sim$ 20 K, when it begins to rise. The lower temperature annealed film magnetic characterization also follows in accordance

with the structural characterization as its magnetization profile (orange curve in Figures 6.8) mimics the higher temperature annealed film (red curve). However, a closer look unveils a slightly different temperature evolution, with the magnetic ordering starting at higher temperature and in two-steps, as can be more clearly seen in its temperature derivative in Figure 6.8 b). Moreover it does not display any thermal hysteresis as observed in the higher temperature annealed film (red curve in Figure 6.8 a) inset). Such a magnetic behavior, especially its two-step nature, can be attributed to the presence of a small fraction of pure Gd phase that might not mixed completely under this low-temperature. Therefore it results from these two additional annealing treatments that: 1) no significant difference is observed in the 350-450°C temperature range, besides the possible presence of unreacted pure Gd phase; 2) time alone is not enough to promote the 5:4 phase as it leads to the Gd_2O_3 formation, which consumes all the Gd available, leaving virtually none to react with Ge.

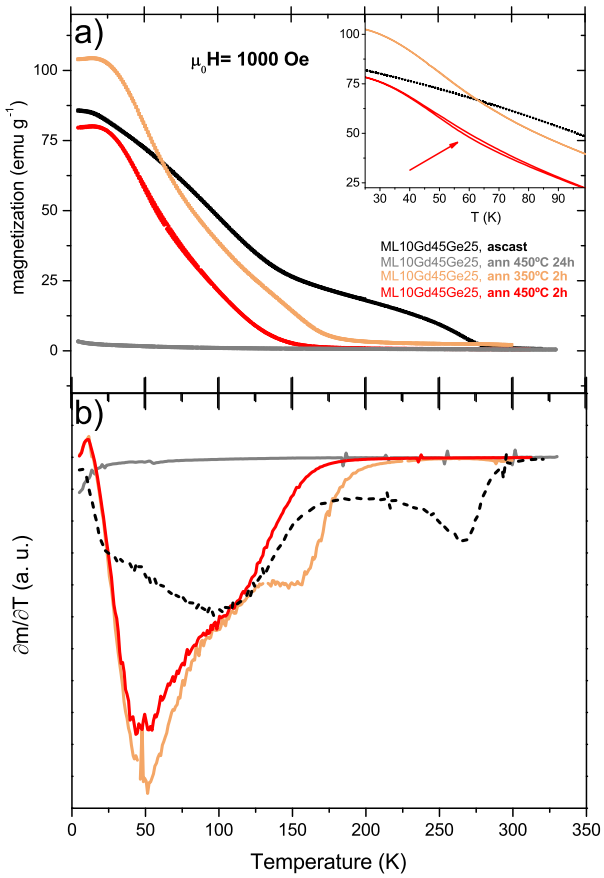

Figure 6.8 – a) Magnetization as a function of temperature for the as-deposited (black) and annealed thin films: at 350°C for two hours (orange), at 450°C for two hours (red) and at 450°C for 24 hours (grey). The 25-100 K temperature region is highlighted in the inset where an arrow points to the small thermal hysteresis observed for the film annealed at 450°C for two hours (red). In b), the temperature derivatives, $\partial m/\partial T$, are displayed for the same temperature interval 5-350 K.

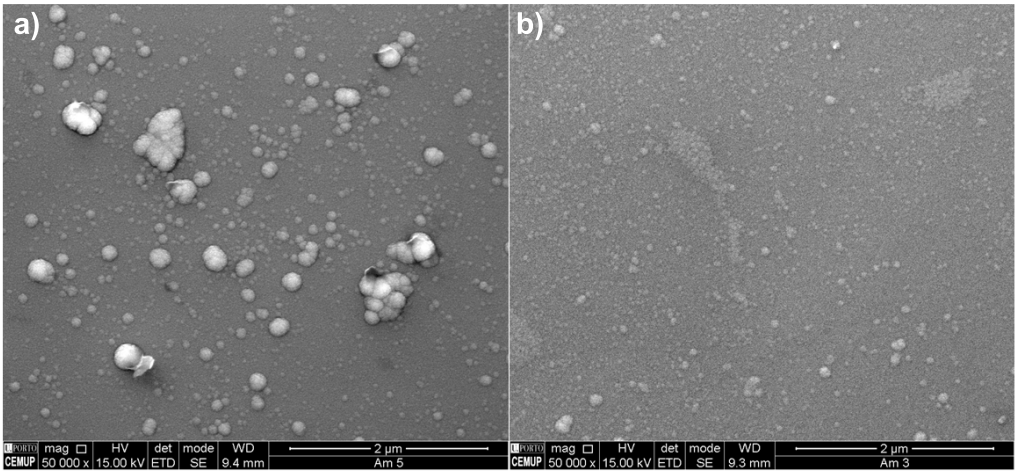

Figure 6.9 – Scanning Electron Microscope (SEM) cross-section view of the as-deposited, a), and annealed at 450°C for two hours, b) of CSGd450Ge250 co-sputtered thin film.

6.2.1.2 Binary GdGe films: Co-sputtered

As schematically illustrated in Figure 6.2, two films were grown by co-sputtering Gd and Ge targets simultaneously with two different ”equivalent thicknesses” (they are not real thicknesses in the same sense of the multilayered set, since here both Gd and Ge are intermixed and no individual smooth and continuous layer is formed): 450 and 250 nm of Gd and Ge for the CSGd450Ge250 and 600 and 100 nm for CSGd600Ge100. Such individual thicknesses were chosen to match the 5:4 Gd/Ge atomic ratio (CSGd450Ge250) and a Gd-richer proportion 4:1 ratio. The latter was chosen to account for the Gd portion that becomes easily oxidized, compensating the amount that is lost for the sesquioxide. These two co-sputtered films were deposited over a thin Titanium buffer layer ($\sim$ 10 nm) and were covered also by a thin Ti cap layer (10 nm). Figure 6.9 presents two top-view images obtained by secondary electrons in SEM of the as-deposited, a), and annealed for two hours at 450°C of the CSGd450Ge250 co-sputtered thin films. As is clearly seen, both films present continuous surface on top of which there are agglomerates of nanoparticles with a large size distribution. Unfortunately, EDS analysis was not conclusive about the stoichiometry of these agglomerates. The annealing promoted a segregation of the large agglomerates into smaller and more evenly distributed, resembling the morphology observed in the pure Gd thin films, shown in Figure A.1. From these images, it is observed that the Ti capping layer is not homogeneous or uniformly distributed, which suggests its inability to prevent Oxygen diffusion towards the film.

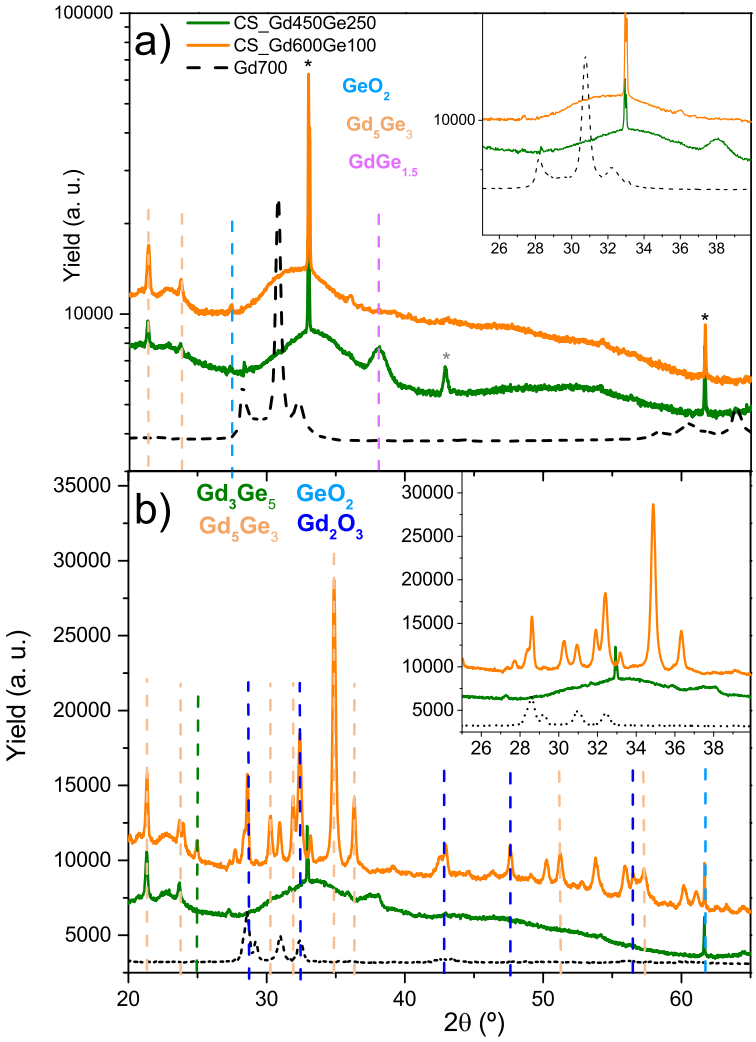

Figure 6.10 – X-ray diffractograms for as-deposited, a), and annealed at 450°C for two hours, b), set of GdGe co-sputtered thin films, plotted together with the Pt covered Gd pure thin films in the 20-65° 2θ interval. The 26-40° 2θ regions are highlighted in the insets.

The X-ray diffractograms of the as-deposited and annealed GdGe co-sputtered thin films are shown in Figure 6.10 a) and b). No significant changes where observed in the CSGd450Ge250 after annealing, where only a slight enhancement of the Gd_5Ge_3-associated peaks in the 20-25° 2θ interval is registered, while maintaining the broad peaks centered at around 33° and 36°. Contrastingly, the annealed CSGd600Ge100 presents several new and sharp peaks, signalling a crystallization phenomena induced by the annealing process. The major change occurs along the 25-40° 2θ interval, where several new peaks emerge also associated with the Gd-rich Gd_5Ge_3 phase. This Gd_5Ge_3 phase enrichment is coherent with the larger Gd/Ge atomic ratio ~ 4 in comparison with the ~ 1.25 for CSGd450Ge250. Simultaneously, the Gd oxide, Gd_2O_3 phase is also favoured during annealing as signalled by the appearance of five new peaks along the whole 2θ interval inspected.

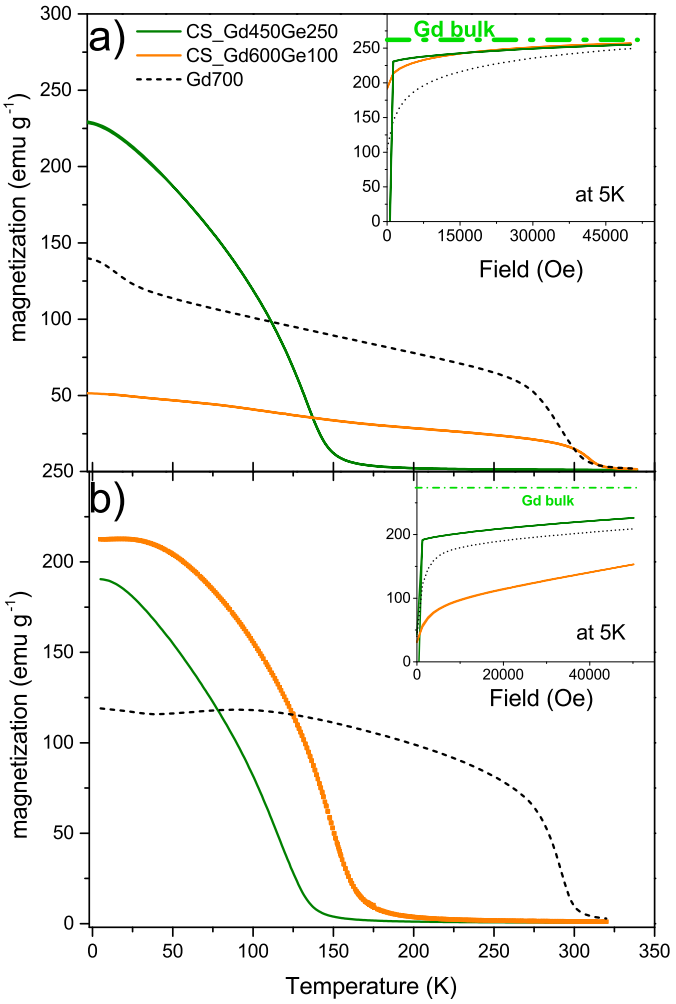

Figure 6.11 – Magnetization of the as-deposited, a), and annealed at 450°C for two hours, b), of GdGe co-sputtered thin films, plotted together with the Pt covered Gd pure thin films in the 5-330 K temperature interval and under an applied magnetic field μ_0H=0.1 T. In the inset, the magnetization versus the applied magnetic field isothermal curve extracted at 5 K is plotted for all films.

Despite the absence of the typical Gd hcp pure phase peaks in the 25-35° 2θ interval of the X-ray diffractogram, the as-deposited CSGd600Ge100 exhibits the Gd-associated PM->FM magnetic ordering at T_C~293 K. Differently, the CSGd450Ge250 exhibits a magnetization temperature dependency similar to that found for the amorphous-like, thinnest GdGe multilayer, MLGd4.5Ge2.5: a magnetic order emerges at T''~ 165 K and the transition reaches its center at T''' ~ 114 K. Coherently with the XRD analysis, the annealing also did not promote significant changes in the magnetization behavior, where only a small decrease on the ordering temperatures was observed. As suggested by the XRD analysis, the annealing induced a major change in the CSGd600Ge100 magnetization behavior, with the absence of the typical bulk Gd high-temperature T_C, but instead a major transition is observed at ~ 140 K. Similarly to the multilayered Gd-Ge

system, the low-temperature 350°C (for 2 hours) and the longer annealing 24h (450°C) were also tested and similar conclusions were found, and hence are not presented here.

6.2.1.3 Ternary Gd-Si-Ge: Co-sputtered and Multilayered

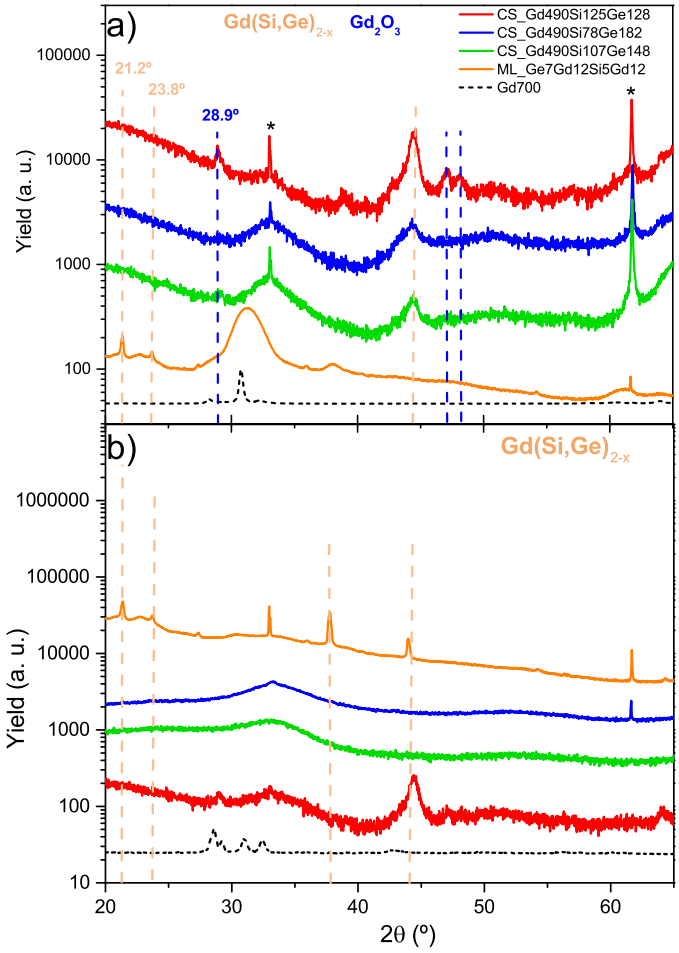

Figure 6.12 – X-ray diffractograms for as-deposited, a), and annealed at 450°C for two hours, b), set of Gd-Si-Ge co-sputtered and multilayered thin films, plotted together with the Pt covered Gd pure thin films in the 20-65° 2θ interval. The CSGd490Si125Ge128, CSGd490Si78Ge182, CSGd490Si107-Ge148 and the multilayer equivalent MLGe7Gd12Si5Gd12 are represented in red, blue, green and orange, respectively.

Four different Gd-Si-Ge continuous thin films were deposited with individual thicknesses matching the following: 1) a slightly Si-rich $Gd_5Si_{2.1}Ge_{1.9}$ (co-sputtered); 2) Ge-rich $Gd_5Si_{1.3}Ge_{2.7}$ (co-sputtered) and 3) $Gd_5Si_{1.8}Ge_{2.1}$ (co-sputtered and multilayer). The 1st stoichiometry was achieved by co-sputtering 490, 125 and 128 nm of Gd, Si and Ge, respectively, by using appropriate 73 W(DC), 140 W(RF) and 20 W (DC) powers to each sputtering target - CSGd490Si125Ge128. The 2nd stoichiometry, matching the

same as that of the nanogranular thin film reported in previous chapters, was obtained by depositing simultaneously 490, 78, 182 nm under 106 W (DC), 120 W (RF) and 39 W powers for Gd, Si and Ge, respectively - CSGd490Si78Ge182. The 3rd stoichiometry was achieved in two ways. By co-sputtering 490, 107 and 148 nm under 70 W (DC), 120 W (RF) and 25 W (DC) powers for Gd, Si and Ge, respectively and by depositing 20 times repeated multilayer composed of Ge(7.4 nm)/Gd(12.3 nm)/Si(5 nm)/Gd(12 nm)-MLGe7Gd12Si5Gd12. All four films were deposited with a 4 mBar Ar pressure on a SiO_2/Si substrate at room temperature. After deposition, one sample of each thin film was subjected to the same heat treatment performed to the binary Gd-Ge films: heat treatment at 450 °C for two hours, followed by a rapid cooling under vacuum pressure (10^{-7} mBar). Figure 6.12 presents the X-ray diffractograms of the as-deposited, a), and annealed, b), thin films of the three Co-sputtered and one multilayered Gd-Si-Ge in the 20-65° 2θ interval, together with the as-deposited and annealed Pt covered pure Gd thin films. Generally, these diffractograms indicate a highly amorphous-like nature of the as-deposited thin films. The three co-sputtered films present very similar diffractograms with a wide bump-like peak centered around 2θ = 33°, similarly to what was observed in the co-sputtered binary Gd-Ge thin films (Figure 6.10 a)). Additionally an intense but also broad peak is observed centered around 2θ = 44°, which might be associated with a Si/Ge-rich phase, $Gd(Si,Ge)_{2-x}$. The CSGd490Si125Ge128 film displays three extra peaks that are likely signalling the Gd sesquioxide, Gd_2O_3, presence. Slightly different crystallinity is observed in multilayer MLGe7Gd12Si5Gd12, that despite also exhibiting a bump-like peak, shifted to lower 2θ, 31°, it does not exhibit the 2θ = 44° broad peak. Furthermore, the low-angle peaks at 21.2 and 23.8°, previously observed in the annealed Gd-Ge multilayers or the as-deposited co-sputtered binary Gd-Ge films, are also present in this Gd-Si-Ge as-deposited multilayer. In contrast with the previous mentioned systems, the annealing does not to promote crystallinity in the Gd-Si-Ge ternary co-sputtered films, as their diffractograms are very similar to the as-deposited fims. The 2θ = 44° broad peak becomes absent in the annealed films, except for the CSGd490Si125Ge128 annealed film. The multilayered MLGe7Gd12Si5Gd12 annealed thin film presents additional peaks around 38° and 44°, which signals an enhancement of the $Gd(Si,Ge)_{2-x}$ phase induced by the annealing.

The magnetization temperature dependence of the as-deposited, a), and annealed, b), thin films of the three Co-sputtered and one multilayer Gd-Si-Ge in the 20-65° 2θ interval, together with the as-deposited and annealed Pt covered pure Gd thin films, are plotted in Figures 6.13 a) and b). The magnetization profile of the three as-deposited co-sputtered films is very similar in between them and also to the previously presented binary thinnest multilayer MLGd4.5Ge2.5 and to the CSGd450Ge250: a paramagnetic behavior is observed down to a temperature T'' that lies in the 150-200 K temperature interval, where the magnetic transition begins displaying the typical ferromagnetic convex profile, reaching its center at T''' in the 75-125 K temperature interval. The temperatures T'' and T''' are higher for the CSGd490Si78Ge182, followed by CSGd490Si125Ge128

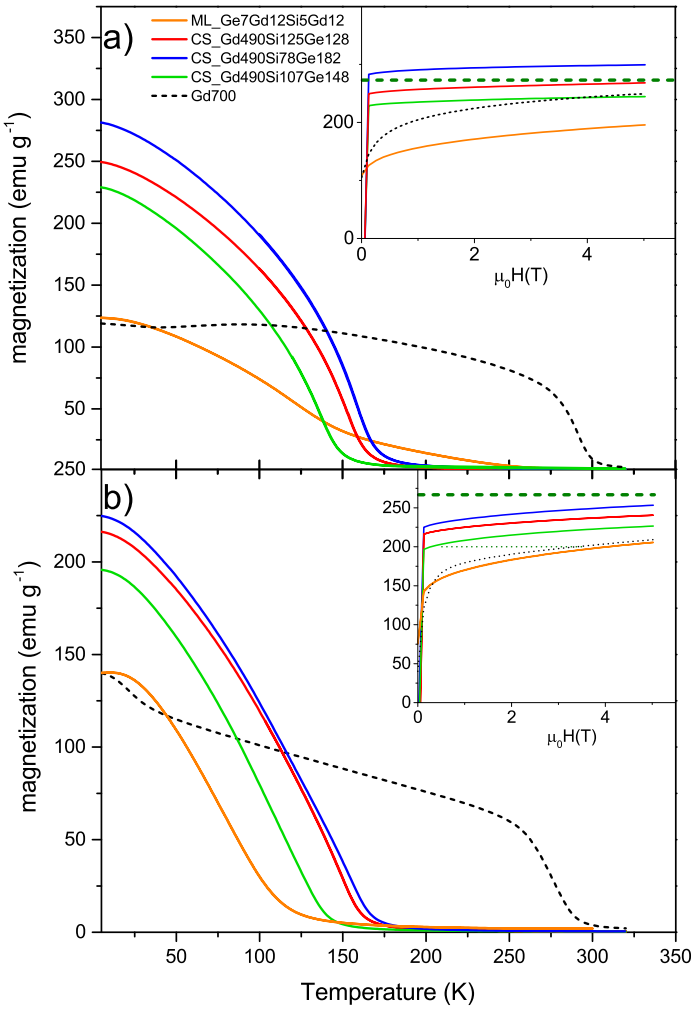

Figure 6.13 – Magnetization of the as-deposited, a), and annealed at 450°C for two hours, b), set of Gd-Si-Ge co-sputtered and multilayered thin films, plotted together with the Pt covered Gd pure thin films in the 5-330 K temperature interval. The CSGd490Si125Ge128, CSGd490Si78Ge182, CS-Gd490Si107Ge148 and the multilayer equivalent MLGe7Gd12Si5Gd12 are represented in red, blue, green and orange, respectively. In the insets of a) and b) the magnetization versus field extracted at T=5 K is plotted for all the as-deposited and annealed films.

and CSGd490Si107Ge148, hence showing no monotonous relationship with their stoichiometries. Coherently with the XRD results, the multilayer MLGe7Gd12Si5Gd12 also exhibits a differentiating magnetization behavior: a broader nature is observed with a different transition, occurring via two-steps. On cooling there is a low-magnetization ordering starting at ~ 250 K, that becomes enhanced at T < 150 K. In fact, a similar behavior had already been found in the binary multilayer $MLGd_9Ge_5$, whose individual layers thicknesses are very close to the ones deposited for this ternary multilayer. Furthermore, the three co-sputtered ternary films exhibit very large magnetization values under a 5 T applied magnetic field and at 5 K, as shown in Figure 6.13 a) inset. In particular, the as-deposited CSGd490Si78Ge182 exhibits a maximum of 299 emu g^{-1},

surpassing the experimental bulk Gd value and the theoretically expected by Gd intrinsic magnetic moment. Such result must be an overestimation caused by the significantly large errors on the calculation of the magnetization per unit of mass of these films. The CSGd490Si125Ge128, CSGd490Si107Ge148 and the multilayer MLGe7Gd12Si5Gd12 magnetic moments represent 99 %, 91 % and 73 % of the theoretical Gd value. In consonance with the XRD characterization, the three annealed co-sputtering films magnetic measurements show no significant changes in their magnetization profile, where only the CSGd490Si78Ge182 magnetic ordering temperature is decreased by few degrees, becoming closer to the CSGd490Si125Ge128 M(T) curve. Whereas, in the ternary multilayer the annealing induces relevant changes: the suppression of the high-temperature transition and the development of a plateau-like at T < 50 K. Hence, the annealed multilayer MLGe7Gd12Si5Gd12 M(T) curve resembles very much the one exhibited by the annealed multilayer MLGd9Ge5. As displayed in Figure 6.13 b) inset, the annealing induced an overall magnetization decrease in all the ternary films.

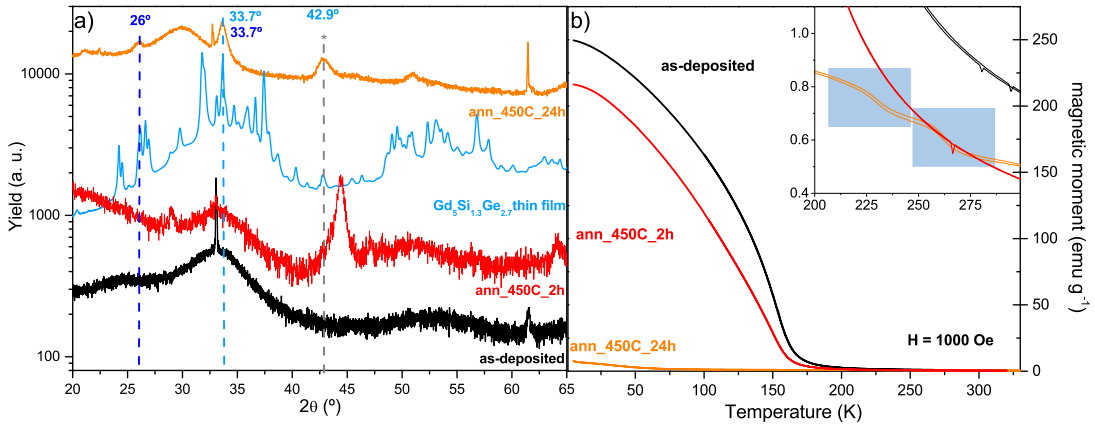

Figure 6.14 – a) X-ray patterns for the as-deposited (black) and annealed at 450°C for two (red) and for twenty four (24) hours (orange) CSGd490Si125Ge128 and the nanogranular $Gd_5Si_{1.3}Ge_{2.7}$ thin film (light blue) reported in the previous chapters. For the latter, a wavelength conversion was performed from the Synchrotron tuned wavelegnth (0.774901 Å) to the Copper wavelength (1.540598 Å). The dashed vertical lines signal Gd_2O_3 (dark blue) the 5:4 (light blue) and the sample holder (grey) associated peaks. b) Magnetization as a function of temperature of as-deposited (black) and annealed at 450°C for two (red) and for twenty four (24) hours (orange) CSGd490Si125Ge128 thin film, measured on cooling and heating under $\mu_0 H = 0.1$ T. In the inset the 200-300 K temperature window is enlarged.

Similarly to the previous sets of films, a longer annealing (24h) at 450 °C was tested and its structural and magnetic properties were evaluated as depicted in Figure 6.14 a) and b). As the as-deposited (black) and the shorter annealing (red), the longer annealing (orange) pattern also presents a bump-like nature, however the major bump is slightly shifted towards lower angles (centered at 30°). Additionally, the longer anneal-

ing also promoted the emergence of three broad peaks (26°, 33.7° and 42.9°) that were not displayed in the shorter annealing. As mentioned before, the correct assignment of each peak to a specific phase is difficult due to the large variety of possible phases, however, as highlighted in Figure 6.14 a) these three peaks can be indexed to both the Gd_2O_3 and the 5:4 phase (the $Gd_5Si_{1.3}Ge_{2.7}$ thin film pattern is displayed for the sake of comparison). The magnetic characterization gives us further hints about the phases present. In particular the strong paramagnetic-like behavior observed for the longer annealed film, as shown in Figure 6.14 b), must be associated with the Gd sesquioxide, as observed previously for the other longer annealed films. Nevertheless, a closer look, as displayed in Figure 6.14 b) inset, reveals the presence of two broadened and low amplitude magnetic transitions at T $\sim$ 230 K and 260 K. These transitions, despite small, represent a reliable evidence of the presence of two 5:4 phases - in a very small fraction - because, assuming the magnetic ordering temperatures of the different Gd Gd-Si-Ge phases at the bulk scale, only the 5:4 phases could guarantee a T_C in this temperature range. The CSGd490Si125Ge128 deposited film implies a slightly Si-rich $Gd_5Si_{2.1}Ge_{1.9}$ stoichiometry, which according with the bulk literature should imply a T_C above 275 K. The lower T_C values observed here might be a consequence of Si deficiency in the small portions of 5:4 phase - as explained in the Introduction chapter, the T_C decreases with the decrease of Si in the $Gd_5(Si_xGe_{1-x})_4$ [13,80]. Hence, despite enhancing significantly the Gd sesquioxide formation, the longer annealing also promotes a small fraction of 5:4 phases. This suggests an alternative approach to perform shorter, but higher temperature annealings, as will be tested in the next section.

6.2.2 High-temperature annealings

A second batch of thin films were prepared in order to test the influence of higher temperature (T > 500°C) ex-situ annealings. The thin film deposition procedures (multilayer and co-sputtering) followed were the same as for the first batch, with different details. Instead of Ti, Ta buffer and cap layers (15 nm) were deposited, because Ta is more chemically inert and immobile than Ti, allowing a better oxidation protection and presents less risk of inter-mixing with Gd, Si or Ge. Furthermore, in order to promote diffusion during the deposition, three different substrate temperatures were tested (200, 400, 600°C). The heat treatments also followed the same procedure as previously described: rapid heating (by inserting the quartz tube in the furnace just at the desired temperature), under a vacuum pressure (< $10x10^{-5}$ mbar), typically lasting for 30 minutes followed by quenching the tube down to the room temperature. The pure Gd as-deposited and annealed films structural and magnetic characterization can be found in section A.

6.2.2.1 Multilayered Gd-Ge films

In this second batch only the thicker Gd45Ge25 (10 bi-layers) and the Gd23Ge13 (20 bi-layers) were deposited because the lack of crystallinity observed for the thinner mul-

tilayers in Appendix 6.2.1.1.

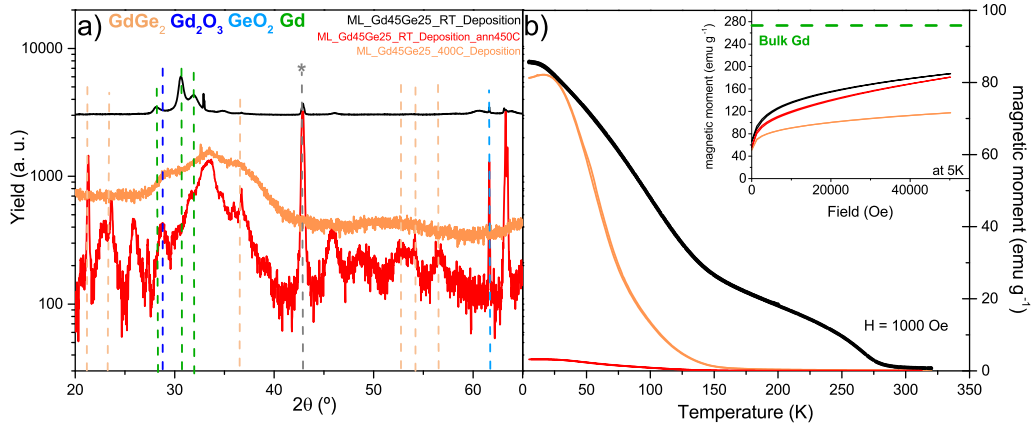

Figure 6.15 – a) X-ray diffraction patterns for the as-deposited at room temperature (black) and at 400°C (orange) and annealed at 450°C for two hours after being deposited at room temperature (red). The dashed vertical lines signal Gd_2O_3 (dark blue), GeO_2 (light blue), $GdGe_2$ (orange) and pure Gd (green) associated peaks. b) Magnetization as a function of temperature of as-deposited at room temperature (black) and at 400°C (orange) and annealed at 450°C for two hours after being deposited at room temperature (red) measured on cooling and heating under $\mu_0 H = 0.1$ T. In the inset their respective magnetizations as a function of the field up to 5 T measured at 5 K.

The XRD spectrum of the as-deposited films (at room temperature- 1st batch (black) and at 400°C (orange)) and the 1st batch - annealed at 450°C for two hours (red) are shown in Figure 6.15 a). As can be seen the MLGd45Ge25 film deposited at 400°C did not show any peaks, but instead a broad bump centered at ~ 33° associated with an amorphous Gd-Ge phase, similar to what was previously observed in the thinner GdGe multilayers and in the co-sputtered CSGd450Ge250 film. Despite not presenting sharp peaks, the broad bump shape resembles the peak structure observed for the film annealed at 450°C for two hours after room temperature deposition and contrasts with the well-defined Gd hcp structure observed in the film deposited at room temperature. Coherently, their magnetic behaviors also differ: the film deposited at 400°C orders magnetically only below 150 K, exhibiting a M(T) curve similar to the film annealed at 450°C and at 350°C for two hours after room temperature deposition, as can be seen by comparison with Figure 6.15. As explained previously, such a low ordering temperature can be associated with three different causes, where here in particular we highlight the formation of a GdGe amorphous phase whose magnetic ordering temperature occurs in 100-170 K interval[292]. Moreover its comparatively low magnetization at 5 K, plotted in Figure 6.15 b) inset, means that more than half of the Gd atoms are not magnetically correlated at this temperature.

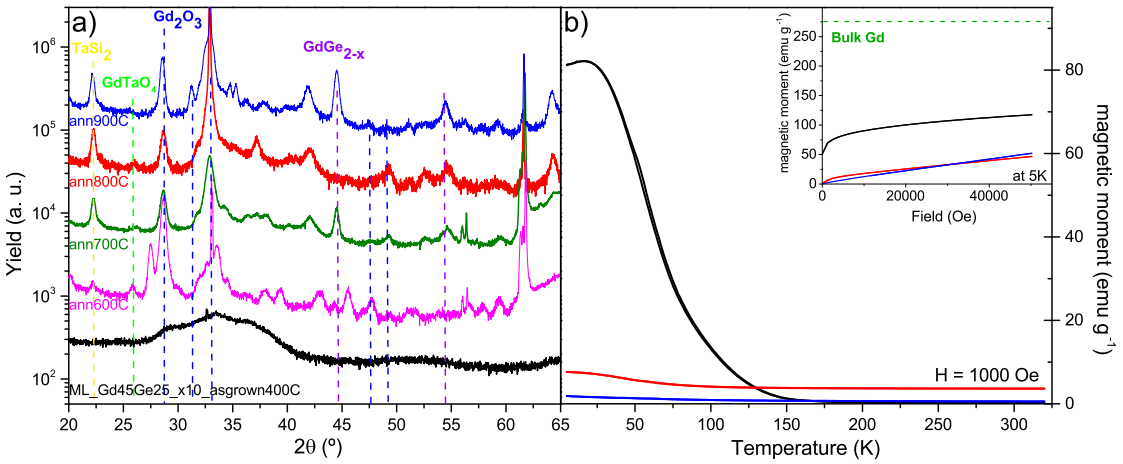

Figure 6.16 – a) X-ray diffraction patterns for the as-deposited at 400°C (black) and the same film annealed at different temperatures for 30 minutes: 600°C (purple), 700°C (green), 800°C (red) and 900°C (blue). The dashed vertical lines signal $TaSi_2$ (yellow), Gd hcp (orange), Gd_2O_3 (dark blue), $GdGe_2$ (purple) and $GdTaO_4$ (green) associated peaks. b) Magnetization as a function of temperature of the as-deposited (black) and annealed films at 800°C (red) and at 900°C (blue) for 30 minutes measured on cooling and heating under $\mu_0 H = 0.1$ T. In the inset their respective magnetizations as a function of the field up to 5 T measured at 5 K.

The film deposited at 400°C was further annealed (ex-situ) for 30 minutes at five different temperatures (600°C, 700°C, 800°C, 900°C and at 1000°C) and their XRD spectra are portrayed in Figure 6.16 a), except for the 1000°C annealed film which peeled off after the annealing. As can be seen a set of 2-3 intense reflections were found in the 25-35° 2θ interval, identical to the ones observed for the pure Gd film annealed at 600°C, 700°C and 800°C and associated with the Gd sesquioxide. These peaks emerge right after the 600°C annealing and become more intense with increasing temperature up to the 900°C signaling an expected enhanced Gd oxidation with increasing temperature. At low angle (~ 22.5°) another peak is observed that is thought to belong to a $TaSi_2$ phase, known to crystalize in this temperature range[316]. The formation of this Ta disilicide phase might occur due to the high mobility of the Si atoms in this temperature range: Si atoms from the SiO_2 or even from the Si substrate can diffuse towards the Ta buffer layer and eventually even through, intermixing with Ta immobile atoms and forming $TaSi_2$[316]. As previously observed for low-temperature annealings, the $GdGe_{2-x}$ phases are also thought to be responsible for peaks occurring at $2\theta > 45$ °. Additionally, a smaller peak is observed at $2\theta \sim 26°$ which is thought to be associated to the ternary phase $GdTaO_4$[317]. Such phase can occur specially in the interlayer region between the Ta buffer layer and first Gd layer, where Oxygen might be absorbed, both from the SiO_2 layer and laterally from air. In summary, the increasing temperature seems to stabilize and enhance the oxidation of the thin film, mostly by forming the Gd_2O_3 phase, but also other Oxygen-based phases such as $GdTaO_4$. The magnetization as a function of temperature of the film deposited at 400°C (black), annealed at 800°C (red) and at

900°C (blue) are represented in Figure 6.16 b), together with their magnetization versus applied field measured at 5 K in Figure 6.16 b) inset. This information corroborates the assumptions made after the XRD measurements, i.e. the high-temperature heat treatments promote paramagnetic phases with special emphasis to the Gd_2O_3 phase, but also to other Gd-Si-Ge-Ta silicates, paramagnetic phases. Such enhancement explains the drastic decrease on the magnetic moment value after the annealings. These results are similar to the ones obtained for low-temperature annealings of the first batch.

6.2.2.2 Co-sputtered Gd-Ge films

Three co-sputtered CSGd450Ge250 thin films were deposited at three different substrate temperatures, namely at room-temperature, 400°C and 600°C and their XRD spectra are portrayed in Figure 6.17. The three films exhibit very similar spectra: a very broad (a FWHM greater than 5°) reflection centered around 33°. Two additional bumps build up on top of the large peaks, one around 30° for the room temperature deposition and the other one around 37.5°, also observed in the as-deposited at 600°. Such additional features might be associated with larger nano-crystalline Gd grains. Moreover, these spectra are identical to the multi-layered MLGd45Ge25 deposited at 400°C, plotted in Figure 6.16. Despite not shown here, the magnetic behavior of these three films is identical among them and identical to the MLGd45Ge25 deposited at 400°C, i.e. a magnetic ordering occurring only below 150 K probably associated with amorphous-like Gd-Ge phases. The same five heat treatments were performed to the CSGd450Ge250 as-deposited at 400°C, namely at five different temperatures (600°C, 700°C, 800°C, 900°C and at 1000°C) for 30 minutes - however, as happened for the multilayered films, the highest temperature annealing lead to its peel off. A very interesting evolution occurred with the increase of the annealing temperature from a magnetic and structural point of view as can be seen in Figures 6.18 a) and b). The strong amorphous nature of the as-deposited film, evolves to a clearly crystallized system, just after 30 minutes at 600°C. By the similarities of the XRD spectrum and the suppression of the magnetization values as a function of temperature observed for the multilayered sample, MLGd45Ge25, it is correct to assume that this temperature promotes the almost complete oxidation of the thin film, resulting not only on the formation of the Gd sesquioxide phase but also others, such as $GdTaO_4$ and silicates Gd-Si-Ge-O-Ta. Nevertheless, unexpectedly at 700°C, the formation of other crystalline phases seems to prevent or at least diminish the consumption of Gd by Oxygen based phases. In particular, the enhancement of the peaks at $\sim$ 35.2°, 36.6° and 51.7°, associated with Gd-Si-Ge ternary phases, and the enhancement of the magnetization values with the increasing annealing temperature are two illustrative examples of this phenomenon.

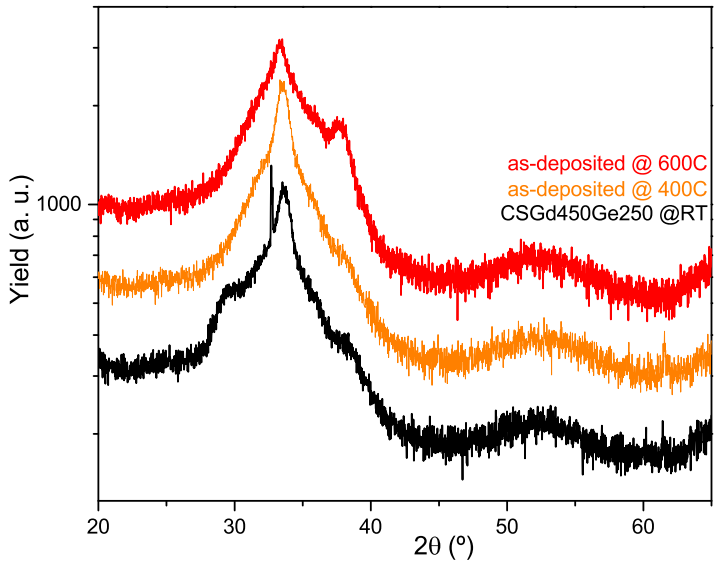

Figure 6.17 – X-ray diffraction patterns for the co-sputtered CSGd450Ge250 films as-deposited at room-temperature (black), at 400°C (orange) and at 600°C (red).

Furthermore, the emergence of thermal and magnetic hysteresis in the magnetization versus temperature and versus applied field curves for the higher temperature annealed films (specially clear in the M(T) curve of the film annealed at 800°C and on the M(H) curve on the film annealed at 900°C - Figure 6.19) reinforces the hypothesis of Gd-Si-Ge ternary phases formation. Nevertheless, it should not be disregarded that the Gd_5Ge_3 phase also exhibit field-induced transition at low temperatures[283,318]. In fact, these two phases have very similar magnetic behavior: both evolve from a paramagnetic towards a ferromagnetic phase at temperatures below 100 K (and eventually towards an AFM phase for lower temperatures). This fact makes it very hard to distinguish them and allow us to believe that the high-temperature annealings of the CSGd450Ge250 film promotes a mixture of these two phases (together with other non-magnetic ones). In Figure 6.19 the magnetization as a function of the applied magnetic field for three different CSGd450Ge250 films are presented: as-deposited thin film (black), annealed at 600°C (orange) and at 900°C (red) measured at 5 K. In accordance with the previously discussed structural and magnetic features, the thin film as-deposited at 400°C presents the highest magnetization value (66 % of the bulk Gd moment), followed by the annealed at 900°C (58 %) and the annealed at 600°C (15 %). The M(H) curve of the film annealed at 900°C is highlighted due to the presence of magnetic hysteresis, typically associated with a strong magnetostructural coupling. Although not shown here, the magnetic isotherms measured at 10 K, 20 K, 30 K and 40 K also exhibit this magnetic irreversibility that ceases to exist at 60 K, as can be seen in Figure 6.19. This feature evolves with temperature, in particular the magnetic field value at which the irreversibility starts, H_C, decreases with the increase of temperature in accordance with a PM to

a magnetic field induced FM state transition. In addition with increasing temperature, the transition becomes less sharp (possibly due to its incompleteness), occurring in a narrower field range, as becomes clear from a closer look to the 50 K isotherm curves.

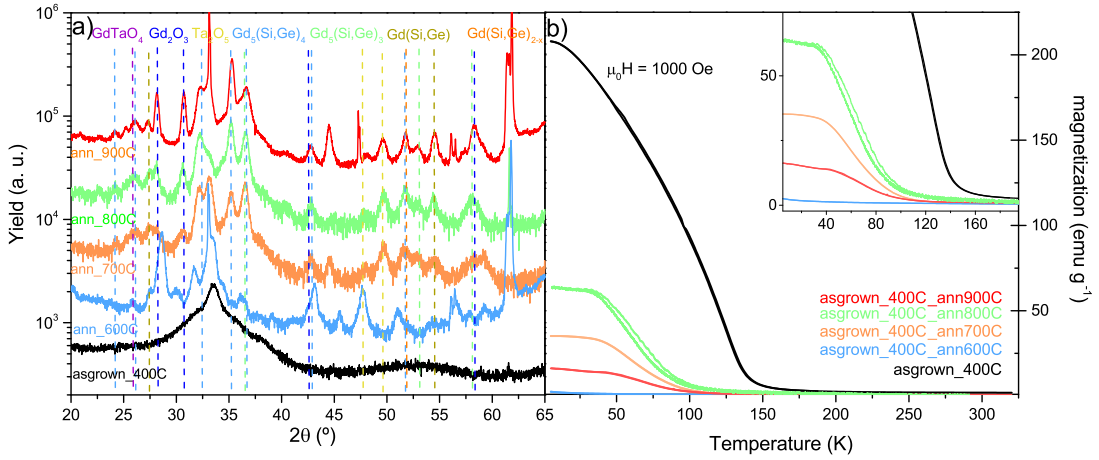

Figure 6.18 – a) X-ray diffraction patterns for the co-sputtered CSGd450Ge250 as-deposited at 400°C (black) and the same film annealed at different temperatures for 30 minutes: 600°C (light blue), 700°C (orange), 800°C (green) and 900°C (red). The dashed vertical lines signal Ta_2O_5 (light yellow), Gd_2O_3 (dark blue), $Gd(SiGe)_2$ (orange), $GdTaO_4$ (purple), $Gd_5(Si,Ge)_3$ (green), $Gd_5(Si,Ge)_4$ (light blue) and the Gd(Si,Ge) (dark yellow) associated peaks. b) Magnetization as a function of temperature of the as-deposited (black) and annealed films at 600°C (light blue), 700°C (orange), 800°C (green) and 900°C (red) measured on cooling and heating under μ_0H = 0.1 T. In the inset a closer look at the same magnetization profiles in the 0-200 K temperature range.

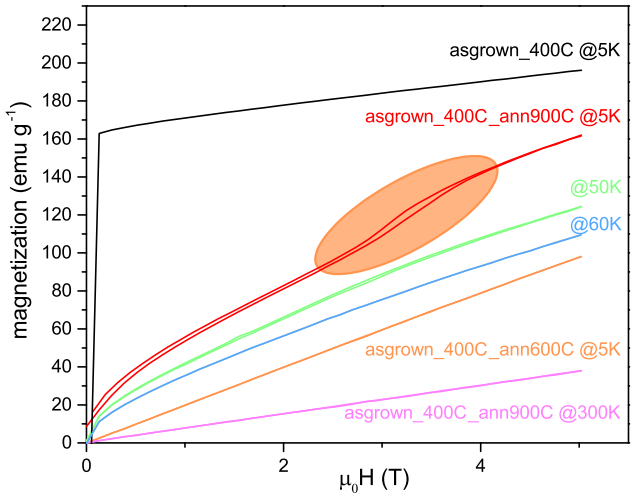

Figure 6.19 – Magnetization versus applied magnetic field of the as-deposited thin film (black), annealed at 600°C (orange) and at 900°C (red) measured at 5 K, and for the 900°C measured at 50 K (green), 60 K (light blue) and 300 K (pink) measured with increasing and decreasing field.

6.2.2.3 Ternary Gd-Si-Ge: Co-sputtered

A Ge-rich ternary composition was also tested by Co-sputtering 490, 168 and 89 nm of Gd, Ge and Si, respectively (CSGd490Si89Ge168) into a SiO_2/Si at room temperature. Based on the previous results, only the highest temperature annealings were tested (800°C and 900°C and 1000°C) and four different annealing times at 900°C (15, 30, 60 and 180 minutes) followed by air quenching. The 1000°C and 900°C for 180 minutes annealings resulted in the thin film complete peel off. The remaining annealed films were characterized by XRD and SQUID measurements, as displayed in Figure 6.20 a) and b).

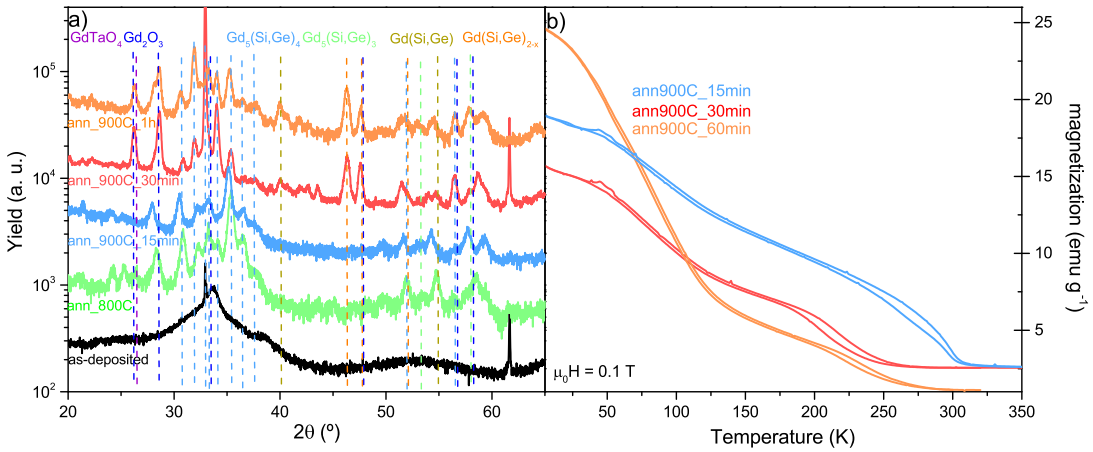

Figure 6.20 – a) X-ray diffraction patterns of the co-sputtered CSGd490Si89Ge168 as-deposited at room temperature (black) and the same film annealed at 800°C (green), 900°C for 15 (light blue), 30 (red) and for 60 minutes (orange). The dashed vertical lines signal Gd_2O_3 (dark blue), $GdTaO_4$ (purple), $Gd_5(Si,Ge)_4$ (light blue), $Gd_5(Si,Ge)_3$ (green), the Gd(Si,Ge) (dark yellow) and the $Gd(SiGe)_2$ (orange) associated peaks. b) Magnetization as a function of temperature of the annealed films at 900°C for 15 (yellow), 30 (red) and for 60 minutes (orange) measured on cooling and heating under $\mu_0 H$ = 0.1 T. In the inset the same set of magnetization profiles plus the as-deposited at room temperature (black) and annealed at 800°C (green).

As observed previously, there is a clear enhancement of the $Gd_5(Si,Ge)_4$ phase with the annealing temperature, from 800°C to 900°C. Interestingly, only 15 minutes at 900°C are enough to promote the $Gd_5(Si,Ge)_4$ phase, as illustrated by the increase in the peaks associated with this phase and more clearly by the magnetic transition at $T_C \sim$ 290 K and its correspondent thermal hysteresis, displayed in Figure 6.21 a) and b). The 30 minutes annealing XRD spectrum and M(T) curves also denotes the formation of this phase, in particular the large increase in the peaks intensity associated with this phase in the 30-35° range, and the large thermal hysteresis presented by its M(T) curves and its $T_C \sim$ 215 K. Finally, the 60 minutes annealing continues to present signals of the desired phase, with a T_C similar to that of the 30 minutes annealing, however with a smaller hysteretic area and with an intensity enhancement of XRD peaks intensities associated with secondary phases, namely at 46, 47 and 58°. There are magnetic features worth highlighting in these three films annealed at 900°C, in particular a) the significantly larger

T_C exhibited by the 15 minutes annealing (~ 290 K) in comparison with the 30 and 60 minutes annealing (~ 215 K); b) the non-zero magnetization above T_C for the 15 and 30 minutes annealings; c) the significant magnetization enhancement for temperatures below 150 K for the 60 minute annealing and finally, d), the bump-like feature observed at ~ 50 K for 15 and 30 minutes annealing. The first feature might be due to the formation of different Si-rich $Gd_5(Si,Ge)_4$ phases - which would explain the higher T_C - since, in these materials, the T_C increases with the Si content, as explained in chapter 2, section 2.4. Again, the non-zero magnetization might be due to magnetic impurities incorporated during the handling, whereas the abnormality observed around 45 K is thought to be caused by an Oxygen contamination present inside SQUID chamber - Oxygen undergoes a phase transition at this temperature and this bump-like feature is typically associated with it. Finally the peaks enhancement for the 60 minutes annealed film is attributed to the higher presence of $Gd(Si,Ge)_{2-x}$ phases, as previously observed for other annealed films.

The magnetization of the as-deposited and annealed at 900°C films measured at 5 K are depicted in Figure 6.21 a) and demonstrate the expected abrupt decrease of its maximum value with the 900°C heat treatments, from 87% (as-deposited) down to 34% (annealed at 900°C for 15 minutes) of the theoretical Gd saturation magnetization. As detailed above, such decrease results from the formation of paramagnetic phases, such as Gd oxide, that also further explain the paramagnetic linear behavior observed for these films, in contrast to the almost saturated regime observed for the as-deposited film. The film annealed for 30 minutes exhibits the same metamagnetic-like transition as previously observed for other films and possibly associated with the $Gd_5(Si,Ge)_3$ phase.

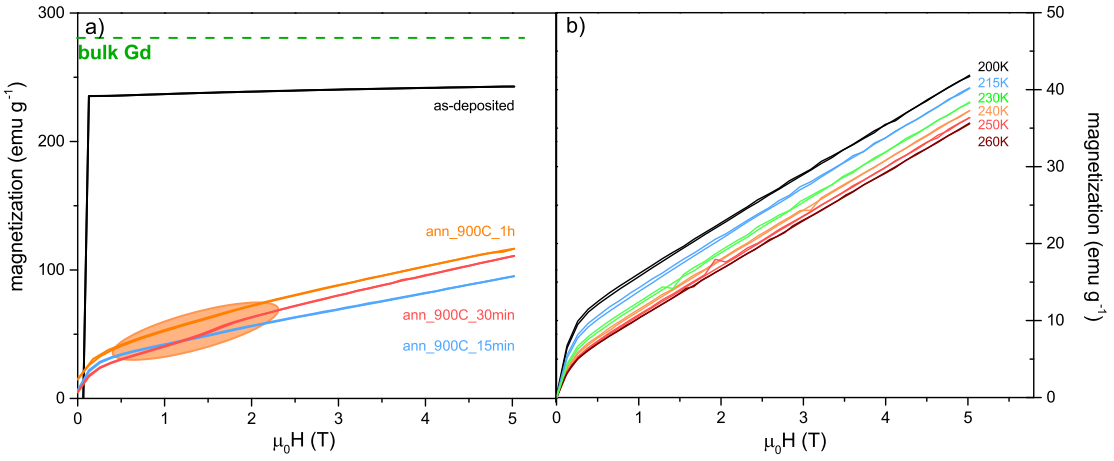

Figure 6.21 – a) Magnetization as a function of applied magnetic field at 5 K for CSGd490Si89Ge168 film as-deposited at room temperature (black) and the same film annealed at 900°C for 15 (light blue), 30 (red) and for 60 minutes (orange) . b) Magnetization as a function of magnetic field measured at 200 K, 215 K, 230 K, 240 K, 250 K and 260 K of the film annealed at 900°C 30 minutes measured while increasing and decreasing field.

In order to further inspect the magnetic properties of the film annealed at 900°C for 60

minutes, its magnetization as function of magnetic field was inspected for several temperatures within the temperature interval where the thermal hysteresis was observed, 6.21 b). A very small magnetic hysteresis is present at small field values, however no metamagnetic-like transition (as observed in the bulk counterparts) was detected along this field range and a typical paramagnetic-linear behavior is observed for all isotherms. Unfortunately, this result suggests that the minority $Gd_5(Si,Ge)_4$ phase magnetic susceptibility is smaller than the majority paramagnetic phase one and hence the latter masks the former, inhibiting the detection of metamagnetic transitions even if they do occur.

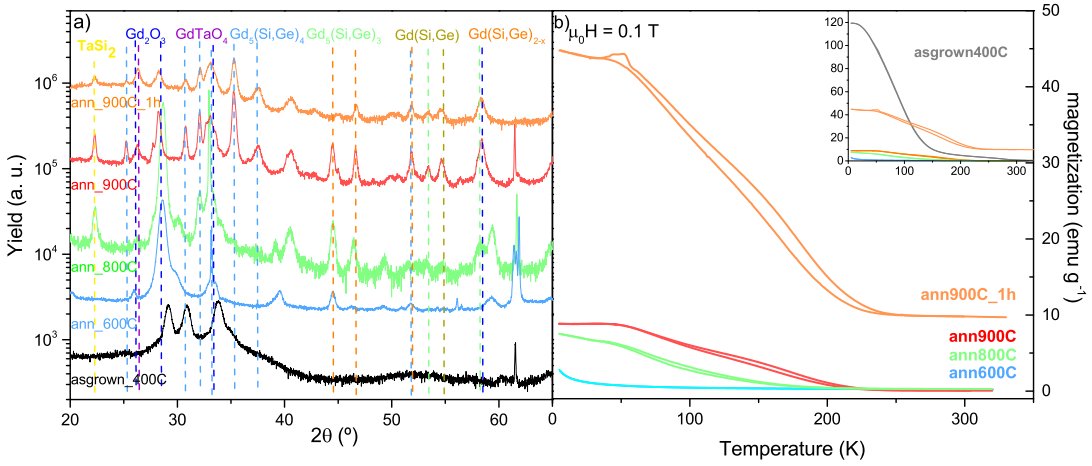

Figure 6.22 – SEM images formed by secondary, a), and backscattered, b), electrons at 500 and 50 times magnification of the top-view of the CSGd490Si89Ge168 annealed at 900°C for 30 minutes. In a) inset, a 5000 times magnified image obtained by secondary electrons of the border region between the darker and lighter regions is shown, highlighting two regions Z2 and Z1, where EDS analysis was performed. b) inset displays an image magnified 1000 times obtained by backscattered electrons, where cracks are clearly seen.

Such a high content of paramagnetic phase is corroborated by SEM analysis. There is a high density of cracks and consequently a very rough morphology as is clearly seen in the top-view images of the film annealed at 900°C for 30 minutes, in Figures 6.22 a) and b). As highlighted in Figure 6.22 a) and b) inset, the cracks occur in the darker regions areas and eventually they can lead to partial peel-off. Figure 6.22 a) inset shows a higher magnification of a region where film has been peeled and where two regions, lighter (Z1) and darker (Z2), are identified. EDS analysis in these two regions revealed that Z1 composition is SiO_2 plus Ta and Z2 is only Si. This means that the buffer layer, SiO_2, has diffused either towards the film - which would explain the high portion of Oxygen-based phases present in annealed films - or towards the substrate. Furthermore, this SiO_2 diffusion must be also related to the crack formation - as they tend to occur exactly above these darker regions.

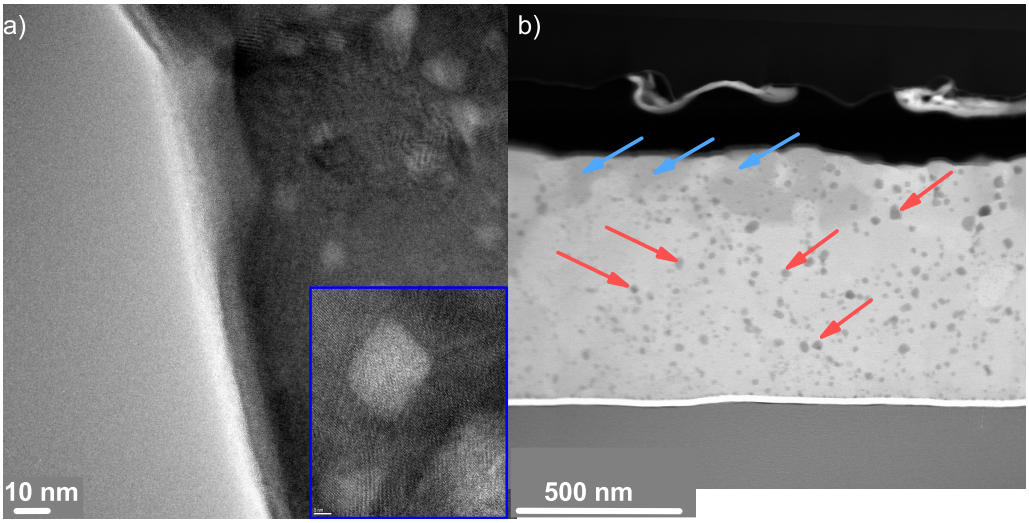

Figure 6.23 – a) Bright Field TEM (with an aperture selecting diffracted beams) cross-section overview image of the CSGd490Si89Ge1680 annealed at 900°C for 30 minutes. In the inset HRTEM image with larger magnification shows crystal order both in the dark matrix and in the lighter diamond-like feature. b) Smaller magnification image obtained in STEM mode, where EDS analysis was performed. Each arrow color correspond to the same group of crystallographic grains.

A more thorough composition analysis was performed by TEM and STEM, as displayed in Figures 6.23 a) and b). In Figure 6.23 a) the upper interface air/film is pictured where a lighter, thin and non-uniform Ta layer is clearly identified, followed by a similarly thin, but darker layer already in the film region. The thin film area is very heterogeneous, comprising a greyish matrix with darker regions of undefined shape and circular-like brighter regions. Crystallinity is observed throughout the whole film area, however the crystallographic grains size is expected to be very small, within the 10-50 nm range. In figure 6.23 b) a film cross-sectional image obtained by STEM mode is presented, where the arrows identify regions of similar compositions, as inspected by EDS. The light grey matrix was found to be composed of Gd (55%), Ge (26%), Si(3%), O(13%) and Ar(3%), e.g. a Gd-rich Gd-Ge-Si-O phase. The smaller and darker circular-like spots, signalled by the red arrows, correspond to Gd (45%), Ge (29%), Si(14%), O(8%) and Ar(4%) - corresponding to a Ge-rich $Gd_5(Si,Ge)_4$ with Oxygen penetration; and the slightly lighter regions, identified by the light blue arrows, are composed of Gd (40%), Ge (26%), Si(27%), O(7%) - being associated with a $Gd(Si,Ge)_{2-x}$ phase.

6.2.2.4 Ternary Gd-Si-Ge: Multilayered

As a result of the unsuccessful crystallization of the thinner multilayered films (both the binary Gd-Ge and the ternary Gd-Si-Ge) in the first batch, the Gd-Si-Ge ternary multilayered film of the second batch nearly doubled the individual thicknesses of the three elements, while changing slightly the stoichiometric composition from $Gd_5Si_{1.8}Ge_{2.2}$ (1st batch) towards a Si-richer composition $Gd_5Si_2Ge_2$, resulting in 10 repetitions of the same set of layers, composed by: 12 nm, 22 nm, 11 nm and 22 nm of Ge, Gd, Si and again Gd. The Gd-Si-Ge multilayered film (averaging total thickness 670 nm) was de-

posited on top of a heated (400°C) SiO_2/Si substrate and was preceded by a 15 nm thick Ta buffer and finalized with the same 15 nm Ta cap layer. Figures 6.24 a) and b) display the XRD spectra and the magnetization profile of both the as-deposited sample and the ex-situ annealed samples at 600°C (light blue), 800°C (green), 900°C for 30 minutes (red) and for 60 minutes (orange). The XRD diffraction patterns exhibit a similar evolution with the annealing temperature as was observed for the CSGd450Ge250: firstly a drastic transformation was observed after the 600°C annealing from the pure Gd hcp phase observed in the as-deposited sample towards a pattern mostly dominated by the Gd_2O_3 phase (with two high-intense peaks at 28° and 33°) and secondly a gradual evolution with the appearance of several new peaks at 22° ($TiSi_2$), 44.6° and 46.7° ($Gd_5(Si,Ge)_3$), 53.4° and 54.8° (Gd(Si,Ge)) and finally 30.8°, 32°, 35.4°, and 37.5° probably associated with $Gd_5(Si,Ge)_4$ phase. Such evolution is confirmed by the second annealing at 900°C for 60 minutes, which presents an identical spectrum as that of the annealed at 900°C for only 30 minutes. Furthermore this evolution is also corroborated by the magnetization as a function of temperature profiles for the different annealed films. The sample annealed at 600°C shows the typical paramagnetic-like behavior associated with the Gd_2O_3 phase, whereas the 800°C and 900°C annealed films exhibit an unique profile with a widespread thermal hysteresis that becomes wider with increasing temperature and time, evolving from a 150 K (800°C) to 200 K width (900°C, 60 minutes). Surprisingly the magnetization of the film annealed at 900°C for 60 minutes retains a significant value even for temperatures above 250 K, which might be associated with some FM contaminations possibly occurring during the handling of this film.

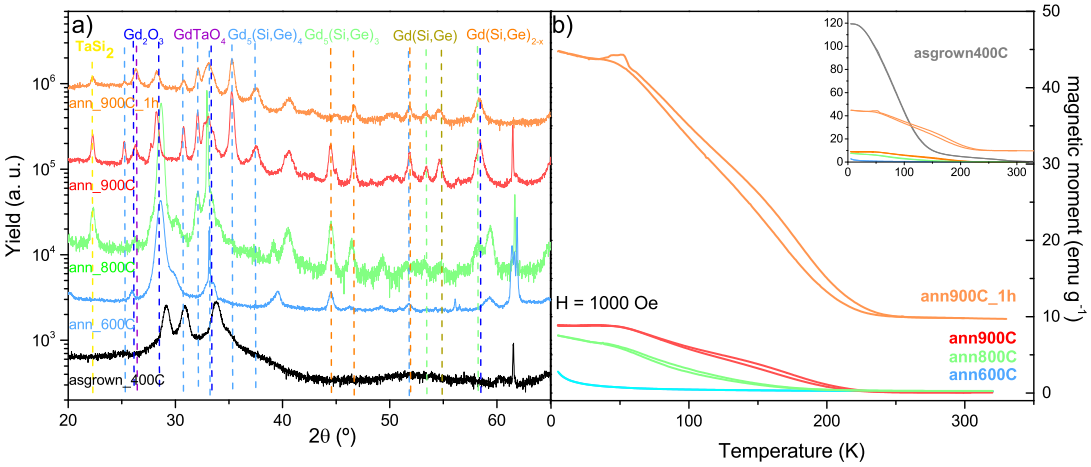

Figure 6.24 – a) X-ray diffraction patterns of the multilayered MLGe12Gd22Si11Gd22x10 as-deposited at 400°C (black) and the same film annealed at 600°C (light blue), 800°C (green), 900°C for 30 minutes (red) and for 60 minutes (orange). The dashed vertical lines signal $TaSi_2$ (light yellow), Gd_2O_3 (dark blue), $GdTaO_4$ (purple), $Gd_5(Si,Ge)_4$ (light blue), $Gd_5(Si,Ge)_3$ (green), the Gd(Si,Ge) (dark yellow) and the $Gd(SiGe)_2$ (orange) associated peaks. b) Magnetization as a function of temperature of the annealed films at 600°C (light blue), 800°C (green) and 900°C for 30 minutes (red) and 60 minutes (orange) measured on cooling and heating under $\mu_0 H$ = 0.1 T. In the inset the same set of magnetization profiles plus the as-deposited at 400°C.

As mentioned for CSGd450Ge250 the thermal hysteresis is a signature of strong magnetostructural coupling and a first-order nature of the magnetic transition in the film. Nevertheless, in contrast with the CSGd450Ge250 film, here such high-temperature thermal hysteresis (only finishes completely at 250 K) can only be attributable to a $Gd_5(Si,Ge)_4$ phase, since the other phase with large magnetostructural coupling ($Gd_5(Si,Ge)_3$) only begins to order magnetically at temperatures below 100 K. According to this reasoning it is correct to assume that the annealing temperature (up to 900°C) and the longer time (up to 60 minutes), enhances the presence of the $Gd_5(Si,Ge)_4$ phase. Higher and longer annealings were tested, namely at 950°C and at 1000°C and also at 900°C for 3h but all these films were peeled off after the annealing. The bulk $Gd_5Si_2Ge_2$ counterpart magnetization presents a very sharp transition at $\sim$ 275 K, being nearly constant both before and after that temperature. The annealed film magnetization behavior is clearly different, displaying a broad and smooth transition, beginning at around 50 K and finishing at 250 K. Such broadening might be a consequence of disorder distribution, as was previously explained for a similar broadening in the magnetization of the $Gd_5Si_{1.3}Ge_{2.7}$ nanogranular film and as was theoretically accounted by Amaral and Amaral[201]. Microscopically, such distribution might be associated with a wide grain size distribution subjected to a wide range of intrinsic pressures or to a wide range of slightly different chemical compositions. Furthermore, the lower temperature transition, in comparison with the exhibited by the bulk counterpart, might be explained by a Si-deficiency in the $Gd_5(Si,Ge)_4$ present phases due to the emergence of other phases, such as the $TaSi_2$. The magnetization of the film annealed at 900°C for 30 minutes was also evaluated as a function of the magnetic field for different temperatures as represented in Figure 6.25. Below 50 K, an irreversible metamagnetic transition was observed for fields around 2 T as had happen in the CSGd450Ge250 system, that gradually smoothes, disappearing above 50 K. In the 50-100 K range, no metamagnetic transition is observed, but instead a broadened hysteresis between the increasing/decreasing field curves. Unfortunately, the diamagnetic contribution of the Si substrate shadows the pure magnetic response of the film, inhibiting the observation and understanding of the thin film magnetization versus field behavior for temperatures above 100 K. The magnetization versus field curves at 5 K for all MLGe12Gd22Si11Gd22x10 films shows a large drop of the maximum magnetization value as a function of increasing temperature, from $\sim$ 60% for the as-deposited at 400°C down to 34% for the annealed at 600°C, decreasing slightly for the higher temperatures annealings, 31% at 800°C and 900°C.

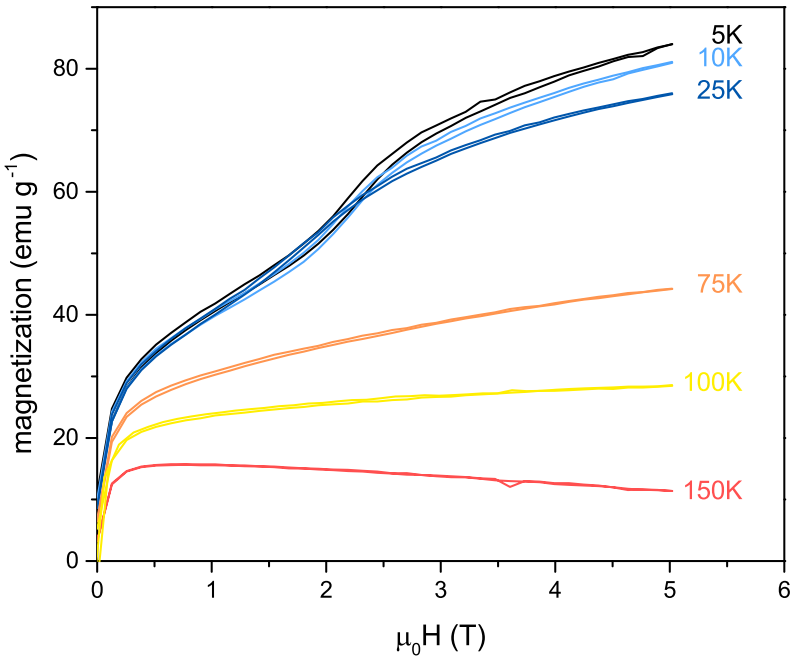

Figure 6.25 – Magnetization versus applied magnetic field of the MLGe12Gd22Si11Gd22x10 annealed at 900°C for 60 minutes measured at 5K (black), 10K (light blue), 25K (dark blue), 75K (orange), 100K (yellow) and 150K (red), under increasing and decreasing field in the 0-5.5 T interval.

In order to better understand the different phase distribution along the thin film and the effects of high-temperature annealings at the surface, both SEM and TEM analysis were performed at the MLGe12Gd22Si11Gd22x10 annealed at 900°C for 60 minutes. SEM images of the top of the film show several morphological features, as shown in Figures 6.26. The Figure 6.26 a) displays an image constructed by backscattered electrons, where several circular and darker regions are present. Within these circular regions, it is possible to distinguish linear and connected cracks and a different morphology than the rest of the thin film. Their darker color means that the phases formed in these regions have a smaller atomic mass than the rest of the film: i.e. these regions are most probably Oxygen based phases as Gd_2O_3 and $GdTaO_4$ in contrast with the higher atomic mass phases, such as Gd(Si,Ge), $Gd_5(Si,Ge)_3$ and $Gd_5(Si,Ge)_4$ present in the remaining area. The most plausible explanation for this phenomena, is the significantly different thermal expansion coefficients of the different phases formed during the heating (in the annealing process) are sufficient to promote cracks at the surface of the film, making the Ta cap layer discontinuous and consequently opening gaps where the Oxygen could easily penetrate and form Oxygen based phases. In Figure 6.26 b) a more general overview of the film is given, demonstrating the large concentration of these circular features, corroborating the analysis of the XRD and magnetization results.

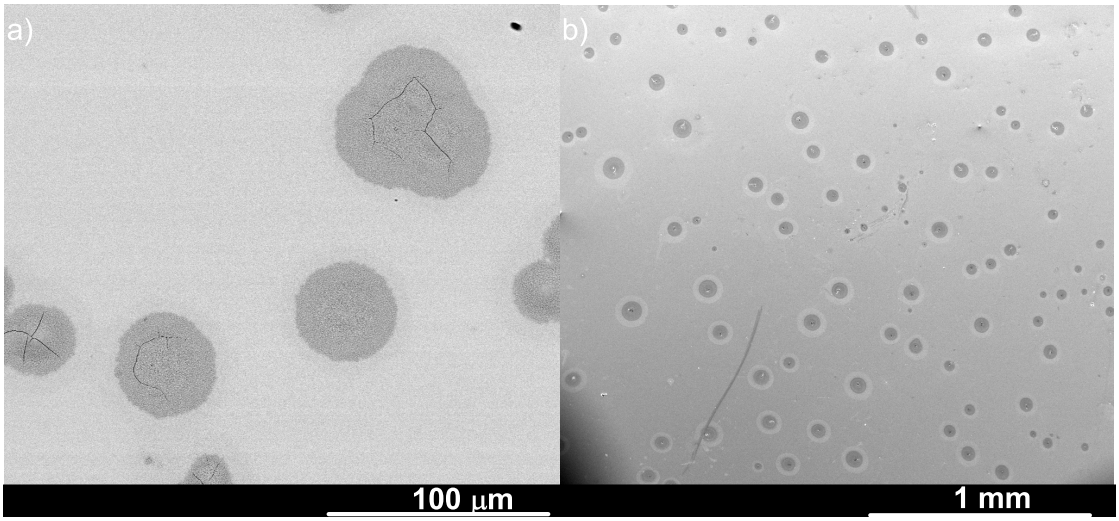

Figure 6.26 – SEM images formed by backscattered, a), and Secondary, b), electrons at 1000 and 75 times magnification of the top-view of the MLGe12Gd22Si11Gd22x10 annealed at 900°C for 60 minutes.

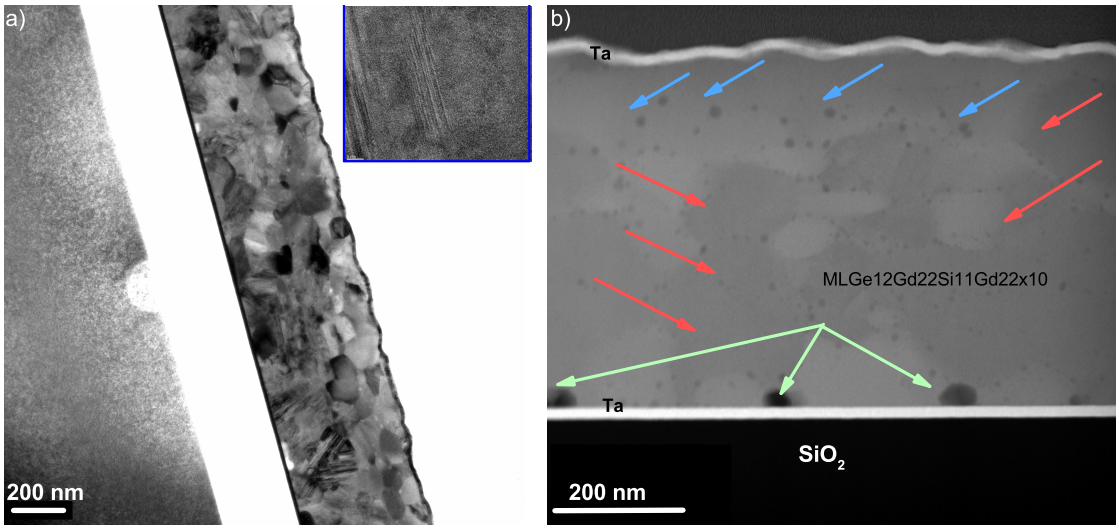

Figure 6.27 – a) Bright Field TEM (with an aperture selecting diffracted beams) cross-section overview image of the MLGe12Gd22Si11Gd22x10 annealed at 900°C for 60 minutes. A highly magnified HRTEM image exhibits the atomic periodicity, and hence crystallinity. b) Smaller magnification image obtained in STEM mode, where EDS analysis was performed. Each arrow color correspond to the same group of crystallographic grains.

The thin film cross-section profile was evaluated by TEM. As seen in Figure 6.27 a) a plethora of different grains is present in the thin film, showing high atomic periodicity - crystallinity, as highlighted in Figure 6.27 a) inset - demonstrating the high-polycrystalline character of the thin film. Figure 6.27 b) displays a more rough cross-sectional view obtained by STEM mode where EDS analysis was performed for different regions, marked with the arrows. Three main different phases were identified, namely: the small and darker circular spots, signalled by the light blue arrows, being Gd (49%), Ge (25%), Si(5%) and O(21%) - corresponding to a $Gd_5(Si,Ge)_3$ with Oxygen penetra-

tion; the larger circular regions near the Ta buffer layer, signalled by the green arrows, Oxygen-rich phase with Gd(36%), Ge (11%), Si(4%), O(38%) and F (9%) - possibly associated with Gd_2O_3 and other Oxygen rich phases; and the larger darker areas, signalled by the red arrows, with Gd(53%), Ge (21%), Si(20%), O(5%) and F (1%) - associated with the $Gd_5(Si,Ge)_4$ phase. By image contrast, it is possible to estimate a $\sim$50% $Gd_5(Si,Ge)_4$ phase fraction. All the atomic amounts were estimated with an error smaller than 1%. Although it is not possible to make a quantitative analysis of the phase amounts present in the film, there are some interesting phenomena worth highlighting: 1. the general Si-deficiency in all identified phases; 2. the Oxygen presence throughout the whole film thickness; 3. the formation of large regions rich in Oxygen next to the Ta buffer layer which might be a consequence of cracks occurring also at the bottom of the thin film (as at its top) that promote the Oxygen diffusion from the SiO_2 layer towards the film.

6.3 Discussion and Conclusions

Although additional studies are necessary to completely track the different phase formations in these various thin film systems, the morphological, structural and magnetic analysis performed allow to uncover the principal phenomena occurring during the deposition and annealing in these thin films. An overall view provides important information, such as: the pure Gd thin film deposited at room-temperature on top of the substrate used for all thin films here presented (SiO_2/Si) crystallizes in the hexagonal close packed structure (hcp), similar to what is typically observed in its bulk counterpart. The same hcp structure was also found for the thicker multi-layered films deposited at room temperature, whereas the films deposited at higher temperatures (400 °C and 600 °C) did not exhibit crystallinity, but rather a typical bump-like peak centered at 30°, typical of amorphous Gd[280,319]. Similarly, all the other as-deposited films, multilayers and co-sputtered, exhibit an amorphous/nanocrystalline-like nature. The Gd crystallization inhibition in these latter films must be due to their very small individual Gd thickness (<20 nm for the multilayered systems) or to the additional disorder introduced by a simultaneous sputtering of Ge and/or Si. Vaskovskiya and co-workers have reached similar conclusions in their Gd/Si and Gd/Cu multilayered system studies, where they have found that Gd individual layers with thickness $\sim$ 15 nm, crystallize in hcp phase even with nanometer size grains (5 nm diameter)[306]. Moreover, they observed a cross-over, from crystalline to amorphous nature, for Gd individual thicknesses below 10 nm, which is in complete accordance with the results presented here. An annealing at 450 °C for two hours was found to be enough to promote Ge-diffusion into the Gd layers in all the binary multilayers, as clearly illustrated by the SEM images 6.4. For the thicker multilayers, the annealing destroys the pure Gd hcp structure, revealed by the absence of the XRD peaks and the suppression of the high-temperature magnetic transition, but

promotes the formation of multi-phases, including: Gd_2O_3, GeO_2, the Ge-rich phases as $GdGe_{2-x}$ and $GdGe_{1.5}$, and Gd-rich phases as Gd_5Ge_3 or the Gd_5Ge_4. Due to the overlap of diffracted peaks associated with these different phases, in particular in the 20-40° 2θ interval, an error-free phase attribution is not possible. Very likely, there is oxide formation of both Gd (mostly) and Ge, as is supported by the appearance of diffracted peaks and the clear growth of PM contribution to the overall magnetization of the annealed films. Is is expected that a significant amount of Gd is consumed by the Gd oxidation, which unbalances the deposited Gd/Ge 5:4 atomic ratio, changing it up to 1:1 or even 1:1.5, hence favoring the Ge-rich phases formation. Furthermore, in accordance with the Gd-Ge phase diagram, the Ge-rich phases formation is certainly favored as it is the phase that should occur first, at lower temperatures. According to Chen and co-workers, for a Gd molar fraction equal to or below 0.5 (in a Gd-Si system), the estimated free energy of the different Gd-Si phases is significantly lower for the $GdSi_2$/$GdSi_{2-x}$ phases, as represented in Figure 6.28 b)[320].

Several previous reports on the analogous Rare-earth/Silicon binary thin film systems support this argument, by reporting the early formation of the equivalent $GdSi_{2-x}$[303,321,322]. In particular, Chen and co-workers have demonstrated that the Si/Ge -rich phase forms preferentially in the rare-earth/Si-Ge interlayer region[320] together with an amorphous a-interlayer, as schematically illustrated in Figure 6.28.

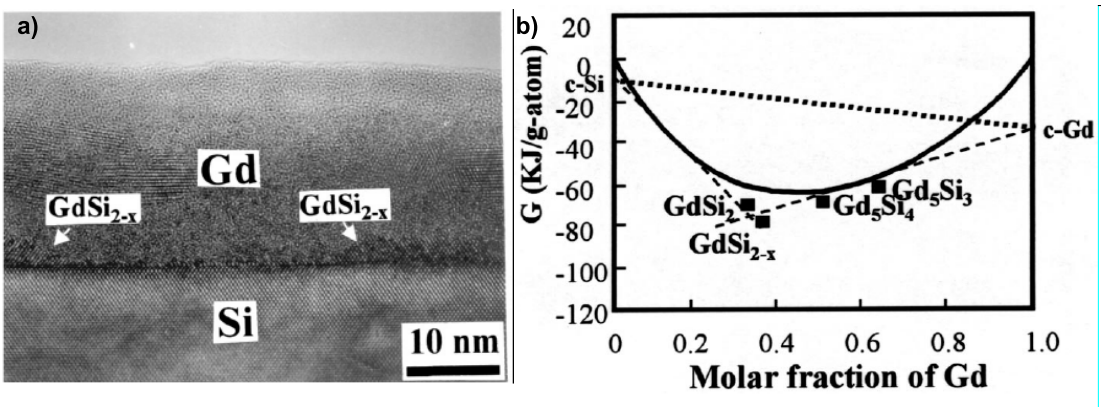

Figure 6.28 – a) Cross-section transmission electron microscopy images of an annealed (250 °C for 60 minutes) ~ 15 nm thick Gd film deposited on top of a Si wafer, followed by the deposition of amorphous silicon (20 nm) to serve as capping layer. Both the amorphous a-interlayer and the Si-rich phase $GdSi_{2-x}$ are formed at the interface between Gd and Silicon substrate. b) the Gibbs Free Energy of different Gd-Si binary crystalline phases is plotted as function of Gd molar content. Figures extracted from reference[320].

Therefore, as shown in Figures 6.29 and 6.28, the Rare-Earth crystalline silicide $RESi_{2-x}$ was found to nucleate at the a-interlayer/Si interface in films after prolonged and/or high-temperature annealing. Simultaneous growth of the a-interlayer and crystalline phase was observed, however the growth rate of the amorphous a-interlayer was faster than the growth of epitaxial silicide phase in annealed samples. Essentially, they have shown that there is a competition between the growth of epitaxial silicide regions

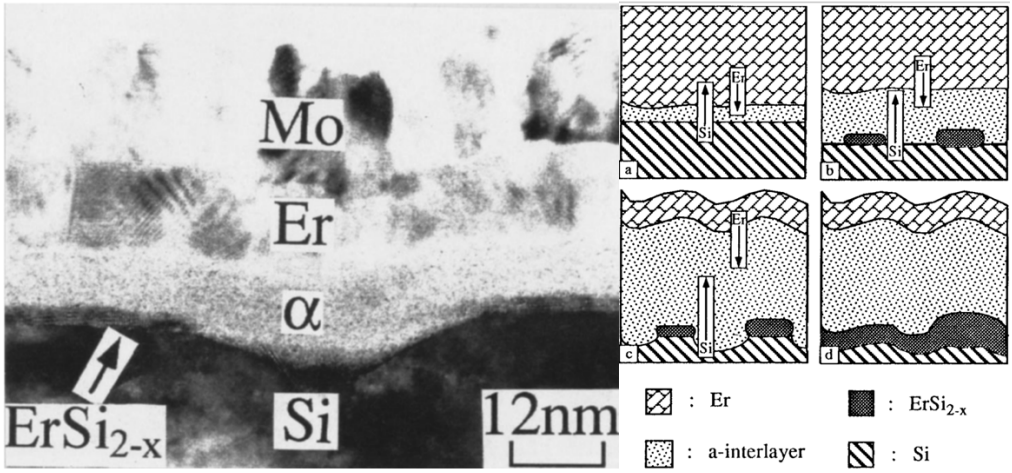

Figure 6.29 – At the left, cross-section transmission electron microscopy images of an annealed (270 °C for three hours) ~ 15 nm thick Er film deposited on top of a Si wafer, followed by the deposition of Molybdenum (20 nm) to serve as capping layer. Both the amorphous a-interlayer and the Si-rich phase $ErSi_{2-x}$ are formed in the region between the Rare-Earth and Silicon layers. At the right, a schematic representation of the Si and Er diffusion and the formation of the a-interlayer and the $ErSi_{2-x}$ phase is shown as a function of time for 270 °C annealings. Figure extracted from reference [303].

in the coarsening process with the growth of an amorphous interlayer. A high density of recessed amorphous regions was found to form between isolated epitaxial silicide regions which led to uneven silicide/Si interfaces and eventually pinholes or cracks in the silicide films at high temperatures. These results suggest a similar phenomena to be occurring in the Gd-Ge multilayers here presented. The "*thicker*" multilayers exhibit a similar competition between the crystalline $GdGe_{2-x}$ and the amorphous Gd-Si-Ge a-interlayer. Whereas, for the "*thinner*" multilayers, the amorphous a-interlayer dominates the competition leaving virtually no Gd or Ge to form the crystalline $GdGe_{2-x}$ phase. This hypothesis is supported by the broad peak observed in the these multilayers and is reinforced by temperature interval where the magnetic ordering occurs (100-150 K interval, as was previously observed for a wide range of amorphous Gd alloys [306,323,324]. Similarly, in the binary CSGd450Ge250 and in the three ternary co-sputtered films, the amorphous GdGe phase is dominant, despite the absence of the interlayers region. In contrast, the Gd-rich co-sputtered film CSGd600Ge100, undergoes a clear amorphous-crystalline phase transformation during the low-temperature annealing. The Gd excess, initially thought to account for the Gd oxidation, unbalanced the sensitive 5:4 Gd/Ge atomic ratio, favoring the crystallization of the Gd_5Ge_3.

The second batch of thin films, deposited to test high-temperature annealings, were covered with a 15 nm Ta cap layer instead of the Ti, used in the first batch. Unfortunately, despite Ta being more immobile and less-reactive with other elements than Ti, it was not enough to inhibit neither Gd oxidation or Ta-Si and Gd-Ta-O silicates crystal-

lization, as coherently demonstrated by the XRD, SQUID and SEM analysis of different pure Gd thin film annealings. The formation of these secondary phases is explained by the oxygen easy film penetration. SEM images (Figure A.5) of the annealed films display several cracks at the films surface, leaving a large cross-sectional area for the Oxygen to penetrate, which is even further enhanced by the high temperatures applied. As explained by Choi and co-workers[325] and schematically illustrated in Figure A.5 b), the different thermal expansions of the phases formed during the annealing (Ta, RE sesquioxide, Gd-O-Si/Ge and Si/Ge-rich phases) and near the film surface, lead to compressive stresses during the rapid cooling process after annealing, that can eventually be large enough and generate cracks at the surface.

The binary multilayered films exhibit a similar behavior as the pure Gd films, i.e. the high-temperature annealings promote the Oxygen formation throughout the thin film leading to the formation of Gd-O and Gd-Ta-O phases (mostly Gd_2O_3), as well as some minor $GdGe_{2-x}$ and $TaSi_2$ phases. These $GdGe_{2-x}$ phases are expected to form mostly at the interface region between a Gd and a Ge layer, as observed for the low-temperature annealings. The appearance of a $TaSi_2$ phase unveils that most probably at such high temperatures Si dissociates from Oxygen in the SiO_2 buffer layer and diffuses towards the Ta buffer layer. Furthermore, in contrast with the room-temperature deposited, the films deposited at 400°C did not crystallize at the Gd hcp structure, but instead in an amorphous/nanocrystalline Gd phase.

Similarly, despite the more homogeneous distribution of Gd and Ge, the as-deposited co-sputtered GdGe thin films also present an amorphous nature, regardless of the deposition temperature up to 600°C. However, differently than the multilayered system, here the high-temperature annealings, specially at T > 700°C, do promote a minority Gd_5Ge_4 formation, as confirmed by the structural and magnetic properties inspection. Unfortunately the formation of Gd oxide phases continues to be the dominant one, hence inhibitting the formation of a higher Gd_5Ge_4 phase amount. The high-temperatures (up to 900°C) applied to these films are closer to the Gd_5Ge_4 formation temperature for bulk compounds (1600°C) as presented in Figure 6.1 and Reference[269]. It is plausible to assume that in the case of no Gd consumption by Gd based oxides phases, this annealing temperature (900°C) or even at higher temperatures would allow the enhancement of the Gd_5Ge_4 phase amount. Moreover, a magnetic-field induced transition was observed in the film annealed at 900°C, which was attributed to a Gd_5Ge_3 phase, due to the similarities, i.e. magnetic irreversibility, hysteretic area decrease with increasing temperature and disappearance of hysteresis for T > 50 K with the Gd_5Ge_3 bulk counterpart[283,318]. The Gd_5Ge_3 phase is also expected from the Gd-Ge phase diagram, being the Gd-rich neighbor of the Gd_5Ge_4 phase.

For temperatures higher than 800°C, the annealings of the ternary multilayered and co-sputtered Gd-Si-Ge were enough to promote (a minority) fraction of the desired $Gd_5(Si,Ge)_4$, as evidenced by the XRD and the magnetic properties. In particular their magnetization thermal hysteresis evidences the strong first-order character presented

by this phase, in accordance with its bulk counterpart. The thin film magnetization thermal hysteresis was found to be broader, ~200 K, than the one found in typical bulk counterparts, ~20 K. This broadening is thought to be related with a large composition range of Si/Ge ratio, x in $Gd_5(Si_x,Ge_{1-x})_4$, probably being formed at different Gd-Si, Gd-Ge interlayer regions, which causes a range of different T_C [26], as theoretically expected [201]. As observed in the CSGd450Ge250 film, here the $Gd_5(Si,Ge)_4$ only begins to form at T > 800°C, whereas until this temperature the Gd sesquioxide associated peaks completely dominate the XRD spectrum. Moreover, a similar magnetic-field induced metamagnetic transition at low temperature associated with the $Gd_5(Si,Ge)_3$ is also observed in this system. Despite these interesting results, the Gd-oxide based phases still dominate the film overall structure and magnetism, as signalled by the strong attenuation of the magnetization absolute value with annealing temperature. In fact the low-moment presented by the film becomes masked by the diamagnetic behavior of the Si substrate (which has a volume more than 100 times larger than the film - Si substrate thickness is typically between 100-400 μm), preventing the expected observation of magnetic hysteresis in magnetization isotherms measured in the thermal hysteresis interval (50-250 K), and consequently a correct estimation of the magnetic entropy change. The SEM and TEM images allowed to confirm the plethora of different structural phases and the nanometer-size crystallographic grains, with the $Gd_5(Si,Ge)_4$ grains being in the order of 100nm, whereas the $Gd_5(Si,Ge)_3$ grains are in the order of ~ 10 nm. Moreover the largely irregular and with high cracks density Ta cap layer observed in TEM cross-section and SEM top view images allow to explain the oxygen high-penetration into the film. Additionally also a large Oxygen penetration was detected at the bottom of the film, near the Ta buffer layer, probably arising from Oxygen diffusion from the SiO_2 buffer layer. Such results reinforce the necessity to rethink the whole multilayered structure. In particular the presence of the thick SiO_2 layer, initially added to mimick the nanogranular $Gd_5Si_{1.3}Ge_{2.7}$ thin film conditions, is dispensable as it seems to have two deleterious effects: 1) by acting as an Oxygen source to the $Gd_5(Si,Ge)_4$ film and 2) adding complexity to the already complex thermal expansion behaviors of the different phases formed in the whole system, which leads to enhanced induced stress and eventually helps the crack formation observed in these systems. The selection of the buffer and cap layers and their thicknesses must also be evaluated with care due to the high-temperature annealings necessary for the $Gd_5(Si,Ge)_4$ crystallization. Mardani and co-workers have shown that TaN buffer and cap layers are more effective in preventing oxidation and the formation of cracks of a Cu film than pure Ta (buffer and cap layer) [326]. Although the system here presented is different, TaN should be tested in a future work. In comparison with the ternary multilayered, the co-sputtered ternary film CSGd490Si89Ge168 shows even higher Gd-oxide based phases, but also evidences the formation of the $Gd_5(Si,Ge)_4$ phase after high-temperature annealings (T > 800°C). Interestingly, its magnetization profile as a function of temperature shows a sharper and irreversible transition at T_C ~ 204 K (on cooling) with a smaller thermal hysteresis of only 14 K ($T_{C'}$ ~ 218 K on heat-

ing), in comparison with the 200 K exhibited by the multilayered film. The sharper T_C allows to infer that there is a narrower Si/Ge ratio range in the $Gd_5(Si_x,Ge_{1-x})_4$ phase and the observed T_C matches the one expected from the stoichiometric Gd, Si and Ge deposited amounts, namely the $Gd_5Si_{1.5}Ge_{2.5}$ composition[110]. However the shorter, 15-minutes, 900°C annealing yielded a higher T_C ($\sim$ 284 K), which is associated with a Si-richer $Gd_5(Si_x,Ge_{1-x})_4$ composition, close to $Gd_5Si_2Ge_2$[26], whereas the longer, 60-minutes, resulted in a similar T_C as the one observed for 30 minutes. Therefore, the T_C evolution with annealing time suggests that there is a specific minimum time for the Si,Ge to diffuse and reach homogenization within the $Gd_5(Si_x,Ge_{1-x})_4$ phases. Apparently, 15 minutes are enough to crystallize the $Gd_5(Si_x,Ge_{1-x})_4$, however a longer time is required for the Si,Ge homogenization.

In this case, it is also not possible to observe the magnetic hysteresis expected for magnetization isotherms measured as a function of field for fixed temperatures along the interval where temperature hysteresis was observed. The large paramagnetic susceptibility of the majority Gd-oxide based phases masks the ferromagnetic and possible metamagnetic behavior of the minority $Gd_5Si_{1.5}Ge_{2.5}$ phase. This film also exhibits much smaller $Gd_5(Si,Ge)_4$ crystallite grains (10 nm), in contrast with the multilayered film. Therefore, the two systems (multilayered and co-sputtered) present a large susceptibility to Oxygen penetration, probably both by the top (due to the crack formation) and by the bottom (the Oxygen diffusion from the SiO_2 is clearly observed in the SEM top-view images 6.22).

6.4 Conclusions and future work

In summary, the ”thicker” Gd-Ge multilayers (ML10Gd45Ge25 and ML20Gd23Ge13) mimic the pure Gd film, by crystallizing in the same hcp structure as a pure Gd film deposited at room temperature. All the other samples, multilayers and co-sputtered, exhibit an amorphous/nanocrystalline-like nature both at room temperature or at higher temperatures (400 and 600°C). Such inhibition in these latter films must be due to their very small individual Gd thickness (< 20 nm, on the multilayered systems) or to the additional disorder introduced by a simultaneous sputtering of Ge or Ge and Si, similar to what was observed in a previous report[306], where they found that there is a crossover, from crystalline to amorphous nature, for Gd individual thicknesses below 10 nm. It was shown that the low-temperature annealings, namely at 450 °C, are sufficient to activate Ge/Si-diffusion into the Gd layers in all the multilayered systems. In the thicker multilayers, it destroys the pure Gd hcp structure, but promotes the formation of a plethora of different phases, including: the Gd oxide, Gd_2O_3, the Ge oxide, GeO_2, the Ge-rich phases as $GdGe_{2-x}$ and $GdGe_{1.5}$, and a minority of Gd-rich phases as Gd_5Ge_3 or the Gd_5Ge_4. There is a favouring of the Ge/Si-rich crystalline ($Gd(Si,Ge)_{2-x}$) and amorphous (a-interlayer) phases because not only they form at low-temperature (ac-

cording to Gd-Ge/Gd-Si bulk phase diagrams), but also several previous reports have reported their formation in pure Gd thin films deposited in Si/Ge substrates (or equivalent buffer layers). In particular, it has been shown that they form preferentially in the rare-earth/Si-Ge interlayer region together with an amorphous a-interlayer. In the "thicker" Gd-Ge multilayers, there is a competition between the crystalline $GdGe_{2-x}$ and the amorphous a-interlayer. Whereas, for the "thinner" multilayers, the amorphous a-interlayer dominates the competition, leaving virtually no Gd or Ge to form the crystalline $GdGe_{2-x}$ phase. This hypothesis is supported by the broad peak observed in the "thinner" multilayers and is reinforced by temperature interval where the magnetic ordering occurs (100-150K interval, as was previously observed for a wide range of amorphous Gd alloys[306,323,324]. Similarly, in the binary CSGd450Ge250 and in the three ternary co-sputtered films, the amorphous Gd(Ge,Si) phase is dominant, despite the absence of the interlayers region. The high-temperature annealings test demonstrated that the majority of the Gd present in the film forms different Gd-oxide based phases beginning with 600°C but lasting up to 900°C. Such a high content of Oxides phases is explained by the easy oxygen penetration into the film both through the top (due to the crack formation) and the bottom (due to oxygen diffusion from the SiO_2 buffer layer) of the film. Hence, in a future work, in order to prevent oxygen diffusion towards the film, different methods should be tested, including: different buffer and cap layers, e.g. the more immobile TaN; similar annealings under ultra high-vacuum conditions; pulsed laser annealings (to promote higher temperature and localized heating of the material); a higher-temperature heated substrate, namely at 800/900°C, depositions; Nevertheless, the higher-temperature annealings, namely at 800°C and 900°C in the co-sputtered and multilayered ternary films, are enough to promote the crystallization of different phases such as $Gd(Si,Ge)_{2-x}$ (as the low-temperature annealings), Gd(Si,Ge), $Gd_5(Si,Ge)_3$ and the desired $Gd_5(Si,Ge)_4$. In fact, particularly for the ternary multilayer, a large amount ($\sim$50%) of $Gd_5(Si,Ge)_4$ phase fraction was found after 900°C annealing. Moreover, a refined transition temperature tuning (within the 5:4 set of phases) was also shown possible in the co-sputtered ternary films, through the time control of a 900°C annealing. The irreversibility presented by the magnetization profiles as a function of temperature suggests a first-order nature for the magnetic transition and consequently the strong magneto-volume coupling exhibited by its bulk counterpart and responsible for its giant magneto-responsive properties (magnetocaloric, magnetostriction and magnetoresistive effects).

CHAPTER 7

Conclusions and Perspectives

In this final chapter, the most important achievements described throughout this thesis will be summarized. The results answering the questions formulated in the introduction chapter will be remarked, and new questions opening future work paths will be stated. At the end, the perspectives for future work will be indicated as well as some promising preliminary results.

In summary, this thesis was devoted to the preparation, basic and advanced characterization of $Gd_5(Si_xGe_{1-x})_4$ nanostructured materials. It can be roughly divided in two parts. (i) basic and advanced characterization of nanogranular $Gd_5(Si_xGe_{1-x})_4$ thin film and (ii) nanofabrication, detailed characterization and optimization of $Gd_5(Si_xGe_{1-x})_4$ continuous thin films.

In the first part of the thesis, a thorough and advanced characterization was performed on a $Gd_5(Si_xGe_{1-x})_4$ nanogranular thin film prepared by femto-second pulsed laser deposition, which included the magnetocaloric effect, thermal expansion, electrical resistivity and how these properties varied along different thermal treatments and cycling. In the second part, the process of optimizing the 5:4 phase, $Gd_5(Si_xGe_{1-x})_4$, is thoroughly described following two main approaches: multilayered and co-sputtered continuous thin films. Detailed structural, magnetic and morphological properties of continuous thin films were evaluated as a function of different ex-situ thermal treatments. Based on these complementary analysis, an optimized process is suggested.

7.1 Main conclusions

7.1.1 $Gd_5(Si,Ge)_4$ nanogranular thin film displaying large magnetocaloric effect

Along the first part of chapter 4 we presented, for the first time in the literature, a $Gd_5(Si_xGe_{1-x})_4$ thin film which retains the magnetostructural transition as observed in its bulk counterpart. This was achieved through a top down approach by using ultrashort laser pulses used for its deposition, the thin film was found to have granular-like morphology, consisting on a stack of nanoparticles with a Lorentzian distribution of diameters (with an average particle size of $\sim$ 80 nm). The thin film chemical composition was inspected by EDS and was found to be similar to the target material within at most a 5%

variation, i.e., $Gd_5Si_{1.3}Ge_{2.7}$. In comparison with its bulk counterpart, the nanogranular thin film shows a broader magnetic response, a 13 K increase on its magnetostructural transition temperature (T_{MS}), a lower -ΔSm^{MAX} ($\sim$ 35% of the bulk value), but a higher -ΔSm_{FWHM} and a large reduction of magnetic hysteretic losses. Despite lower than the bulk, the -ΔSm^{MAX} estimated for this thin film lies in the top-five higher intrinsic -ΔSm^{MAX} reported for thin films so far.

Structurally, the nanogranular thin film unit cell volume was found to be $\sim$ 2% smaller than its bulk counterpart at room temperature. However, similarly to the bulk overall behaviour, a giant and anisotropic thermal expansion was also observed across the magnetostructural transition. As observed in bulk compounds, the thermal expansion across the transition is highly anisotropic: the a-parameter changes Δa/a $\sim$ 1.2% in comparison with the much smaller variation of the other parameters: Δb/b $\sim$ -0.03% and Δc/c$\sim$ -0.4%, which resulted in a ΔV/V $\sim$ 0.8%. The observed anisotropy is in accordance with the interslab adjacent movement expected for the magnetostructural transition and similarly observed in the parent bulk compound. This magnetic-field induced structural transition is expected to contribute to about 50% of the total -ΔSm^{MAX}.

The changes on the magnetic and structural properties, namely its T_{MS} increase and unit cell volume compression (V), in comparison with the bulk counterparts are conjectured to be associated with stress at the nanoparticles surface. There is an intrinsic stress at the nanogranules surface whose value is inversely proportional to the nanoparticle diameter, d[10] - such stress is the equivalent to an applied hydrostatic pressure. For nanoparticle with d in the 1-100 nm range it implies an equivalent hydrostatic pressure in the 1-50 kBar range[10]. In parallel, the thoroughly studied pressure dependence of both V and T_{MS} on bulk materials allowed the independent estimation of the pressure needed for the observed volume contraction and T_{MS} increase which resulted in the same pressure interval 8-11 kBar. Therefore, three independent calculations to estimate the mean pressure revealed to be coherent and to narrow down the pressure interval at these nanoparticles surface as is schematically illustrated in Figure 7.1. Furthermore a distribution of nanoparticles sizes implies a distribution of pressures which in turn implies a distribution of T_{MS} and hence a general broadening of the magnetic responses.

7.1.2 $Gd_5(Si,Ge)_4$ nanogranular thin film negative thermal expansion

Surprisingly, a drastic change in the $Gd_5(Si,Ge)_4$ thermal expansion temperature dependence was observed as a consequence of the size-reduction. It evolved from a positive (in bulk) to a negative thermal expansion coefficient (in nanoparticles). Part of this behavior, namely across the magnetostructural transition, was reviewed in the previous subsection, highlighting its important contribution for the MCE exhibited by this thin film. However, at the nanoscale an unique thermal expansion behavior was detected outside the magnetostructural transition temperature interval, both below (90-160 K, LT regime)

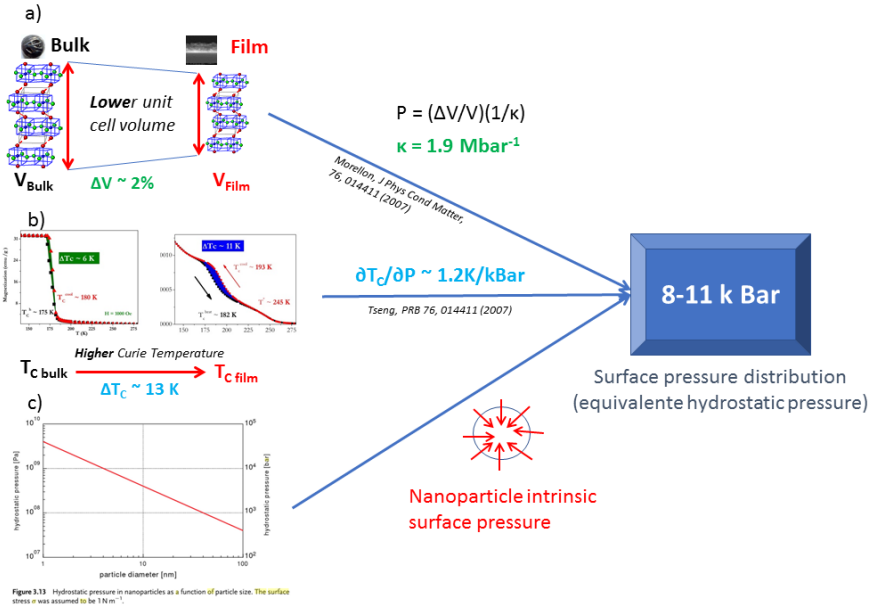

Figure 7.1 – Schematic representation of the three independent mean pressure estimations at the $Gd_5Si_{1.3}Ge_{2.7}$ nanoparticles surface: a) via linear compressibility of unit cell volume; b) via the Curie temperature pressure dependence and c) via the surface pressure dependence on the nanoparticle diameter, d. All three estimations match the 8-11 kBar pressure interval.

and above it (255-340 K, HT regime): namely the negative thermal expansion.

In the LT regime a large and negative volume thermal expansion coefficient was unveiled: $\beta_{LT}=\Delta V^{LT}/\Delta T \sim$ -32.2 ppm K^{-1}, whereas in the HT regime it increases significantly to $\beta_{HT} \sim$ -69 ppm K^{-1}. The observed β_{HT} is much larger than the ones found in Graphene (-7 ppm K^{-1} [11]), and more than doubles that observed in ZrW_2O_8 ,-28.2 ppm K^{-1} [12].

To our knowledge, it was the first time that NTE behavior was detected in magnetic nanoparticles even above their magnetic ordering temperature. The NTE behaviour observed is not completely understood, however some important underlying mechanisms were highlighted. It arises as a consequence of the scale reduction and its main atomic mechanism is thought to be the bond flexing of the key Ge3-Gd1-Ge3 triplet chain. This triplet ϕ angle mimics the unit cell volume behavior, reinforcing the direct and linear correlation between the two. Such atomic mechanism behaves in a similar fashion as the M-O-M flexing in the well-known metal-open-framework (MOF) materials. It is also known as tension effect and is the main responsible for the large NTE observed in MOF materials. Despite the fact that further studies on the bulk and nanoscale are needed to unveil the broader origin of this size induced effect, it is suggested that the nanogranules large surface stress induces lattice softening, changing the phonon spectra and promoting the Ge3-Gd1-Ge3 transverse and low frequency vibrations that result in an overall contraction behavior. Such overall temperature dependency competes with the magnetovolume expansion force below the magnetic ordering temperature - explaining the lower coefficient of thermal expansion for LT, $\beta_{LT} < \beta_{HT}$ As suggested by Barrera and

co-authors review[187], the higher surface/volume ratio for nanogranules and the fact that the coordination numbers are lower at the surface, generally promotes more open structures enhancing the role of the tension effect and therefore leading to changes in the thermal expansion behavior, as was observed here.

7.1.3 Magnetostructural training effect on $Gd_5Si_{1.3}Ge_{2.7}$ nanogranular thin film

The study on the $Gd_5Si_{1.3}Ge_{2.7}$ nanogranular thin film here presented concerned the temperature dependence (100-300 K) of its electrical resistivity and its evolution during thermal cycles (18 cycles). The dynamical studies are crucially important for technological applications, such as magnetic refrigeration and others (as they allow to mimick a real-life device operation) and also for fundamental (scientific) curiosity as they help unveiling the most important mechanisms underlying dynamical phenomena, such as the martensitic-like transitions evolution. Nevertheless, these studies have received significantly less attention than static ones.

A general negative electrical resistivity thermal derivative ($\partial\rho/\partial T < 0$) was observed revealing a semiconducting-like behavior. Such behavior contrasts with the metallic-like ($\partial\rho/\partial T > 0$) observed in bulk Gd_5Si_x, Ge_{4-x} compounds and is thought originate on the size reduction effect on the thermal expansion behavior (that is positive at the bulk scale but negative at the nanoscale, as detailed in chapter 4).

This general trend is interrupted by a two-step positive ($\partial\rho/\partial T > 0$), metallic-like resistivity thermal dependency that is caused by two consecutive transitions: a magnetostructural at lower temperatures and a purely magnetic one at higher temperatures. A strong correspondence between the phase fractions undergoing each transition, as estimated by the Rietveld analysis of Synchrotron XRD data (chapter 4), and the resistivity change across each step was successfully made.

A general picture for the avalanche-like behavior observed in the high temperature step was proposed based on the severe strains induced by the magnetostructural transition. This picture is compatible with the evolution of the transition temperatures (with thermal cycles) at which the avalanche-like regime begins and ends, assuming an internal stress formation that builds up at every thermal cycle due to the large volume induced change across the magnetostructural transition.

Furthermore, the magnetic and electrical resistivity thermal hysteresis reduction with thermal cycles was explained in light of a learning process through which the system is permanently searching for an optimized percolation path which corroborates with the increase of the thermal activation energy with the number of cycles.

Additionally, the invariance of the residual resistivity values under cycling, contrasting with the bulk counterparts behavior, is a clear-cut signal of the absence of major cracks in the overall thin film, which might be a result arising from higher degree of freedom in this low-density material. We believe this work demonstrates the impor-

tance of using a short-range order probe, such as the electron mean free path, to sense mesoscopic physical mechanisms. These short-range order techniques will have an enhanced relevance on the inspection of micro and nanostructures as pointed by Miller and co-authors[39] and soundly exemplified by Uhlir and co-workers recent report[62].

7.1.4 Thermal treatments effects on $Gd_5(Si,Ge)_4$ nanogranular thin film

For bulk materials, thermal treatments have been reported in the literature as a very important tool for the optimization of the crystallographic phases responsible for the GMCE[153,154,229,230]. In particular, annealing temperatures below 700 K lead to an increase of the orthorhombic I, O(I), phase hence minimizing the MCE in $Gd_5Si_2Ge_2$ bulk material, whereas high annealing temperatures, e.g. at T=1473 K promoted an increase in the MCE[229,231].

In order to understand the effect of annealing at the nanoscale, in comparison to the bulk scale, four different annealing temperatures were applied to the nanogranular $Gd_5Si_{1.3}Ge_{2.7}$ thin film: 573, 673, 773, and 873 K.

It was found that annealings temperatures below 773 K were responsible for the suppression of the Magnetostructural Transition observed in the as-deposited film. The absence of magnetostructural transition lead to a 68% decrease in the magnetic entropy change peak value, $-\Delta Sm^{MAX}$, and a 21% decrease in its Refrigerant Capacity, RCP.

On a positive note, there was a 25% increase in its T_C, which became closer to room temperature (T = 253 K) and an increase of ΔT_{FWHM} from= 23 to 49 K in its operational temperature interval upon annealing.

These drastic changes in the magnetic behavior for the annealed film were attributed to the suppression of the O(II) phase, corroborated by the absence of diffracted peaks associated with this phase in the XRD spectra at room temperature. The 68% decrease of $-\Delta Sm^{MAX}$ in the annealed sample corroborates and even overcomes the expected 50% contribution assigned to the magnetostructural transition[77]). The knowledge acquired with the study presented in this chapter, specially that concerning the heat treatments conditions, was critically important for the continuous thin films fabrication described in chapter 6.

7.1.5 Continuous $Gd_5(Si,Ge)_4$ thin films

As referred above, chapter 6 is dedicated to describe our effort to achieve a morphologically different thin film (namely a continuous $Gd_5(Si,Ge)_4$ thin film) and is devoted to a more fundamental problem: the deposition and post-treatment optimization of continuous $Gd_5(Si,Ge)_4$ thin films deposited by Sputtering. It followed two main deposition approaches: the (i) multilayer and the co-sputtering (ii) of the specific pure chemical elements (from $\sim$ 99.9 % pure Sputtering targets), which, after deposition, were subjected to the same thermal treatments (450 ° C for two hours followed by air-quenching).

From all the deposited films, only the ”thicker” Gd-Ge multilayers (MLGd45Ge25 and MLGd23Ge13, e.g. multilayered films with individual 45/23 nm and 25/13 nm thick Gd and Ge layers, repeated 10 and 20 times) mimic the pure Gd film, crystallizing in a similar hcp structure. All the other samples, multilayers and co-sputtered, exhibit an amorphous/nanocrystalline-like nature. The Gd crystallization inhibition in these latter films must be due to their very small individual Gd thickness (<20 nm) (on the multilayered systems) or to the additional disorder introduced by a simultaneous sputtering of Ge and/or Si, similar to what was observed in a previous report, where they found that there is a cross-over, from crystalline to amorphous nature, for Gd individual thicknesses below 10 nm[306].

Two sets of annealings were performed in the as-deposited films: at low-temperatures (< 500°C) and at high-temperatures (> 500°C). Generally, all annealings lead to the oxidation of the majority of the film.

In particular, it was found that the low-temperature annealings are enough to promote Ge-diffusion into the Gd layers in all multilayers. For the thicker multilayers, it promotes the formation of a plethora of multi-phases, including: the Oxygen-based Gd oxide, Gd_2O_3, the Ge oxide, GeO_2, the Ge-rich phases as $GdGe_{2-x}$ and $GdGe_{1.5}$, and the Gd-rich phases as Gd_5Ge_3 or the Gd_5Ge_4. There is a particular favouring of the Ge/Si-rich crystalline ($Gd(Si,Ge)_{2-x}$) and amorphous (a-interlayer) phases, because not only they form at low-temperatures (according to Gd-Ge/Gd-Si bulk phase diagrams), but also verified by previous reports that have demonstrated the formation in pure Gd thin films deposited in Si/Ge substrates (or equivalent buffer layers). Their crystallization occurs preferentially at the Rare-Earth/Si-Ge interlayer region[320] together with the amorphous a-interlayer. In the ”thicker” Gd-Ge multilayers, there is a competition between the crystalline $GdGe_{2-x}$ and the amorphous a-interlayer. For the ”thinner” multilayers, the amorphous a-interlayer dominates the competition leaving virtually no Gd or Ge to form the crystalline $GdGe_{2-x}$ phase. This hypothesis is supported by the broad peak observed by XRD in the ”thinner” multilayers and is reinforced by the temperature interval where the magnetic ordering occurs in the 100-150K interval, as was previously observed for a wide range of amorphous Gd alloys[306,323,324]. Similarly, in the binary and ternary co-sputtered films, the amorphous Gd(Si,Ge) phase is dominant for the low-temperature annealings. The only exception is the Gd-rich co-sputtered film CSGd600Ge100, that undergoes a clear amorphous-crystalline phase transformation during the annealing. The Gd excess, initially thought to account for the Gd oxidation, unbalanced the sensitive 5:4 Gd/Ge atomic ratio and favored the crystallization of the Gd_5Ge_3.

Heated substrates at different temperatures (22, 400, 600°C) promoted the Gd amorphization of both multi-layered and co-sputtered films and apparently add no benefitial effect to the $Gd_5(Si,Ge)_4$ phase formation.

The high-temperature annealings demonstrated the possibility to form the desired $Gd_5(Si,Ge)_4$ phase. Nevertheless, a large amount of the Gd present in the film forms dif-

ferent Gd-oxide based phases. Their formation begins even at 350°C (low-temperature annealings) but lasts up to 900°C. Such a generally high content of Oxides phases is explained by the easy Oxygen penetration into the film both through the top (due to the crack formation) and the bottom (due to Oxygen diffusion from the SiO_2 buffer layer) of the film.

Interestingly, it was found that 800°C annealings of the co-sputtered and multilayered ternary films, is sufficient to promote the crystallization of small fractions of the desired $Gd_5(Si,Ge)_4$, together with other Gd-Si-Ge-O phases, such as the ones found in the low-temperature annealings, namely $Gd(Si,Ge)_{2-x}$, Gd(Si,Ge) and $Gd_5(Si,Ge)_3$, but also Ta-based phases that are formed at both the cap-film (up) and the film-buffer interfaces (bottom).

The different phases crystallization form a complex polycrystalline system with a correspondingly complex set of different thermal expansion behaviors, which is thought to be the origin of crack formation. In particular, the different thermal expansion of the phases crystallizing at the top and bottom, mostly Ta and Oxygen based phases, cause compressive stresses that eventually become so large that the film cracks.

The characterization of the 900°C annealed ternary films unveils promising results in regard of their $Gd_5(Si,Ge)_4$ phase content: T_C similar to the bulk counterpart and the thermal irreversibility presented by M(T) curves suggest a first-order nature and consequently a strong magneto-volume coupling exhibited, similar as that exhibited by its bulk counterpart, and responsible for giant magneto-responsive properties (magnetocaloric, magnetostriction and magnetoresistive effects). Furthermore, the microscopic analysis of these films demonstrated their complex polycrystalline nature and the generally small crystal grain sizes. In particular, EDS analysis corroborated the presence of small grain sizes with $Gd_5(Si,Ge)_4$ stoichiometry and the different crystallite sizes in the multilayer film ($\sim$ 100 nm) and the co-sputtered film ($\sim$ 10 nm). In particular TEM analysis demonstrated that such high-temperature annealings are able to induce $\sim$ 50% of the desired $Gd_5(Si,Ge)_4$ phase. Such small crystallite grain sizes, observed in TEM, corroborate with the observed broadening of the XRD reflections. Such FWHM enhancement, suggests that the XRD technique might not be suitable for the correct phase amount estimation procedure or to track the atomic structure temperature dependence across a magnetostructural transition.

Furthermore, both the small nanogranules ($\sim$ 80 nm) in the $Gd_5Si_{1.3}Ge_{2.7}$ thin film and the small ($\sim$ 100 nm) crystallite grain sizes in the continuous thin films, still undergo magnetostructural transition, revealing that the critical size below which the surface effects become dominating and the magnetostructural becomes suppressed was not yet reached.

Top-view SEM images demonstrated that a strong diffusion of the SiO_2 buffer layers occurs at the high-temperature annealed films. In future work, in order to prevent Oxygen diffusion towards the film, different methods should be tested, including: different buffer and cap layers, e.g. the more immobile TaN; similar annealings under ultra

high-vacuum conditions; pulsed laser annealings (to promote higher temperature and localized heating of the material); a higher-temperature heated substrate, namely at 800/900°C, depositions;

From the results here presented it is plausible to assume that if no Gd was consumed by the Gd oxides phase formation such high-temperature annealings (900°C) or even at higher temperatures would allow the formation of an almost 100% $Gd_5(Si,Ge)_4$ polycrystalline thin film.

7.2 Future Perspectives

The different studies reported in this thesis unveil the arising of multi-phenomena in $Gd_5(Si,Ge)_4$ materials, when its scale is reduced from the bulk to nano. These new phenomena were observed in a nanogranular $Gd_5(Si,Ge)_4$ elastic, structural, electric and magnetic properties and can open new multi-functional opportunities as will be presented below. Nevertheless, since this constitutes a pioneering work, several scientific questions remain together with some new, potentially interesting, technological applications.

7.2.1 Fundamental (scientific) perspectives

- The ability to tune the $Gd_5Si_{1.3}Ge_{2.7}$ nanoparticles size distribution (mean size, FWHM) will most probably grant the tuning of the magnetic and structural properties. From the magnetic point of view, it would be very interesting to: - Scale-down the nanoparticles mean size below 80 nm to determine the critical diameter below which the magnetostructural transition does not develop; - To narrow the nanoparticles FWHM distribution to sharpen, and possibly, enhance -ΔSm (T) curve and decrease the magnetic and thermal hysteresis observed. From the atomic structure point of view, it would be interesting to: - Perform a more complete study on the evolution of the thermal expansion temperature dependence with the nanoparticles mean size. A cross-over between positive (PTE) and negative thermal expansion (NTE) must occur for nanoparticle diameters above 80 nm, with the potential promise of invar materials. - By narrowing the nanoparticles FWHM distribution a more single-phase like behavior is expected. It would be very interesting to study the atomic structure of such system, namely its thermal expansion temperature dependence.

- The possibility to grow/deposit $Gd_5(Si_xGe_{1-x})_4$ with different Si/Ge ratios, x. The x = 0, Gd_5Ge_4, would be an interesting composition to study, since it presents one of the most exotic magnetic behaviours of this family. Also the study of other Rare-Earth elements (such as Tb or Er) would be worth inspecting, in particular the Er_5Si_4 composition, because of its inverse structural transition direction (on

cooling, transforms from the low-volume, O(I), structure to the high-volume, M, structure).

- Production of $Gd_5(Si_xGe_{1-x})_4$ nanoparticles via nanosecond laser deposition (cheaper and much more accessible than the femtosecond laser system used for the deposition of the $Gd_5Si_{1.3}Ge_{2.7}$ nanogranular thin film here studied). In fact, this work is under progress at our lab. Preliminary, but promising results have demonstrated the ability to produce $Gd_5(Si_xGe_{1-x})_4$ nanoparticles with diameters below 10 nm via nanosecond laser deposition.

- To inspect the influence of high hydrostatic pressure (> 11 kBar) on $Gd_5(Si_xGe_{1-x})_4$ bulk materials, specifically on their thermal expansion temperature dependence: to check whether or not there is a pressure threshold beyond which the thermal expansion becomes negative.

- Perform extended experimental (Raman and Inelastic Neutron Scattering) and theoretical (density functional calculations) studies to widen the very basic knowledge on the lattice dynamics of this family of alloys, both at the bulk and at the micro and nanoscale. To our knowledge, there are no Raman studies of these materials reported in the literature.

- To extend the Synchrotron XRD experiments to temperature up to 773 K, in order to investigate: at what temperature does the NTE disappears and the thermal expansion becomes positive; inspect if there is another structural transition occurring at high-temperatures, as occurs in the bulk case[153].

- Concerning continuous thin films, both the multilayer and co-sputtering approaches have shown promising results, specially for high-temperature ex-situ annealings. Nevertheless, the experimental study here reported demonstrates the complexity of achieving almost pure $Gd_5(Si_xGe_{1-x})_4$ phase and it should be considered as some initial steps towards this goal. Here the main lines of action are highlighted: depositions at higher-temperature (800-900 °C) heated substrates in ultra-high vacuum chambers; tests with more stable and unreactive capping and buffer layers (TaN can be a good example, as reported in reference[326]); tests with substrates stable and diffusion less up to high-temperatures (900°C or close); SiO_2 should not be used as a buffer layer, since as became clear here, it might act as another oxygen source; ex-situ pulsed laser annealings - short and high-energetic laser pulses leading to high heating and cooling rates in specific thin film area (where the laser spot hits).

- The stabilization of a small crystalline grain sizes suggests that XRD technique might not be the most suitable to identify structural transitions as the ones observed in the $Gd_5(Si_xGe_{1-x})_4$. Such transitions typically imply small peak shifts, specially the O(II) - O(I) transition, which might not be observed because of the

diffracted peaks broadening. As an alternative to track structural transitions, both temperature and field-induced, the cantilever method is suggested. Preliminary work performed in collaboration with INESC-MN in Lisbon, have already delivered promising results. The dislocation by few nanometers of the tip of a cantilever deposited with a magnetostrictive film (as a preliminary example the magnetostrictive alloy, $Fe_{65}Co_{33}$, was used) through the application of a small magnetic field (H < 50 Oe) was demonstrated.

7.2.2 Technological perspectives

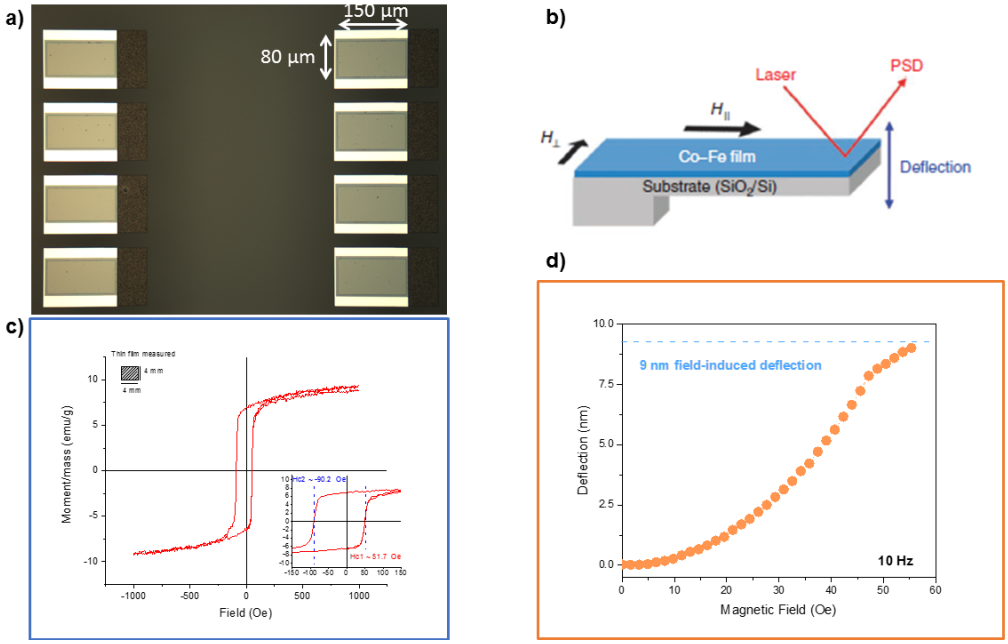

Figure 7.2 – a) SEM top-view of a set of eight cantilevers with special focus to the 150 x 80 μm four cantilevers. b) Schematic representation of the 100 nm thick $Fe_{65}Co_{33}$ film on top of a SiO_2 based cantilever with a gap of 1 μm, and the deflection measurement setup, as extracted from reference [196]. c) $Fe_{65}Co_{33}$ film magnetization as a function of magnetic field measure at room temperature, with a coercive field of ~ 50 Oe (0.005 T). d) Magnetostrictive cantilever tip deflection as a function of magnetic field, measured through a laser displacement sensor .

From the technological point of view there are interesting opportunities, namely in the following topics:

- The colossal striction observed in the $Gd_5Si_{1.3}Ge_{2.7}$ nanoparticles can help the development of high sensitivity strictive sensors/actuators (due to strain), and unravel new opportunities for artificial multifunctional materials, such as composites or multilayer deposition with piezoelectric materials;

- The possibility to grow/deposit $Gd_5(Si_xGe_{1-x})_4$ nanoparticles with different Si/Ge ratios, x, such as x = 0.5, that in the bulk form undergoes a magnetostructural transition close to room temperature (275 K). Such compositions, or even x > 0.5,

could be particularly suited for the nanomedicine applications, such as: hyperthermal therapy[49] or drug delivery[50];

- Typically, NTE materials are almost unexplored but technologically very promising as they can compensate the common Positive Thermal Expansion observed in the vast majority of materials. In particular, nanoparticles are especially useful for this purpose as they can intermix easily in a composite, ensuring the desired tuning of the thermal expansion of the composite. In this regard, Bragg gratings optical fiber coatings[226] or in printed circuit boards[227] are two examples of the importance of correcting the thermal expansion of a material.

- Wireless actuation of micro and nano structures such as cantilevers by depositing a $Gd_5(Si_xGe_{1-x})_4$ thin film, with $x \sim 0.5$. As already mentioned preliminary work performed in collaboration with INESC-MN in Lisbon, have already delivered promising results as discussed above and presented in Figure 7.2. The dislocation by $\sim$ 10 nanometers of the tip of a cantilever deposited with a magnetostrictive film through the application of a small magnetic-field ($H < 50$ Oe) was already demonstrated. Potential actuation applications such as the actuation of valves and sensor in microfluidics are promising.

Publications related to the PhD work

Several contributions were made to the scientific community related to the work developed in the present thesis, including: 10 oral communications, 9 poster presentations and the 14 (overall) publications, including:

1. J.H. Belo, A.M. Pereira, J. Ventura, G.N.P. Oliveira, P.B. Tavares, L. Fernandes, P.A. Algarabel, C. Magen, L. Morellon, M.R. Ibarra and J.P. Araújo., Phase Control studies in $Gd_5Si_2Ge_2$ Giant Magnetocaloric Compound, JALCOM **529**, 89-95 (2012)

2. J. H. Belo, A. M. Pereira, J. S. Amaral, V. S. Amaral and J. P. Araújo, On the Curie temperature dependency of the Magnetocaloric effect, Appl. Phys. Lett. **100**, 242407 (2012).

3. J. H. Belo, A. M. Pereira, J. P. Araujo, C. de la Cruz, A. M. dos Santos, J. N. Gonçalves, V. S. Amaral, P.A. Algarabel, C. Magen, L. Morellon, M.R. Ibarra and J.P. Araújo, Tailoring the Magnetism of $Tb_5Si_2Ge_2$ Compounds by La Substitution, Phys. Rev. B **86**, 014403 (2012).

4. J H Belo, A M Pereira, C Magen, L Morellon, P A Algarabel, M R Ibarra and J P Araújo, Critical magnetic behavior of magnetocaloric materials with the Gd_5Si_4-type structure, J. Appl. Phys. **113**, 133909 (2013).

5. Ravi Hadimani, J. H. B. Silva, Andre M. Pereira, D. L. Schlagel, T. A. Lograsso, Yang Ren, Xiaoyi Zhang, David C. Jiles and J. P. Araújo, Note: Ravi Hadimani and J. Horta Belo Silva contributed equally to this work., $Gd_5(Si, Ge)_4$ thin film displaying large magnetocaloric and strain effects due to magnetostructural transition, Appl. Phys. Lett. **106**, 032402 (2015).

6. A.L. Pires, J.H. Belo, I.T. Gomes, R.L. Hadimani, D.C. Jiles, L. Fernandes, P.B. Tavares, J.P. Araújo, A.M.L. Lopes and A.M. Pereira Note: A. L. Pires and J. H. Belo contributed equally to this work, Annealing influence on the magnetostructural transition in $Gd_5Si_{1.3}Ge_{2.7}$ thin films, Mater. Lett. **159**, 301–304 (2015).

7. J.H. Belo, M.B. Barbosa, A.L. Pires, R.M. Costa, J.G.V. Teixeira, J. Silva, P.A. Algarabel, C. Magen, L. Morellon, J.S. Amaral, U.Zeitler, G. Veerendra, A.M. dos Santos, Y. Ren, M.R. Ibarra, J.P. Araújo and A.M. Pereira, Insights on the origin of the Tb_5Ge_4 magnetocaloric effect, Physica B **513**, 72-76 (2017).

8. Ana Lúcia Pires, João Horta Belo, Armandina Maria Lima Lopes, Isabel T. Gomes, Luis Morellón, Cesar Magen, Pedro Antonio Algarabel, Manuel Ricardo Ibarra, André Miguel Pereira and João Pedro Araújo Note: A. L. Pires and J. H. Belo contributed equally to this work, Phase Competitions behind the Giant Magnetic Entropy Variation $Gd_5Si_2Ge_2$ and $Tb_5Si_2Ge_2$ Case Studies, Entropy **16**, 3813-3831 (2014).

Several collaborations also took place, resulting in the following publications:

1. A. M. Pereira, E. Kampert, J. M. Moreira, U. Zeitler, J. H. Belo, C. Magen, P. A. Algarabel, L. Morellon, M. R. Ibarra, J. N. Gonçalves, J. S. Amaral, V. S. Amaral, J. B. Sousa and J. P. Araújo, Unveiling the (De)coupling of magnetostructural transition nature in magnetocaloric $R_5Si_2Ge_2$ (R=Tb, Gd) materials, Appl. Phys. Lett. **99**, 132510 (2015).

2. A. L. Pires, J. H. Belo, I. T. Gomes, L. Fernandes, P. B. Tavares, A. M. L. Lopes, A. M. Pereira and J. P. Araújo, On the Growth and Physical-chemical Characterization of $Tb_5Si_2Ge_2$ Thin Films Produced by Electron-beam Evaporation, Mater. Today Proc. **2**, (2015).

3. A. L. Pires , J. H. Belo, I. T. Gomes, R. L. Hadimani, D. L. Schlagel, T. A. Lograsso, D. C. Jiles, A. M. L. Lopes, J. P. Araújo and A. M. Pereira, Suppression of magnetostructural transition on GdSiGe thin film after thermal cyclings, Thin Solid Films **621**, 247–252 (2017).

4. A.L. Pires, J.H. Belo, J.Turcaud, G.N.P. Oliveira, J.P. Araújo, A.Berenov, L.F.Cohen, A.M.L. Lopes and A.M.Pereira, Influence of short time milling in $R_5(Si, Ge)_4$, R = Gd and Tb, Mater. Des. **85**, 32-38 (2015).

5. Joel B. Puga, Bernardo D. Bordalo, Daniel J. Silva, Miguel M. Dias, João H. Belo, João P. Araújo, Joana C.R.E. Oliveira, André M. Pereira and João Ventura, Novel thermal switch based on magnetic nanofluids with remote activation, Nano Energy **31**, 278-285 (2017).

6. Raquel Martins, Paulo Caldas, Bruno Teixeira, João Azevedo, José Monteiro, João H. Belo, João P. Araújo, José L. Santos and Gaspar Rego, Cryogenic Temperature Response of Reflection-Based Phase-Shifted Long-Period Fiber Gratings, J. Lightwave Technol . **33**, (2015).

7. Rui M. Costa, João H. Belo, Marcelo B. Barbosa, Pedro A. Algarabel, César Magén, Luis Morellón, Manuel R. Ibarra, João N. Gonçalves, Nuno M. Fortunato, João S. Amaral, João P. Araújo, André M. Pereira, On the nature of the (de)coupling of the magnetostructural transition in Er_5Si_4, Phys. Status Solidi B, 170014, (2017)

Bibliography

[1] I. International Institute of Refrigeration, The Role of Refrigeration in the Global Economy, Inf. Note Refrig. Technol. / **29** (November, 2015).

[2] D. R. Brown, J. A. Dirks, N. Fernandez, T. B. Stout, The Prospects of Alternatives to Vapor Compression Technology for Space Cooling and Food Refrigeration Applications, Energy Eng. **109** (6) (2012) 7–20. doi:10.1063/1.3567920.

[3] L. Morellon, P. A. Algarabel, M. Ibarra, J. Blasco, B. García-Landa, Z. Arnold, F. Albertini, Magnetic-field-induced structural phase transition in Gd5Si1.8Ge2.2, Phys. Rev. B - Rapid Commun. **58** (22) (1998) 721–724.

[4] V. K. Pecharsky, K. A. Gschneidner, Giant magnetocaloric effect in Gd5(Si2Ge2), Phys. Rev. Lett. **78** (23) (1997) 4494–4497. doi:10.1103/PhysRevLett.78.4494.

[5] L. Morellon, Z. Arnold, C. Magen, C. Ritter, O. Prokhnenko, Y. Skorokhod, P. A. Algarabel, M. R. Ibarra, J. Kamarad, Pressure enhancement of the giant magnetocaloric effect in Tb5Si2Ge2, Phys. Rev. Lett. **93** (13). doi:10.1103/PhysRevLett.93.137201.

[6] R. Niemann, O. Heczko, L. Schultz, S. Fähler, Metamagnetic transitions and magnetocaloric effect in epitaxial Ni–Co–Mn–In films, Appl. Phys. Lett. **97** (22) (2010) 222507. doi:10.1063/1.3517443.

[7] M. F. Ozaydin, H. Liang, Multi-energy conversion of Gd5(Si2Ge2)-poly (vinylidene fluoride), a hybrid material, Appl. Phys. Lett. **105** (6) (2014) 062903. doi:10.1063/1.4893296.

[8] A. Khan, D. E. Nikonov, S. Manipatruni, T. Ghani, I. A. Young, Voltage induced magnetostrictive switching of nanomagnets: Strain assisted strain transfer torque random access memory, Appl. Phys. Lett. **104** (26) (2014) 262407. doi:10.1063/1.4884419.

[9] K. Roy, Ultra-low-energy non-volatile straintronic computing using single multiferroic composites, Appl. Phys. Lett. **103** (17) (2013) 173110. doi:10.1063/1.4826688.

[10] D. Vollath, Nanomaterials, An Introduction to Synthesis, Properties and Application, 2nd Edition, WILEY-V C H VERLAG GMBH, 2013.

[11] W. Bao, F. Miao, Z. Chen, H. Zhang, W. Jang, C. Dames, C. N. Lau, Controlled ripple texturing of suspended graphene and ultrathin graphite membranes., Nat. Nanotechnol. **4** (9) (2009) 562–6. arXiv:0903.0414, doi:10.1038/nnano.2009.191.

[12] T. A. Mary, J. S. O. Evans, T. Vogt, A. W. Sleight, Negative Thermal Expansion from 0.3 to 1050 Kelvin in ZrW2O8, Science (80-.). **272** (5258) (1996) 90–92. doi:10.1126/science.272.5258.90.

[13] V. K. Pecharsky, K. A. Gschneidner, Gd5(SixGe1-x)4 : An Extremum Material, Adv. Mater. **13** (9) (2001) 683–686.

[14] Y. Mudryk, D. Paudyal, V. Pecharsky, K. Gschneidner, Magnetostructural transition in Gd5Si0.5Ge3.5: Magnetic and x-ray powder diffraction measurements, and theoretical

calculations, Phys. Rev. B **77** (2) (2008) 024408. doi:10.1103/PhysRevB.77.024408.

[15] A. Smith, Who discovered the magnetocaloric effect?, Eur. Phys. J. H **38** (4) (2013) 507–517. doi:10.1140/epjh/e2013-40001-9.

[16] W. F. Giauque, A Themodynamic treatment of certain magnetic effects. A proposed method of producing temperatures considerably below 1 degree absolute, J. Am. Chem. Soc. **49** (1927) 1864–1870.

[17] P. Debye, Einige Bemerkungen zur Magnetisierung bei tiefer Temperatur, Ann. Phys. **386** (25) (1926) 1154–1160. doi:10.1002/andp.19263862517.

[18] W. F. Giauque, D. P. MacDougall, Attainment of Temperatures Below 1° Absolute by Demagnetization of Gd2(SO4)3·8H2O, Phys. Rev. **43** (9) (1933) 768–768. doi:10.1103/PhysRev.43.768.

[19] G. V. Brown, Magnetic heat pumping near room temperature, J. Appl. Phys. **47** (8) (1976) 3673–3680. doi:10.1063/1.323176.

[20] M. P. Annaorazov, S. A. Nikitin, A. L. Tyurin, K. A. Asatryan, A. K. Dovletov, Anomalously high entropy change in FeRh alloy, J. Appl. Phys. **79** (3) (1996) 1689–1695. doi:10.1063/1.360955.

[21] L. Morellon, J. Stankiewicz, B. García-Landa, P. A. Algarabel, M. R. Ibarra, Giant magnetoresistance near the magnetostructural transition in Gd5(Si1.8Ge2.2), Appl. Phys. Lett. **73** (23) (1998) 3462. doi:10.1063/1.122797.

[22] E. Levin, V. Pecharsky, K. Gschneidner, Spontaneous generation of voltage in Gd5(SixGe4-x) during a first-order phase transition induced by temperature or magnetic field, Phys. Rev. B **63** (17) (2001) 174110. doi:10.1103/PhysRevB.63.174110.

[23] V. K. Pecharsky, A. P. Holm, K. A. Gschneidner, R. Rink, Massive magnetic-field-induced structural transformation in Gd5Ge4 and the nature of the giant magnetocaloric effect, Phys. Rev. Lett. **91** (19) (2003) 197204.

[24] R. L. Hadimani, P. A. Bartlett, Y. Melikhov, J. E. Snyder, D. C. Jiles, Field and temperature induced colossal strain in Gd5(SixGe1−x)4, J. Magn. Magn. Mater. **323** (5) (2011) 532–534. doi:10.1016/j.jmmm.2010.10.004.

[25] N. A. de Oliveira, Giant magnetocaloric and barocaloric effects in R5Si2Ge2 (R = Tb, Gd), J. Appl. Phys. **113** (3) (2013) 033910. doi:10.1063/1.4776729.

[26] V. K. Pecharsky, K. A. Gschneidner, Tunable magnetic regenerator alloys with a giant magnetocaloric effect for magnetic refrigeration from 20 to 290 K, Appl. Phys. Lett. **70** (24) (1997) 3299. doi:10.1063/1.119206.

[27] V. Provenzano, A. J. Shapiro, R. D. Shull, Reduction of hysteresis losses in the magnetic refrigerant Gd5Ge2Si2 by the addition of iron., Nature **429** (6994) (2004) 853–857. doi:10.1038/nature02657.

[28] S. Fujieda, A. Fujita, K. Fukamichi, Large magnetocaloric effects in NaZn13-type La(Fe xSi1-x)13 compounds and their hydrides composed of icosahedral clusters, Sci. Technol. Adv. Mater. **4** (4) (2003) 339–346. doi:10.1016/j.stam.2003.07.002.

[29] F. Hu, B. Shen, J. Sun, Magnetic entropy change in Ni51.5Mn22.7Ga25.8 alloy, Appl. Phys. Lett. **76** (23) (2000) 3460–3462. doi:10.1063/1.126677.

[30] N. T. Trung, L. Zhang, L. Caron, K. H. J. Buschow, E. Brück, Giant magnetocaloric effects by tailoring the phase transitions, Appl. Phys. Lett. **96** (17) (2010) 172504. doi:10.1063/1.3399773.

[31] V. Franco, J. S. Blázquez, B. Ingale, a. Conde, The Magnetocaloric Effect and Magnetic Refrigeration Near Room Temperature: Materials and Models, Annu. Rev. Mater. Res. **42** (1) (2012) 305–342. doi:10.1146/annurev-matsci-062910-100356.

[32] A. Kitanovski, J. Tušek, U. Tomc, U. Plaznik, M. Ožbolt, A. Poredoš, Magnetocaloric Energy Conversion, Green Energy and Technology, Springer International Publishing, Cham, 2015. doi:10.1007/978-3-319-08741-2.

[33] I. A. Radulov, K. P. Skokov, D. Y. Karpenkov, T. Gottschall, O. Gutfleisch, On the preparation of La(Fe,Mn,Si)13Hx polymer-composites with optimized magnetocaloric properties, J. Magn. Magn. Mater. **396** (2015) 228–236. doi:10.1016/j.jmmm.2015.08.044.

[34] J. Liu, T. Gottschall, K. P. Skokov, J. D. Moore, O. Gutfleisch, Giant magnetocaloric effect driven by structural transitions., Nat. Mater. **11** (7) (2012) 620–6. doi:10.1038/nmat3334.

[35] J. Lyubina, R. Schaefer, N. Martin, L. Schultz, O. Gutfleisch, Novel Design of La(Fe, Si)(13) Alloys Towards High Magnetic Refrigeration Performance, Adv. Mater. **22** (33) (2010) 3735. doi:10.1002/adma.201000177.

[36] Y. Shao, M. Zhang, H. Luo, A. Yan, J. Liu, Enhanced thermal conductivity in off-stoichiometric La-(Fe,Co)-Si magnetocaloric alloys, Appl. Phys. Lett. **107** (15). doi:10.1063/1.4933261.

[37] J. A. Turcaud, K. Morrison, A. Berenov, N. M. Alford, K. G. Sandeman, L. F. Cohen, Microstructural control and tuning of thermal conductivity in La 0.67Ca0.33MnO3±δ, Scr. Mater. **68** (7) (2013) 510–513. doi:10.1016/j.scriptamat.2012.11.036.

[38] J. D. Moore, G. K. Perkins, Y. Bugoslavsky, M. K. Chattopadhyay, S. B. Roy, P. Chaddah, V. K. Pecharsky, K. A. Gschneidner Jr., L. F. Cohen, Reducing the operational magnetic field in the prototype magnetocaloric system Gd5Ge4 by approaching the single cluster size limit, Appl. Phys. Lett. **88** (7) (2006) 72501. doi:10.1063/1.2173631.

[39] C. W. Miller, D. D. Belyea, B. J. Kirby, Magnetocaloric effect in nanoscale thin films and heterostructures, J. Vac. Sci. Technol. A Vacuum, Surfaces, Film. **32** (4) (2014) 040802. doi:10.1116/1.4882858.

[40] X. Moya, S. Kar-Narayan, N. D. Mathur, Caloric materials near ferroic phase transitions., Nat. Mater. **13** (5) (2014) 439–50. doi:10.1038/nmat3951.

[41] A. Smith, C. R. Bahl, R. Bjørk, K. Engelbrecht, K. K. Nielsen, N. Pryds, Materials Challenges for High Performance Magnetocaloric Refrigeration Devices, Adv. Energy Mater. **2** (11) (2012) 1288–1318. doi:10.1002/aenm.201200167.

[42] D. Doblas, L. M. Moreno-Ramírez, V. Franco, A. Conde, A. V. Svalov, G. V. Kurlyandskaya, Nanostructuring as a procedure to control the field dependence of the magnetocaloric effect, Mater. Des.. doi:10.1016/j.matdes.2016.11.085.

[43] R. L. Hadimani, J. H. B. Silva, A. M. Pereira, D. L. Schlagel, T. A. Lograsso, Y. Ren, D. C. Jiles, J. P. Araújo, Gd5(Si,Ge)4 thin film displaying large magnetocaloric and strain effects due to magnetostructural transition, Appl. Phys. Lett. **5** (106) (2015) 32402. doi:10.1063/1.4906056.

[44] J. M. Lommel, Magnetic and Electrical Properties of FeRh Thin Films, J. Appl. Phys. **37** (3) (1966) 1483. doi:10.1063/1.1708527.

[45] J. Lyubina, Recent advances in the microstructure design of materials for near room temperature magnetic cooling (invited), J. Appl. Phys. **109** (7). doi:10.1063/1.3540372.

[46] V. Chaudhary, R. Ramanujan, Magnetocaloric Properties of Fe-Ni-Cr Nanoparticles for Active Cooling, Sci. Rep. **6** (September) (2016) 35156. doi:10.1038/srep35156.

[47] D. H. Mosca, F. Vidal, V. H. Etgens, Strain engineering of the magnetocaloric effect in MnAs epilayers, Phys. Rev. Lett. **101** (12). doi:10.1103/PhysRevLett.101.125503.

[48] J. Y. Duquesne, J. Y. Prieur, J. Agudo Canalejo, V. Etgens, M. Eddrief, A. Ferreira, M. Marangolo, Ultrasonic triggering of giant magnetocaloric effect in MnAs thin films, Phys. Rev. B **86** (3) (2012) 035207. arXiv:arXiv:1206.5217v1, doi:10.1103/PhysRevB.86.035207.

[49] M. R. Barati, C. Selomulya, K. G. Sandeman, K. Suzuki, Extraordinary induction heating effect near the first order Curie transition, Appl. Phys. Lett. **105** (16). doi:10.1063/1.4900557.

[50] A. Tishin, Y. Spichkin, V. Zverev, P. Egolf, A review and new perspectives for the magnetocaloric effect: New materials and local heating and cooling inside the human body, Int. J. Refrig. **68** (2016) 177–186. doi:10.1016/j.ijrefrig.2016.04.020.

[51] R. E. Rosensweig, Heating a magnetic fluid with alternating magnetic field., J. Mag. Mag. Mater. **252** (2002) 370–374.

[52] P. W. Egolf, N. Shamsudhin, S. Pané, D. Vuarnoz, J. Pokki, A. G. Pawlowski, P. Tsague, B. De Marco, W. Bovy, S. Tucev, M. H. D. Ansari, B. J. Nelson, Hyperthermia with rotating magnetic nanowires inducing heat into tumor by fluid friction, J. Appl. Phys. **120** (6). doi:10.1063/1.4960406.

[53] L. J. Love, J. F. Jansen, T. E. McKnight, Y. Roh, T. J. Phelps, A magnetocaloric pump for microfluidic applications, IEEE Trans. Nanobioscience **3** (2) (2004) 101–110. doi:10.1109/TNB.2004.828265.

[54] A. López-Ortega, M. Estrader, G. Salazar-Alvarez, A. G. Roca, J. Nogués, Applications of exchange coupled bi-magnetic hard/soft and soft/hard magnetic core/shell nanoparticles, Phys. Rep. **553** (2015) 1–32. arXiv:1406.3966, doi:10.1016/j.physrep.2014.09.007.

[55] R. Caballero-Flores, V. Franco, a. Conde, L. F. Kiss, L. Peter, I. Bakonyi, Magnetic Multilayers as a Way to Increase the Magnetic Field Responsiveness of Magnetocaloric Materials, J. Nanosci. Nanotechnol. **12** (9) (2012) 7432–7436. doi:10.1166/jnn.2012.6521.

[56] M. Chmielus, X. X. Zhang, C. Witherspoon, D. C. Dunand, P. Müllner, Giant magnetic-field-induced strains in polycrystalline Ni-Mn-Ga foams., Nat. Mater. **8** (11) (2009) 863–6. doi:10.1038/nmat2527.

[57] N. Nersessian, S. W. Or, G. P. Carman, S. K. McCall, W. Choe, H. B. Radousky, M. W. McElfresh, V. K. Pecharsky, A. O. Pecharsky, Gd5Si2Ge2 composite for magnetostrictive actuator applications, Appl. Phys. Lett. **84** (23) (2004) 4801–4803. doi:10.1063/1.1760891.

[58] M. Cleveland, H. Liang, Magnetocaloric piezoelectric composites for energy harvesting,

Smart Mater. Struct. **21** (4) (2012) 047002. doi:10.1088/0964-1726/21/4/047002.

[59] B. Barkley, C. Sanchez, H. Liang, In Situ Strengthening of the Aluminum-based Gadolinium Alloy Composite for Tribological Applications, J. Tribol. **134** (1) (2012) 011603. doi:10.1115/1.4005648.

[60] R. Wu, F. Shen, F. Hu, J. Wang, L. Bao, L. Zhang, Y. Liu, Y. Zhao, F. Liang, W. Zuo, J. Sun, B. Shen, Critical dependence of magnetostructural coupling and magnetocaloric effect on particle size in Mn-Fe-Ni-Ge compounds, Sci. Rep. **6** (November 2015) (2016) 20993. doi:10.1038/srep20993.

[61] V. Mello, A. L. Dantas, A. S. Carriço, Magnetocaloric effect of thin Dy films, Solid State Commun. **140** (9-10) (2006) 447–451. doi:10.1016/j.ssc.2006.09.013.

[62] V. Uhlíř, J. A. Arregi, E. E. Fullerton, Colossal magnetic phase transition asymmetry in mesoscale FeRh stripes, Nat. Commun. **7** (October) (2016) 13113. arXiv:1605.06823, doi:10.1038/ncomms13113.

[63] T. Delay, The Emerging Cold Economy, Carbon Trust.

[64] K. A. G. Jr., V. K. Pecharsky, Magnetocaloric effect and magnetic refrigeration, J. Mag. Magn. Mat. **200** (1999) 44–56.

[65] N. Nishida, T. Furubayashi, M. Shinohara, Y. Takano, Y. Miura, K. Ono, H. Ishimoto, Two-Stage Nuclear Demagnetization Refrigerator reaching 27 microkelvin, J. Low Temp. Phys. **55**.

[66] N. A. de Oliveira, P. J. von Ranke, M. V. Tovar Costa, A. Troper, Magnetocaloric effect in the intermetallic compounds RCo2 (R=Dy,Ho,Er), Phys. Rev. B **66** (9). doi:10.1103/PhysRevB.66.094402.

[67] H. J. A.C., P. S, Magnetocaloric effect in dysprosium, J. Appl. Phys. **36** (11) (1965) 3628–3631.

[68] A. Planes, L. Mañosa, M. Acet, Magnetocaloric effect and its relation to shape-memory properties in ferromagnetic Heusler alloys., J. Phys. Condens. Matter **21** (23) (2009) 233201. doi:10.1088/0953-8984/21/23/233201.

[69] J. Kaštil, P. Javorský, J. Kamarád, E. Šantavá, Magnetocaloric effect of Gd-Tb alloys: Influence of the sample shape anisotropy, Appl. Phys. A Mater. Sci. Process. **104** (1) (2011) 205–209. doi:10.1007/s00339-010-6105-2.

[70] A. S. Andreenko, K. P. Belov, S. A. Nikitin, A. M. Tishin, Magnetocaloric effects in rare-earth magnetic materials, Sov. Phys. - Uspekhi **32** (8) (1989) 649–664. doi:10.1070/PU1989v032n08ABEH002745.

[71] H. Wada, Y. Tanabe, Giant magnetocaloric effect of MnAs1-xSbx, Appl. Phys. Lett. **79** (20) (2001) 3302–3304. doi:10.1063/1.1419048.

[72] S. Fujieda, A. Fujita, K. Fukamichi, Large magnetocaloric effect in La(FexSi1-x)(13) itinerant-electron metamagnetic compounds, Appl. Phys. Lett. **81** (7) (2002) 1276–1278. doi:10.1063/1.1498148.

[73] J. H. Belo, J. S. Amaral, A. M. Pereira, V. S. Amaral, J. P. Araújo, On the Curie temperature dependency of the magnetocaloric effect, Appl. Phys. Lett. **100** (24) (2012) 8–12. doi:10.1063/1.4726110.

[74] C. P. Bean, D. S. Rodbell, Magnetic Disorder as a First-Order Phase Transformation, Phys. Rev. **126** (1) (1962) 104–115.

[75] P. Weiss, L'hypothèse du champ moléculaire et la propriété ferromagnétique, J. Phys. Théorique Appliquée **6** (1) (1907) 661–690. doi:10.1051/JPHYSTAP:019070060066100.

[76] A. M. Pereira, E. Kampert, J. C. Moreira, U. Zeitler, J. H. Belo, C. Magen, P. A. Algarabel, , L. Morellon, M. R. Ibarra, J. N. Gonçalves, J. S. Amaral, V. S. Amaral, J. B. Sousa, J. P. Araújo, Unveiling the (De)coupling of magnetostructural transition nature in magnetocaloric R5Si2Ge2 (R=Tb, Gd) materials, Appl. Phys. Lett. **99** (13) (2011) 132510.

[77] V. K. Pecharsky, K. A. Gschneidner Jr., Y. Mudryk, D. Paudyal, Making the most of the magnetic and lattice entropy changes, J. Magn. Magn. Mater. **321** (21) (2009) 3541–3547. doi:10.1016/j.jmmm.2008.03.013.

[78] A. M. Pereira, A. M. dos Santos, C. Magen, J. B. Sousa, P. A. Algarabel, Y. Ren, C. Ritter, L. Morellon, M. R. Ibarra, J. P. Araújo, Understanding the role played by Fe on the tuning of magnetocaloric effect in Tb5Si2Ge2, Appl. Phys. Lett. **98** (12) (2011) 122501. doi:10.1063/1.3567920.

[79] K. G. Sandeman, Magnetocaloric materials: The search for new systems, Scr. Mater. **67** (6) (2012) 566–571. doi:10.1016/j.scriptamat.2012.02.045.

[80] K. A. GschneidnerJr, V. K. Pecharsky, A. O. Tsokol, Recent developments in magnetocaloric materials, Reports Prog. Phys. **68** (6) (2005) 1479–1539. doi:10.1088/0034-4885/68/6/R04.

[81] B. G. Shen, J. R. Sun, F. X. Hu, H. W. Zhang, Z. H. Cheng, Recent Progress in Exploring Magnetocaloric Materials, Adv. Mater. **21** (45) (2009) 4545–4564. doi:10.1002/adma.200901072.

[82] Y. Mudryk, V. K. Pecharsky, K. A. J. Gschneidner, Handbook on the Physics and Chemistry of Rare Earths Includind Actinides (Vol. 44), North Holland, 2014.

[83] J. S. Amaral, N. J. O. Silva, V. S. Amaral, A mean-field scaling method for first- and second-order phase transition ferromagnets and its application in magnetocaloric studies, Appl. Phys. Lett. **91** (17). doi:10.1063/1.2801692.

[84] V. S. Amaral, J. S. Amaral, Magnetoelastic coupling influence on the magnetocaloric effect in ferromagnetic materials, J. Magn. Magn. Mater. **272** (Part 3, SI) (2004) 2104–2105. doi:10.1016/j.jmmm.2003.12.870.

[85] V. Franco, J. S. Blázquez, A. Conde, V. Franco, J. S. Blázquez, A. Conde, Field dependence of the magnetocaloric effect in materials with a second order phase transition : A master curve for the magnetic entropy change Field dependence of the magnetocaloric effect in materials with a second order phase transition : A master cur, Appl. Phys. Lett. **222512** (2006) 24–27. doi:10.1063/1.2399361.

[86] N. A. de Oliveira, P. J. von Ranke, Theoretical aspects of the magnetocaloric effect, Phys. Rep. **489** (4-5) (2010) 89–159. doi:10.1016/j.physrep.2009.12.006.

[87] J. Lyubina, M. D. Kuz'min, K. Nenkov, O. Gutfleisch, M. Richter, D. L. Schlagel, T. A. Lograsso, K. A. Gschneidner, Magnetic field dependence of the maximum magnetic entropy change, Phys. Rev. B **83** (1) (2011) 012403. doi:10.1103/PhysRevB.83.012403.

[88] J. Katriel, Continued-Fraction Approximation for the Inverse Brillouin Function, Phys. Status Solidi **307** (1987) 307–310.

[89] A. Cohen, A Padé approximant to the inverse Langevin function, Rheol. Acta **30** (3) (1991) 270–273. doi:10.1007/BF00366640.

[90] A. S. Arrott, Approximations to Brillouin functions for analytic descriptions of ferromagnetism, J. Appl. Phys. **103** (7) (2008) 1–3. doi:10.1063/1.2836337.

[91] H. E. Stanley, Introduction to Phase Transitions and Critical Phenomena, Clarendon Press, Oxford, 1971.

[92] K. W. Zhou, Y. H. Zhuang, J. Q. Li, J. Q. Deng, Q. M. Zhu, Magnetocaloric effects in (Gd1-xTbx)Co-2, Solid State Commun. **137** (5) (2006) 275–277. doi:10.1016/j.ssc.2005.11.023.

[93] J. Mira, J. Rivas, L. E. Hueso, F. Rivadulla, M. A. Lopez Quintela, Drop of magnetocaloric effect related to the change from first- to second-order magnetic phase transition in La2/3(Ca1-xSrx)1/3MnO3, J. Appl. Phys. **91** (10 I) (2002) 8903–8905. doi:10.1063/1.1451892.

[94] Z. D. Han, Z. H. Hua, D. H. Wang, C. L. Zhang, B. X. Gu, Y. W. Du, Magnetic properties and magnetocaloric effect in Dy(Co1-xFex)(2) alloys, J. Magn. Magn. Mater. **302** (1) (2006) 109–112. doi:10.1016/j.jmmm.2005.08.013.

[95] O. Tegus, E. Bruck, L. Zhang, Dagula, K. H. J. Buschow, F. R. de Boer, Magnetic-phase transitions and magnetocaloric effects, Phys. B - Cond. Matter **319** (1-4) (2002) 174–192. doi:10.1016/S0921-4526(02)01119-5.

[96] N. H. Duc, D. T. K. Anh, P. E. Brommer, Metamagnetism, giant magnetoresistance and magnetocaloric effects in RCO2-based compounds in the vicinity of the Curie temperature, Phys. B - Cond. Matter **319** (1-4) (2002) 1–8. doi:10.1016/S0921-4526(02)01099-2.

[97] K. Sandeman, DDREAM (2017).
URL http://www.drream.eu/Mission.html

[98] N. Haque, A. Hughes, S. Lim, C. Vernon, Rare Earth Elements: Overview of Mining, Mineralogy, Uses, Sustainability and Environmental Impact, Resources **3** (4) (2014) 614–635. doi:10.3390/resources3040614.

[99] G. S. Smith, A. G. Tharp, W. Johnson, Rare earth-germanium and silicon compounds at 5:4 and 5:3 compositions, Acta Cryst. **22** (1967) 940–943.

[100] F. Holtzberg, R. J. Gambino, T. R. McGuire, New ferromagnetic 5:4 compounds in the rare earth silicon and germanium systems, J. Phys. Chem. Solids **28** (11) (1967) 2283–2289.

[101] L. Morellon, J. Blasco, P. A. Algarabel, M. R. Ibarra, Nature of the first-order antiferromagnetic-ferromagnetic transition in the Ge-rich magnetocaloric compounds Gd5(SixGe1-x)4, Phys. Rev. B **62** (2) (2000) 1022–1026.

[102] R. D. Shull, V. Provenzano, A.J. Shapiro, A. Fu, M. W. Lufaso, J. Karapetrova, G. Kletetschka, V. Mikula, The effects of small metal additions (Co,Cu,Ga,Mn,Al,Bi,Sn) on the magnetocaloric properties of the Gd5Ge2Si2 alloy, J. Appl. Phys. **99** (8) (2006) 08k908. doi:10.1063/1.2173632.

[103] V. K. Pecharsky, G. D. Samolyuk, V. P. Antropov, A. O. Pecharsky, K. A. Gschneidner, The effect of varying the crystal structure on the magnetism, electronic structure and ther-

modynamics in the Gd-5(SixGe1-x)(4) system near x=0.5, J. Solid State Chem. **171** (1-2) (2003) 57–68. doi:10.1016/S0022-4596(02)00146-9.

[104] W. Choe, V. K. Pecharsky, A. O. Pecharsky, K. A. Gschneidner, V. G. Young, G. J. Miller, Making and breaking covalent bonds across the magnetic transition in the giant magnetocaloric material Gd5Si2Ge2, Phys. Rev. Lett. **84** (20) (2000) 4617–4620.

[105] A. O. Pecharsky, V. K. Pecharsky, K. A. Gschneidner, Phase relationships and low temperature heat capacities of alloys in the Y5Si4–Y5Ge4 pseudo binary system, J. Alloys Compd. **379** (1-2) (2004) 127–134. doi:10.1016/j.jallcom.2004.03.069.

[106] A. O. Pecharsky, K. A. Gschneidner, V. K. Pecharsky, C. E. Schindler, The room temperature metastable / stable phase relationships in the pseudo-binary Gd5Si4–Gd5Ge4 system, J. Alloys Compd. **338** (2002) 126–135.

[107] C. Ritter, L. Morellón, P. A. Algarabel, C. Magen, M. R. Ibarra, Magnetic and structural phase diagram of Tb5(SixGe1-x)4, Phys. Rev. B **65** (9) (2002) 094405. doi:10.1103/PhysRevB.65.094405.

[108] M. A. Ruderman, C. Kittel, Indirect exchange coupling of nuclear magnetic moments by conduction electrons, Phys. Rev. **96** (1) (1954) 99–102. doi:10.1103/PhysRev.96.99.

[109] D. Haskel, Y. B. Lee, B. N. Harmon, Z. Islam, J. C. Lang, G. Srajer, Y. Mudryk, K. A. Gschneidner, V. K. Pecharsky, Role of Ge in bridging ferromagnetism in the giant magnetocaloric Gd5(Ge1-xSix)4 alloys, Phys. Rev. Lett. **98** (24) (2007) 247205. doi:10.1103/PhysRevLett.98.247205.

[110] W. Choe, G. J. Miller, J. Meyers, S. Chumbley, A. O. Pecharsky, “Nanoscale zippers´´ in the crystalline solid. Structural variations in the giant magnetocaloric material Gd5Si1.5Ge2.5, Chem. Mater. **15** (7) (2003) 1413–1419. doi:10.1021/cm020928l.

[111] C. Magen, Z. Arnold, L. Morellon, Y. Skorokhod, P. A. Algarabel, M. R. Ibarra, J. Kamarad, Pressure-Induced Three-Dimensional Ferromagnetic Correlations in the Giant Magnetocaloric Compound Gd5Ge4, Phys. Rev. Lett. **91** (20) (2003) 207202. doi:10.1103/PhysRevLett.91.207202.

[112] L. Manosa, D. Gonzalez-Alonso, A. Planes, E. Bonnot, M. Barrio, J.-L. Tamarit, S. Aksoy, M. Acet, Giant solid-state barocaloric effect in the Ni-Mn-In magnetic shape-memory alloy, Nat. Mater. **9** (6) (2010) 478–481. doi:10.1038/NMAT2731.

[113] D. Paudyal, V. Pecharsky, K. Gschneidner, B. Harmon, Electron correlation effects on the magnetostructural transition and magnetocaloric effect in Gd5Si2Ge2, Phys. Rev. B **73** (14) (2006) 144406. doi:10.1103/PhysRevB.73.144406.

[114] G. J. Liu, J. R. Sun, J. Lin, Y. W. Xie, T. Y. Zhao, H. W. Zhang, B. G. Shen, Entropy changes due to the first-order phase transition in the Gd5SixGe4−x system, Appl. Phys. Lett. **88** (21) (2006) 212505. doi:10.1063/1.2201879.

[115] A. Pires, J. Belo, A. Lopes, I. Gomes, L. Morellón, C. Magen, P. Algarabel, M. Ibarra, A. Pereira, J. Araújo, Phase Competitions behind the Giant Magnetic Entropy Variation: Gd5Si2Ge2 and Tb5Si2Ge2 Case Studies, Entropy **16** (7) (2014) 3813–3831. doi:10.3390/e16073813.

[116] J. H. Belo, M. Barbosa, A. Pires, R. M. Costa, J. Teixeira, J. Silva, P. A. Algarabel, C. Magen, L. Morellon, J. Amaral, U. Zeitler, G. Veerendra, A. M. dos Santos, Y. Ren, M. R.

Ibarra, J. P. Araujo, A. M. Pereira, Insights on the origin of the Tb5Ge4 Giant Magnetocaloric effect, Phys. B **513** (March) (2017) 72–76. doi:10.1016/j.physb.2017.03.009.

[117] K. Gschneidner, Y. Mudryk, V. Pecharsky, On the nature of the magnetocaloric effect of the first-order magnetostructural transition, Scr. Mater. **67** (6) (2012) 572–577. doi:10.1016/j.scriptamat.2011.12.042.

[118] M. P. Maley, H. A. Blackstead, P. L. Donoho, Microwave magnetoelastic effect in thin films of Dy, Ho, Gd, and Er, J. Appl. Phys. **37** (3) (1966) 1006–1007. doi:10.1063/1.1708308.

[119] C. W. Miller, D. V. Williams, N. S. Bingham, H. Srikanth, Magnetocaloric effect in Gd/W thin film heterostructures, J. Appl. Phys. **107** (9) (2010) 09A903. doi:10.1063/1.3335515.

[120] H. F. Kirby, D. D. Belyea, J. T. Willman, C. W. Miller, Effects of preparation conditions on the magnetocaloric properties of Gd thin films, J. Vac. Sci. Technol. A Vacuum, Surfaces, Film. **31** (3) (2013) 031506. doi:10.1116/1.4795817.

[121] B. J. Kirby, J. W. Lau, D. V. Williams, C. A. Bauer, C. W. Miller, Impact of interfacial magnetism on magnetocaloric properties of thin film heterostructures, J. Appl. Phys. **109** (6) (2011) 063905. doi:10.1063/1.3555101.

[122] M.-H. Phan, S.-C. Yu, Review of the magnetocaloric effect in manganite materials, J. Magn. Magn. Mater. **308** (2) (2007) 325–340. doi:10.1016/j.jmmm.2006.07.025.

[123] M. Gajdzic, T. Trappmann, C. Surgers, H. V. Lohneysen, Morphology and magnetic properties of submonolayer Gd films, Phys. Rev. B (Condensed Matter Mater. Physics) **57** (6) (1998) 3525–3530.

[124] Y. Yamada, M. Okada, P. Jin, M. Tazawa, K. Yoshimura, The Curie temperature dependence on preparation conditions for Gd thin films, Thin Solid Films **459** (1-2) (2004) 191–194. doi:10.1016/j.tsf.2003.12.081.

[125] E. A. Tereshina, S. Khmelevskyi, G. Politova, T. Kaminskaya, H. Drulis, I. S. Tereshina, Magnetic ordering temperature of nanocrystalline Gd: enhancement of magnetic interactions via hydrogenation-induced “negative” pressure, Sci. Rep. **6** (November 2015) (2016) 22553. doi:10.1038/srep22553.

[126] V. O. Vas’kovskii, A. V. Svalov, A. V. Gorbunov, N. N. Shchegoleva, S. M. Zadvorkin, Structural and magnetic phase transformations in multilayer gadolinium films, Phys. Solid State **43** (4) (2001) 698–704. doi:10.1134/1.1365996.

[127] G. Scheunert, W. R. Hendren, C. Ward, R. M. Bowman, Magnetization of 2.6 T in gadolinium thin films, Appl. Phys. Lett. **101** (14) (2012) 142407. doi:10.1063/1.4757126.

[128] T. P. Bertelli, E. C. Passamani, C. Larica, V. P. Nascimento, A. Y. Takeuchi, M. S. Pessoa, Ferromagnetic properties of fcc Gd thin films, J. Appl. Phys. **117** (20) (2015) 203904. doi:10.1063/1.4921813.

[129] B. M. S. Bist, O. N. Srivastava, A new f.c.c. gadolinium phase and its oxidation, J. Less-Common Met. **33** (1) (1973) 99–103. doi:10.1016/0022-5088(73)90060-X.

[130] D. H. A. L. Anselmo, V. D. Mello, M. S. Vasconcelos, Simulation of the magnetocaloric effect in Tb nanofilms, AIP Conf. Proc. **79** (2014) 79–81. doi:10.1063/1.4870199.

[131] F. C. M. Filho, V. D. Mello, A. L. Dantas, F. H. S. Sales, A. S. Carriço, Giant magnetocaloric effect of thin Ho films, J. Appl. Phys. **109** (7) (2011) 07A914. doi:10.1063/1.3549566.

[132] G. Scheunert, C. Ward, W. R. Hendren, A. A. Lapicki, R. Hardeman, M. Mooney, M. Gubbins, R. M. Bowman, Influence of strain and polycrystalline ordering on magnetic properties of high moment rare earth metals and alloys, J. Phys. D. Appl. Phys. **47** (41) (2014) 415005. doi:10.1088/0022-3727/47/41/415005.

[133] T. Zhou, M. Cher, L. Shen, J. Hu, Z. Yuan, On the origin of giant magnetocaloric effect and thermal hysteresis in multifunctional α-FeRh thin films, Phys. Lett. A **377** (42) (2013) 3052–3059. doi:10.1016/j.physleta.2013.09.027.

[134] W. Lu, P. Huang, K. Li, B. Yan, Effect of substrate temperature on the crystallographic structure and first-order magnetic phase transition of FeRh thin films, J. Mater. Res. **28** (08) (2013) 1042–1046. doi:10.1557/jmr.2013.61.

[135] A. Hillion, A. Cavallin, S. Vlaic, A. Tamion, F. Tournus, G. Khadra, J. Dreiser, C. Piamonteze, F. Nolting, S. Rusponi, K. Sato, T. J. Konno, O. Proux, V. Dupuis, H. Brune, Low temperature ferromagnetism in chemically ordered FeRh nanocrystals, Phys. Rev. Lett. **110** (8) (2013) 1–5. doi:10.1103/PhysRevLett.110.087207.

[136] M. F. H. Wolff, D. Görlitz, K. Nielsch, M. E. Messing, K. Deppert, Synthesis and magnetic characterization of MnAs nanoparticles via nanoparticle conversion., Nanotechnology **22** (5) (2011) 055602. doi:10.1088/0957-4484/22/5/055602.

[137] P. N. Hai, M. Tanaka, Memristive magnetic tunnel junctions with MnAs nanoparticles, Appl. Phys. Lett. **107** (12). doi:10.1063/1.4931141.

[138] P. Tian, Y. Zhang, K. Senevirathne, S. L. Brock, A. Dixit, G. Lawes, S. J. L. Billinge, Diverse structural and magnetic properties of differently prepared MnAs nanoparticle, ACS Nano **5** (4) (2011) 2970–2978. doi:10.1021/nn200020r.

[139] D. C. Dunand, P. Müllner, Size effects on magnetic actuation in Ni-Mn-Ga shape-memory alloys., Adv. Mater. **23** (2) (2011) 216–32. doi:10.1002/adma.201002753.

[140] P. Ranzieri, S. Fabbrici, L. Nasi, L. Righi, F. Casoli, V. A. Chernenko, E. Villa, F. Albertini, Epitaxial Ni–Mn–Ga/MgO(100) thin films ranging in thickness from 10 to 100nm, Acta Mater. **61** (1) (2013) 263–272. doi:10.1016/j.actamat.2012.09.056.

[141] A. Roytburd, T. Kim, Q. Su, J. Slutsker, M. Wuttig, Martensitic transformation in constrained films, Acta Mater. **46** (14) (1998) 5095–5107. doi:10.1016/S1359-6454(98)00165-7.

[142] G. A. Malygin, Size effects under martensitic deformation of shape-memory alloys, Tech. Phys. **54** (12) (2009) 1782–1785. doi:10.1134/S106378420912010X.

[143] S. Vinodh Kumar, R. Singh, S. Seenithurai, S. Bysakh, M. Manivel Raja, M. Mahendran, Phase structure and magnetic properties of the annealed Mn-rich Ni–Mn–Ga ferromagnetic shape memory thin films, Mater. Res. Bull. **61** (2015) 95–100. doi:10.1016/j.materresbull.2014.10.008.

[144] N. Teichert, a. Auge, E. Yüzüak, I. Dincer, Y. Elerman, B. Krumme, H. Wende, O. Yildirim, K. Potzger, a. Hütten, Influence of film thickness and composition on the martensitic transformation in epitaxial Ni–Mn–Sn thin films, Acta Mater. **86** (2015) 279–285. doi:10.1016/j.actamat.2014.12.019.

[145] R. Vishnoi, R. Singhal, D. Kaur, Thickness dependent phase transformation of magnetron-sputtered Ni-Mn-Sn ferromagnetic shape memory alloy thin films, J. Nanoparticle Res.

13 (9) (2011) 3975–3990. doi:10.1007/s11051-011-0321-3.

[146] S. Jin, T. H. Tiefel, M. McCormack, R. A. Fastnacht, R. Ramesh, L. H. Chen, Thousandfold change in resistivity in magnetoresistive La-Ca-Mn-O films, Science (80-.). **264** (5157) (1994) 413–415. doi:10.1126/science.264.5157.413.

[147] Z. Wang, T. Tang, Y. Wang, S. Zhang, Y. Du, Room temperature large magnetoresistance and magnetocaloric properties of La0.78Ag0.22MnO3 film, J. Magn. Magn. Mater. **246** (1-2) (2002) 254–258. doi:10.1016/S0304-8853(02)00063-X.

[148] X. Moya, L. E. Hueso, F. Maccherozzi, A. I. Tovstolytkin, D. I. Podyalovskii, C. Ducati, L. C. Phillips, M. Ghidini, O. Hovorka, A. Berger, M. E. Vickers, E. Defay, S. S. Dhesi, N. D. Mathur, Giant and reversible extrinsic magnetocaloric effects in La0.7Ca0.3MnO3 films due to strain, Nat. Mater. **12** (1) (2013) 52–8. doi:10.1038/nmat3463.

[149] S. N. Sambandam, B. Bethala, D. K. Sood, S. Bhansali, Evaluation of silicon nitride as a diffusion barrier for Gd-Si-Ge films on silicon, Surf. Coat. Technol. **200** (5-6) (2005) 1335–1340. doi:10.1016/j.surfcoat.2005.08.130.

[150] P. Trevizoli, C. Alves, M. A. B. Mendes, A. M. G. Carvalho, S. Gama, Powder metallurgy influences on the magnetic properties of Gd5.09Ge2.03Si1.88 alloy, J. Magn. Magn. Mater. **320** (8) (2008) 1582–1585. doi:10.1016/j.jmmm.2008.01.007.

[151] D. M. Rajkumar, M. M. Raja, R. Gopalan, V. Chandrasekaran, Magnetocaloric effect in high-energy ball-milled Gd5Si2Ge2 and Gd5Si2Ge2/Fe nanopowders, J.. Magn.. Magn.. Mater.. **320** (8) (2008) 1479–1484. doi:10.1016/j.jmmm.2007.12.005.

[152] G. Giovanna do Couto, V. Svitlyk, M. Jafelicci, Y. Mozharivskyj, Bulk and high-energy ball-milled Gd5Si2Ge2: Comparative study of magnetic and magnetocaloric properties, Solid State Sci. **13** (1) (2011) 209–215. doi:10.1016/j.solidstatesciences.2010.11.016.

[153] A. O. Pecharsky, K. A. Gschneidner, V. K. Pecharsky, The giant magnetocaloric effect of optimally prepared Gd5Si2Ge2, J. Appl. Phys. **93** (8) (2003) 4722–4728. doi:10.1063/1.1558210.

[154] J. H. Belo, A. M. Pereira, J. Ventura, G. N. P. Oliveira, J. P. Araujo, P. B. Tavares, L. Fernandes, P. A. Algarabel, C. Magen, L. Morellon, M. R. Ibarra, Phase control studies In Gd5Si2Ge2 giant magnetocaloric compound, J. Alloys Compd. **529** (2012) 89–95.

[155] K. Chaudhary, S. Z. H. Rizvi, J. Ali, Laser-Induced Plasma and its Applications, in: Plasma Sci. Technol. - Prog. Phys. States Chem. React., InTech, 2016. doi:10.5772/61784.
URL http://www.intechopen.com/books/plasma-science-and-technology

[156] I. T. Gomes, Manganite thin films deposited on piezoelectric substrates, Ph.D. thesis, Universidade do Minho (2013).

[157] T. H. Maiman, Stimulated Optical Radiation in Ruby, Nature **187** (4736) (1960) 493–494. doi:10.1038/187493a0.

[158] D. B. Chrisey, G. K. Hubler, Pulsed laser deposition of thin films, J. Wiley, 1994.

[159] D. P. Norton, A. Goyal, J. D. Budai, D. K. Christen, D. M. Kroeger, E. D. Specht, Q. He, B. Saffian, M. Paranthaman, C. E. Klabunde, D. F. Lee, B. C. Sales, F. A. List, Epitaxial YBa2Cu3O7 on Biaxially Textured Nickel (001): An Approach to Superconducting Tapes with High Critical Current Density, Science (80-.). **274** (5288).

[160] R. Ramesh, A. Inam, W. K. Chan, B. Wilkens, K. Myers, K. Remschnig, D. L. Hart, J. M. Tarascon, Epitaxial Cuprate Superconductor/Ferroelectric Heterostructures, Science (80-.). **252** (5008) (1991) 944–946.

[161] D. H. Wang, L. Yan, C. K. Ong, Y. W. Du, BiFeO3 film deposited on Si substrate buffered with La0.7Sr0.3MnO3 electrode, Appl. Phys. Lett. **89** (18) (2006) 182905. doi: 10.1063/1.2374805.

[162] M. Martino, M. Cesaria, A. P. Caricato, G. Maruccio, A. Cola, I. Farella, La0.7Sr0.3MnO3 thin films deposited by pulsed laser ablation for spintronic applications, Phys. status solidi **208** (8) (2011) 1817–1820. doi:10.1002/pssa.201084037.

[163] J. Shen, Z. Gai, J. Kirschner, Growth and magnetism of metallic thin films and multilayers by pulsed-laser deposition, Surf. Sci. Rep. **52** (5) (2004) 163–218. doi: 10.1016/j.surfrep.2003.10.001.

[164] T. J. Jackson, S. B. Palmer, Oxide superconductor and magnetic metal thin film deposition by pulsed laser ablation: a review, J. Phys. D. Appl. Phys. **27** (8) (1994) 1581–1594. doi:10.1088/0022-3727/27/8/001.

[165] S. Amoruso, G. Ausanio, R. Bruzzese, M. Vitiello, X. Wang, Femtosecond laser pulse irradiation of solid targets as a general route to nanoparticle formation in a vacuum, Phys. Rev. B **71** (3) (2005) 033406. doi:10.1103/PhysRevB.71.033406.

[166] M. A. Sobhan, M. Ams, Ultrafast laser ablative generation of gold nanoparticles: the influence of pulse energy, repetition frequency and spot size, J. Nanoparticle Res. **12** (2010) 2831–2842. doi:10.1007/s11051-010-9868-7.

[167] N. G. Semaltianos, S. Logothetidis, W. Perrie, S. Romani, R. J. Potter, S. P. Edwardson, F. P, S. M, D. G, W. K. G, Silicon nanoparticles generated by femtosecond laser ablation in a liquid environment, J. Nanoparticle Res. **12** (12) (2010) 573–580. doi: 10.1007/s11051-009-9625-y.

[168] L. Mercadier, D. M. Rayner, P. B. Corkum, Control of Femtosecond Laser Ablation of Thin Films from a Dielectric Surface by Nonlinear Interaction with the Substrate, Phys. Rev. Appl. **2** (3) (2014) 034001. doi:10.1103/PhysRevApplied.2.034001.

[169] M. System, Sputtering Diagram (2017).
URL http://www.m-system.co.jp/newsletter/182/clip{_}contents.html

[170] Aja International Inc., Aja International Inc. (2017).
URL http://www.ajaint.com/sputtering-systems.html

[171] M. W. Thompson, II. The energy spectrum of ejected atoms during the high energy sputtering of gold, Philos. Mag. **18** (152) (1968) 377–414. doi:10.1080/14786436808227358.

[172] Claudionico, SEM diagram (2013).
URL https://upload.wikimedia.org/wikipedia/commons/4/49/ElectronInteractionwithMatter

[173] J. I. Goldstein, D. E. Newbury, P. Echlin, D. C. Joy, A. D. Romig, C. E. Lyman, C. Fiori, E. Lifshin, Scanning Electron Microscopy and X-Ray Microanalysis : a Text for Biologists, Materials Scientists, and Geologists, Springer US, 1992.

[174] National Programme on Technology Enhanced, SEM and TEM (2003).
URL http://nptel.ac.in/courses/102103044/module3/lec18/1.html

[175] C. Kisielowski, B. Freitag, M. Bischoff, H. van Lin, S. Lazar, G. Knippels, P. Tiemeijer, M. van der Stam, S. von Harrach, M. Stekelenburg, M. Haider, S. Uhlemann, H. Müller, P. Hartel, B. Kabius, D. Miller, I. Petrov, E. Olson, T. Donchev, E. Kenik, A. Lupini, J. Bentley, S. Pennycook, I. Anderson, A. Minor, A. Schmid, T. Duden, V. Radmilovic, Q. Ramasse, M. Watanabe, R. Erni, E. Stach, P. Denes, U. Dahmen, Detection of Single Atoms and Buried Defects in Three Dimensions by Aberration-Corrected Electron Microscope with 0.5-Å Information Limit, Microsc. Microanal. **14** (05) (2008) 469–477. doi:10.1017/S1431927608080902.

[176] FEI, FEI Tecnai F30.
URL https://www.fei.com/products/tem/tecnai/

[177] Rigaku, Powder diffraction optics for SmartLab X-ray diffractometer, Rigaku J. **26** (2) (2010) 29–30.

[178] W. H. Bragg, W. L. Bragg, The reflexion of x-rays by crystals, Proc. R. Soc. A Math. Phys. Eng. Sci. **88** (605) (1913) 428–438. doi:10.1103/PhysRev.18.396.

[179] APS, APS.
URL https://www1.aps.anl.gov/Users-Information/Getting-Started/Introduction-to-APS

[180] T. F. Team, Full Prof.
URL https://www.ill.eu/sites/fullprof/

[181] H. M. Rietveld, A profile refinement method for nuclear and magnetic structures, J. Appl. Crystallogr. **2** (2) (1969) 65–71. doi:10.1107/S0021889869006558.

[182] A. Le Bail, H. Duroy, J. Fourquet, Ab-initio structure determination of LiSbWO6 by X-ray powder diffraction, Mater. Res. Bull. **23** (3) (1988) 447–452. doi:10.1016/0025-5408(88)90019-0.

[183] Q. Design, SQUID.
URL https://lot-qd.de/en/products/materials-science/magnetometers/

[184] L. Caron, Z. Q. Ou, T. T. Nguyen, D. T. Cam Thanh, O. Tegus, E. Brück, On the determination of the magnetic entropy change in materials with first-order transitions, J. Magn. Magn. Mater. **321** (21) (2009) 3559–3566. doi:10.1016/j.jmmm.2009.06.086.

[185] M. Nazih, A. de Visser, L. Zhang, O. Tegus, E. Bruck, Thermal expansion of the magnetorefrigerant Gd5(Si,Ge)(4), Solid State Commun. **126** (5) (2003) 255–259. doi:10.1016/S0038-1098(03)00131-5.

[186] J. P. Attfield, Condensed-matter physics: A fresh twist on shrinking materials, Nature **480** (7378) (2011) 465–466. doi:10.1038/480465a.

[187] G. D. Barrera, J. A. O. Bruno, T. H. K. Barron, N. L. Allan, Negative thermal expansion, J. Phys. Conden. Matt. **17** (2005) R217–R252. doi:10.1088/0953-8984/17/4/R03.

[188] M. V. . Schilfgaarde, I. A. Abrikosov, B. Johansson, Origin of the Invar effect of iron-nickel alloys, Nature **400** (July) (1999) 46–49. doi:10.1038/21848.

[189] X. G. Zheng, H. Kubozono, H. Yamada, K. Kato, Y. Ishiwata, C. N. Xu, Giant negative thermal expansion in magnetic nanocrystals., Nat. Nanotechnol. **3** (12) (2008) 724–6. doi:10.1038/nnano.2008.309.

[190] W. H. Li, S. Wu, C. Yang, S. Lai, K. Lee, H. L. Huang, H. D. Yang, Thermal Con-

traction of Au Nanoparticles, Phys. Rev. Lett. **89** (13) (2002) 135504–1 –135504–4. doi:10.1103/PhysRevLett.89.135504.

[191] V. Iannotti, S. Amoruso, G. Ausanio, A. C. Barone, C. Campana, X. Wang, L. Lanotte, Ultrafast pulsed laser deposition as a method for the synthesis of innovative magnetic films, Appl. Surf. Sci. **255** (10) (2009) 5224–5227. doi:10.1016/j.apsusc.2008.10.088.

[192] F. Garrelie, C. Donnet, A. S. Loir, N. Benchikh, New trends in femtosecond Pulsed Laser Deposition and femtosecond produced plasma diagnostics, SPIE Proc. **6261** (2006) 9.

[193] S. Eliezer, N. Eliaz, E. Grossman, D. Fisher, I. Gouzman, Z. Henis, S. Pecker, Y. Horovitz, M. Fraenkel, S. Maman, Y. Lereah, Synthesis of nanoparticles with femtosecond laser pulses, Phys. Rev. B **69** (14) (2004) 144119. doi:10.1103/PhysRevB.69.144119.

[194] W. H. Qi, M. P. Wang, Y. C. Su, Size effect on the lattice parameters of nanoparticles, J. Mater. Sci. **2** (4) (2002) 877–878.

[195] Z. Huang, P. Thomson, S. Di, Lattice contractions of a nanoparticle due to the surface tension: A model of elasticity, J. Phys. Chem. Solids **68** (4) (2007) 530–535. doi:10.1016/j.jpcs.2007.01.016.

[196] D. Hunter, W. Osborn, K. Wang, N. Kazantseva, J. Hattrick-Simpers, R. Suchoski, R. Takahashi, M. L. Young, A. Mehta, L. Bendersky, S. E. Lofland, M. Wuttig, I. Takeuchi, Giant magnetostriction in annealed Co(1-x)Fe(x) thin-films., Nat. Commun. **2** (May) (2011) 518. doi:10.1038/ncomms1529.

[197] M. Wun-Fogle, J. B. Restorff, K. Leung, J. R. Cullen, A. E. Clark, Magnetostriction of Terfenol-D heat treated under compressive stress, IEEE Trans. Magn. **35** (5) (1999) 3817–3819.

[198] E. Liu, W. Wang, L. Feng, W. Zhu, G. Li, J. Chen, H. Zhang, G. Wu, C. Jiang, H. Xu, F. de Boer, Stable magnetostructural coupling with tunable magnetoresponsive effects in hexagonal ferromagnets., Nat. Commun. **3** (May) (2012) 873. doi:10.1038/ncomms1868.

[199] J. X. Zhang, B. Xiang, Q. He, J. Seidel, R. J. Zeches, P. Yu, S. Y. Yang, C. H. Wang, Y.-H. Chu, L. W. Martin, A. M. Minor, R. Ramesh, Large field-induced strains in a lead-free piezoelectric material., Nat. Nanotechnol. **6** (2) (2011) 98–102. doi:10.1038/nnano.2010.265.

[200] K. Takenaka, Y. Okamoto, T. Shinoda, N. Katayama, Y. Sakai, Colossal negative thermal expansion in reduced layered ruthenate, Nat. Commun. **8** (2017) 14102. doi:10.1038/ncomms14102.

[201] J. S. Amaral, V. S. Amaral, Disorder effects in giant magnetocaloric materials, Phys. Status Solidi **211** (5) (2014) 971–974. doi:10.1002/pssa.201300749.

[202] V. S. Kumar, R. Chukka, Z. Chen, P. Yang, L. Chen, Strain dependent magnetocaloric effect in La0.67Sr0.33MnO3 thin-films, AIP Adv. **3** (5) (2013) 052127. doi:10.1063/1.4807739.

[203] Q. Zhang, S. Thota, F. Guillou, P. Padhan, V. Hardy, A. Wahl, W. Prellier, Magnetocaloric effect and improved relative cooling power in (La(0.7)Sr(0.3)MnO(3)/SrRuO(3)) superlattices, J. Phys. Condens. Matter **23** (5). doi:10.1088/0953-8984/23/5/052201.

[204] V. Recarte, J. I. Pérez-Landazábal, V. Sánchez-Alárcos, V. A. Chernenko, M. Ohtsuka,

Magnetocaloric effect linked to the martensitic transformation in sputter-deposited Ni–Mn–Ga thin films, Appl. Phys. Lett. **95** (14) (2009) 141908. doi:10.1063/1.3246149.

[205] S. Singh, S. W. D'Souza, K. Mukherjee, P. Kushwaha, S. R. Barman, S. Agarwal, P. K. Mukhopadhyay, A. Chakrabarti, E. V. Sampathkumaran, Magnetic properties and magnetocaloric effect in Pt doped Ni-Mn-Ga, Appl. Phys. Lett. **104** (23) (2014) 231909. doi:10.1063/1.4883404.

[206] D. D. Belyea, T. S. Santos, C. W. Miller, Magnetocaloric effect in epitaxial La0.56Sr0.44MnO3 alloy and digital heterostructures, J. Appl. Phys. **111** (7) (2012) 07A935. doi:10.1063/1.3677670.

[207] J. D. Moore, K. Morrison, K. G. Sandeman, M. Katter, L. F. Cohen, Reducing extrinsic hysteresis in first-order La(Fe,Co,Si)13magnetocaloric systems, Appl. Phys. Lett. **95** (25) (2009) 252504. doi:10.1063/1.3276565.

[208] D. J. Silva, B. D. Bordalo, A. M. Pereira, J. Ventura, J. P. Araújo, Solid state magnetic refrigerator, Appl. Energy **93** (2012) 570–574. doi:10.1016/j.apenergy.2011.12.002.

[209] Y. C. Tseng, D. Haskel, J. C. Lang, S. Sinogeikin, Y. Mudryk, V. K. Pecharsky, K. A. Gschneidner Jr., Effect of hydrostatic pressure upon the magnetic transitions in the Gd5(SixGe1-x)(4) giant magnetocaloric compounds: X-ray magnetic circular dichroism study, Phys. Rev. B **76** (1). doi:10.1103/PhysRevB.76.014411.

[210] Y. C. Tseng, D. Haskel, J. C. Lang, Y. Mudryk, V. K. Pecharsky, K. A. Gschneidner, Pressure tuning of the magnetic transition in Gd5(Si0.375Ge0.625)4 giant magnetocaloric effect material, J. Appl. Phys. **103** (7) (2008) 07B301. doi:10.1063/1.2828514.

[211] Y. Tseng, D. Haskel, N. Souza-Neto, Y. Mudryk, V. Pecharsky, K. Gschneidner, Pressure-induced removal of magnetostructural inhomogeneity in Ge-rich Gd5(SixGe1−x)4 giant magnetocaloric alloys, Phys. Rev. B **78** (21) (2008) 214433. doi:10.1103/PhysRevB.78.214433.

[212] L. Morellon, Z. Arnold, P. A. Algarabel, C. Magen, M. R. Ibarram, Y. Skorokhod, Pressure effects in the giant magnetocaloric compounds Gd5(SixGe1-x)4, J. Phys. Condens. Matter **16** (9) (2004) 1623–1630.

[213] D. Vollath, Nanoparticles - Nanocomposites Nanomaterials, vch, wiley Edition, VCH, Wiley, 2013.

[214] K. Takenaka, Negative thermal expansion materials: technological key for control of thermal expansion, Sci. Technol. Adv. Mater. **13** (1) (2012) 013001. doi:10.1088/1468-6996/13/1/013001.

[215] A. Malhotra, M. Maldovan, Impact of Phonon Surface Scattering on Thermal Energy Distribution of Si and SiGe Nanowires., Sci. Rep. **6** (April) (2016) 25818. doi:10.1038/srep25818.

[216] R. Huang, Y. Liu, W. Fan, J. Tan, F. Xiao, L. Qian, L. Li, Giant negative thermal expansion in NaZn13-type La(Fe, Si, Co)13 compounds, J. Am. Chem. Soc. **135** (31) (2013) 11469–11472. doi:10.1021/ja405161z.

[217] J. Arvanitidis, K. Papagelis, S. Margadonna, K. Prassides, A. N. Fitch, Temperature-induced valence transition and associated lattice collapse in samarium fulleride., Nature **425** (6958) (2003) 599–602. doi:10.1038/nature01994.

[218] Y. W. Long, N. Hayashi, T. Saito, M. Azuma, S. Muranaka, Y. Shimakawa, Temperature-induced A-B intersite charge transfer in an A-site-ordered LaCu3Fe4O12 perovskite., Nature **458** (7234) (2009) 60–3. doi:10.1038/nature07816.

[219] A. L. Goodwin, The ins and outs of thermal expansion, Nat. Nanotechnol. **3** (2008) 711–712. doi:10.1016/j.tcb.2004.07.007.

[220] V. Korthuis, N. Khosrovani, A. W. Sleight, N. Roberts, R. Dupree, W. W. Warren, Negative thermal expansion and phase transitions in the ZrV2-xPxO7 series, Chem. Mater. **7** (2) (1995) 412–417. doi:10.1021/cm00050a028.

[221] A. L. Goodwin, M. Calleja, M. J. Conterio, M. T. Dove, J. S. O. Evans, D. A. Keen, L. Peters, M. G. Tucker, Colossal positive and negative thermal expansion in the framework material Ag3[Co(CN)6]., Science **319** (5864) (2008) 794–7. doi:10.1126/science.1151442.

[222] Y. Mudryk, D. Paudyal, V. K. Pecharsky, K. A. Gschneidner, S. Misra, G. J. Miller, Controlling Magnetism of a Complex Metallic System Using Atomic Individualism, Phys. Rev. Lett. **105** (6) (2010) 66401. doi:10.1103/PhysRevLett.105.066401.

[223] C. Pantea, A. Migliori, P. B. Littlewood, Y. Zhao, H. Ledbetter, J. C. Lashley, T. Kimura, J. V. Duijn, G. R. Kowach, Pressure-induced elastic softening of monocrystalline zirconium tungstate at 300 K, Phys. Rev. B (Condensed Matter Mater. Physics) **73** (214118) (2006) 1–5. doi:10.1103/PhysRevB.73.214118.

[224] C. Magen, L. Morellon, P. A. Algarabel, M. R. Ibarra, Z. Arnold, J. Kamarad, T. A. Lograsso, D. L. Schlagel, V. K. Pecharsky, A. O. Tsokol, K. A. Gschneidner Jr., Hydrostatic pressure control of the magnetostructural phase transition in Gd5Si2Ge2 single crystals, Phys. Rev. B **72** (2) (2005) 24416. doi:10.1103/PhysRevB.72.024416.

[225] L. C. Kozy, N. Tahir, W. Tremel, Particle size and morphology control of the negative thermal expansion material cubic zirconium tungstate, J. Mater. Chem. **7** (2009) 2760–2765. doi:10.1039/b820014a.

[226] K. Kintaka, J. Nishii, P. G. Kazansky, Temperature sensitivity of GeBSiO2 waveguide Bragg gratings on a crystallized glass substrate, Opt. Lett. **27** (16) (2002) 1394–1396.

[227] J. S. O. Evans, Negative thermal expansion materials, J. Chem. Soc. Dalt. Trans. **19** (19) (1999) 3317–3326. doi:10.1039/a904297k.

[228] P. Lampen, N. S. Bingham, M. H. Phan, H. Kim, M. Osofsky, a. Piqué, T. L. Phan, S. C. Yu, H. Srikanth, Impact of reduced dimensionality on the magnetic and magnetocaloric response of La0.7Ca0.3MnO3, Appl. Phys. Lett. **102** (6) (2013) 062414. doi:10.1063/1.4792239.

[229] H. Fu, X. T. Zu, X. He, W. S. He, T. D. Shen, The effect of low temperature annealing on the structure of Gd5Si2Ge2 alloy, J. Alloys Compd. **431** (1-2) (2007) 89–92.

[230] T. Zhang, Y. Chen, B. Teng, Y. Tang, H. Fu, M. Tu, The structure and magnetocaloric effect of rapidly quenched Gd5Si2Ge2 alloy with low-purity gadolinium, Mater. Lett. **61** (2) (2007) 440–443. doi:10.1016/j.matlet.2006.04.084.

[231] Y. Mozharivskyj, A. O. Pecharsky, V. K. Pecharsky, G. J. Miller, On the high-temperature phase transition of Gd5Si2Ge2, J. Am. Chem. Soc. **127** (1) (2005) 317–324. doi:10.1021/ja048679k.

[232] O. Tegus, E. Bruck, K. H. J. Buschow, F. R. de Boer, Transition-metal-based magnetic refrigerants for room-temperature applications, Nature **415** (6868) (2002) 150–152.

[233] J. Lyubina, K. Nenkov, L. Schultz, O. Gutfleisch, Multiple Metamagnetic Transitions in the Magnetic Refrigerant La(Fe, Si)(13)H(x), Phys. Rev. Lett. **101** (17). doi: 10.1103/PhysRevLett.101.177203.

[234] T. Krenke, E. Duman, M. Acet, E. F. Wassermann, X. Moya, L. Mañosa, A. Planes, Inverse magnetocaloric effect in ferromagnetic Ni–Mn–Sn alloys, Nat. Mater. **4** (2005) 450–454.

[235] K. P. Skokov, K. H. Muller, J. D. Moore, J. Liu, A. Y. Karpenkov, M. Krautz, O. Gutfleisch, Influence of thermal hysteresis and field cycling on the magnetocaloric effect in LaFe11.6Si1.4, J. Alloys Compd. **552** (2013) 310–317. doi:10.1016/j.jallcom.2012.10.008.

[236] A. Waske, L. Giebeler, B. Weise, A. Funk, M. Hinterstein, M. Herklotz, K. Skokov, S. Fahler, O. Gutfleisch, J. Eckert, Asymmetric first-order transition and interlocked particle state in magnetocaloric La(Fe,Si)13, Phys. Status Solidi - Rapid Res. Lett. **9** (2) (2015) 136–140. doi:10.1002/pssr.201409484.

[237] J. B. Sousa, A. M. Pereira, F. C. Correia, J. M. Teixeira, J. P. Araújo, R. P. Pinto, M. E. Braga, L. Morellon, P. A. Algarabel, C. Magen, M. R. Ibarra, Multi-step and anomalous reproducible behaviour of the electrical resistivity near the first-order magnetostructural transition of Gd5(Si0.1Ge0.9)4, J. Phys. Condens. Matter **17** (15) (2005) 2461–2476. doi: 10.1088/0953-8984/17/15/017.

[238] F. J. Perez-Reche, F. Casanova, E. Vives, L. Manosa, A. Planes, J. Marcos, X. Batlle, A. Labarta, Acoustic emission across the magnetostructural transition of the giant magnetocaloric Gd5Si2Ge2, Phys. Rev. B **73** (1). doi:10.1103/PhysRevB.73.014110.

[239] E. M. Levin, A. O. Pecharsky, V. K. Pecharsky, K. A. Gschneidner Jr., Transformations in the Gd5(Si1.95Ge2.05) alloy induced by the temperature and magnetic-field cycling through the first-order magnetic-martensitic phase transition, Phys. Rev. B **63** (6) (2001) 644261.

[240] A. M. Pereira, J. P. Araújo, J. R. Peixoto, M. E. Braga, P. A. Algarabel, C. Magen, L. Morellon, M. R. Ibarra, J. B. Sousa, Electron scattering processes in Ho5(Si,Ge)4 compounds: Electrical resistivity studies, Phys. Rev. B **83** (14) (2011) 144117. doi: 10.1103/PhysRevB.83.144117.

[241] E. M. Levin, V. K. Pecharsky, J. Gschneidner K.A., G. J. Miller, Electrical resistivity, electronic heat capacity, and electronic structure of Gd5Ge4, Phys. Rev. B **64** (23) (2001) 2351031–23510311.

[242] E. M. Levin, V. K. Pecharsky, K. A. Gschneidner Jr., Magnetic-field and temperature dependencies of the electrical resistance near the magnetic and crystallographic first-order phase transition of Gd5(Si2Ge2), Phys. Rev. B **60** (11) (1999) 7993–7997. doi: 10.1103/PhysRevB.60.7993.

[243] R. L. Hadimani, D. C. Jiles, Resistivity recovery in Gd5 Si2.09 Ge1.91 by annealing, J. Appl. Phys. **107** (9) (2010) 134–137. doi:10.1063/1.3355355.

[244] A. M. Pereira, J. P. Araujo, J. R. Peixoto, M. E. Braga, P. A. Algarabel, C. Magen, L. Morellon, M. R. Ibarra, J. B. Sousa, Electron scattering processes in Ho(5)(Si(x)Ge(1-x))(4) compounds: Electrical resistivity studies, Phys. Rev. B **83** (14).

doi:10.1103/PhysRevB.83.144117.

[245] E. M. Levin, A. O. Pecharsky, V. K. Pecharsky, K. A. Gschneidner, Transformations in the Gd5Si1.95Ge2.05 alloy induced by the temperature and magnetic-field cycling through the first order magnetic martensitic phase transition, Phys. Rev. B **63** (6) (2001) 064426. doi:10.1103/PhysRevB.63.064426.

[246] B. Banerjee, On a generalised approach to first and second order magnetic transitions, Phys. Lett. **12** (1) (1964) 16–17. doi:10.1016/0031-9163(64)91158-8.

[247] H. Yang, G. Rao, G. Liu, Z. Ouyang, W. Liu, X. Feng, W. Chu, J. Liang, Crystal structures of compounds in the pseudobinary system Gd5Ge4–La5Ge4, J. Alloys Compd. **361** (1) (2003) 113–117. doi:10.1016/S0925-8388(03)00384-0.

[248] J. E. Iglesias, H. Steinfink, The crystal structure of Gd5Si4, J. Less Common Met. **26** (1) (1972) 45–52. doi:10.1016/0022-5088(72)90007-0.

[249] O. J. Guentert, R. L. Mozzi, IUCr, The monoclinic modification of gadolinium sesquioxide Gd2O3, Acta Crystallogr. **11** (10) (1958) 746–746. doi:10.1107/S0365110X58002012.

[250] A. Yan, A. Handstein, P. Kerschl, K. Nenkov, K. H. Muller, O. Gutfleisch, Effect of composition and cooling rate on the structure and magnetic entropy change in Gd5SixGe4Ax, J. Appl. Phys. **95** (11).

[251] J. C. Debnath, J. H. Kim, Y. Heo, a. M. Strydom, S. X. Dou, Correlation between structural parameters and the magnetocaloric effect in epitaxial La0.8Ca0.2MnO3/LaAlO3 thin film, J. Appl. Phys. **113** (6) (2013) 063508. doi:10.1063/1.4790876.

[252] Y. Zhang, R. A. Hughes, J. F. Britten, W. Gong, J. S. Preston, G. A. Botton, M. Niewczas, Epitaxial Ni–Mn–Ga films derived through high temperature in situ depositions, Smart Mater. Struct. **18** (2) (2009) 025019. doi:10.1088/0964-1726/18/2/025019.

[253] L. Morellon, P. A. Algarabel, C. Magen, M. R. Ibarra, Giant magnetoresistance in the Ge-rich magnetocaloric compound, Gd-5(Si0.1Ge0.9)(4), J. Mag. Mag. Mater. **237** (2) (2001) 119–123. doi:10.1016/S0304-8853(01)00506-6.

[254] J. P. Araujo, A. M. Pereira, M. E. Braga, R. P. Pinto, J. M. Teixeira, F. C. Correia, J. B. Sousa, L. Morellon, P. A. Algarabel, C. Magen, M. R. Ibarra, Transport and magnetic study of the spin reorientation transition in the Tb5(Si0.5Ge0.5)4 magnetocaloric compound, J. Phys. Condens. Matter **17** (32) (2005) 4941–4949.

[255] W. Choe, V. K. Pecharsky, A. O. Pecharsky, K. A. Gschneidner Jr., V. G. Young Jr., G. J. Miller, Making and Breaking Covalent Bonds across the Magnetic Transition in the Giant Magnetocaloric Material Gd5(Si2Ge2), Phys. Rev. Lett. **84** (20) (2000) 4617–4620.

[256] J. Stankiewicz, L. Morellon, P. Algarabel, M. Ibarra, Hall effect in Gd5(Si1.8Ge2.2), Phys. Rev. B **61** (19) (2000) 12651–12653.

[257] D. Raj Kumar, M. Manivel Raja, K. Prabahar, V. Chandrasekaran, A. Poddar, R. Ranganathan, K. Suresh, Effect of Si/Ge ratio on resistivity and thermopower in Gd5SixGe4−x magnetocaloric compounds, J. Magn. Magn. Mater. **323** (13) (2011) 1750–1754. doi:10.1016/j.jmmm.2011.01.017.

[258] F. Casanova, A. Labarta, X. Batlle, F. J. Perez-Reche, E. Vives, L. Manosa, A. Planes, Direct observation of the magnetic-field-induced entropy change in Gd5(SixGe1-x)4 giant

magnetocaloric alloys, Appl. Phys. Lett. **86** (26) (2005) 1–3. doi:10.1063/1.1968431.

[259] S. Velez, J. M. Hernandez, A. Fernandez, F. Macià, C. Magen, P. A. Algarabel, J. Tejada, E. M. Chudnovsky, Magnetic deflagration in Gd5Ge4, Phys. Rev. B **81** (6) (2010) 064437. doi:10.1103/PhysRevB.81.064437.

[260] L. Manosa, A. Planes, E. Cesari, Acoustic Emission Amplitude Distribution During the Martensitic Transformation of Cu-Zn-Al Alloys, J. Phys. D Appl. Phys. **22** (22) (1989) 977–982.

[261] J. Baró, J.-M. Martín-Olalla, F. J. Romero, M. C. Gallardo, E. K. H. Salje, E. Vives, A. Planes, Avalanche correlations in the martensitic transition of a Cu-Zn-Al shape memory alloy: analysis of acoustic emission and calorimetry., J. Phys. Condens. Matter **26** (2014) 125401. doi:10.1088/0953-8984/26/12/125401.

[262] F. Perez-Reche, F. Casanova, E. Vives, A. Mañosa, L. Labarta, A. Planes, J. Marcos, X. Batlle, Acoustic emission across the magnetostructural transition of the giant magnetocaloric Gd5Si2Ge2, Phys. Rev. B **73** (1) (2006) 1–5. doi:10.1103/PhysRevB.73.014110.

[263] A. Waske, L. Giebeler, B. Weise, A. Funk, M. Hinterstein, M. Herklotz, K. Skokov, S. Fahler, O. Gutfleisch, J. Eckert, Asymmetric first-order transition and interlocked particle state in magnetocaloric La(Fe,Si) 13, Phys. status solidi - Rapid Res. Lett. **9999** (9999) (2015) n/a–n/a. doi:10.1002/pssr.201409484.

[264] A. Pires, J. Belo, I. Gomes, R. Hadimani, D. Schlagel, T. Lograsso, D. Jiles, A. Lopes, J. Araújo, A. Pereira, Suppression of magnetostructural transition on GdSiGe thin film after thermal cyclings, Thin Solid Films. doi:10.1016/j.tsf.2016.09.013.

[265] C. Magen, L. Morellon, P. A. Algarabel, M. R. Ibarra, Z. Arnold, C. Ritter, Hydrostatic Pressure Effects in the Magnetocaloric Compounds R 5 (Si x Ge 1 − x) 4, Adv. Solid State Phys. **46** (2008) (2008) 241–253.

[266] O. Z.W., N. Yoshii, S. Rao, G. H. Wang, Y. Pecharsky, C, V. K. Pecharsky, K. Gschneidner Jr., Field-induced magnetostructural transition in Gd5Ge4 studied by pulsed magnetic fields, Phys. Rev. B **77** (18). doi:10.1103/PhysRevB.77.184426.

[267] R. A. Booth, S. A. Majetich, The magnetocaloric effect in thermally cycled polycrystalline Ni-Mn-Ga, J. Appl. Phys. **111** (7) (2012) 134–137. doi:10.1063/1.3676608.

[268] S. Chatterjee, S. Giri, S. Majumdar, Metastability and inverse magnetocaloric effect in doped manganite (Nd(0.25)Sm(0.25)Sr(0.5)MnO3) and ferromagnetic shape memory alloy (Ni2Mn(1.36)Sn(0.64)): a comparison., J. Phys. Condens. Matter **24** (36) (2012) 366001. doi:10.1088/0953-8984/24/36/366001.

[269] A. B. Gokhale, G. J. Abbaschian, The Gd-Ge (Gadolinium-Germanium) system, Bull. Alloy Phase Diagr. **10** (2) (1989) 147–152.

[270] H. Okamoto, Comment on Gd-Si, J. Phase Equilibria **16** (2) (1995) 198–199.

[271] L. S. Chumbley, O. Ugurlu, R. W. McCallum, K. W. Dennis, Y. Mudryk, G. Jr., V. K. K.A. Pecharsky, Linear microstructural features in R5(Si,Ge)4-type alloys: Difficulties in identification, Acta Mater. **56** (3) (2008) 527–536. doi:10.1016/j.actamat.2007.10.009.

[272] J. S. Meyers, L. S. Chumbley, F. Laabs, A. O. Pecharsky, Determination of phases in as prepared Gd5(SixGe1-x)4, where x=0.5, Scr. Mater. **47** (8) (2002) 509–514. doi:

10.1016/S1359-6462(02)00166-5.

[273] D. Pan, L. M. Liu, B. Slater, A. Michaelides, E. Wang, Melting the ice: On the relation between melting temperature and size for nanoscale ice crystals, ACS Nano **5** (6) (2011) 4562–4569. doi:10.1021/nn200252w.

[274] G. L. Allen, R. A. Bayles, W. W. Gile, W. A. Jesser, Small particle melting of pure metals, Thin Solid Films **144** (2) (1986) 297–308. doi:10.1016/0040-6090(86)90422-0.

[275] J. W. Gibbs, The Collected Works of J. Willard Gibbs, yale unive Edition, Yale University, 1948.

[276] G. Molnár, I. Geröcs, G. Petö, E. Zsoldos, E. Jároli, J. Gyulai, Thickness-dependent formation of Gd-silicide compounds, J. Appl. Phys. **64** (12) (1988) 6746. doi:10.1063/1.342006.

[277] J. E. E. Baglin, Diffusion marker experiments with rare-earth silicides and germanides: Relative mobilities of the two atom species, J. Appl. Phys. **52** (4) (1981) 2841. doi:10.1063/1.329015.

[278] S. Jin, H. Bender, M. F. Wu, a. Vantomme, H. Pattyn, G. Langouche, Epitaxial growth of Gd silicides prepared by channeled ion implantation, J. Appl. Phys. **81** (7) (1997) 3103. doi:10.1063/1.364344.

[279] P. Simonnin, Thermal, Electrical, and Magnetic Properties of the Amorphous Alloys RExSi1-x, Phys. Status Solidi A **551** (98).

[280] G. Peto, E. Zsoldos, N. Q. Khanh, Z. E. Horvath, Amorphous alloy formation and thickness dependent growth of Gd – silicides in solid phase thin film reaction, Thin Solid Films (1998) 417–420.

[281] S. Auffret, J. Pierre, B. Lambert-Andron, R. Madar, E. Houssay, D. Schmitt, E. Siaud, Magnetic properties versus crystal structure in heavy rare-earth silicides RSi2-x, Phys. B **173** (1991) 265–276.

[282] L. Tung, M. Lees, G. Balakrishnan, D. Paul, P. Schobinger-Papamantellos, O. Tegus, P. Brommer, K. Buschow, Field-induced magnetic phase transitions in a GdSi single crystal, Phys. Rev. B **71** (14) (2005) 144410. doi:10.1103/PhysRevB.71.144410.

[283] P. Kushwaha, R. Rawat, Low temperature irreversible field induced magnetic transition in Gd5Ge3, Solid State Commun. **152** (19) (2012) 1824–1828. doi:10.1016/j.ssc.2012.07.008.

[284] I. Mayer, I. Shidlovsky, M5X3 -Type Rare Earth Silicides and Germanides and Their Ternary Phases with Carbon, Inorg. Chem. **828** (15) (1969) 1963–1966.

[285] F. Canepa, S. Cirafici, M. Napoletano, Magnetic properties of Gd5T 3 intermetallic compounds (T = Si,Ge,Sn), J. Alloys Compd. **335** (2002) 3–6.

[286] K. S. V. L. Narasimhan, H. Steinfink, E. V. Ganapathy, The Magnetic Susceptibilities of Some Rare Earth Silicides and Germanides with the D88 Structure The Magnetic Susceptibilities of Some Rare Earth SUicides and Germanides with the DB8 Structure *, J. Appl. Phys. **51** (May 2016). doi:10.1063/1.1657101.

[287] P. H. Tobash, G. Difilippo, S. Bobev, N. Hur, J. D. Thompson, J. L. Sarrao, M. Physics, L. Alamos, K. Magnetization, Structure and Properties of Gd3Ge4: The Orthorhombic RE3Ge4 Structures Revisited (RE =Y, Tb−Tm), Society **46** (21) (2007) 8690–8697.

[288] N. N. Greenwood, A. Earnshaw, The Lanthanide Elements (Z = 58–71), in: Chem. Elem., Elsevier, 1997, pp. 1227–1249. doi:10.1016/B978-0-7506-3365-9.50036-5.
URL http://linkinghub.elsevier.com/retrieve/pii/B9780750633659500365

[289] H. E. Nigh, Magnetization and electrical resistivity of gadolinium single crystals, Ph.D. thesis, Iowa State University (1963).

[290] J. Rubio-Zuazo, M. Vila, A. Muñoz-Martín, A. Bernabé, C. Prieto, Gd thin films: relationship between elastic properties and microstructure, J. Alloys Compd. **324** (2001) 107–110.

[291] H. Zeng, Y. Wu, J. Zhang, C. Kuang, M. Yue, S. Zhou, Grain size-dependent electrical resistivity of bulk nanocrystalline Gd metals, Prog. Nat. Sci. Mater. Int. **23** (1) (2013) 18–22. doi:10.1016/j.pnsc.2013.01.003.

[292] R. J. Gambino, T. R. McGuire, Concentration dependence of magnetic and transport properties of amorphous Gd-Ge alloys, IEEE Trans. Magn. **M** (5) (1984) 398–402.

[293] R. J. Gambino, T. R. McGuire, K. Fukamichi, Magnetic properties and Hall effect of amorphous GdAu films, J. Appl. Phys. **52** (3) (1986) 2190–2192. doi:10.1063/1.328874.

[294] N. Heiman, N. Kazama, Magnetization of amorphous RExCu1− x alloys (RE=Gd, Tb, Dy, Ho), J. Appl. Phys. **49** (3) (1978) 1686–1688. doi:10.1063/1.324888.

[295] A. K. Burnham, Oxidation kinetics for thin rare-earth metal films, J. Vac. Sci. Technol. A Vacuum, Surfaces, Film. **5** (4) (1987) 1713. doi:10.1116/1.574515.

[296] G. Molnar, G. Peto, E. Kotai, E. Zsoldos, J. Gyulai, Oxidation of Gd Thin Films on Si Substrates via Grain Boundaries I, Surf. Interface Anal. **19** (1992) 469–472.

[297] I. Warshaw, R. Roy, Polymorphism of the Rare Earth Sesquioxides, J. Phys. Chem. **65** (11) (1961) 2048–2051. doi:10.1021/j100828a030.

[298] E. H. Williams, The Magnetic Properties of Some Rare Earth Oxides at Low Temperatures, Phys. Rev. **14** (1919) 348–351.

[299] S. L. Bud'ko, P. C. Canfield, Evaluation of a long-time temperature drift in a commercial Quantum Design MPMS SQUID magnetometer using Gd2O3 as a standard, J. Magn. Magn. Mater. **299** (2) (2006) 281–287. arXiv:0503110, doi:10.1016/j.jmmm.2005.04.014.

[300] G. Adachi, N. Imanaka, The Binary Rare Earth Oxides, Chem. Rev. **98** (4) (1998) 1479–1514. arXiv:arXiv:1011.1669v3, doi:10.1021/cr940055h.

[301] X. Tang, J. Katcki, E. Dubois, N. Reckinger, J. Ratajczak, G. Larrieu, P. Loumaye, O. Nisole, V. Bayot, Very low Schottky barrier to n-type silicon with PtEr-stack silicide, Solid. State. Electron. **47** (11) (2003) 2105–2111. doi:10.1016/S0038-1101(03)00256-9.

[302] R. D. Thompson, K. N. Tu, G. Ottaviani, Phase transformations of alloys on a reactive substrate: Interaction of binary alloys of transition and rare-earth metals with silicon, J. Appl. Phys. **58** (2) (1985) 705–710. doi:10.1063/1.336186.

[303] C. H. Luo, L. J. Chen, Growth kinetics of amorphous interlayers and formation of crystalline silicide phases in ultrahigh vacuum deposited polycrystalline Er and Tb thin films on (001)Si, J. Appl. Phys. **82** (8) (1997) 3808. doi:10.1063/1.365743.

[304] W. Huang, G. P. Ru, Y. L. Jiang, X. P. Qu, B. Z. Li, R. Liu, Improvement of Er-silicide formation on Si(100) by W capping, Thin Solid Films **516** (12) (2008) 4252–4257. doi:10.1016/j.tsf.2007.12.154.

[305] N. Reckinger, X. Tang, V. Bayot, D. A. Yarekha, E. Dubois, S. Godey, X. Wallart, G. Larrieu, A. Aszcz, J. Ratajczak, P. J. Jacques, J. P. Raskin, Low Schottky barrier height for ErSi2-x /n-Si contacts formed with a Ti cap, J. Appl. Phys. **104** (10). doi:10.1063/1.3010305.

[306] V. Vas'kovskiy, A. Svalov, A. Gorbunov, N. Schegoleva, S. Zadvorkin, Structure and magnetic properties of Gd/Si and Gd/Cu multilayered films, Phys. B Condens. Matter **315** (1-3) (2002) 143–149. doi:10.1016/S0921-4526(01)01451-X.

[307] D. V. W. Jr, Characterization of the Structural and Magnetic Properties of Gd Thin Films, MasterThesis, Univ. South Florida.

[308] K. M. Kant, C. R. H. Bahl, N. Pryds, A. Smith, J. Schou, Structural and magnetic properties of Gd / Fe multilayers grown by pulsed laser deposition, J. Optoelectron. Adv. Mater. **12** (3) (2010) 576–579.

[309] K. B. Chung, Y. K. Choi, M. H. Jang, M. Noh, C. N. Whang, Phase selective synthesis of gadolinium silicide films on Si(111) using an interfacial SiO2 layer, J. Appl. Phys. **94** (1) (2003) 212. doi:10.1063/1.1581342.

[310] J. E. E. Baglin, Diffusion marker experiments with rare-earth silicides and germanides: Relative mobilities of the two atom species, J. Appl. Phys. **52** (4) (1981) 2841. doi: 10.1063/1.329015.

[311] D. Haskel, G. Srajer, J. C. Lang, J. Pollmann, C. S. Nelson, J. S. Jiang, S. D. Bader, Enhanced interfacial magnetic coupling of GdFe Multilayers, Phys. Rev. Lett. **87** (20) (2001) 207201. doi:10.1103/PhysRevLett.87.207201.

[312] L. Mouketo, N. Binggeli, B. M'Passi-Mabiala, Magnetism at the V/Gd interface., J. Phys. Condens. Matter **22** (18) (2010) 186003. doi:10.1088/0953-8984/22/18/186003.

[313] D. Michels, C. Krill III, R. Birringer, Grain-size-dependent Curie transition in nanocrystalline Gd: the influence of interface stress, J. Magn. Magn. Mater. **250** (2002) 203–211. doi: 10.1016/S0304-8853(02)00385-2.

[314] N. Momozawa, Thickness-dependent Curie temperature of Gd (0001)/W (110) and its dependence on the growth conditions, Phys. Rev. B **47** (17) (1993) 571–574.

[315] C.-J. Hsu, S. V. Prikhodko, C.-Y. Wang, L.-J. Chen, G. P. Carman, Magnetic anisotropy in nanostructured gadolinium, J. Appl. Phys. **111** (5) (2012) 053916. doi:10.1063/1.3691220.

[316] R. Hübner, M. Hecker, N. Mattern, V. Hoffmann, K. Wetzig, C. Wenger, H. J. Engelmann, C. Wenzel, E. Zschech, J. W. Bartha, Structure and thermal stability of graded Ta-TaN diffusion barriers between Cu and SiO2, Thin Solid Films **437** (1-2) (2003) 248–256. doi: 10.1016/S0040-6090(03)00664-3.

[317] X. Niu, M. Xie, F. Zhou, R. Mu, X. Song, S. An, Substituent influence of yttria by gadolinia on the tetragonal phase stability for Y2O3-Ta2O5-ZrO2 ceramics at 1300C, J. Mater. Sci. Technol. **30** (4) (2014) 381–386. doi:10.1016/j.jmst.2013.12.008.

[318] Y. Narumi, Y. Tanaka, N. Terada, M. Rotter, K. Katsumata, T. Fukui, M. Iwaki, K. Kindo, H. Toyokawa, A. Tanaka, T. Tsutaoka, T. Ishikawa, H. Kitamura, Magnetization process and the associated lattice deformations in an intermetallic compound Gd5Ge3, J. Phys. Soc. Japan **77** (5) (2008) 1–4. doi:10.1143/JPSJ.77.053711.

[319] G. Gadioli, F. Rouxinol, R. Gelamo, L. Cardoso, S. Gama, M. B. de Moraes, Magnetic and

structural studies on nanostructured Gd/Cr multilayer films, Thin Solid Films **545** (2013) 496–502. doi:10.1016/j.tsf.2013.07.066.

[320] J. C. Chen, G. H. Shen, L. J. Chen, Growth kinetics of amorphous interlayers by solid-state diffusion in ultrahigh vacuum deposited polycrystalline Gd thin films on (001)Si, J. Appl. Phys. **84** (11) (1998) 6083. doi:10.1063/1.368920.

[321] A. Travlos, N. Salamouras, E. Flouda, Epitaxial erbium silicide films on(100) silicon: growth, structure and electrical properties, Appl. Surf. Sci. **120** (3-4) (1997) 355–364. doi:10.1016/S0169-4332(97)00382-6.

[322] J. C. Chen, G. H. Shen, L. J. Chen, Formation of Gd oxide thin films on (111)Si, Appl. Surf. Sci. **142** (1) (1999) 120–123. doi:10.1016/S0169-4332(98)00663-1.

[323] H. F. Belliveau, Y. Y. Yu, Y. Luo, F. X. Qin, H. Wang, H. X. Shen, J. F. Sun, S. C. Yu, H. Srikanth, M. H. Phan, Improving mechanical and magnetocaloric responses of amorphous melt-extracted Gd-based microwires via nanocrystallization, J. Alloys Compd. **692** (2017) 658–664. doi:10.1016/j.jallcom.2016.08.254.

[324] F. Qin, N. Bingham, H. Wang, H. Peng, J. Sun, V. Franco, S. Yu, H. Srikanth, M. Phan, Mechanical and magnetocaloric properties of Gd based amorphous microwires, Acta Mater. **61** (4) (2013) 1284–1293. doi:10.1016/j.actamat.2012.11.006.

[325] J. Choi, S. Choi, J. Kim, S. Na, H. J. Lee, S. H. Lee, H. Kim, Silicide formation process of Er films with Ta and TaN capping layers, ACS Appl. Mater. Interfaces **5** (23) (2013) 12744–12750. doi:10.1021/am4041338.

[326] S. Mardani, H. Norstrom, U. Smith, J. Olsson, S. L. Zhang, Influence of tantalum tantalum nitride barriers and caps on the high-temperature properties of copper metallization for wide-band gap applications, Microelectron. Eng. **137** (1) (2015) 37–42. doi:10.1016/j.mee.2015.01.023.

[327] M. Soffner, J. Tedesco, F. Pedrochi, G. Gadioli, M. de Moraes, a.O. Guimarães, E. da Silva, a.M. Mansanares, Photothermally modulated magnetic resonance applied to the study of the magnetic phase transition in gadolinium thin films, Thin Solid Films **520** (9) (2012) 3634–3640. doi:10.1016/j.tsf.2011.12.042.

[328] A. M. Pires, M. R. Davolos, C. O. Paiva-Santos, E. B. Stucchi, J. Flor, New X-ray powder diffraction data and Rietveld refinement for Gd2O3 monodispersed fine spherical particles, J. Solid State Chem. **171** (1-2) (2003) 420–423. doi:10.1016/S0022-4596(02)00224-4.

[329] A. Nissim, A. Raveh, J. Sariel, M. Mintz, Effect of substrate bias voltage on the properties of magnetron-sputtered gadolinium layers, Surf. Coatings Technol. **201** (16-17) (2007) 7054–7059. doi:10.1016/j.surfcoat.2007.01.017.

[330] T. Laurila, K. Zeng, J. K. Kivilahti, J. Molarius, I. Suni, Chemical stability of Ta diffusion barrier between Cu and Si, Thin Solid Films **373** (1-2) (2000) 64–67. doi:10.1016/S0040-6090(00)01102-0.

[331] H. Yu, S. Zhu, X. Yang, X. Wang, H. Sun, M. Huo, Synthesis of Coral-Like Tantalum Oxide Films via Anodization in Mixed Organic-Inorganic Electrolytes, PLoS One **8** (6) (2013) 6–11. doi:10.1371/journal.pone.0066447.

[332] L. Liu, Y. Wang, H. Gong, Annealing effects of tantalum films on Si and SiO2/Si substrates in various vacuums, J. Appl. Phys. **90** (1) (2001) 416–420. doi:10.1063/1.1372662.

APPENDIX A

Pure Gd films

A.0.0.1 Pure Gd films annealed at low temperatures

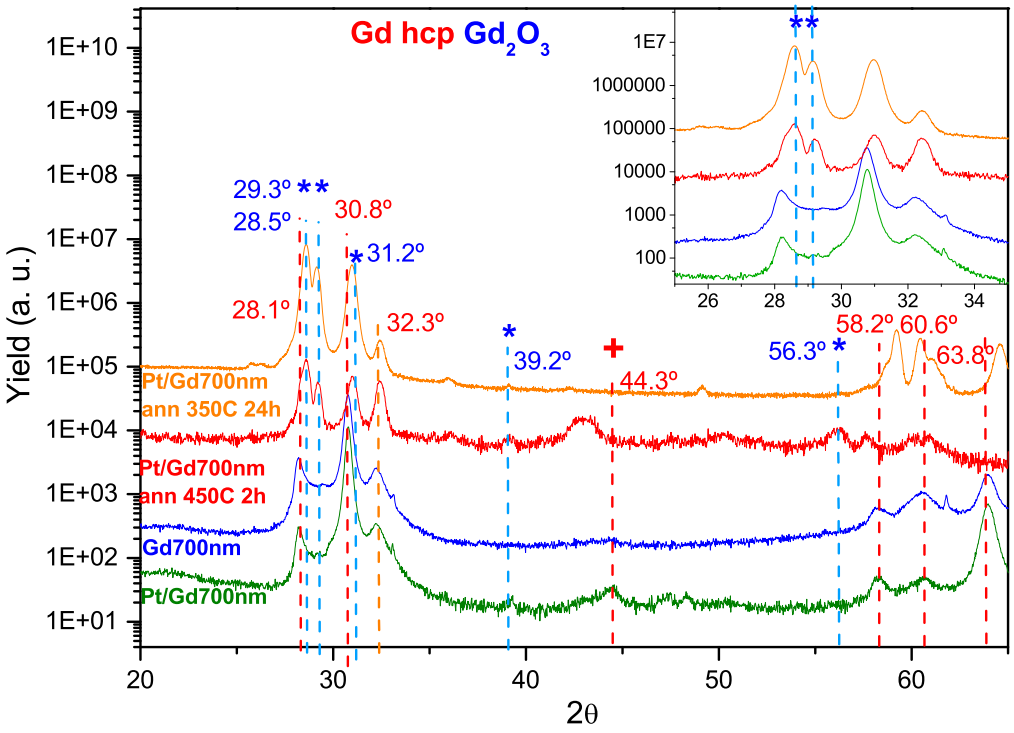

Figure A.1 – X-ray diffraction patterns of as-cast (blue) and annealed at 450°C for two hours (red) and at 350°C for 24 hours (orange) Platinum covered Gd thin film and uncovered Gd as-cast thin film (green) in the 20-65° two θ range. Inset shows enlarged 25-35° 2θ interval.

Two pure Gadolinium thin films were deposited on top of room temperature SiO_2 (~ 800 nm)/Si substrate: one covered with 10 nm Pt cap layer and the other with no buffer. Gd was sputtered using a DC source with 80 W power and an Argon working pressure of 4 mBar inside the chamber. Previous calibration depositions yielded an estimated 10 nm/min Gd deposition rate under these conditions. Both thin films have an estimated thickness of ~ 700nm,. As can be seen in Figure A.1 both Pt covered and uncovered (green and blue curves, respectively) Gd thin films present a very similar XRD spectra, revealing a similar crystallography: hcp structure, P63/mmc space group, with a

preferential orientation towards the (0 0 2) Miller index atomic plane. The hcp is the most common Gd structure and the (0 0 2) preferential orientation has been found in previous reports on Gd thicker films grown at room temperature or above it[127,128]. The $2\theta \sim 44.3°$, more clearly seen in Pt covered thin film, might be associated with a small fraction of body centered cubic structure (bcc, Im3m space group). Furthermore, a very small peak is observed at $2\theta \sim 29.3°$, which can be clearly associated with the Gd sesquioxide, Gd_2O_3. The Pt covered thin film was subjected to ex-situ annealings: the film wrapped

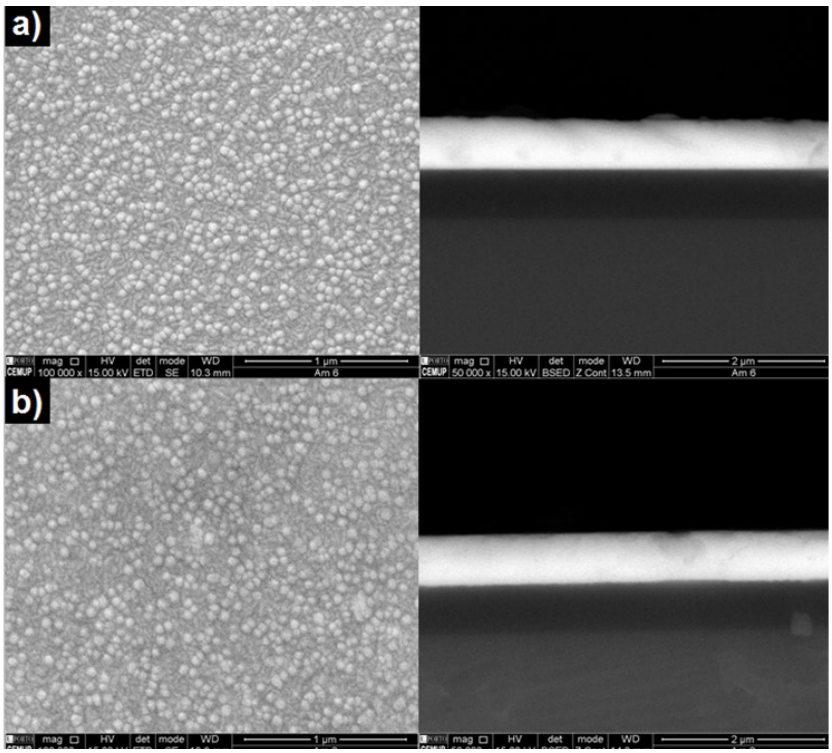

Figure A.2 – Top and cross-section SEM view (left and right) of as-cast (a)) and annealed (b)) Platinum covered Gd thin film.

in a Zr foil, was inserted in a furnace at 350°C and 450°C inside a quartz tube which was evacuated by a vacuum pump down to $5x10^{-6}$ mBar. The annealings lasted for 24 and 2 hours, respectively, after which the quartz tube, with the film inside, was removed from the furnace and was left to cool down at the room temperature. There are significant crystallographic changes upon annealing, in particular in the narrow [28, 33]° 2θ interval: a drastic decrease of the most intense peak at $2\theta \sim 30.8°$, a large rise of the $2\theta \sim 29.3°$ peak and the "*shifts*": 28.1 –> 28.5° and 30.8 –> 31.2°, clearly signal the decline of the Gd hcp phase and the rise of the Gd sesquioxide. Such changes are even more drastic for the longer annealing, where Gd_2O_3 is the majority phase and only a small Gd hcp fraction was retained. The emergence of 39.2° and 56.3° peaks, also associated with Gd_2O_3, corroborate this interpretation. Scanning Electron Microscopy (SEM) images of both as-cast and annealed (2h) thin films are shown in Figure A.2. A very irregular morphology is observed for both as-cast and annealed film: the thin (5 nm) Pt capping layer is not uniformly distributed along the thin film surface but rather in small clusters of

lumps with few tenths of nanometers wide. The annealing does not seem to have altered significantly the film morphology. Similar lumps were also observed in a Er film covered by a thin W capping layer after annealing, where the lumps were associated with an Er-W minority phase formation[304]. Here, a similar process might have occurred, with Pt forming amorphous-like lumps, instead of a proper continuous and homogeneous layer capable of preventing Gd oxidation. Hence, the inhomogeneous Pt distribution, allowed the Oxygen penetration during the annealing and the temperature provided (350°C and 450°C) to the system was enough to promote the Gd_2O_3 formation. The diffractograms of the two annealings illustrate well the Gd consumption by Oxygen over time, forming Gd_2O_3. Although it is not easy to index the structure of peaks in the 55-65° 2θ interval to any Gd or Gd_2O_3 phases it is possible to conjecture that it is associated with the formation of Gd-Pt-Si-O silicates. The as-deposited Pt covered and the two annealed Gd thin films magnetization were studied by SQUID magnetometry on cooling under an applied magnetic field μ_0H=0.1 T. Both magnetization as a function of temperature (M(T)) curves are plotted in Figure A.3. The three samples exhibit a paramagnetic to ferro(ferri)magnetic state at a well defined temperature: Curie temperature, $T_C^{as} \sim 273$ K, $T_C^{ann350} \sim 290$ K, $T_C^{ann450} \sim 296$ K. Interestingly, the annealed magnetization/mass at the lowest temperature (5 K) evolves significantly with the annealing, being ~ 140, 120 and 35 emu g^{-1} for the as-deposited, the annealed at 450°C (2 h) and the 350°C (24 h), respectively.

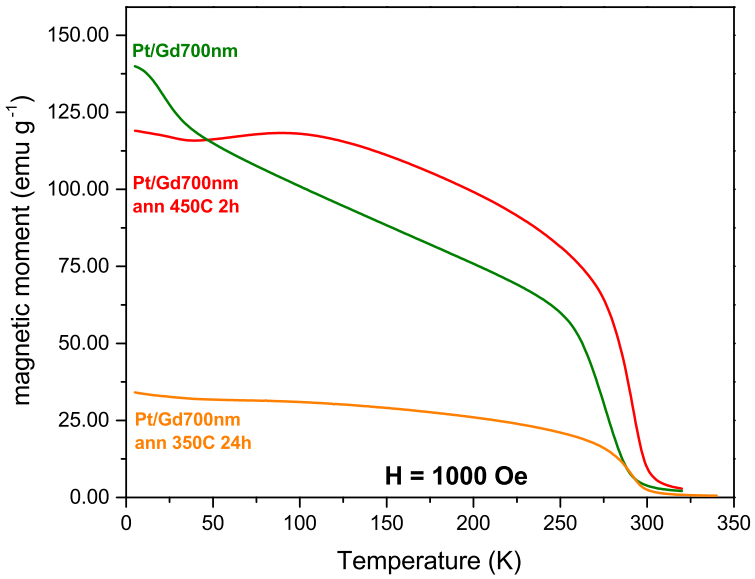

Figure A.3 – Magnetization as a function of temperature for the Pt covered Gd as deposited thin film (green), after a two-hours annealing at 450°C (red) and after a 24 hours annealing at 350°C under an applied magnetic field μ_0H=0.1 T. The total magnetization was normalized to the estimated Gd mass of each thin film sample.

Moreover, no further magnetization increase is observed in the annealed films, in contrast with the feature observed at T=T′=22 K for the as-deposited film. Furthermore, their magnetization as a function of applied field was also assessed at 5 K (not shown

here), where despite no saturation was observed for any film, a typical ferromagnetic-like field dependency was found together with a small paramagnetic contribution. The maximum magnetization values obtained at μ_0H=5 T were 7.02, 5.88 and 2.10 μ_B , which correspond to approximately 93 %, 78 % and 28 % of the theoretical Gd value (7.55 μ_B), for the as-deposited and the annealed (450°C for 2 h and the 350°C for 24 h) films, respectively. The magnetization results corroborate the morphological and structural analysis: Gd_2O_3 is promoted with the annealing process at the expense of Gd pure phase, which results in a loss of overall magnetization, as the Gd atoms in the sesquioxide phase just order their magnetic moments along the field direction at temperatures very close to absolute zero (as occurs for all pure paramagnets). Here, despite the lower temperature, the 24 hours annealing at 350°C is enough to enhance the Gd sesquioxide phase formation. Paradoxically, the remaining Gd phase, strengthens its magnetic correlations, increasing its Curie temperature by a maximum of 23 K (from 273 K to 296 K). As suggested in previous reports, such enhancement, must be a consequence of structure stabilization achieved through annealings[327].

A.0.0.2 Pure Gd films annealed at high temperatures

A pure Gd thin film was deposited on top of the 15 nm Ta buffer layer with an overall thickness of 225 nm which is finally covered by another 15 nm of a Ta cap layer. Five thermal treatments lasting 30 minutes were performed for several pieces of the same original Gd thin film by varying the annealing temperature: 600°C, 700°C, 800°C, 900°C and 1000°C. All were terminated through a quenching to room temperature.

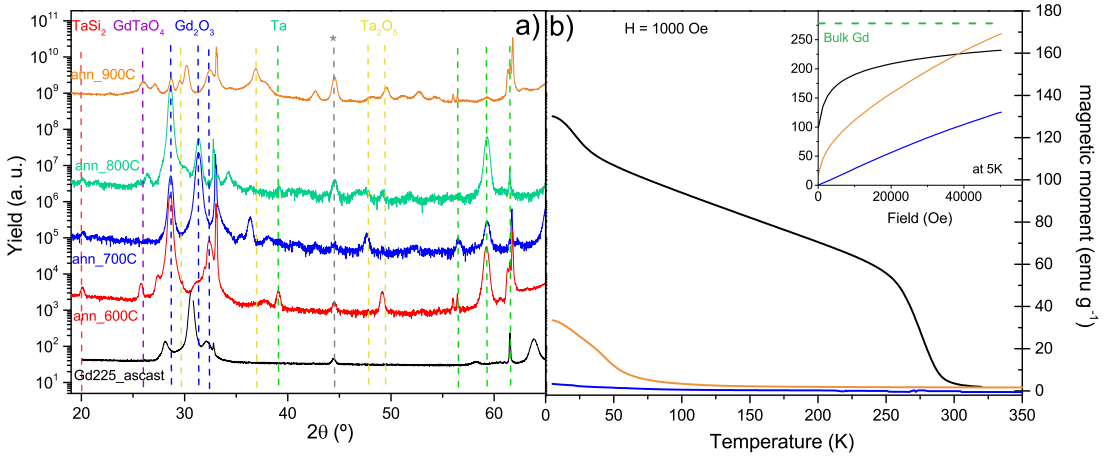

Figure A.4 – a) X-ray diffraction patterns for the as-deposited (black) and annealed for 30 minutes at 600°C (red), 700°C (blue), 800°C (green) and 900°C (orange). The dashed vertical lines signal Gd_2O_3 (dark blue), Ta (green), Ta_2O_3 (yellow), $TaSi_2$ (red) and $GdTaO_4$ (purple) associated peaks. b) Magnetization as a function of temperature of as-deposited (black) and annealed for 30 minutes at 700°C (blue) and 900°C (orange) measured on cooling and heating under μ_0H=0.1 T. In the inset the magnetization as a function of the field up to 5 T.

The structural investigation by XRD demonstrates that the as-deposited thin film crystallized mostly in the same hcp structure, P63/mmc space group, with a preferential orientation towards the (0 0 2) Miller index atomic plane as the previously prepared pure Gd thin film. As for the annealed films, they can be divided in two groups: one comprising the 600°C (red), 700°C (blue), 800°C (green) and the other one for 900°C (orange), portrayed in Figure A.4. Hence, for temperatures T < 900°C, the same set of the three most intense peaks (in the 2θ 25-35° interval) emerge, being indexed to the Gd sesquioxide[328,329]. Furthermore, at high 2θ angles ~ 60° one observes the emergence of another set of three peaks in this temperature range which might be associated to the Ta layers crystallization, known to occur within this temperature interval[316,330,331]. At 900°C (orange curve in Figure A.4) additional phases crystallize such as Ta_2O_5[331,332] and $GdTaO_4$[317] as represented by the dash vertical lines in Figure A.4, and most certainly Gd-Si-Ta-O silicates[325]. The magnetization as a function of temperature of the as-deposited and annealed at 700°C (blue) and at 900°C (orange) measured on cooling and under the influence of a 0.1 T magnetic field, measured on cooling. A drastic reduction of the magnetization values was observed for the annealed samples, revealing a paramagnetic like behavior, similar to the one found for the low-temperature annealed pure Gd films. However, as inspected by the magnetization as a function of magnetic field measured at 5 K, the annealed film at 900°C (orange) demonstrates a stronger FM-like behavior than the annealed film at 700°C (blue), which might be associated with the formation of spurious Gd silicates for higher formation. In Figure A.5 a) two top-views of the film annealed at 900°C are presented, with focus given to the fragmented microstructure, caused by the formation of cracks. In Figure A.5 a) inset, a textured morphology is observed probably associated with crystalline Ta[331].

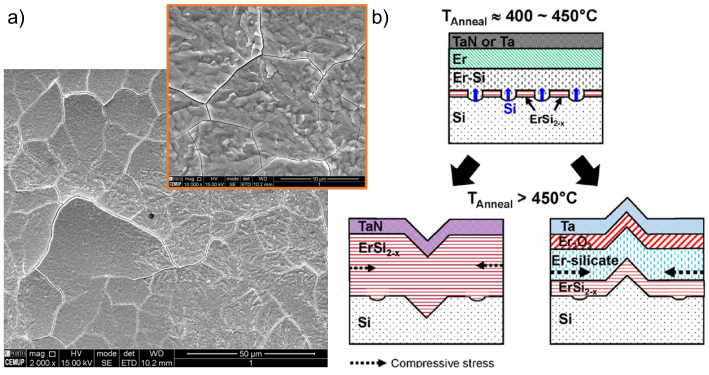

Figure A.5 – a) SEM pictures with 2000 and 10000 (inset) times magnification of the surface of the pure Gd annealed film at 900°C for 30 minutes, revealing cracks at the surface. b) Schematic illustration of bump-like features generated by compressive stress due to the thermal expansion coefficients of the different phases that typically crystallize in a Ta/Rare-Earth/Si system at T > 450°C, as represented in Reference[325].